Physical Diagnostics of Cartilage Degeneration

by

Steven Treppo

S.M., Mechanical Engineering,
Massachusetts Institute of Technology, 1994
B.A.Sc., Mechanical Engineering,
University of Toronto, 1992

Submitted to the Harvard–M.I.T.
Division of Health Sciences and Technology
in Partial Fulfillment of the
Requirements for the Degree of
Doctor of Philosophy

at the

Massachusetts Institute of Technology
January 1999
[February, 1999]

Signature of Author _____
Harvard–M.I.T. Division of Health Sciences and Technology
January 11, 1999

Certified by _____
Alan J. Grodzinsky, Sc.D., Thesis Supervisor
Professor of Electrical, Mechanical, and Bioengineering, M.I.T.

Accepted by _____
Martha L. Gray, Ph.D.
J. W. Kieckhefer Associate Professor of Electrical Engineering
Co-Director, Division of Health Sciences and Technology

Physical Diagnostics of Cartilage Degeneration

by

Steven Treppo

Submitted to the Harvard–M.I.T. Division of Health Sciences and Technology in partial fulfillment of the requirements for the Degree of Doctor of Philosophy, January 11, 1998.

Abstract

Establishing the link between macroscopic electromechanical properties, biochemical composition and ultrastructural organization in cartilage will elucidate the role of mechanical forces in regulating the biosynthetic activity of chondrocytes to maintain a functional extracellular matrix (ECM), and how this process is compromised as osteoarthritis (OA) progresses. Assessment of physical properties of articular cartilage may lead to a better understanding of why certain joints are more prone to OA. Symptomatic OA develops rarely in the ankle (<1%), and the prevalence is independent of age, while in the knee the prevalence increases to 10% in those over 65 years of age. In this study, a protocol was developed to assess the biomechanical properties and biochemical composition of human knee and ankle cartilage. It was found that the ECM of the talar (ankle) cartilage is denser with higher charged glycosaminoglycan content and lower water content, consistent with a higher equilibrium modulus and dynamic stiffness, and lower hydraulic permeability. This denser ECM may be chondroprotective. Its biomechanical properties may endow it with an increased stability to loading, protecting the chondrocyte and making the cartilage less susceptible to OA. These findings demonstrate the utility of diagnostic tools which assess the physical properties of cartilage.

It had been previously shown that damage due to trypsin, which predominately degrades proteoglycan, can be sensitively detected by surface electromechanical spectroscopy measurements. We, therefore, tested the hypothesis that surface electromechanical spectroscopy measurements could sensitively detect degradative changes in cartilage matrix caused by collagenases MMP-1 and MMP-13. We found that MMP-1 induced damage to the collagen-aggrecan network was detected by changes in the current-generated stress response. In addition, the measurement of total tissue impedance using interdigitated electrodes placed on the cartilage surface was capable of detecting superficial (MMP-13) and deeper (MMP-1) lesions caused by collagenase *in vitro*. The ability of surface electromechanical spectroscopy to detect changes in both electrokinetic and impedance properties enhances its potential diagnostic capabilities *in vivo*.

Diagnostic applications of surface electromechanical spectroscopy *in vivo* require the measurement of current-generated stress and impedance non-destructively during arthroscopic or open joint procedures. Therefore, an electrokinetic surface probe has been designed with a 4.5 mm diameter active area. Its size makes it possible to use it within an arthroscopic canula. Its multiple wavelength capability permits the spatial localization of surface cartilage lesions typical of early progressive OA. This a step toward providing physicians with a diagnostic tool for determining cartilage degeneration in the clinic.

Thesis Supervisor:

Alan J. Grodzinsky, Sc.D. .. Professor of Electrical, Mechanical, and Bioengineering
Massachusetts Institute of Technology

Thesis Committee:

Roger D. Kamm, Ph.D. ..... Professor of Mechanical Engineering
Massachusetts Institute of Technology

Myron Spector, Ph.D. ..... Director of Orthopaedic Research
Brigham and Womens Hospital

Stephen B. Trippel, M.D. ..... Associate Professor of Orthopaedic Surgery
Harvard Medical School

Ada A. Cole, Ph.D. (Reader) ..... Associate Professor of Biochemistry
Rush Medical College, Chicago, IL

Ivan G. Otterness, Ph.D. (Reader) ..... Research Advisor
Pfizer Central Research, Groton, CT

Acknowledgements

When I began searching for lab in which to do my Ph.D. research, the Continuum Electromechanics Lab was often recommended. Over the years, I have come to understand the reasons. Al is its leader, and deserves many thanks. He walked a fine line to provide the complete freedom and gentle guidance that helped to produce my work. His enthusiasm is infectious, and patience boundless. I appreciate his magical ability to set high standards for my work through a little coaxing and even fewer words.

I would like to thank my thesis committee members, Prof. Myron Spector, Prof. Roger Kamm and Dr. Stephen Trippel for there guidance and support of my work. I am indebted to our collaborators. Dr. Klaus Kuettner, Dr. Ada Cole and the group at Rush Medical Center in Chicago were instrumental in all aspects of the human knee and ankle work. Dr. Ivan Otterness and his colleagues at Pfizer provided enzymes and the necessary background to interpret our results. I thank Ada and Ivan, who provided a careful review of the thesis.

A thanks to all those who have probed, especially Emerson, Nik, and Dave for titrating the long hours with the appropriate laughter. Special thanks to David Breslau for his design expertise and Jim Byrne for patiently teaching me how to machine.

Another reason for the great reviews stem from the people. If nothing else, the lab was a fun place to work. Linda is the main reason and social coordinator, while Han-Hwa (who showed up late in the game) was great to work with. Eliot provided technical help.

Friends will be the richest gift MIT provided. I am not even going to start with Paula. In my mind she is simply "my friend". I just consider myself lucky to have known her, everything else is icing on the cake. Jorge, my only roommate (ever), it is your charge to continue the *kaizen* toward the utopian, "Arnie lifestyle". Shin is the first person I met on arrival to MIT, and has been a giving friend ever since.

I realized very early on that one of the toughest things about MIT was being away from "The Boys". I savor the time we spend together, and fill in the gaps with the memories.

Nothing would have been possible without Sandra, my wife, my saviour. We have been through more than we can remember, and it is, thankfully, only beginning. Markus is the best thing to ever happen to us, and Sandra and I hope that we can emulate the examples we had in our parents. My family always provides unconditional love and support. I will always be grateful to my father for teaching me that, "If you want something done right, you have to do it yourself". It is so true.

This research was sponsored by MEMP/HST, Pfizer, Inc., a NIH SBIR grant to Wagner and Associates, and a Poitras Fellowship.

Contents

Abstract **2**

Acknowledgements **4**
Contents **5**
List of Figures **9**
List of Tables **24**

I Introduction **25**
1.1 Articular Cartilage . . . 25
1.1.1 Structure . . . 26
1.1.2 Function . . . 36
1.2 Cartilage Diagnostics . . . 38
1.3 Osteoarthritis . . . 42
1.3.1 Epidemiology . . . 43
1.3.2 Pathogenesis . . . 43
1.3.3 Mechanical Changes . . . 44
1.3.4 Biochemical Composition Changes . . . 45
1.3.5 Diagnosis . . . 45
1.3.6 Arthroscopy . . . 46
1.3.7 Treatment . . . 47
1.4 Repair of Focal Defects . . . 47
1.5 *In Vivo* Human Cartilage Probes . . . 49
1.6 Electromechanical Surface Spectroscopy . . . 51
1.7 Previous Work on the Electrokinetic Surface Probe . . . 53
1.7.1 Probe Sensitivity to Cartilage Fixed Charge Density . . . 53
1.7.2 Variable Wavelength Imaging of Current-Generated Stress Following Loss of Aggrecan . . . 54
1.7.3 *In Vivo* Arthrosopic Handheld Electrokinetic Probes . . . 58
1.8 Cartilage Diagnostics: A Paradigm . . . 58
1.9 Outline of Results . . . 60

II Comparison of Biomechanical and Biochemical Properties of Cartilage from Human Knee and Ankle **62**
2.1 Abstract . . . 62
2.2 Introduction . . . 63
2.3 Materials and Methods . . . 66
2.3.1 Cartilage Explant . . . 66
2.3.2 Physical Properties . . . 68
2.3.3 Biochemical Composition and Swelling . . . 68
2.3.4 Statistical Analysis . . . 69

2.4 Results 69
2.4.1 Biochemical Composition and Swelling 70
2.4.2 Physical Properties 70
2.4.3 Site Dependent Inhomogeneities Within a Joint Surface 72
2.4.4 Depth Dependent Inhomogeneities in Physical Properties and Biochemical Composition 73
2.4.5 Relationships Between Physical and Compositional Properties 74
2.5 Discussion 75

III Effects of MMP-1 and MMP-13 Induced Matrix Degradation on Electrokinetic and Dielectric Properties of Adult Articular Cartilage by Surface Spectroscopy 79
3.1 Introduction 79
3.2 Methods 82
3.2.1 Statistical Analysis 85
3.3 Results 86
3.3.1 Immunohistochemistry 86
3.3.2 Quantitative Analysis of Matrix Damage 86
3.3.3 Current-Generated Stress 87
3.3.4 Impedance 88
3.4 Discussion 88

IV Effects of Trypsin Induced Matrix Degradation on the Dielectric Properties of Newborn Articular Cartilage by Surface Spectroscopy 93
4.1 Introduction 93
4.2 Theoretical Considerations 97
4.3 Materials and Methods 100
4.3.1 Specimen Preparation and Experimental Setup 100
4.3.2 Measurement of Cartilage Impedance 103
4.4 Results 106
4.5 Discussion 108

V Development of a Arthroscopic *In Vivo* Electrokinetic Surface Probe 114
5.1 Introduction: Design Paradigms 114
5.2 Design and Construction of the HHV5.0 Probe 117
5.2.1 Electrode/Transducer Structure Design 118
5.2.2 Probe Body Design 121
5.2.3 ETS Fabrication 121
5.2.4 HHV5.0 Probe Body Construction 125
5.2.5 Probe Assembly 127
5.2.6 Electrode Chloridation 128
5.3 Calibration 129

5.3.1 Hardware setup . . . 130
5.3.2 Procedure . . . 130
5.4 Current-Generated Stress . . . 131
5.4.1 Hardware Setup . . . 131
5.4.2 Procedure . . . 131
5.4.3 Correcting for Parasitic Capacitance . . . 131
5.5 Results . . . 133
5.6 Discussion . . . 135

VI Summary **137**

A Past, Present and Future of Cartilage Repair & Electromechanical Property Assessment in Cartilage Repair Model Systems **139**
A.1 Introduction . . . 139
A.2 Scope . . . 140
A.3 Past . . . 140
A.4 Present . . . 143
A.4.1 Cartilage Basics . . . 143
A.4.2 Response to Injury . . . 144
A.4.3 Present Clinical Approaches to Healing of Articular Cartilage 146
A.5 Future . . . 151
A.5.1 Cell Based Cartilage Resurfacing . . . 151
A.5.2 Assessing the Success of Focal Repair for the Long Term . . . 154
A.5.3 Case Study: Growth-Factor Induced Repair of Partial Thickness Articular Cartilage Defects . . . 155
A.5.4 Summary of Factors Affecting Future Development . . . 156
A.6 Examples Electromechanical Property Assessment in Cartilage Repair Model Systems . . . 157
A.6.1 Bioreactor Cultivation Conditions Modulate the Composition and Mechanical Properties of Tissue Engineered Cartilage . . 158
A.6.2 Integration of Engineered Cartilage into Natural Cartilage: *In Vitro* Studies . . . 163

B Measurement of the DNA Content in Human Adult Articular Cartilage Using Hoechst Dye 33258 **169**
B.1 Introduction . . . 169
B.2 Materials and Methods . . . 170
B.3 Results . . . 171
B.4 Discussion . . . 174

C Determination of Hydroxyproline Content of Articular Cartilage Samples **177**
C.1 Introduction . . . 177

C.2 Materials and Methods 177
C.2.1 Chemicals/Supplies 177
C.2.2 Protocol 178
C.3 Theoretical Considerations 181
C.4 Validation 184
C.5 Sensitivity and Conversion to Collagen Content 185

D Development of a Arthroscopic *In Vivo* Electrokinetic Surface Probe - Details 188
D.1 Hand Held Version 5.0 Probe 188
D.2 Design Iterations of ETS Electrode Patterns 189
D.3 Wavelength Calculation For Circular Electrodes 190

E Intrinsic Parameter Estimation Based on Electromechanical Surface Spectroscopy Measurements 192
E.1 Introduction 192
E.2 Material and Methods 193
E.2.1 Electrokinetic Probe Fabrication 193
E.2.2 Experimental Chamber 195
E.2.3 Cartilage Explants 197
E.2.4 Confined Compression Testing 198
E.2.5 Current-Generated Stress 198
E.2.6 Piezo Calibration 199
E.2.7 Biochemical Compositional Analysis 200
E.3 Theoretical Considerations - Modeling and Parameter Estimation . . 201
E.3.1 Relevant Parameters 201
E.3.2 Response of the CGS Model to Parameter Changes 203
E.4 Preliminary Experimental Results 204
E.4.1 Results From a Typical Experiment 204
E.4.2 Confined Compression Results 206
E.4.3 CGS and Parameter Estimation Results 206
E.4.4 Summary of Results 208
E.5 Discussion 209

F Development of an Analytical Approximation to CGS Using a Dimensional Analysis Technique 212
F.1 Introduction 212
F.2 Current-Generated Stress 213
F.3 Impedance 218

References 219

List of Figures

1.1 A schematic depicting the three main structural components of cartilage: chondrocytes (large round cells), proteoglycans (bottle brush structures), and collagen fibrils. Tissue mechanical properties depend on the organization, structure and amount of these macromolecules present in the ECM. Collagen type II fibrils (along with small amounts of types IX and XI) form the framework for cartilage as a dense crosslinked network with proteoglycans embedded within. Proteoglycans contain polyanionic negative fixed charge sulfated glycosaminoglycan (sGAG) chains that create a large osmotic swelling pressure, drawing water into the ECM, while expanding (applying tension) the collagen network. 27

1.2 A schematic of a microscopic view of an aggrecan proteoglycan molecule showing aggrecan with its associated sGAG chains attached to hyaluronate via a link protein (adapted from Heinegard et al. [99]). At physiologic pH, the high density of fixed COO^- and SO_3^- groups are formed by incorporating newly synthesized aggrecan onto immobile hyaluranon via a link protein. 28

1.3 Mechanical deformations applied through the porous electrode to the ECM at the cartilage surface results in fluid flow and movement of entrained (+) counterions relative to the fixed charged groups found on PGs. This charge separation produces an electric field antiparallel to fluid flow and the resulting open circuit voltage is called the streaming potential. 38

1.4 Applied current density produces coupled fluid and solid mechanical effects. (1) Electrophoretic force on matrix fixed charged groups (toward + electrode) and (2) Electroosmotic flow of interstitial fluid (toward - electrode). 39

1.5 Surface probe consisting of excitation electrode array and mechanical surface stress sensor mounted on cartilage. Theoretical analysis has shown that current-generated stress can be measured by applying a standing wave of current to the cartilage surface of an intact joint, allowing for a non-destructive measurement. The current-generated stress in the bulk tissue is complex but related to the intra-tissue current density profile shown by the arrows [199]. This field can have an independently imposed temporal frequency and spatial wavelength (λ). The penetration depth of the measurement is proportional to the spatial wavelength (λ) and also increases with decreasing frequency [199](Courtesy S. Berkenblit [13]). 52

1.6 Current-generated stress amplitude (A) normalized to its response at pH 7, and phase (B) versus bath pH for adult bovine cartilage, tested with an applied current density of 1 mA/cm^2 at 0.025 (filled circles), 0.1 (filled triangles), and 1.0 Hz (filled squares). Magnitude of the fixed charge density (C) in adult bovine cartilage by chemical titration. The net charge changes sign as it passes through the isoelectric point (IEP) in the range pH 2.4-2.8. The minimum stress amplitude (a) and a 180^o phase shift (b) occur close to the IEP (Courtesy of S. Berkenblit [13]). 55

1.7 Schematic of a probe with four independently addressable electrodes. By varying the external connections to each electrode, multiple wavelengths λ can be applied using a single device. Depicted is a "long" (A) and "short" (B) wavelength pattern (related to the electrode spacing, λ), where the relative depth of penetration of the current is represented by the arrows. If the shaded region represents degraded cartilage, examination of short and long wavelength responses enable spatial imaging of the pattern degradation. 56

1.8 Ratio of short-wavelength to long-wavelength stress response measured in full-thickness calf cartilage-bone plugs, both before (filled squares) and after (open squares) 2 hours of surface trypsin digestion to remove proteoglycans from the extracellular matrix (N=4, mean $\pm$SEM). Current-generated stress was measured with a multiple-wavlength probe. Up to frequencies of 0.25 Hz, post-digestion values were significantly different from controls (filled star for $p \leq 0.01$, open star $p \leq 0.05$ by ANOVA) (Courtesy of S. Berkenblit [13]). 57

1.9 The handheld probe has been used to make *in vivo* measurements with a canine model during an open joint procedure (open circles). The data is in close agreement with output acquired from adult bovine cartilage (closed circles) with the same device. 59

1.10 Schematic representation of our approach to cartilage diagnostics. Confined compression tests and electrokinetic surface probe measurements are both experimental techniques that give data which reveals information about the state of cartilage. These data can be inputs into models which have been developed to estimate the material properties of AC. In addition we can perturb AC by enzyme treatment or by using osteoarthritic tissue, and then go through the experiments and modeling to see how each technique is sensitive to biochemical and/or structural changes in AC. 60

2.1 Top left, the distal femur taken inferiorly depicting the locations of the 6 harvest sites: The patellar surface of the distal femur (FP) and anterior (C) and posterior (P) of the femoral condyles always taken from both the medial (M) and lateral (L) aspects. Bottom left, the proximal tibial surface with the menisci removed. Cores were removed from the anterior (A) and posterior (P) aspects. Top right, the talar surface of the talocrural joint with 9.5 mm diameter cores removed for the anterior (A) and posterior (P) aspects. The schematic on the bottom right shows the top 1 mm slice of cartilage being removed from the knee (tibiofemoral) and ankle (talar) cores with the additional cartilage down to the tidemark also removed from the knee cores. From each cartilage plug, four 3 mm disks were punched for electromechanical testing and/or biochemical composition analysis. 67

2.2 The biochemical composition of the pooled cartilage samples of the top 1 mm of talar (TA), distal femur (F), and tibial plateau (TP). (A) The water content of TA was lower than that of the F and the TP, while F was lower than TP. (B) The swelling ratio (SR)(defined in text) was higher in TP than TA or F. (C) The sGAG/WW was higher in the TA than either the F or TP. (D) HYPRO/WW was significantly lower in the TP than the TA. Bars correspond to the mean ± SE, and the differences assessed by ANOVA with Fisher's LSD test: filled star, F or TP significantly different than TA; open star, TP significantly different than F; filled square, TP significantly different than F and TA; all $p < 0.01$. 71

2.3 The electromechanical properties of the pooled cartilage samples of the top 1 mm of talar (TA), distal femur (F), and tibial plateau (TP). (A) The equilibrium modulus (H_A) was higher for TA than F and TP, and F was higher than TP. (B) The dynamic stiffness (shown at 0.1Hz) exhibited the same trend as H_A over the entire frequency range studied. (C) The hydraulic permeability was lower in TA and F than that of TP. (D) The streaming potential (shown at 0.1Hz) was lower in TP than TA in the 0.1 to 1.0 Hz frequency range. Bars correspond to the mean ± SE, and the differences assessed by ANOVA with Fisher's LSD test: filled star, F or TP significantly different than TA; open star, TP significantly different than F; filled square, TP significantly different than F and TA; all $p < 0.01$. 72

2.4 sGAG/WW and H_A for the 14 anatomic sites (n=6-8 per site) using the nomenclature of Figure 2.1: talus (TA) separated into anterior (A) and posterior (P); distal femur (F) separated into patellar surface of the femur (FP), and the anterior (C) and posterior (P) aspects of the femoral condyles; and tibial plateau (TP) separated into anterior (A) and posterior (P) aspects. Each location is also separated into medial (black bars) and lateral (white bars). There were no significant differences within a joint surface; However, sGAG/WW of the medial aspect of the anterior femoral condyle was significantly higher than that of the opposing medial aspect of the anterior tibial plateau (filled star, $p<0.05$), and the H_A values of the corresponding opposing surfaces approached significance (open circle, $p = 0.062$). Bars correspond to the mean ± SE, and the differences assessed by ANOVA and Fisher's LSD test. 73

2.5 Depth dependent properties of pooled cartilage samples from the distal femur. The top 1 mm slice had significantly higher water content (A), lower sGAG/WW (B), lower H_A (C) and lower dynamic stiffness at 0.1 Hz (D) than the second slice containing the remaining cartilage down to the subchondral bone. Bars correspond to the mean ± SE; differences were assessed by ANOVA and Fisher's LSD test: filled star, $p < 0.01$. 74

2.6 Scatter plots showing the variation in equilibrium modulus H_A with sGAG/WW (A) and water content (B). The data are shown for the different joint surfaces: filled circles - talar (TA), open circles - distal femur (F), and filled squares - tibial plateau (TP). H_A increased with increasing sGAG/WW for all joint surfaces (TA: Pearson's $R = 0.617$, F: $R = 0.594$ and TP: $R = 0.663$, all $p < 0.01$). With increasing water content, the H_A decreased for all joint surfaces (TA: $R = -0.176$, F: $R = -0.617$, $p < 0.01$ and TP: $R = 0.376$, $p < 0.05$); this decrease was significantly faster for TA than TP ($p < 0.05$). 75

3.1 When the current is applied in a short wavelength configuration (B) the current is more confined to the upper surface of the tissue. By comparison, with a long wavelength excitation (A), the current can penetrate the full depth, including regions that may not be effected by the enzyme. The crosshatched area represents degraded cartilage where the poroelastic properties may have been altered. By comparing the current-generated stress in both configurations, a short over long stress ratio (SR) can be calculated. The SR will decrease if the surface region is more degraded, allowing spatial localization of degradation. The overlying surface spectroscopy probe has independently addressable piezoelectric and current application (those in contact with the cartilage) electrodes 0.8 mm in width, with a 0.8 mm gap. The spatial wavelength of the interdigitated electrode structure (λ) is defined as twice the electrode spacing. The piezo electrodes are used measure the voltage created by the normal mechanical stresses which is proportional to the current-generated stress, whereas the the voltage drop across the excitation electrodes can be recorded simultaneously for electrical impedance. 80

3.2 Cartilage/bone cores were removed from the femoropatellar groove of adult bovines (A) and mounted in a confining chamber containing buffer (0.1 M NaCl and 0.05 M Trizma, pH 7.4), or buffer + 10 μg/ml rhMMP-1 or rhMMP-13 such that the enzyme could only penetrate into the cartilage from the intact articular surface. After digestion, the buffer was collected and examined to assess the extent of matrix degradation after treatment (B). An 800 μm thick disk was then removed from the cartilage/bone cores (C) without disrupting the articular surface and then placed in contact with a four electrode variable wavelength surface probe for CGS and impedance measurements (D). After testing, the cartilage disks are subject to immunohistochemical analysis, with sections stained by monoclonal antibody 9A4 to localize damage to the collagen matrix (E). 83

3.3 Immunohistochemical staining with 9A4 (mAb to collagen C-terminal neoepitope) was absent in control tissue (A), and was most intense in the superficial layer of MMP-1 and MMP-13 treated tissue (B and C). MMP-1 cleaved to an increasing depth with time; staining was apparent to a depth of 0.8 mm by 24 hours (below the border of B). In contrast, staining for MMP-13 appeared confined to the surface, only penetrating 50 μm (C). Arrows indicate the surface of the cartilage. . 86

3.4 The release of PG and HYP constituents (as % of total) increased with time of treatment by MMP-1 (B), and was greater than that released by MMP-13 treatment by 24 hours (A). With MMP-1 treatment, the release of hydroxylysyl pyridinoline cross-links were detected after 24 hours. Bars correspond to the mean ± SE, N=4. 87

3.5 The short-wavelength to long-wavelength stress response ratio (SR) for control disks (0 hour) and disks after 24 hours MMP-1 treatment. MMP-1-induced degradation caused a decrease in this ratio by 24 hours, significantly different at 0.025 Hz ($p < 0.01$). In contrast, there were no significant differences between controls and disks treated with MMP-13 by 24 hours (data not shown). Mean ± SE (N=4-7), and the differences against controls assessed by students t-test: filled star, $p < 0.01$. 88

3.6 The electrical impedance of cartilage treated 24 hours with MMP-13 (filled circles) and MMP-1 (filled square), in the long wavelength configuration compared with controls (triangles). The impedance increased significantly after treatment, particularly at the higher frequencies. Mean ± SE (N=4-11), and the differences against controls assessed by students t-test: filled star, $p<0.01$, and open star, $p<0.05$. 89

4.1 Schematic of the current source used for impedance measurements. A sinusoidal input voltage (V_{in}) to the current source resulted in a current I_c to the cartilage. The voltage difference $V_{out} - V_m$, between electrodes on the cartilage, divided by the current I_c is the measured impedance, Z_{meas}. This purely electrical measurement can be made simultaneously with the current generated stress response at the prescribed input frequencies or sequentially at only other frequency (i.e., 1 kHz)[Courtesy S. Berkenblit [13]]. 94

4.2 The impedance of disks treated 24 hours with MMP-13 (filled circles) versus controls (open circles), in the short-wavelength configuration. The impedance increased significantly after treatment, particularly at the higher frequencies (at 0.25 Hz, open star, $p < 0.05$). 95

4.3 The impedance of disks treated 24 hours with MMP-13 at 1 kHz. The impedance decreased significantly after treatment for all wavelengths studied short, long and extra-long (at 0.25 Hz, open star, $p < 0.05$). The associated wavelengths were 2.2, 4.4, and 8.8 mm, respectively. The buffer represent the impedance of the probe electrodes in contact with the buffer only which includes the interfacial impedance of the electrode-electrolyte interface. 96

4.4 The effect sGAG content and applied strain on impedance (resistive) simulated using equations 4.1- 4.6 and a first order estimate of the impedance from the electrode geometry. The simulation assumes typical values for a newborn bovine articular cartilage disk 9.5 mm in diameter and 1 mm thick: a sGAG/WW of 4.1% and a hydration 4.4 (or 81.4% water content). In addition, the two electrodes are modeled having an area of 4.57 mm^2 and a center-to-center distance of 1.62 mm. sGAG loss was modeled as a uniform loss throughout the volume, by directly reducing the amount in Equation 4.6 as indicated. 100

4.5 The femoropatellar groove from newborn steers were obtained and 9.5 mm diameter cartilage/bone cores were removed (A). The cores randomized to the 4-hour trypsin treatment group were mounted in a confining chamber containing buffer + 1 mg/ml trypsin (B). After 4 hours, the cores were removed from the chamber and a 1 mm thick slice was removed with a sledge microtome, without disrupting the articular surface (C), and placed in contact with a four electrode variable wavelength surface probe (D) in a short-wavelength configuration. The digestion buffer was collected and examined to assess the extent of matrix PGs degradation. The cartilage disk was subjected to increasing strain levels of 0-50% in an unconfined compression arrangement. A sinusoidal current density of 1 mA/cm^2 was applied to the tissue over the frequencies of 1-1000 Hz at each strain level. The cartilage disks were digested and sGAG content found by DMMB dye binding assay. 101

4.6 A. Equivalent-circuit model for the impedance measured with the surface probe. An equivalent shunt impedance, Z_{sh}, is modeled in parallel with the cartilage impedance impedance, Z_C; in addition, a series component, Z_{ser}, is assumed to be present at the electrode-electrolyte interface, evenly divided between the positive and negative electrodes. B. Similarly, once the cartilage is removed, the probe is in contact with the buffer only. 104

4.7 Trypsin treatment significantly reduced the amount of sGAG per WW in the tissue (A, open star $p<0.01$ versus 4-hour trypsin treatment, filled star versus control, n=4-6). The 0, 4, and 24 hour controls correspond to a percent loss of sGAG from the tissue of 4, 90, and 99%, respectively. The loss of sGAG content was concomitant with a significant increase in tissue hydration compared to controls(B). 107

4.8 A summary of the impedance results of trypsin treated tissue as a function of strain and frequency (A-D). The magnitude of the impedance decreases with increasing frequency for all treatment cases, with increasing strain, there is a monotonic increase of the impedance, for all frequencies. As frequency increases, the difference between the control and the treatment groups decreases, and ultimately at 1000 Hz the control (0-hour) falls between the 4 and 24-hour treatment groups for all strain levels. Also, as the frequency increases the differences between the two treatment groups became more significant at 1 kHz (4 and 24-hour). 108

4.9 The increased hydration while tissue sGAG content is decreasing suggests damage to the collagen although little or no damage can be detected in the trypsin degradation products released to the media. In the C- and N-terminal regions, three lysines (87-17C) form crosslinks between the teliopeptide regions and the helical domain of the type II collagen. Opening of the collagen network structure may occur when trypsin cleaves the arginine site (boxed R) on the C-terminal of teliopeptide region (15C), without releasing crosslinks to the media for detection [Figure adapted from [59]]. 111

5.1 An expanded schematic of the handheld version 5.0 electrokinetic surface probe (HHV5.0). The ETS (A) is held in place within a body by an inner core (B) pressing it against a plastic (torlon) sheath (C), then a stainless steel tube (D) with a screwed pusher/plunger (E). A backing plate bonded to the ETS is seated into the inner core (F). A torlon sheath is placed over the core and ETS, while making electrical connections from the silver side to the driving electrode wires. These parts are assembled with a screw from stainless steel tube (D) to a thread on the plunger (E) to create a sealed environment [Courtesy E. Quan [187]]. 119

5.2 Dimensions of each layer of ETS material. Sheets of the material for the various layers are cut to the appropriate size and then laminated together with appropriate adhesives. The 25.4 μm silver sheet for the excitation electrodes is 18×18 mm, the 25.4 μm thick Mylar metallized (on one surface) is 15×15 mm, while the 52 μm thick Kynar film is punched to a disk of 4.5 mm in diameter. The silver sheet is bonded to the non-metallized side of the Mylar using a two-part Tycel epoxy, while the Kynar is bonded to the metallized side of the Mylar with a manually applied thin film of silver conducting epoxy[Courtesy E. Quan [187]]. 123

5.3 Patterns created for the excitation electrodes on the silver sheet (right), and sensor electrodes on the Kynar sheet (left) with the Postscript language. The patterns were converted to negative images (masks) on two photographic transparencies for photofabrication. The rosette pattern around the Kynar electrodes are a template for cutting during the probe assembly stage. 124
5.4 During the probe assembly stage, a 0.33 mm thick crucifix shaped plastic backing plate is attached to the piezo side of the ETS. The backing plate aligns the ETS onto the probe within a machined recess on the end of the inner core and, thus ensures it to be flat, while creating the proper orientation to line up the electrical contacts[Courtesy E. Quan [187]]. 128
5.5 Schematic of proposed embodiment within a joint cavity left), and a photograph of an assembled HHV5.0 probe (right). 129
5.6 Electrode polarity configurations short (A) and extra-long (B) wavelengths. The polarity of the four silver chloride electrodes could be externally connected. When the current is applied in a short wavelength configuration (A) the current is more confined to the upper surface of the tissue. By comparison, with a extra-long wavelength excitation (B), the current can penetrate the full depth, including regions that may not be effected by a tissue degradation. By comparing the current-generated stress in both configurations a short over long stress ratio (SR) can be calculated. The SR will decrease if the surface region is more degraded, allowing spatial localization of degradation [Adapted from Courtesy E. Quan [187]]. 132
5.7 Piezo response for each channel at various dynamic amplitudes and frequencies. As with previous probe designs, the calibration signals increased linearly with increasing dynamic amplitude and decreased with increased frequency. 133
5.8 Differential amplitude from channels 1-2 and channels 3-4 at various applied current densities and frequencies (A,B). Driving current is in a short wavelength configuration. The differential output increased with increasing current density and decreased with increasing frequencies as previously characterized. The calculated CGS, using calibration results, showed similar trends to the differential piezo output (C,D). These results suggest the importance of observing the individual responses of each electrode separately, rather than pooling electrode responses. 134

5.9 Differential amplitude and CGS response from an extra-long wavelength configuration (electrodes 1-4) at various applied current densities and frequencies The results were consistent with previous results with the HHV4.0 probe. The extra-long wavelength CGS results, as expected, are larger in magnitude than the short wavelength and decreased with increasing frequency. 135

A.1 Tissue growth and composition: sulfated glycosaminoglycan (sGAG) and total collagen as % of wet weight. Data represent mean±SD (N = 6) for the initial 3-day cell-polymer constructs, 6-week tissue constructs from static flasks, mixed flasks and rotating vessels, and freshly explanted bovine calf articular cartilage. Pairwise comparison between the rotating vessels and other experimental groups for sGAG (filled stars, $p < 0.01$) and total collagen (open stars, $p < 0.05$). 161

A.2 Tissue biomechanics in static and dynamic confined compression: equilibrium confined-compression modulus, H_A, and hydraulic permeability, k_p, at 30% strain, calculated using the equilibrium modulus and dynamic stiffness. Data represent mean±SD (N = 3-4) 6-week constructs from static flasks, mixed flasks and rotating vessels and bovine articular cartilage. Pairwise comparison probabilities between the rotating vessels and other experimental groups for sGAG (filled stars, $p < 0.001$) and total collagen (open stars, $p < 0.05$). 162

A.3 Model system. Cell-polymer constructs cultured for 3-6 days in spinner flasks (group 1) or for 4-5 weeks in rotating bioreactors (group 2) were sutured into cartilage rings and cultured for 4-8 weeks in rotating bioreactors. 165

A.4 Biomechanical integrity was assessed by adhesive strength of the construct-explant interface measured as the stress required to fracture the integration site by a plunger applied to the construct surface during a push-through test. The sample is placed in the apparatus between an annular support ring and the main body covered with a fine sandpaper to ensure mechanical no-slip. The top housing is screwed on the main body to secure the annulus surrounding the interface. The plunger is connected to a load cell and the main body is advanced toward to the engage the interface against the plunger under displacement control. . 166

A.5 A typical measured load-displacement curve as the plunger is forced through the construct-explant interface in the push-through test. As a measure of adhesion strength, the force at ultimate failure, F_{ult}, is normalized to the cross-sectional area of the interface. 167

A.6 The adhesive strength at construct-explant interface was approximately 65% higher for composites made with 6 day rather than 5 week constructs or native cartilage controls. These data indicate that the time of construct cultivation needs to be optimized to achieve a certain minimum compressive stiffness, which is important for construct survival while maintaining sufficient potential for its integration with the adjacent tissue. 168

B.1 A scatter plot comparing the apparent cell density (using the Kim et al. method directly) and the corrected cell density for selected cartilage samples from Chapter II. The corrected cell density was calculated from the difference of separate measurements by adding buffer + Hoechst Dye 33258 or buffer alone to the samples. The lines indicate the expected cell density (15.0 x 10^6 cells/ml). Thus, the apparent cell density is an overestimate at 33.1±9.9 x 10^6 cells/ml (n = 56), while the correction method lowers the values into a more appropriate range at 18.3±4.5 x 10^6 cells/ml. 172

B.2 The Hoechst Dye 33258 enhancement (no dye ratio measurement subtracted from the dye measurement) of an adult human articular sample. The three dimensional plot was created by acquiring spectra at emission wavelengths from 300-600 nm and the excitation wavelengths from 300-500 nm. The maximal dye enhancement was approximately at an excitation of 350 nm and emission of 530 nm as indicated. . . . 173

B.3 The data of Figure B.2 is re-plotted to separate the buffer + Hoechst dye (filled circles) and the buffer only (open circles) to more closely examine the spectra at an excitation of 350 nm (left) and emission of 530 nm (right). The adjusted excitation and emission wavelength combination (350 nm and 530 nm, respectively) show that in this case the autofluorescence is close to zero. This contrasts to the regular wavelength combination (excitation 358 nm and emission 458 nm, respectively), where a significant autofluorescence exists. 174

C.1 The original amount of sample in the cryovial (1) is processed through the pyrex tube (2), the Kimax tube (3), and finally the absorbance is measured in the microplate (4). The volume are defined as that of the: V^1 original papain digest, V_S^2 amount transferred for hydrolyzation, V_T^2 post-titration, V_S^3 amount transferred to Kimax tube, V_{CT}^3 amount of Chloramine-T added, V_{pDAB}^3 amount of pDAB added, V_S^4 amount aliqouted to the well of the microplate. 182

C.2 The original amount of standard in the cryovial (1) is processed through the Kimax tube (3), and the absorbance is measured in the microplate (4). The volume are defined as that of the: ${}^{std}V^1$ original papain digest, ${}^{std}V_S^3$ amount transferred to Kimax tube, ${}^{std}V_{CT}^3$ amount of Chloramine-T added, ${}^{std}V_{pDAB}^3$ amount of pDAB added, ${}^{std}V_S^4$ amount aliqouted to the well of the microplate. 183

C.3 The standard curve is created by plotting the absorbance values at 560 nm against the known concentrations, where ${}^{std}C_4 = \frac{{}^{std}C_1}{2}$ for the volumes used: ${}^{std}V_S^3$ = 1 ml,${}^{std}V_{CT}^3$= 0.5 ml, and ${}^{std}V_{pDAB}^3$= 0.5 ml. In this case, the best fit relationship is: Absorbance = -0.01695 $[{}^{std}C_4]^2$ + 0.2626 ${}^{std}C_4$ + 0.02153 (R=0.9970). 185

C.4 A scatterplot of the the hydroxyproline measured by calorimetric method correlated with the corresponding value measured by HPLC (N=60). Samples are from various sites within the human knee and ankle joints from Chapter II. The two methods are highly correlated (R^2=0.84), and the calorimetric method underestimates with respect to the HPLC method in the range of 50 - 125 μg HYPRO. 186

C.5 Scatterplot of the HYPRO measured versus its known collagen content. The lower bound of the sensitivity of the method was determined to be ~100μg/ml of type II collagen or ~10μg/ml of HYPRO. The samples included in the boxed area were insufficiently resolved using this method. The samples in the range of 100-1000 μg/ml collagen content were used to establish that the ratio of collagen to HYPRO at ~7.4 for this assay (straight line). 187

D.1 Dimensioned drawing of the components of the HHV5.0 probe: (A) the ETS, (B) inner core, (C) torlon sheath, (D) stainless steel tube, (E) screwed pusher/plunger, and (F) recess for backing plate in the inner core [Courtesy E. Quan [187]]. 188

D.2 First iteration of HHV5.0 ETS electrode patterns. Left - Piezo electrodes; Right - Silver electrodes. The piezo electrodes made contact with the brass rods through four 0.03 inch diameter circular extensions Figure D.2, and the total active area of each piezo electrode was 0.63 mm^2. The subsequent design took advantage of the empty areas not utilized by making the contact a subportion of the electrode, increasing the area per electrode. Compare to Figure 5.3. 189

D.3 A schematic layout of the HHV5.0 and HHV4.0 for design purposes, used in Table D.1. The areas (A_1 and A_2), and lengths (w,g,w_1,l) are adjustable parameters in electrode design. 191

E.1 Schematic of modeling and fitting performed to yield material parameters using both CC and CGS data. The CC data are inputs into a 1-D model which utilizes the uniaxial configuration used during testing. The probe measurements give data in the form of current-generated stress. The aspect ratio of the probe electrodes with respect to the cartilage approximates a two-dimensional geometry where a 2-D multi-boundary value problem is appropriate. Both techniques are used to estimate the material properties of cartilage and can be compared. In addition, the parameters estimated by the CC model can be used as inputs into the 2-D MBV and the expected CGS can be computed and compared to the measured CGS. 194
E.2 Schematic of the different layers of the ETS structure. The 4mm overlap of the Kynar film is used for grounding in the test chamber. . . . 194
E.3 Electrode patterns on the silver (right) and Kynar (left) sides of the ETS. The inner electrodes on both the silver and Kynar sides are used for applying current and measuring sensor voltage output, respectively. The hemispherical outer electrodes on the silver side are used for measuring streaming potentials during CC testing. 195
E.4 Cross sectional view showing all relevant connections of the upper and lower parts of the PMMA confining chamber with the ETS mounted in between. Inset - Top view of the upper part of the PMMA confining chamber. 196
E.5 Cartilage explant process; (A) Femoropatellar groove is exposed. (B) The groove and underlying bone are removed. (B) The groove is halved and sliced to yield 2 slices of cartilage from which 13.5 mm discs are punched using a stainless steel punch. 197
E.6 Figure showing the set up for CC and CGS measurements. The cartilage is placed above the probe in the PMMA confining chamber. A porous platen is placed on top of the sample and the chamber is filled with 0.15M Trizma/NaCl buffer. The chamber is mounted in the Dynastat, which imposes strains with a servo controlled actuator and measures stresses via a load cell placed in contact with the porous platen. Streaming potentials are measured from a platinum electrode submerged in the electrolyte bath and grounded to the large Ag/AgCl electrodes fabricated onto the probe. 199
E.7 Typical piezo calibration plot, showing magnitude and phase for either electrode (left or right) for lowest and highest frequency (others in between). Here the calibration is approximately 10 mV/kPa for each Kynar electrode both pads at all frequencies. 200

E.8 Dependency of model CGS prediction on varying Poisson's ratio from 0.01 to 0.25. The boundary conditions are identical to those from the actual experiment (reflecting boundary at y = 4.87 mm, 1 electrode pair, spacing and width=1 mm), the cartilage thickness was set at 2 mm, applied current density of 1 mA/cm^2; the porosity, k_{22}, k_e, and the aggregate modulus H_A were also set at 0.71, 0.94 S/m, 9.0 mV/kPa, 3.0 μm/s)/(MPa/mm), and 0.6 MPa respectively. Varying Poisson's ratio does not significantly change the predicted CGS with respect to 0.1. 204

E.9 The effect on CGS of varying the aggregate modulus H_A, permeability k_p, or electromechanical coupling coefficient k_e at an applied current density frequency of 0.25 Hz (the behavior is similar for other frequencies). Note that increasing H_A and k_e results in an increase in CGS magnitude, while increasing k_p has the inverse effect. The phase becomes more negative for increasing H_A and k_p, but does not change significantly for variations in k_e. 205

E.10 Plot of displacement and load during a typical experiment. The time course is as follows: step displacements up to experimental offset stress with stress relaxation, dynamic displacements, CGS measurements, and step displacements to complete static CC data acquisition. Values are negative since positive displacement is defined as tension. 205

E.11 Stress strain behavior of cartilage. In this experiment, the experimental offset strain was 7.61%. H_A is calculated by the slope of the curve around this offset. 206

E.12 Plot showing the dynamic stiffness and streaming potential versus frequency results for a typical experiment. The free parameters in the model used to fit the data (dots) are k_p, k_e, and H_A. Ks is a stiffness assigned to the porous platen which contributes to the overall stiffness sensed by the load cell. The modulus, H_A, shown above is a free parameter in the fitting, and is different from the value obtained from the stress strain behavior, because it is fitted allowing for the contribution of electrokinetic effects rather than the classical equilibrium modulus. The phase angle data for the streaming potential is not used in the model fitting, as a result there is a slight discrepancy between the fit curve and data. 207

E.13 Plot of current-generated stress vs. frequency for the same experiment shown in Figure E.12. A current density of 1.00 (mA/cm^2) was applied at frequencies of 0.025, 0.05, 0.1, 0.25, 0.5, and 1 Hz. This data is a result of applying the calibration as discussed. 208

E.14 Typical parameter estimation results and predicted CGS compared to observed CGS. The predicted CGS (filled squares) agrees well with the observed CGS (filled circles). In this particular experiment the k_p value obtained from the fit matches the k_p obtained from the CC results well. However, the MBV k_e is higher than the CC k_e. In addition, if the k_p and k_e obtained from CC are used in the computational model, the expected current-generated stress (filled triangles) is less than the observed CGS, due to the predicted k_e. 209

F.1 A scatter plot of the computational solution of the current-generated stress multi-boundary value problem plotted against the dimensionless groups combined by a power law. The log-log representation of the data suggests the power law fit to the output of the computational model approximates the CGS quite well over a 5 decade range with a R^2 of 0.99. The simulation was over the range of parameter values given in the upper left and the subsequent permutations (n=6561). The values of ν and ϕ were not varying due to the lack of sensitivity of the model to these parameters. The deviatory points from the upper part of the scatter plot (indicated by the arrow) represent points simulated with $k_p = 100$ (μm/s)/(MPa/mm) and $k_e = 100$ mV/MPa, that are the upper limit of the physical values expected from articular cartilage measurements. 217

List of Tables

C.1 Table that represents the concentration of HYPRO as the sample is processed: from the cryovial, to pyrex tube, to Kimax tube, and finally to the well of the microplate for the absorbance measurement. 183

C.2 Table that represents the concentration of HYPRO as the standards are processed: from the cryovial, to Kimax tube, and finally to the well of the microplate for the absorbance measurement. 184

D.1 A comparison of the design parameters for the various probe designs, along with the resultant wavelengths. HHV4.o was not a multiple wavelength probe. The design of HHV5.0 was always constrained that each of the four electrodes had the same area. 190

E.1 The results of six experiments performed. The thicknesses in these experiments ranged from 1 mm to 3 mm, while the experimental strain varied from 4% to 17% compression. Values of the porosity and k_{22}, the electrical conductivity, which were obtained from biochemical analysis of the sample following the experiment are also shown. The values of H_A shown in the table were determined from the stress strain behavior of the AC disc. A current density of 1.00 mA/cm^2 was applied the cartilage in all but the first experiment in which 1.24 mA/cm^2 was applied. k_p (μm/s)/(MPa/mm); k_e (mV/kPa). 210

Chapter I

Introduction

1.1 Articular Cartilage

The function of organs in the human body are a direct consequence of their inherent structure. The function of the organ as a whole is more than the sum total of its individual constituents. Articular cartilage (AC) is a rich and illustrative example. An understanding of the composition and physical properties of AC are essential to diagnose disease with any given device to aid in patient care. AC is a dynamic, living tissue that responds to stimuli in its environment (i.e. external loading, fluid flow, electric fields), and the cells of cartilage (chondrocytes) are able to maintain its intricate extracellular matrix (ECM). The scientific data collected over the past 25 years for normal cartilage, supports a hypothesis that a feedback between mechanical stimulation and chondrocytes must exist to maintain cartilage homeostasis [172].

By gross visualization, during knee arthroscopy or an open joint procedure, normal AC appears as a homogeneous shiny white substance covering the ends of articulating bones. It is a thin layer from 1 mm to 6 mm depending on the joint and particular surface location. In the presence of synovial fluid, AC provides a very low friction surface that has a coefficient of friction that is less than that of ice on ice [164]. A closer inspection at the light microscopic level reveals AC as a very complex ECM of macromolecules with chondrocytes embedded within.

Cartilage is a unique organ as it is aneural, alymphatic and avascular. Nutrient exchange to the chondrocytes proceeds by diffusion from synovial fluid at the articular surface and from the subchondral bone below. The lack of a blood supply has severely limits its ability to repair following injury. The absence of innervation means that pain is transduced from the surrounding bone through unshielded force, or from the joint capsule in response to an inflammatory stimuli.response.

The complex structure of AC acts as a load-bearing, shock-absorbing, wear-resistant material to protect joint surfaces. In addition to a low friction surface, AC has a high compressive strength critical to pain free joint function. Compressive loads are distributed over a larger area, while also acting as a damping element during high impact loading (i.e. jumping). Cartilage is also strong in tensile loading when subject to shear stresses due to the sliding nature of joint function (i.e. knee joint or intervertebral disk). Lubrication by the synovial fluid also reduces shear stresses and helps protect the cartilage from trauma. These macroscopic mechanical properties are a direct consequence of the composition, as will be elucidated.

1.1.1 Structure

Articular cartilage is mostly water (60 - 80% of total weight) and ECM which comprises the bulk of the dry weight [88, 148]. The primary structural components of articular cartilage (AC) ECM are produced and maintained by the chondrocytes enmeshed within it. Tissue mechanical properties depend on the organization and structure of macromolecules present in the ECM. The ECM is made up of mainly collagen type II fibrils (along with small amounts of types IX and XI collagen), charged proteoglycans (PGs), and cells. Collagen and PGs form the framework for cartilage that resists applied mechanical forces (Figure 1.1). The collagen forms a dense crosslinked network with PGs embedded within. Proteoglycans are macromolecules that contain polyanionic sulfated glycosaminoglycan (sGAG) chains. The negative fixed charge density of sGAGs is approximately 5.3 mEq/gm dry weight in normal human femoral head cartilage [32]. Electroneutrality is preserved by a slight excess of mobile positive ions within the tissue. At the macroscopic level a Donnan osmotic swelling force develops [55, 231], caused by the electrostatic charge repulsion between the fixed anionic groups that draws water into the ECM, expanding the collagen network.

The chondrocytes are responsible for PG turnover (synthesis and degradation).

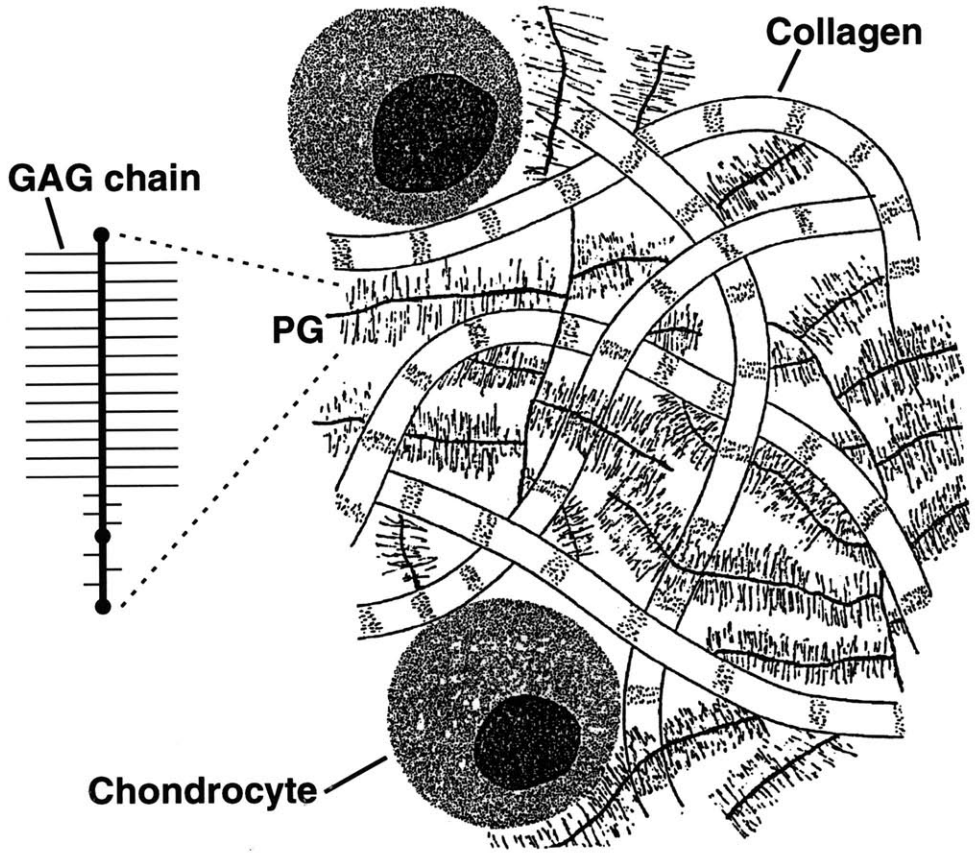

Figure 1.1: A schematic depicting the three main structural components of cartilage: chondrocytes (large round cells), proteoglycans (bottle brush structures), and collagen fibrils. Tissue mechanical properties depend on the organization, structure and amount of these macromolecules present in the ECM. Collagen type II fibrils (along with small amounts of types IX and XI) form the framework for cartilage as a dense crosslinked network with proteoglycans embedded within. Proteoglycans contain polyanionic negative fixed charge sulfated glycosaminoglycan (sGAG) chains that create a large osmotic swelling pressure, drawing water into the ECM, while expanding (applying tension) the collagen network.

The most abundant PG is aggrecan (molecule $\sim$ 2 MDa, aggregate $\sim$ 200 MDa), that has an extended protein core with up to 150 chondroitin sulfate and keratan sulfate chains attached in a "bottle brush" structure providing a high concentration of anions (Figure 1.2). When first synthesized, aggrecan is mobile, but quickly binds to immobile hyaluranon, stabilized by a link protein, creating the high density of fixed COO^- and SO_3^- groups at physiologic pH [96].

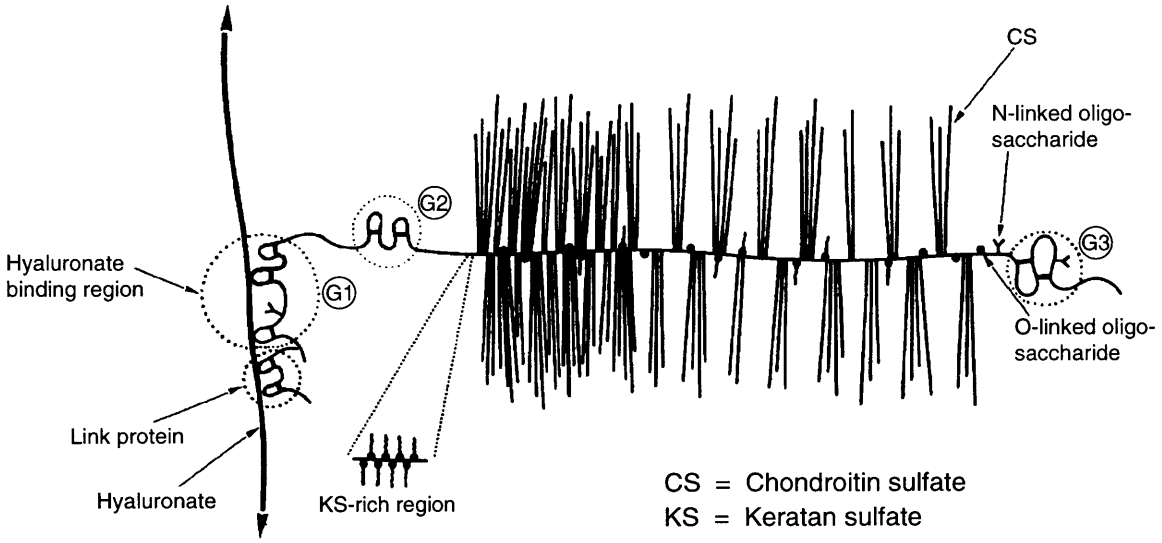

Figure 1.2: A schematic of a microscopic view of an aggrecan proteoglycan molecule showing aggrecan with its associated sGAG chains attached to hyaluronate via a link protein (adapted from Heinegard et al. [99]). At physiologic pH, the high density of fixed COO^- and SO_3^- groups are formed by incorporating newly synthesized aggrecan onto immobile hyaluranon via a link protein.

Many other soluble factors play an important role in the maintenance process by participating as mediators of turnover and production of ECM, including ions, growth factors, hormones, cytokines, proteinases (e.g. matrix metalloproteinases) and their inhibitors. Numerous factors are required to maintain homostasis. They can be produced by the chondrocytes themselves or synthesized elsewhere and transported into the ECM [168]. These factors affect the chondrocytes through cell surface receptors and their transport through the ECM can be prohibited, resulting in pathology [79].

At the ends of articulating joints, the AC is 3 - 4 mm thick, with areas on the patella as high as (6 - 8 mm). Microscopically mature AC has 3 zones based on the shape of the chondrocytes and distribution of the type II collagen. The tangential layer has flat chondrocytes, tangential collagen fibril orientation and a sparse PG content. The intermediate layer is the thickest, with round chondrocytes. oriented in vertical columns. Finally, the basal layer has round chondrocytes and contains the

tidemark that separates the uncalcified (nourished by the synovial fluid) and calcified cartilage (that gets fed by the episphyseal vessels). It has been reported that no age changes after maturation are discernible based on histology, including no loss of AC [206].

Collagen

Collagen makes up the majority of the dry weight ($\approx$ 50%) of AC [142], as it is also the most common structural protein in the body. In cartilage the most abundant form of collagen (>90%) is type II which acts as the structural meshwork of the ECM with its associated extensive intermolecular crosslinking via trivalent hydroxylysyl pyridinoline residues [58]. The name "collagen" is a generic term for structural molecules that are rich in glycine, proline and hydroxyproline. Striated fibrils, type I, II, and III have three polypeptide chains wound in a triple helical configuration.

Type II collagen is composed of three left handed tightly interwoven alpha chains ($\alpha(\text{II})_1$), 300 nm long and 1.5 nm in diameter, each with a repeating amino acid sequence of Gly-Pro-(Hydroxyproline) [236]. It is this triple helical structure that enables collagen type II to have a high tensile strength. Hydroxylysine (some as hydroxylysyl pyridinoline crosslinks) helps type II collagen link together the ECM network .

Small amounts of collagen type IX help connect the various matrix elements together [28] while type XI ($\approx$3%) regulates the caliber of the fiber [28]. In addition, collagen types VI and X are also present (<1%). Collagen type VI has a crosslinking behavior and an increased amount has been reported in OA models [58], while collagen type X is associated with growth plate cartilage in the hypertrophic zone, and in the calcified layer of mature cartilage.

Proteoglycans

The individual aggrecan monomers are attached to a GAG core (hyaluronate), stabilized by link protein (Figure 1.2), with the number depending on the functional nature of the cartilage [78, 94]. The common PGs that can be found in cartilage include aggrecan, decorin, fibromodulin, and biglycan and make up about 35% of dry weight of AC. Aggrecan molecules form large aggregates ($\sim$ 200MDa) in cartilage [152], forming a hydrogel-like structure that is, in turn, immersed within the collagen type II fibers.

Aggrecan is the major PG in AC (around 90%) and is composed of two types of sulfated GAG (sGAG) [57]: chondroitin-6-sulfate, chondroitin-4-sulfate ($\approx$ 20,000 MW) and keratan sulfate ($\approx$ 5,000 MW). The amount of sGAG attached to each PG varies depending on the functionality and integrity of the tissue [95]. Chondroitin sulfate GAGs are chains of repeating disaccharide units that contain highly charged carboxylate and sulfate groups [151]. The high density of negatively fixed charge groups helps attract positive ions and create an osmotic swelling pressure to imbibe water to help maintain a constant pH within the tissue [94, 149]. There are approximately 100-150 sGAG chains per aggrecan molecule [96], while extremely large aggregates can bind 400-800 [100].

At the molecular level (Figure 1.2), the main unit of the aggrecan molecule is a protein core of approximately 300,000 MW. It has 3 associated globular domains: G1 and G2 at the N-terminus, and G3 at the C-terminus. The GAGs are mostly contained within the G2 to G3 intraglobular domain. Keratan sulfate chains bind, in general, closer to the G1-G2 region (intraglobular domain). The PG vary in total size of aggrecan (1-4$\times 10^6$ MW) due to the varying amount of bound chondroitin sulfate. Therefore, proteoglycan as the name implies, is a combination of 5% protein and 95% carbohydrate [26].

Variation in the concentration of PGs has been observed with depth from the articular surface in immature and mature tissue [15, 226], as well as location

within a joint. Areas bearing higher stresses have also shown to have a higher PG content [124]. The charge groups on the GAG chains are ionized at physiologic pH providing a large osmotic swelling pressure that largely determines the equilibrium compressive modulus [29].

Chondrocytes

The main function of chondrocytes involves replenishment of macromolecular ECM constituents for its preservation in its harsh mechanical environment [99]. With respect to the volume of the cartilage, the chondrocytes account for less than 5% and have a density of $\sim 20 \times 10^3$ cells/mm^3 [26, 219]. In fully developed tissue the size, shape and density of the chondrocytes vary with depth proceeding down from the articular surface. In general, the size increases, the shape moves from flat and elongated to spherical with increasing depth, and the density of cells decreases with increasing depth toward the underlying subchondral bone [219] .

In order to perform their biosynthetic functions, chondrocytes are well equipped with an extensive endoplasmic reticulum and Golgi apparatus as well as mitochondria and secretory vacuoles [219]. Chondrocytes are also involved in regulation of ECM assembly and repair by secreting and mediating their assembly [188]. Because of its ability to produce degradating enzymes as well as their inhibitors, the chondrocytes are believed to participate in the physiologic as well as in the pathologic degradation of ECM [174].

Chondrocytes have also been shown to be able to adapt to the changes by biosynthetically responding to chemical, physical, mechanical and electrical stimuli through their cell receptors [126]. These adaptations, through balancing the homeostasis of the ECM, alter integrity to conform with the stimuli. Biomechanical stimuli of cartilage explants (static or small amplitude dynamic compression) have been found to influence the rate of aggrecan synthesis and catabolism. This behavior may be due to changes in cell shape, specific cell-matrix interactions or change the availability

of growth factors [185]. Investigators are also now beginning to look past the cell membrane to examine the intracellular changes due to mechanical compression on mRNA levels [190] and also how cell deformation affects intracellular organelles like Golgi apparatus or endoplasmic reticulum to fulfill their functions [89].

Water

Water is the most abundant component in AC, and it appears to be compartmentalized. Water that exists in the interstices of collagen molecules and fibrils is intrafibrillar water with the balance in the extrafibrillar space. The distribution between these two compartments has been reported to be a function of the fixed charge density and loading configuration of the tissue [150, 154].

The total amount of water present is dependent on the interaction between the collagen and sGAG components, as the collagen fibril reinforcements in the tissue prevent full expansion by the sGAGs (due to their fixed charge density) and thus constrain water intake. This balance is perturbed in OA cartilage. An increase in water content is observed compared to healthy cartilage, despite an observable reduction in GAG content. The explanation of this contradiction lies in the assumption that damage to the collagen network severely impairs its ability to restrain the sGAG swelling pressure (despite its lower concentration in the tissue), thus the amount of water increases [153]. One of the hallmarks of pathologic cartilage is its increased water content.

Matrix Metalloproteinases

Matrix metalloproteinases (MMP) are an important group of zinc-containing enzymes responsible for the breakdown of ECM components such as collagen and PGs in normal embryogenesis and remodeling as well as in many disease processes like cancer, osteoporosis and arthritis [205,245]. These enzymes are almost universally distributed among mesenchymal cells of all types, and in some epithelial and endothelial cells as

well. The collagenase-1 or MMP-1 was discovered in 1962 by Gross and Lapiere [91], in the tail of a metamorphosing tadpole and played an integral role in the normal resorption of the surrounding connective tissue. The family of MMPs can be divided into 3 subclasses: collagenases (MMP-1, MMP-8, and MMP-13), gelatinases (MMP-2 and MMP-9), and stromelysins [246].

They range in size from 28 kDa to 92 kDa, while their cDNA sequences show considerable homology with each other, i.e. MMP-3 has a 56% homology with MMP-1 [128]. They are secreted as zymogens that lose pro-peptides of about 10 kDa upon activation. Latency is due to the presence of a conserved cysteine that binds to zinc at the active center. Activation results from treatment with trypsin (or other proteinases) or organomercurials (i.e. aminophenylmercuric acetate, APMA) which react with the cysteine. Expression is upregulated through the AP-1 regulatory elements of the gene. Structural integrity is maintained by octahedral binding of calcium ions and zinc is required for catalysis [205]. Each MMP has the ability to cleave one or more components of the ECM and can be inhibited by the family of tissue inhibitor of metalloproteinases (TIMP1-4). TIMP-1 is a 28 kDa protein with a varied extent of glycosylation. It has two distinct domains, that can be dissociated by EDTA at acid pH or by SDS-PAGE and has been implicated in the activation of a number of the members of the MMP family [212].

The collagenase molecule can divided into several distinct structural domains: a signal peptide, a pro-peptide domain that is lost at activation and contains a cysteine residue that is involved in activation, a catalytic domain that separated from the putative zinc binding domain by a fibronectin-like domain, a type V collagen domain of unknown origin, and a C-terminal hemopexin-like domain. The hemopexin-like domain determines substrate binding. In MMP-1, it can be removed by autolysis, leaving a 19 kDa catalytically active domain that can digest proteins, but is inefficient in attacking collagen [43]. In contrast, in MMP-13 this domain is stability bound to the catalytic domain.

MMP-1 cleaves the three helical chains of homotrimeric collagen molecules at specific sites. A helical trimeric fragment of 3/4 (from the N-terminus) and 1/4 sizes are found after digestion of type II collagen.

The MMPs are regulated at the level of gene transcription, i.e. there is no intracellular storage, thus they are synthesized and immediately released into the matrix. It is known that factors affecting cell shape and the actin cytoskeleton induce MMP gene expression [75]. Evidence now exists that factors like IL-1β or TNF-α stimulate MMP activity in cartilage and may play a role in the pathological destruction of cartilage in disease such as RA. These factors further predispose the cartilage to damage by decreasing synthesis of the ECM components [128].

Extensive *in vivo* studies on the activities of MMPs have not been undertaken since they are only present in tissue that are undergoing remodeling or breakdown and in very small amounts (1-10 μg/(g wet tissue)), and are difficult to extract. *In vitro* information is abundant, but whether these results hold true in living tissue has yet to be shown. The method of activation *in vivo* is also not well defined, but could involve other proteinases like plasmin, while stromelysin is required for complete activation of MMPs [85].

MMPs have been shown to be present when cartilage undergoes degeneration [212], thus the pathogenesis of osteoarthritis (OA) and the destruction of AC could be due to the imbalance of MMP and TIMP [49]. The amount of TIMP can be less than 50% that of normal cartilage when OA is present [49].

In a study of the Hartley guinea pig model of spontaneous arthritis, it was found that the presence of active MMP-1 and MMP-13 at the lesion site is consistent with an important role for these enzymes in cartilage degradation of OA in this species [107]. The patterns of MMP-1 and MMP-13 expression varied with the age of the animal (at 2 months, no OA, and at 12 months, OA was diagnosed) and the compartment of the knee (lateral greater than medial), but were localized to the ECM around the lesion sites, coincident with generation of the 1/4 and 3/4 collagen cleavage

products. This study was unable to distinguish whether MMP expression at 2 months was due to normal cartilage remodeling with growth or an early manifestation of OA.

The mainly type II collagen of cartilage is remodeled by three members of the MMP family, collagenase-1 (MMP-1), collagenase-2 (MMP-8), and collagenase-3 (MMP-13). MMP-1 and MMP-13 may contribute to the OA or RA disease progression since they are found to be induced in these tissues at higher levels in disease than normal humans [17, 213, 235]. It was found that the time course of MMP-13 induction in rabbit (this species has a distinct genetic homologue to the human) was more rapid and transient than that of MMP-1 [235], while MMP-13 was found to turn over type II collagen 10 times faster than MMP-1 in humans [167]. In addition, in human tissue, TNF-α stimulated all three interstitial collagenases, while retinoic acid only increased the expression MMP-8 [213]. Equine chondrocytes have also been shown to to respond to IL-1 by increasing MMP-13, which showed 92% homology with the human cDNA sequences [34]. MMP-1 activity has also been found, along with MMP-3, in the granulation tissue associated with inflammation in lumber disk herniation [155]. MMP-13 has been showed that it can cleave aggrecan at the interglobular domain at the same site as other MMPs and also a novel site (..VKP^{384}-VFE..) [66].

It has also been shown that the initial clip of type II collagen by MMP-13 is followed by a second cleavage, three amino acid carboxy-terminal to the primary cleavage site [17,167]. The second clip is caused by MMP-3 [233], and a third cleavage site was also identified by N-terminal sequencing, three residues carboxy-terminal to the second cleavage site. Vankemmelbeke et al. [233] also clearly demonstrated through staining of cartilage from patients with OA with neoepitope antibodies, that the type II cartilage degradation started at the articular surface and extended into the middle or deep zones with increasing depth into the cartilage. In addition to this depth dependence, recently it has been shown that at the immunohistological level, a direct correlation between the grade of cartilage degradation and the intensity of the immunoreaction can be found [241].

Greenwald et al. [86] recently suggested in studies of bone that tetracycline analogs could be used against pathologically excessive MMP-8 and/or MMP-13 activity, without affecting the levels of MMP-1 that are needed for tissue remodeling. This may be a sign that a similar approach can be applied to control cartilage damage with age, like with OA.

1.1.2 Function

As a consequence of the composition of cartilage, measurable electromechanical properties are exhibited (an area of research referred to as cartilage electromechanics). To consider modeling and analysis of AC behavior, it can be conceptualized as a composite material of a fibrous mesh (collagen) embedded in a highly hydrated charged gel of PGs. Resistance to tension and shear loading is provided by the collagen, whereas the high swelling pressure of the PGs enables cartilage to resist compressive loading. The engineering properties of cartilage, i.e. compressive and tensile strength, have been assessed in many different system. Extraction of PGs has produced a marked decrease in the tissue's equilibrium compressive modulus without effects the tensile stiffness, while selective degradation of the collagen network predominantly affect tensile properties of the tissue [121].

The dynamic behavior of cartilage is the result of interactions between the solid ECM components and the interstitial fluid. Cartilage is most successfully modeled as a poroelastic medium. Such a medium is a fluid-saturated porous material in which viscous effects are predominantly due to frictional interactions between the fluid and solid phases. The literature documents a rich history of mathematical models to describe this physical behavior of cartilage. Early work was begun by Biot almost fifty years ago [18, 19] in the context of geophysics. Using an mixture-theory, where material properties and constitutive relations are derived separately for the fluid and solid phases, a biphasic theory describing the behavior of cartilage was developed by Mow and co-workers [140, 171]. These models fluid flow can be related to mechanical

properties like stiffness [170,171]. Interest today remains high, with continued efforts to produce more complex non-linear models for use with today's powerful computational capacity to more realistically model high strain behavior and the effects of non-homogeneous material properties on experimental measurements [134].

Besides having mechanical properties, cartilage exhibits electrical properties that are coupled with mechanical stresses [90]. It has been previously shown that these electrical interactions play a significant role in cartilage physiology [9,88,90]. This electromechanical transduction effect is a property of the cartilage composition, specifically the PGs [67,133] and two dual phenomena are observed: streaming potential (SP) and current generated stress (CGS) [67,68].

Streaming Potential

As the hydrated ECM of cartilage is mechanically deformed, a flow of interstitial fluid relative to the fixed charge groups of the solid matrix is created. Entrained positive ions are separated from the negatively charged matrix macromolecules, giving rise to a voltage gradient or streaming potential in the direction of fluid flow [69,90,133]. It has been observed that this electromechanical transduction property changes in a very sensitive manner to matrix alterations [67–69,103]. Frank et al. [68] used cylindrical disks of adult bovine femoropatellar groove cartilage that were uniaxially compressed between two silver chloride electrodes (Figure 1.3) where small-amplitude sinusoidal compression (~1% strain) superimposed on a 10–20% static offset compression produced a sinusoidal potential at the same frequency (in the 0.001–20 Hz range). The amplitude and phase varied with frequency in a manner consistent with an electrokinetic mechanism [69,133]. These studies demonstrated that these electromechanical parameters sensitively changed following the loss of PGs from the cartilage, while mechanical properties alone (i.e. stiffness) were less sensitive to matrix changes.

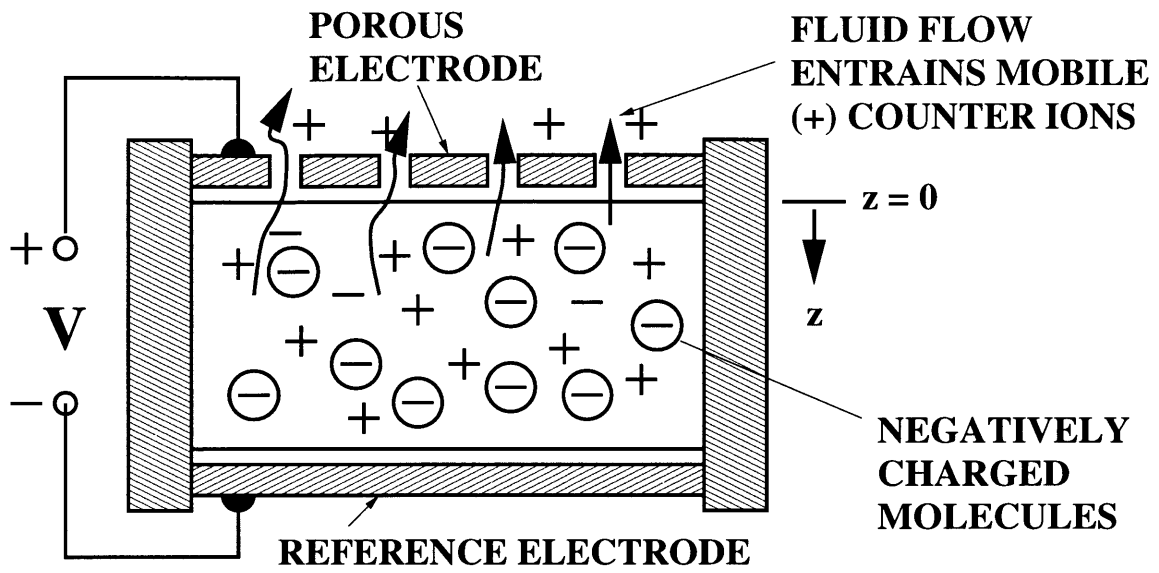

Figure 1.3: Mechanical deformations applied through the porous electrode to the ECM at the cartilage surface results in fluid flow and movement of entrained (+) counterions relative to the fixed charged groups found on PGs. This charge separation produces an electric field antiparallel to fluid flow and the resulting open circuit voltage is called the streaming potential.

Current-Generated Stress (CGS)

The converse electrokinetic effect, known as current-generated stress [69], results when application of current causes an electrophoretic motion of the negatively charged fixed ECM molecules (PGs) towards the positive electrode and an electroosmotic motion of the mobile ions of the fluid phase towards the negative electrode (Figure 1.4). These combined effects produce a measurable bulk mechanical stress at the tissue surface that can be detected by an overlying stress sensor. The altered state of the cartilage ECM caused by loss of PG (fixed charge) will change the CGS response, thus the difference between normal and degraded tissue can thus be detected [15].

1.2 Cartilage Diagnostics

Osteoarthritis (OA) is now generally regarded as a group of overlapping "OA diseases" at a joint surface with a possible imbalance between reparative and degrada-

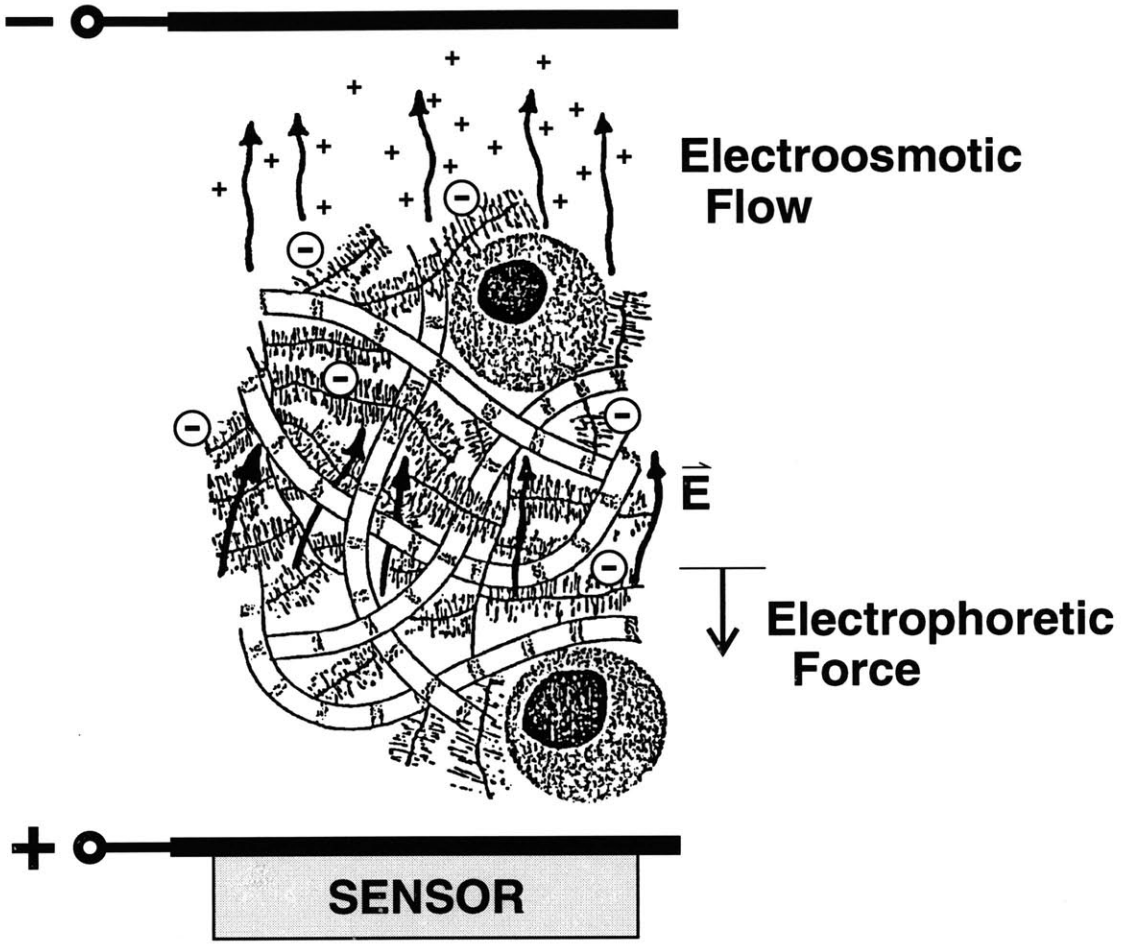

Figure 1.4: Applied current density produces coupled fluid and solid mechanical effects. (1) Electrophoretic force on matrix fixed charged groups (toward + electrode) and (2) Electroosmotic flow of interstitial fluid (toward - electrode).

tive features of cartilage homeostasis [51]. Each disease may have a different etiology, but they all have a similar biologic, morphologic and clinical outcomes. OA has become the most prevalent disease of the joint, with 70% of the population above the age 65 having radiographic evidence. It is a disease that effects the entire joint, not just the cartilage. The end stage is cartilage degeneration with fibrillation, fissures, ulceration, and full thickness loss of the joint surface. Establishing the link between macroscopic electromechanical properties, biochemical composition and ultrastructural organization in cartilage will help elucidate the relationship between

joint loading and progression of OA. This is particularly important in early stages when intervention may be still possible [129]. Having diagnostic tools to assess the physical properties of cartilage during the degenerative process would facilitate longitudinal studies evaluating therapeutic interventions. It might help clinicians better classify OA. Once baseline bulk material properties are characterized with age, the effects of mechanical stimuli on the cellular response can be assessed. These forces significantly influence the biosynthetic activity of chondrocytes as they maintain an ECM to withstand daily activities.

One of the early events in OA at a molecular level, is alteration of the cartilage ECM, and the loss of the highly charged macromolecules (PGs) from the matrix. These changes often occur in localized regions of cartilage along the joint surface and to nonuniform depth. Investigators have hypothesized that such molecular changes should change the tissue's material properties. However, there are few direct quantitative studies of the material properties of human cartilage *in vivo*.

Traumatic injuries can cause focal defects in cartilage adjacent to otherwise normal cartilage. Clinical repair approaches include debridement, microfracture, osteochondral plug resurfacing, and chondrocyte transplantation. During surgical procedures, and the subsequent follow-up, surgeons need to assess the state and functionality of the repair tissue. Often remodeling leads to a fibrocartilage repair tissue which appears cartilage-like but has poor physical properties that ultimately lead to its failure.

In addition, there is a great need for methods to assess the efficacy of therapeutic interventions developed to prevent cartilage destruction [35] or the patency of cartilage repair tissue. Presently, the assessment of cartilage repair is based on gross and microscopic morphological features. Detailed studies have established that the repair tissue is generally of good quality in the short term, but fails with time. At present, this behavior is difficult to explain. The literature shows only a minimal molecular characterization of the types of the cartilage repair tissue. The more that

is understand of the repair process, the higher the chance to produce the optimal outcome; a repair tissue integrated in the native cartilage and biomechanically functional for many years. To assess the quality of the repair tissue, researchers must attempt to compare as many properties as completely as possible to native tissue such as biochemical (PG content, molecular size, and sulfation; collagen content and typing), morphologic (histologic, histochemical, immunohistochemical, and *in situ* hybridization), and biomechanical.

In particular, a comparison of the repair tissue's electromechanical properties to that of native tissue would be helpful. This is probably due to the absence of a non-destructive means of assessing cartilage electromechanical properties in the clinic. Such technology could be used not only to compare repair tissue properties to those of native cartilage, but to determine how the properties change over time as repair succeeds or fails.

Since the destruction of cartilage during progressive OA, and the failure of cartilage repair tissue is ultimately linked to an inability to achieve (or maintain) functional biomechanical properties, it becomes critically important to have assessment tools for physical properties before, during, and after surgery.

Current diagnostic criteria and methods for monitoring OA are based on external physical examination and x-rays: However, only x-rays examine cartilage status and can reveal bone and then joint involvement only in the later stages of disease [169]. There is a major need for early quantitative assessment of degenerative changes in cartilage. Effort to assess OA progress by magnetic resonance imaging (MRI) [93], and improved methods for arthroscopic evaluation of cartilage [52] are ongoing. But yet, clinical MRI approaches do not have the resolution to show such early cartilage changes [165] and do not measure physical properties. Arthroscopy is performed visually without quantitative biophysical methods. Ultimately, arthroscopic methods, give a visual picture of the cartilage that may or may not correlate with its physical properties.

Measurement of biophysical properties of cartilage provide a functional measure of cartilage degradation. It might help to determine whether treatment or altered activity could reverse the early pathological changes of OA [198].

Cartilage exhibits electromechanical transduction properties. We have observed that they change in a very sensitive manner to matrix alterations [22, 67–69, 103]. These studies show that alterations and/or loss of tissue PGs cause changes in tissue electromechanical properties. While PG loss also affected cartilage biomechanical properties, the changes in electromechanical behavior were often far more dramatic and were detected with greater sensitivity. These results provided the basis for an *in vivo* surface electromechanical spectroscopic approach to detect cartilage degeneration.

1.3 Osteoarthritis

Osteoarthritis (OA) is the most common disease that directly affects the everyday mobility and quality of life. It mainly strikes in the last quarter of life. It attacks the tissue of the synovial joints (e.g., knees, hips, and hands) and is characterized by pain and accompanied by limitations in joint motion. It can progress to end-stage, when patients can no longer walk pain-free. Although the disease itself is not a significant source of mortality, it is a great cause of physical suffering. In the US alone, estimates that the number of people suffering from OA will reach 68 million by the year 2010 [130].

Osteoarthritis describes a group of joint disorders that lead to the destabilization of normal AC function. Degradation and synthesis by chondrocytes of ECM are uncoupled [96]. The initiation of OA may be a result of a variety of factors, including genetic, metabolic, developmental, and traumatic. OA is diagnosed clinically with sharp stabbing joint pain, tenderness, and inflammation leading to limitations of joint movement [169]. At the onset of OA there is loss of PG from the ECM [5, 94]. As a result, knowledge of the electromechanical properties of cartilage may be a good way

of diagnosing the state of diseased tissue.

1.3.1 Epidemiology

Evidence of OA has been found even before humans existed, with a natural history that dates back to fossils of ancient mammalian species [63]. In the early 1700s, when English physician William Herberden began carefully documenting lesions he observed in his patient's joints, OA was still not understood. During the mid-20th century, scientists began to classify the different causes of joint pain: hypertrophic (degenerative joint disease), atrophic (rheumatoid arthritis), and OA [63]. It is important to separate rheumatoid arthritis (RA) from OA, since the pathology is different, RA is caused by inflammation in the joint cavity as a result of immunological activity. However, the initial symptoms of RA are hard to distinguish from OA [158].

Epidemiological studies have determined that OA does not discriminate by race, gender or geography. OA is most prevalent in age groups above 65 with a higher incidence among women than men over 50 [62]. It increases with age in both sexes. Degeneration of the joint tissue can be seen in individuals as young as 20 [169]. In addition, individuals having undergone major joint surgeries or experiencing inflammatory joint diseases are more likely to experience OA*. Other risk factors for OA include obesity, joint injury, or a genetic predisposition for OA [131]. Interestingly, OA occurs in certain joints at a much higher rate than others; OA is often seen in knees and hips, but rarely in ankles or elbows [106].

1.3.2 Pathogenesis

Two major pathways of OA progression can be observed through examination of diseased tissue. The first is erosion of the cartilage surface [160]. The initial phases may be confined focally but eventually diffuse to other areas on the surface. Mechanical

*This has a major impact on the validity of proceeding with tramautic surgeries to repair focal defects in young patients.

stresses may induce additional pitting and fissures creating a roughened surface containing ulcerations. Eventually deterioration takes place down to the bone [169]. The subchondral bone loses its convex shape, increasing its thickness to a maximal joint where the most cartilage has been lost. The proliferation of cartilage and bony material called osteophytes occurs at the joint periphery [3]. This overgrowth of tissue may provide some increased joint stability.

There has been much speculation that there is a mechanical and biochemical interaction that initiates the disease. Some possibilities include the release of proteolytic and collagenolytic enzymes from cartilage cells in response to mechanical stimuli which degraded the matrix [169]. Others believe there is a biochemical or immunological abnormality that elicits degradation [37]. Another speculation is that the balance between tissue repair and degeneration is disrupted by mechanical or biomechanical abnormalities. By studying the physiology of the tissue from the molecular level to the organ level, OA progression can be monitored in order to gain understanding the disease process.

1.3.3 Mechanical Changes

The degeneration of cartilage during OA leads to surface fibrillation, deep zone fissuring, tissue erosion and concomitant changes in the material properties of the tissue: decreased tensile strength, compressive equilibrium modulus [211] and increased hydraulic permeability [172]. Increased swelling is also an early event that is normally prevented type IX collagen linking of fibrils [131]. Interestingly, it has been shown that tissue directly adjacent to a visibly degraded area of cartilage also had a decreased tensile stiffness and failure stress that was similar to the degenerated tissue [2, 121]. This suggests that morphology and histological methods of assessing cartilage may not be sufficient.

1.3.4 Biochemical Composition Changes

During OA progression, distinct biochemical changes occur in the cartilage, as first described by Hirsch over 50 years ago [102]. These changes occur throughout the affected joint and have been detected in tissue that may still appeared grossly normal [234].

The PG content of OA cartilage is substantially lower than normal [115, 143] and the degree of loss has been shown to correlate with the severity of the disease [143]. Histologic staining of OA tissue has demonstrated that the PG loss is nonuniform, with depth into the tissue, beginning at the articular surface and proceeding progressively inward [116, 161]. The PGs which remain in the OA cartilage may have a number of qualitative abnormalities, including decreased aggregate formation, decreased size of both PG aggregates and aggrecan subunits, and increased extractability from the tissue. Despite the decreased PG content, OA tissue has a higher water content than normal [145, 211]. This could result from damage to the collagen network, which normally opposes the high swelling forces developed by the PGs [147].

1.3.5 Diagnosis

Efforts are being made to diagnose the disease progression at its earliest stages in order to apply treatment before further damage can occur. Initial diagnosis of OA begins with patients complaining of pain and stiffness in their joints. Further diagnosis can be made using the current gold standard of x-ray radiography. A grading scheme to characterize the damage is utilized, the most commonly used scale of radiographic evidence is the Kellgran and Lawrence method [120]. The scale is numbered from 0 to 4 with 0 being no visible defects and 4 showing visible OA.

Radiographic diagnostic criteria has three main shortcomings: the lack sensitivity, the emphasis is on changes to the bone, and reading the films is subjective with poor reproducibility [25, 51]. Studies have shown that after 2 years of treat-

ment with NSAIDS, the radiographs showed no significant changes [53]. It is possible that the sensitivity is simply too low to detect small treatment effects. The limitations of radiographs include: non-standard and shifting of joint positions, the x-ray beam alignment, radiographic magnification not taken into account and landmarks for measurement can be subject to individual interpretation. These defects have been corrected in current clinical trials. However, x-rays can not visualize cartilage. They measure the space between boney surfaces that could be filled with cartilage and thus, are an indirect measure of the absence of cartilage or a failure of compressive resistance of existing cartilage.

Laboratory methods such as a synovial fluid extraction or a histological examination (Mankin scale) can be used to further investigate the progression of disease [143]. Unfortunately, synovial fluid extraction can only rule out other possible causes for the pain, such as RA. The Mankin scale categorizes the extent of disease progression in tissue via histology but requires a destructive biopsy. Furthermore, histological examination occurs only where tissue was removed.

Other possible methods include MRI, sonography, scintography, and biochemical markers, but they too have limitations in detecting changes in cartilage. New techniques that nondestructively test for OA and its precursors are the driving interests for this study. MRI concentrates on biochemical composition studies that could yield measures of the sGAG and collagen concentrations [92], but at this stage the cost is very high and the fixed charge density too low for adequate resolution.

1.3.6 Arthroscopy

Arthroscopy has become an important technique in the diagnosis and therapy of knee OA [4]. A 4 mm diameter arthroscope and/or surgical instruments along with a light source is inserted into the joint capsule, allowing direct visualization of the cartilage surfaces, ligaments, and menisci. The complication rate and morbidity associated with the procedure are so low, that arthroscopy is increasingly being performed on

joints that are only minimally symptomatic as an exploratory procedure [117]. It can detect before degenerative changes are evident by radiography [64]. The recent advent of a 1.8 mm diameter needle arthroscope is transforming arthroscopic examination from a hospital-based procedure to a routine office procedure [114]. During a typical diagnostic arthroscopic examination of the knee, the orthopedic surgeon can inspect the AC surface for gross changes. There is currently a commercial arthroscopy blunt probe to subjectively assess the degree of softening (known as "grade I chondromalacia") that can result prior to x-ray changes [220].

1.3.7 Treatment

Currently there are no treatments that have shown to cure, prevent or even slow the progression of human OA. Anti-inflammatory or analgesic medications give temporary relief from pain. In addition, a regimen of rest and a change in one's pattern of physical activity can sometimes lessen pain. The methods currently available for therapy of OA (physical therapy, medication, and surgery) are palliative, serving to alleviate symptoms and improve patients' mobility without actually affecting the progression of the disease process.

Considerable research is being done to develop medical techniques and drugs that could improve patient outcome. Assessment of the treatment effects must be made in order to evaluate its efficacy. Hence, innovative diagnostic tools, must be delivered to give a more accurate assessment of tissue integrity. In addition, early detection of OA is critical if drugs are developed to halt progression of OA.

1.4 Repair of Focal Defects

The repair of cartilage focal defects has received a huge amount of attention since the publication of the 1994 by Brittberg et al. [24] in the New England Journal of

Medicine[†]. The enormous amount of research into cartilage repair is demonstrated by the extensive literature developed over the past decade. This interest is well warranted since repair of defects should reduce the future need for surgical procedures such as total knee arthroplasty. For the patient, repair means significantly improving their quality of life by increasing mobility and reducing pain. Ultimately, in today's world of cost conscience managed care through health maintenance organizations, healing cartilage damage could lower the $55 billion that the United States spends yearly on arthritis.

Brittberg et al.'s work centered on the transplantation of cartilage cells (chondrocytes) to a site of focal damage after these cells were expanded in culture. Their report of positive results has re-energized the public interest into the repair of focal lesions in cartilage and possibly preventing OA, topics that have been studied for centuries.

As far back as 1743, Hunter [108] boldly stated "from Hippocrates to the present age it is universally allowed that ulcerated cartilage ... once destroyed, it is not repaired". This is especially a troublesome thought for a young person with a painful focal cartilage lesion resulting from a traumatic injury. This patient may have to endure the pain of this focal lesion progressing to OA for the better part of their live. Luckily, Hunter's observation is not accepted as dogma. The debate as to whether cartilage can be repaired still rages today, but with increasingly better prospects for a solution.

The assessment of the quality of repair tissue has been based on gross and microscopic morphological features, establishing that it is generally good in the short term, but fails with time. The comparison of the repair tissue's electromechanical properties to native tissue could provide a non-destructive means of assessing the functionality of repair tissue with respect to adjacent, unaffected, cartilage.

[†]For a more complete discussion see Appendix A.

1.5 *In Vivo* Human Cartilage Probes

Early degradative changes in human OA cartilage include increased fibrillation of collagen with an accompanying increase in tissue water content (swelling) [147], as well as loss of aggrecan. These matrix changes occur initially in the superficial zone and nonuniformly with depth from the articular surface [148]. The resulting changes in cartilage material properties in animal models of OA have been well documented in studies *in vitro* (e.g., see [172] for review). However, there are fewer studies of physical changes in human OA cartilage. Knowledge of such changes at the molecular and tissue level could help provide a differential diagnostic measurement. The tracking of *in vivo* cartilage physical properties would also aid in longitudinal studies of OA progression, allowing pharmaceutical companies to evaluate the efficacy of a pharmacological intervention. In addition, *in situ* physical diagnostics could provide an objective measurement of the quality of repair cartilage, as tissue engineered cartilage develops toward a clinical reality.

To date, there have been few direct quantitative studies of these material properties of human cartilage *in vivo* using hand-held arthroscopic-like probes. In one study, the structural properties of cartilage were measured in 25 autopsy specimens and during 35 open procedures using load deformation curves in a study by Tkaczuk [224]. The cartilage was classified as healthy or diseased based on x-ray examination and the specimens were on the lateral femoral condyle surface. The measurements were taken with a blunt probe connected firmly to the joint with a custom fixing device, and the thickness assessed as distance between the surface and the point where probe pierced the subchondral bone in a test to failure. He found that there was an age dependence on the stiffness of the cartilage in both sources, but that there were no significant differences found in the stiffness between healthy and diseased cartilage. Any differences that existed may have been masked by the cartilage thickness evaluation in this study.

After many years of experience with a blunt arthroscopic probe to subjectively

assess the integrity of cartilage from the medial facet of the patella, Dashefsky [48] decided to design a more objective measurement apparatus. He used an instrumented indenter attached to a force transducer to qualitatively assess the mechanical properties of chondromalacia of patellar cartilage during arthroscopy. In a group of 107 knees with "patellofemoral symptoms and signs", 90% were evaluated as "soft;" but over half of these "soft" cartilages showed no detectable visual changes of the articular surface of the patella. Interestingly, of 58 patients with no signs or symptoms of the patella, 50% showed softening of the cartilage. These results suggest that physical property changes may not correlate with the patients symptoms until an irreversible threshold of damage occurs with the chronic wear and tear of cartilage.

More recently, Lyyra et al. [136], developed an arthroscopic indenter instrumented with strain gauges for measurement of tissue stiffness *in vivo* (Artscan 1000, Artscan Medical Innovations, Helsinki, Finland). A constant deformation is imposed on the cartilage by the indenter, and the "instantaneous" load response during a 1-second measurement interval is used to evaluate the tissue stiffness before appreciable stress relaxation has occurred. In order to compute an effective dynamic modulus, an independent measurement of tissue thickness is necessary, as with any indentation technique. The device was able to detect differences in the stiffness of cartilage in different regions of normal knees. Interestingly, however, the indenter detected only 30-40% decreases in cartilage stiffness in the most severely affected regions of the patellar cartilage of patients with known chondromalacia [125].

From the above studies, it is important to note that early OA cartilage may appear normal by visual inspection. Given that arthroscopy is one of the most common orthopedic procedures [38], visual inspection alone during arthroscopy may not be sufficient for diagnostic purposes, suggesting the need for quantitative approaches. In addition, these studies suggest that purely mechanical tests alone (e.g., indentation tests) may not provide a sufficiently sensitive index of early degenerative changes in cartilage. This, in part, has motivated the incorporation of cartilage's electromechan-

ical transduction properties into a surface diagnostic probe [16].

1.6 Electromechanical Surface Spectroscopy

This thesis focuses on a new technology for nondestructive measurement of electrical and mechanical properties of AC via electrodes placed on the tissue surface. The long term goal of this research is to enable detection of early stages of cartilage degradation based on the sensitivity of cartilage electromechanical properties to damage of the aggrecan-collagen network and loss of the highly charged aggrecan molecules. Ultimately, this technique may find application in early *in vivo* detection of cartilage degradation via arthroscopy.

Surface spectroscopy describes a technique in which a sinusoidal current density is applied to the surface of a medium, and the resultant response is measured to yield information about the properties of the medium. Frank et al. [68], utilized a uniaxial configuration in which the current was applied via electrodes on opposite ends of a excised cartilage plug. Sachs et al. [199] later completed a mathematical model showing that two silver electrodes placed on the same surface side of cartilage could induce a measurable mechanical response when current is applied in this potentially non-destructive arrangement [199, 200] (Figure 1.5). In parallel, Salant et al. [202] and later Berkenblit et al. [13] improved on this design by designing a configuration in which current could be applied to a single surface of cartilage and the resultant induced mechanical stress could be measured [202].

This work was motivated by advances in dielectric spectroscopy, where surface excitations applied via an interdigitated array of many electrodes yield information about the bulk material properties of dielectric homogeneous materials [251]. By applying a spatially and temporally periodic sinusoidal signal, a simultaneous electrical or mechanical response can be measured at the same surface. This technique is also denoted "spectroscopy," since measurements are taken over a range of imposed frequencies.

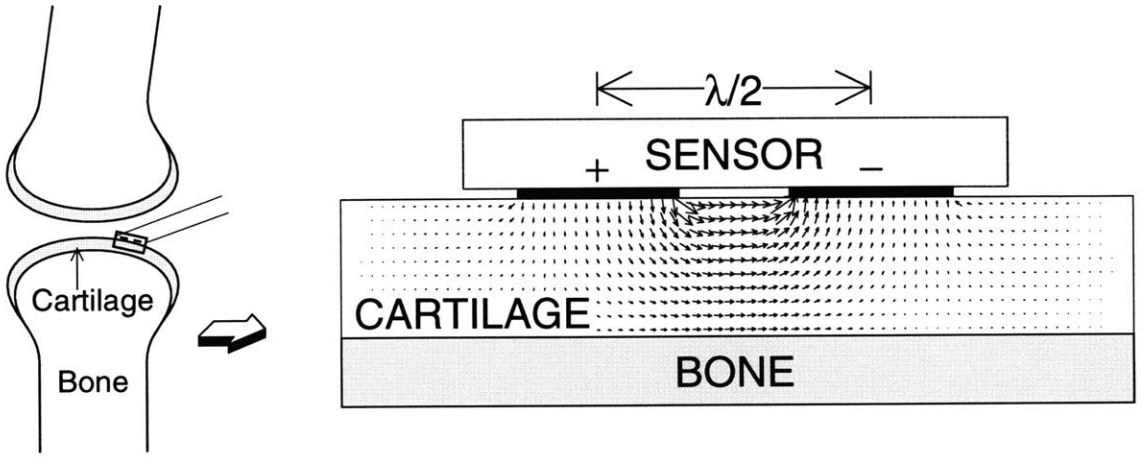

Figure 1.5: Surface probe consisting of excitation electrode array and mechanical surface stress sensor mounted on cartilage. Theoretical analysis has shown that current-generated stress can be measured by applying a standing wave of current to the cartilage surface of an intact joint, allowing for a non-destructive measurement. The current-generated stress in the bulk tissue is complex but related to the intra-tissue current density profile shown by the arrows [199]. This field can have an independently imposed temporal frequency and spatial wavelength (λ). The penetration depth of the measurement is proportional to the spatial wavelength (λ) and also increases with decreasing frequency [199](Courtesy S. Berkenblit [13]).

The general technique has also been termed "imposed ω-k sensing" [162, 251] because the medium is excited at a specified temporal (angular) frequency, ω, by an electrode structure having a spatial period $\lambda = 2\pi/k$ determined by the electrode geometry and hence a dominant wavenumber k. Its advantages are that it can be made nondestructively (an important requirement for *in vivo* measurement of cartilage properties) and the electric fields generated decay exponentially into the material, with a penetration depth on the order of $\lambda/5$ to $\lambda/3$ [237, 251]. Thus, different depths of the material may be tested by varying the imposed spatial wavelength, and spatial inhomogeneities in material properties can be detected by making surface measurements using a series of imposed spatial wavelengths (spatial localization). The depth to which the current penetrates into the medium is proportional to the effective spatial wavelength, which is equal to twice the center-to-center distance between adjacent electrodes. By changing the imposed spatial wavelength (by having independently

addressable electrodes), various depths of the medium can be preferentially assessed.

The spectrometer response depends in a sensitive manner on molecular level changes in the cartilage matrix similar to changes that occur during the earliest phases of OA degeneration [16, 69, 142, 148]. These results provide the fundamental basis for the *in vivo* surface electromechanical spectroscopic approach to detect cartilage degeneration.

1.7 Previous Work on the Electrokinetic Surface Probe

1.7.1 Probe Sensitivity to Cartilage Fixed Charge Density

The high negative fixed charge density of cartilage is associated with the aggrecan molecules of the ECM. The GAG chains attached to aggrecan core protein contain many sulfate and carboxyl groups that are ionized at physiologic pH [88]. These charge groups give rise to the associated electromechanical and physiochemical properties of the tissue under physiological loading conditions [88, 148]. The loss of aggrecan is one of the hallmarks of early cartilage degeneration. Thus, the ability to sensitively measure changes in matrix aggrecan and corresponding changes in physical properties is an important feature for a useful diagnostic probe. The sensitivity of the electromechanical surface probe to changes in cartilage fixed charge density by pH-induced alteration of the ionization state of sGAG charge groups has previously been shown.

These tests were motivated by previous studies of streaming potential and current-generated stress measured on individual disks of cartilage in uniaxial confined compression *in vitro*. In those studies, a decrease in bath pH, which neutralized the sGAG negative charge groups *in situ*, caused a concomitant decrease in the electrokinetic responses [69, 87]. The effects of bath pH on adult bovine cartilage fixed charge density is shown in Figure 1.6(C) [70]. As with human cartilage [148], lowering bath pH below 7 leads to a decrease in fixed charge density as sGAG (and protein)

carboxyl groups become increasingly neutralized. At the isoelectic pH of cartilage, typically in the range pH 2.4-2.8 [88], there is zero net charge; below the isoelectric pH, there is increasing net positive charge associated predominantly with the ionized amino groups of collagens, as sulfate and carboxyl groups are further neutralized.

The effect of bath pH on the current-generated stress induced by the surface probe configuration of Figure 1.5 is shown in Figure 1.6(A,B) [16]. As bath pH is lowered below pH 7, the stress amplitude decreased substantially to a minimum value in range pH 2.4-2.8 (Figure 1.6(A)). This minimum decreased monotonically with decreasing frequency (increasing penetration depth of the poroelastic deformation profile [199]). The amplitude of the stress closely tracked the measured changes in charge density. When the pH was lowered below the isoelectric pH, the stress amplitude began to increase again, and the phase angle changed abruptly by 180^o (Figure 1.6(C)), indicating that the direction of the current-generated stress has been reversed. At and below the isoelectric pH, the 180^o phase shift and the increase in stress amplitude indicate that the positively charged amino groups on the collagen molecules were beginning to dominate the electrokinetic transduction. Taken together, these data show the sensitivity of probe measurements to molecular level changes associated with aggrecan charge.

1.7.2 Variable Wavelength Imaging of Current-Generated Stress Following Loss of Aggrecan

Both the frequency and wavelength of the applied current density affect the depth of penetration of the current induced poroelastic deformation within the tissue. The characteristic depth of penetration of the current density, itself, is approximately 1/3 the spatial wavelength of the current [16]. This wavelength, λ, is determined by the electrode excitation pattern at the cartilage surface. Therefore, a probe with four independently addressable electrodes was constructed (Figure 1.7) such that connection to each electrode could be varied externally, thereby enabling multiple

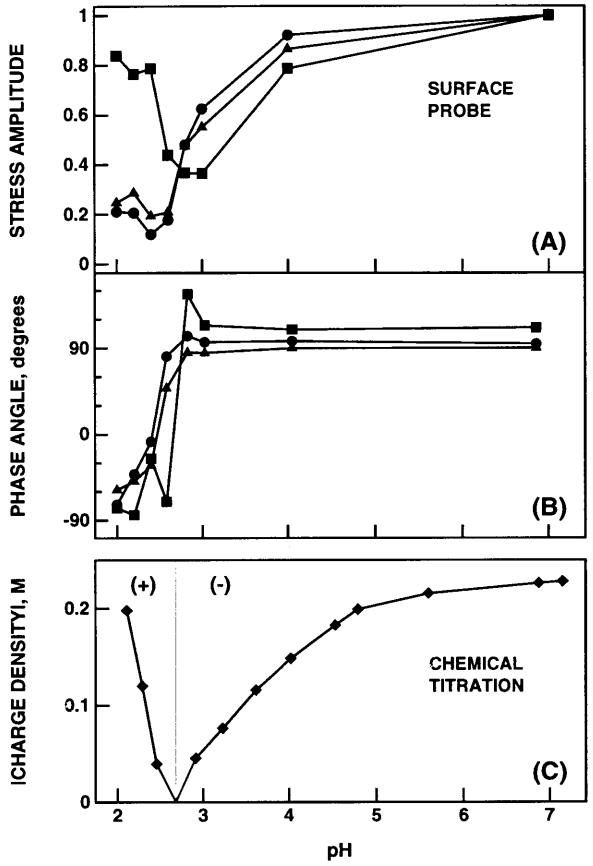

Figure 1.6: Current-generated stress amplitude (A) normalized to its response at pH 7, and phase (B) versus bath pH for adult bovine cartilage, tested with an applied current density of 1 mA/cm^2 at 0.025 (filled circles), 0.1 (filled triangles), and 1.0 Hz (filled squares). Magnitude of the fixed charge density (C) in adult bovine cartilage by chemical titration. The net charge changes sign as it passes through the isoelectric point (IEP) in the range pH 2.4-2.8. The minimum stress amplitude (a) and a 180^o phase shift (b) occur close to the IEP (Courtesy of S. Berkenblit [13]).

wavelengths to be applied using a single device. Applied current densities having short wavelength (Figure 1.7, bottom) compared to cartilage thickness are confined to the superficial region of the tissue; the associated current-generated stress will therefore reflect the properties of the superficial zone. In contrast, long wavelength excitations (Figure 1.7, top) penetrate the full depth of the tissue and thereby reflect the average properties of full thickness cartilage. Thus, combinations of short and long wavelength excitations enable the probe to "image" depth dependent focal lesions.

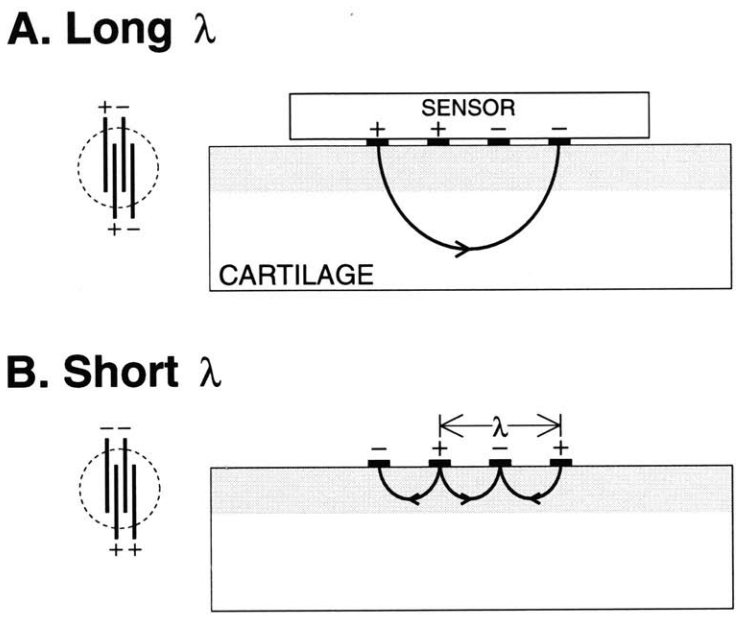

Figure 1.7: Schematic of a probe with four independently addressable electrodes. By varying the external connections to each electrode, multiple wavelengths λ can be applied using a single device. Depicted is a "long" (A) and "short" (B) wavelength pattern (related to the electrode spacing, λ), where the relative depth of penetration of the current is represented by the arrows. If the shaded region represents degraded cartilage, examination of short and long wavelength responses enable spatial imaging of the pattern degradation.

To test the ability of the probe to spatially localize matrix damage, calf cartilage/bone plugs were subjected to trypsin digestion in a specialized diffusion chamber which allowed the enzyme to contact the tissue only at the articular surface. Hence, enzymatic digestion resulted in increased loss of tissue aggrecan starting at the surface and penetrating deeper into the tissue with increasing duration of treatment. The multiple wavelength probe was used to measure the long and short-wavelength stress response of cartilage disks before and after trypsin digestion, as model of aggrecan degradation. In normal tissue, the short-wavelength response was approximately one-half the long-wavelength response (Figure 1.8 [15]), consistent with the spectroscopic nature of the poroelastic response. After a 2-hour trypsin treatment, the short-wavelength response decreased significantly compared to the long-wavelength

response, shown in Figure 1.8 as the ratio of short to long-wavelength signals [15].

This *in vitro* model system provided controlled PG loss from the tissue, and resulted in a significant decrease in the stress compared to controls. Biochemical and histological analyses showed a progressive loss of aggrecan constituents from the ECM, and correlated well with the time dependence of changes in the short to long wavelength response. These results further confirmed the sensitivity of the current-generated stress to molecular level degradation of cartilage, and showed the ability for spatial imaging using this diagnostic approach.

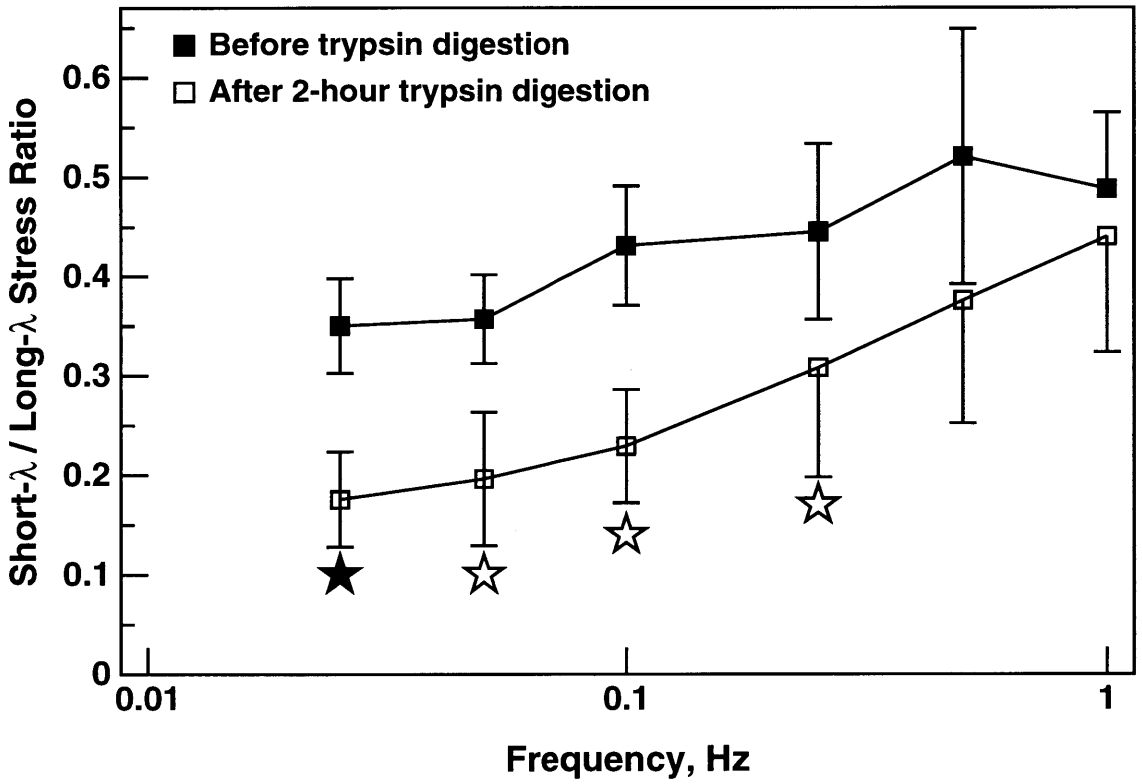

Figure 1.8: Ratio of short-wavelength to long-wavelength stress response measured in full-thickness calf cartilage-bone plugs, both before (filled squares) and after (open squares) 2 hours of surface trypsin digestion to remove proteoglycans from the extracellular matrix (N=4, mean $\pm$SEM). Current-generated stress was measured with a multiple-wavlength probe. Up to frequencies of 0.25 Hz, post-digestion values were significantly different from controls (filled star for $p \leq 0.01$, open star $p \leq 0.05$ by ANOVA) (Courtesy of S. Berkenblit [13]).

1.7.3 *In Vivo* Arthrosopic Handheld Electrokinetic Probes

To be usable arthroscopically, the previously characterized surface sensor/transducer was incorporated into a hand-held probe that can be used in conjunction with a canula into the knee joint. The probe must fulfill certain design criteria: (1) the outer body dimension and shape should fit down an arthroscopic canula; (2) the functional circuitry of the probe must be appropriately sealed to perform in aqueous media; and (3) the PVDF piezo-film output electrodes must be shielded from the excitation electrodes and other sources of electromagnetic fields, to maximize signal to noise on the stress signal. Bombard [20] designed and constructed a prototypical handheld measuring device to measure for current generated stress [20]. A two electrode probe of 1.0 cm outer body diameter was manufactured. On the end, the probe had an electrode transducer system (ETS) which could drive current into the tissue while simultaneously measuring the mechanical response of the tissue. Initial validation was done by mounting the probe in a DynaStat chamber and performing tests on excised bovine cartilage disks. Initial results of current-generated stress from these experiment corresponded with those predicted by the poroelastic theory.

The ease of use of the hand-held probe has allowed testing of cartilage during open joint surgery in a mature canine model. After the femeropatellar groove was uncovered by displacing the patella, the hand-held probe was applied to the distal trochlear notch, and the current-generated stress was measured. The results from 3 normal joint surfaces are compared in Figure 1.9 with data from normal adult bovine cartilage *in vitro*; the frequency response trends are in close agreement.

1.8 Cartilage Diagnostics: A Paradigm

In the context of this thesis a paradigm of cartilage diagnostics that is depicted in Figure 1.10, will be elucidated. Confined compression tests and electrokinetic surface probe measurements are both experimental techniques performed on cartilage that

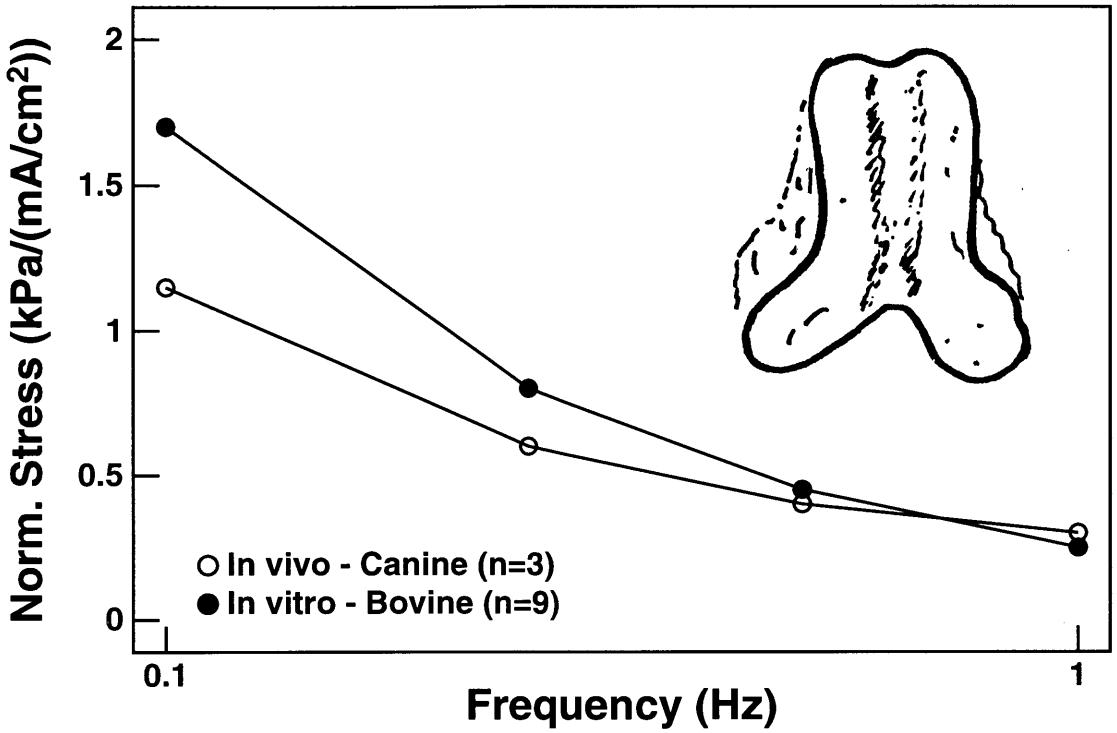

Figure 1.9: The handheld probe has been used to make *in vivo* measurements with a canine model during an open joint procedure (open circles). The data is in close agreement with output acquired from adult bovine cartilage (closed circles) with the same device.

give data which reveals information about the state of cartilage. Confined compression produces streaming potential and mechanical parameters, while the electrokinetic surface probe results in current-generated stress and impedance measurements. These two phenomena are coupled through the physical mechanism from which they are generated, as discussed. Using an appropriate model of cartilage for each experimental configuration and geometry, along with measured biochemical composition, fundamental material properties can be found. Validation of the material properties between confined compression tests and electrokinetic surface probe should be possible. In addition, we can perturb AC by enzyme treatment or by using OA tissue, and then go through the experiments and modeling to see how each technique is sensitive to biochemical and/or structural changes in AC.

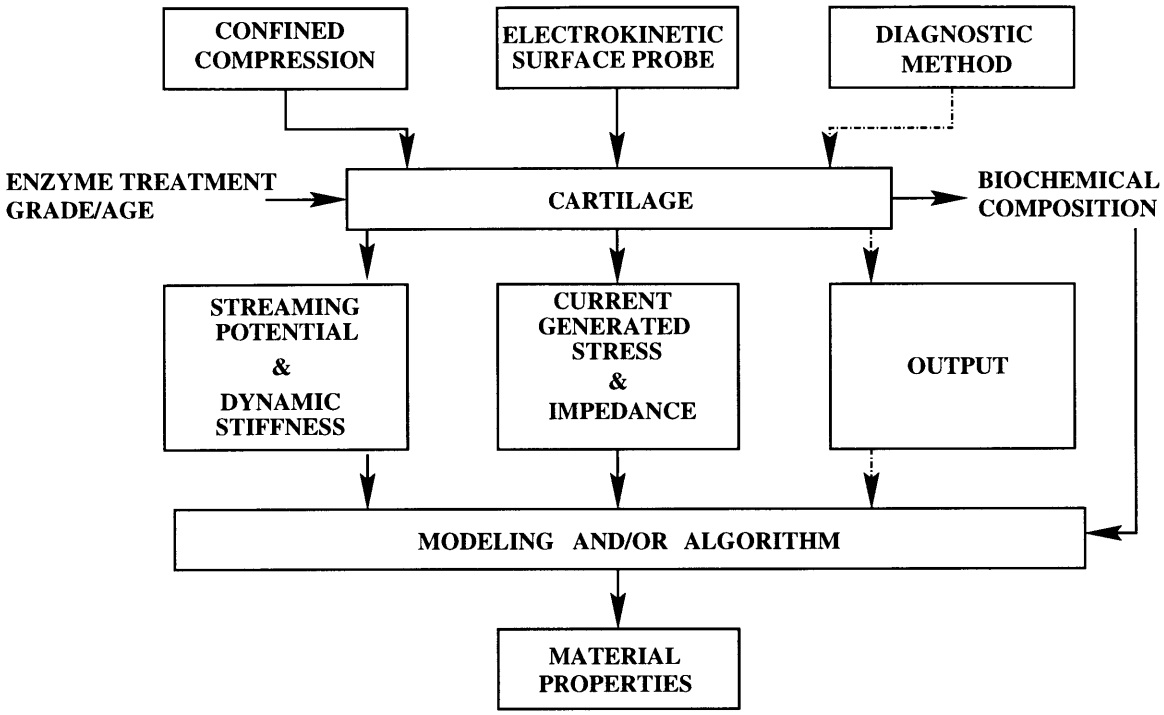

Figure 1.10: Schematic representation of our approach to cartilage diagnostics. Confined compression tests and electrokinetic surface probe measurements are both experimental techniques that give data which reveals information about the state of cartilage. These data can be inputs into models which have been developed to estimate the material properties of AC. In addition we can perturb AC by enzyme treatment or by using osteoarthritic tissue, and then go through the experiments and modeling to see how each technique is sensitive to biochemical and/or structural changes in AC.

1.9 Outline of Results

The thesis reports several methods for cartilage diagnostics, with a focus on the design and use of a surface electromechanical spectroscopy probe for *in vivo*, non-destructive assessment.

In tandem with this introduction, Appendix A outlines in more detail the past, present and future of cartilage repair. It stresses the benefits of using electromechanical methods to assess cartilage repair, and presents the results of preliminary studies, done in collaboration with R. Langer's lab at MIT.

Chapter II presents a comparison of biomechanical and biochemical properties

of cartilage from human knee and ankle pairs. Two appendices presenting details associated with the biochemical composition assessment in human AC will accompany this chapter (Appendix B and C). The ECM of human adult knee and ankle cartilage was found to have a large autofluorescence that can overestimate the cellular contents of cartilage if the Hoechst dye 33258 technique is used. Appendix B will characterize this effect and the proposed methodologies to make more accurate estimations. The most complete biochemical composition assessment for the human cartilage samples necessitated the introduction of a method to measure collagen content into our laboratory. Appendix C outlines the methodology, along with the improvements and optimizations made to the protocol and the validation of the technique.

The effects of collagenases MMP-1, MMP-13, and trypsin induced matrix degradation on the electrokinetic and dielectric properties of AC using surface spectroscopy are outlined in Chapter III and IV. Chapter III focuses on the changes in electrokinetic and dielectric (impedance) properties induced by MMPs, while Chapter IV deals exclusively with the changes in impedance induced by trypsin digestion.

Chapter V reports on the design, construction, and preliminary results of an arthroscopic *in vivo* electrokinetic surface probe with a 4.5 mm diameter active area. In Appendix D, design details are presented.

The thesis will be summarized in Chapter VI.

Appendix E and F outline a study where intrinsic parameter estimation based on electromechanical surface spectroscopy measurements is performed. The objectives were to use current-generated stress from electrokinetic surface probe measurement to infer the intrinsic material properties of AC and to validate the results by comparing them to properties measured on excised tissue via uniaxial confined compression.

Chapter II

Comparison of Biomechanical and Biochemical Properties of Cartilage from Human Knee and Ankle

2.1 Abstract

Cartilage was obtained from eight matched knee (tibiofemoral) and ankle (talocrural) joints of five different donors (14, 22 and 38 years of age, both left and right; 31 and 45, left only) within 24 hours of death. All cartilages were graded as normal. Cylindrical disks of cartilage were harvested from 10 sites within the tibiofemoral joint and 4 sites within the talocrural joint, and uniaxial confined compression measurements were performed to quantify a spectrum of physical properties including the equilibrium modulus (H_A), hydraulic permeability (k_p), dynamic stiffness, streaming potential and electrokinetic coupling coefficient. Matched specimens from these same 14 sites were used for complementary measurements of biochemical composition and molecular interaction, including water content, hypotonic swelling behavior, sulfated glycosaminoglycan content (sGAG), and collagen content. Comparing the top 1 mm slices of talar cartilage to the top 1 mm of tibiofemoral cartilages, the talar cartilage appeared denser with a higher sGAG content, lower water content, higher H_A and dynamic stiffness and lower k_p. H_A increased with increasing sGAG per wet weight, and decreased with increasing water content for all joint surfaces. Non-homogeneous depth-dependent changes in the physical properties and biochemical composition of full thickness distal femoral cartilage were consistent with previous reports. Since cartilage compressive deformation during cyclic loading is confined to the more superficial regions, the differences in properties of the upper regions of the talar versus tibiofemoral cartilages may be important in the etiology of osteoarthritis (OA). We

hypothesize that the denser, stiffer matrix of talar cartilage may reduce the exposure of talar chondrocytes to exogenous catabolic stimulation by impeding transport or endowing it with an increased inherent stability to loading.

2.2 Introduction

Epidemiological studies have shown that approximately 6% of the adult population is affected by symptomatic knee osteoarthritis (OA); this percentage increases to almost 10% in individuals over 65 years of age [62]. Symptomatic OA does develop in the ankle, although rarely ($\leq$1%), and the prevalence does not increase with age [173,184]. In addition, structural changes consistent with OA may develop in a joint long before it is diagnosed radiographically (the gold standard) or clinically, therefore results from radiological studies probably represent an underestimate of the prevalence of this disease [31,194]. In fact, it has been suggested that joint space narrowing should be considered as a late sign of OA [249]. Risk factors in the knee include occupations with high knee stress [46]; in the ankle abnormal mechanics or trauma is the major risk factor [242]. While the two joints carry similar load levels [230], degeneration of tibiofemoral cartilage leads to OA with clinical symptoms, while talar cartilage develops degenerative changes that are non-progressive and that do not appear to progress to OA [106].

The ankle joint is mainly a rolling joint with congruent surfaces at high load, whereas the non-congruent knee joint is characterized by a mixture of sliding, rotation and rolling, possibly predisposing the tibiofemoral joints to a higher incidence of OA. Increased loading of relatively underdesigned joints due to rapid evolutionary changes in human posture may have predisposed specific locations to OA [113]. In a recent study of 470 bilateral ankle donors in the age range of 21-94, with matched knees available from 50 donors, Koepp et al. [127] reported that 62% of ankles and only 35% of knees had no visible degeneration. Further, degeneration of the knee cartilage was always of an equal or higher grade than that of the matched ankle cartilages,

demonstrating that factors affecting the ankle joint (i.e., altered mechanics) could affect the knee as well. They also found that degeneration of the ankle was not necessarily age related [127].

Differences in the biomechanical properties of human ankle versus knee and hip cartilages have been studied. Kempson [122] showed that the tensile fracture stress of ankle cartilage did not change significantly with age, while that of femoral head cartilage decreased significantly with age. Swann and Seedhom [222] measured the indentation stiffness of normal articular cartilage over the surfaces of knee and ankle joints using a constant load 2-second indentation technique, and found that ankle cartilages were stiffer. They reported a relationship between indentation stiffness and the estimated level of stress to which the cartilage was subjected, suggesting an adaptation mechanism as cartilage matures; Yao and Seedhom [250] also reported a possible correlation between cartilage indentation modulus with joint stresses. Thus, the pattern of mechanical stress during joint loading could be an important factor in the etiology of osteoarthritis, since in the ankle, the stresses are higher but more uniform over the surface compared to the knee.

Joint biomechanics, in turn, are affected by articular surface topography [156], cartilage thickness, and joint congruency, which may evolve with age [27]. Ankle cartilage is significantly thinner (1 to 1.45 mm) than knee cartilage (1 to 6 mm) [7]. Joints with higher congruency appear to have thinner cartilage (e.g., talocrural) and have a lower incidence of OA than non-congruent joints like the knee [214]. Using a stereophotogrammetric method, Xu et al. [249] found that opposing surfaces of severely degenerated joints in the human thumb carpometacarpal joint are more congruent than those that are less degenerated.

While biomechanical structure/function relationships may suggest differences in the prevalence of OA between joints, investigators have also found significant differences in the cellular and biochemical properties of knee and ankle cartilages. Ankle chondrocytes are less responsive than those of knee cartilages to catabolic mediators

such as interleukin-1 or fibronectin fragments, and have lower gene expression of certain matrix metalloproteinases (e.g., MMP-8) [41,42,97,119]. Since talar cartilage is thinner, the superficial zone comprises a higher proportion of the full thickness and thus may provide a protective layer more resistant to damage. In addition, the underlying sub-chondral bone in the ankle appears to be less responsive to load alterations, since there is no increase in bone density with severely damaged cartilage as has been reported for the knee [221].

Adult human articular cartilage is expected to exhibit inhomogeneous tissue composition, physicochemical, and electromechanical properties [39, 83, 98, 148, 179, 207]. This is manifested in site dependence [135] along a joint surface and dependence with respect to depth from the articular surface. The natural variation of physical properties in mature human cartilage is of interest as cartilage repair strategies continue to evolve. Especially those that require transplantation of cartilage native to the knee to the ankle like in MosaicPlasty procedures currently being performed. The matching of physical properties and biochemical composition of the cartilages will be a parameter to optimize in order to make this and other graft procedures successful as they are performed by orthopedic surgeons [7, 76].

We hypothesized that such molecular and cellular differences between cartilages from joints with a high incidence (tibiofemoral) versus a low incidence (talocrural) of OA from the same donor could lead to associated differences in the biomechanical and biochemical properties of human knee and ankle cartilages. An understanding of these differences may give insight into the pathogenesis of OA, and may help in the design of therapeutic strategies for detection and treatment [106]. Therefore, the objectives of this study were to quantify physical parameters including the equilibrium modulus, hydraulic permeability, dynamic stiffness, streaming potential and electrokinetic coefficient from normal ankle and knee cartilages from the same donor, and then to compare these physical parameters with measures of biochemical composition and molecular interaction including water content, hypotonic swelling behavior,

sulfated glycosaminoglycan content (sGAG), and collagen content.

2.3 Materials and Methods

2.3.1 Cartilage Explant

This study was approved by the MIT Committee on the use of Humans as Experimental Subjects. Cartilage was obtained from a total of eight matched knee (tibiofemoral) and ankle (talocrural) joints of five different donors (14, 22 and 38 years of age, both left and right; 31 and 45, left only) within 24 hours of death through collaboration with the Regional Organ Bank of Illinois. Joints were obtained intact, opened and tested within 24 hours without freezing at any time. The cartilages from all donors were graded as normal with no visible signs of damage using the Collin's grading system [44], as previously described [173]. Collin's normal grade 0 corresponds to grades 0 - 5 scored on the Mankin Scale [143, 173].

Cartilage/bone cores 9.5 mm in diameter were harvested from 10 sites within the knee joint (both tibiofemoral and femoropatellar compartments) and 4 sites within the talocrural joint (talar cartilage only)(Figure 2.1). The sites on the distal femur included the patellar surface (FP), and anterior (C) and posterior (P) femoral condyles. Cores were always taken from the medial (M) and lateral (L) aspects at every site. On the tibial plateau, cores were taken after removal of the menisci from the anterior (A) and posterior (P) aspects. Similarly, 4 cores were taken from the talar surface, anterior and posterior. A full thickness cartilage plug (approximately 1 mm thick) was microtomed from each talar cartilage/bone core keeping the articular surface intact and producing parallel planed samples using a sledge microtome (Model 860, American Optical, Optical, NY). From each plug, four 3 mm diameter cylindrical disks were punched (Figure 2.1) using a dermal punch (Miltex Instruments, Lake Success, NY), to be used for electromechanical testing and biochemical composition analysis. The full thickness tibiofemoral cartilage was removed as two separate slices. The first

1 mm slice contained the superficial, middle and the upper part of the deep zone [109]. The second slice contained the remainder of the deep zone down to the subchondral bone. This second slice was obtained from selected distal femurs to compare physical properties and biochemical composition with that of the first slice.

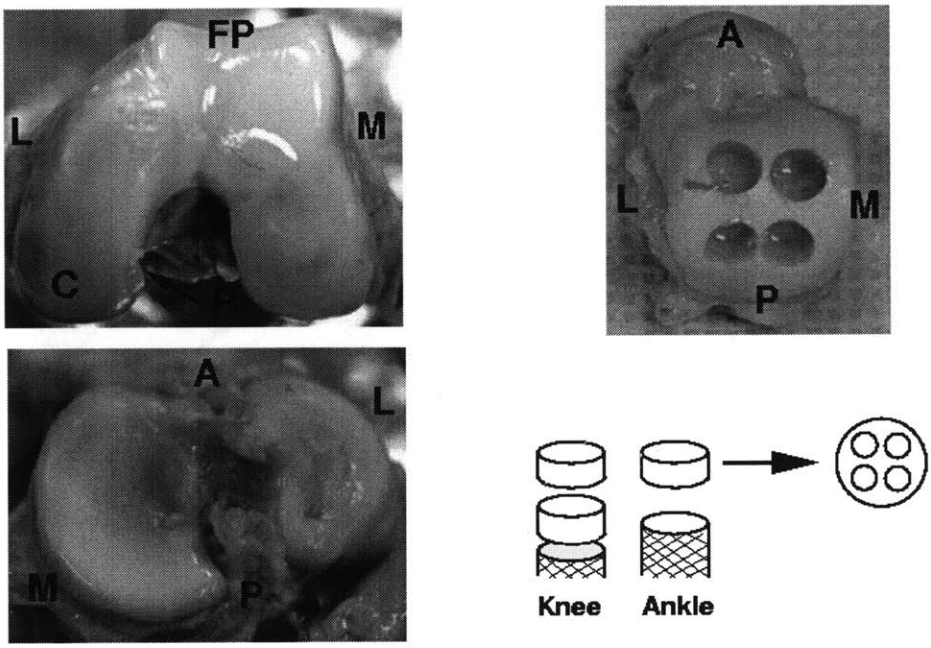

Figure 2.1: Top left, the distal femur taken inferiorly depicting the locations of the 6 harvest sites: The patellar surface of the distal femur (FP) and anterior (C) and posterior (P) of the femoral condyles always taken from both the medial (M) and lateral (L) aspects. Bottom left, the proximal tibial surface with the menisci removed. Cores were removed from the anterior (A) and posterior (P) aspects. Top right, the talar surface of the talocrural joint with 9.5 mm diameter cores removed for the anterior (A) and posterior (P) aspects. The schematic on the bottom right shows the top 1 mm slice of cartilage being removed from the knee (tibiofemoral) and ankle (talar) cores with the additional cartilage down to the tidemark also removed from the knee cores. From each cartilage plug, four 3 mm disks were punched for electromechanical testing and/or biochemical composition analysis.

2.3.2 Physical Properties

One 3 mm disk from each plug was tested in uniaxial confined compression in an electrically insulating poly(methylmethacrylate) chamber mounted in a Dynastat mechanical spectrometer (IMASS, Hingham, MA) interfaced to computer as previously described [23, 69]. Samples were pre-equilibrated in 0.1M NaCl and 0.05M Trizma buffer, pH 7.4, at $\sim 25^{o}$. The articular surface was in contact with a porous platen of ultra high molecular weight polyethylene with a 20μm pore size (Porex, Fairburn, GA).

Static compressive strains were applied in sequential increments of 5-10% up to a maximum of 25%, and the equilibrium stress recorded after each stress relaxation. The equilibrium modulus (H_A) was computed as the best fit to the linear region of the resultant equilibrium stress-strain curve. A 0.5% amplitude sinusoidal strain was superimposed on the 15% static offset strain in the frequency range 0.01 to 1.0 Hz. The oscillatory load response was normalized to the disk area and the amplitude of the applied strain to obtain the dynamic stiffness. The streaming potential, measured as the voltage between a 6.35 mm Ag/AgCl electrode (Annex Research, Costa Mesa, CA) at the base of the testing chamber and one suspended in the buffer, was normalized to the applied strain [67,68]. The equilibrium modulus, dynamic stiffness and streaming potential were used to estimate the hydraulic permeability, and electrokinetic coupling coefficient, using established methods [67, 68]. These parameters help define the ability of the extracellular matrix to withstand compressive loads.

2.3.3 Biochemical Composition and Swelling

The remaining 3 mm disks from each plug were removed from the isotonic buffer, the excess water padded away, and a wet weight (WW) taken (AE163 Balance, Mettler Instrument Corp, Hightstown, NJ). To assess swelling [21,147], disks were then twice re-equilibrated in a hypotonic solution of 0.01 M NaCl at pH 7.0 for 2 hours at room temperature and re-weighed. The disks were then lyophilized, and dry weights taken.

The samples were digested in 1 ml of 125 μg/ml papain solution [201] and aliquots taken to measure sulfated glycosaminoglycan content (sGAG, by dimethylethylene blue dye binding assay [60]) and hydroxyproline content (HYPRO, [244]). The biochemical composition values corresponding to each site were computed as the average over the disks from each plug.

2.3.4 Statistical Analysis

All statistical analysis was performed with the SAS Statistical Software System 6.12 (Cary, NC, USA). Multifactorial analysis of variance (ANOVA), with and without interactions, were performed to examine the effects of categorical data on variables of interest. Significant differences between group means were assessed by Fisher's least significant difference (LSD) test when the F-test of the ANOVA was significant. Linear (Pearson's) correlation coefficients were performed between relevant variables and significance between groups was assessed by Fisher's z-transform method [186]. Sample quantities are expressed as mean $\pm$ SE, and significance was taken as $p<0.05$ or as indicated.

2.4 Results

With three donors, both left and right matched knee and ankles were available, while only left limbs from the two other donors were obtained. To control for this possible bias in the data, the statistical analysis was first performed with the left knee/ankles only. As the contralateral joints were successively added, the results were not significantly changed. In addition, the observed trends were present with each matched ankle-knee pair (data not shown). Thus, the data from all limbs were used for the subsequent analysis.

Initially, multifactor ANOVAs were performed to determine the effect of joint surface, age and left/right location on physical and biochemical properties (male/female differences were not relevant since there was only one female donor

in this study). The ANOVAs revealed that for all variables presented joint surface was a significant determinant, but not location within a joint surface; therefore, data from cores within each joint surface were pooled. Age was also a significant factor (i.e., means from individual pairs of age groups showed significant differences), but only produced the following highly significant correlations: age versus H_A for the talar (TA) and distal femur (F) surfaces (R=0.582 and R=0.562, respectively, both $p<0.01$), age versus sGAG normalized to wet weight for F (R=0.679, $p<0.01$), and age versus water content for the F surface (R=-0.469, $p<0.01$). Finally, left/right differences were not significant for any variable of interest, even when accounting for possible interactions with joint surface.

2.4.1 Biochemical Composition and Swelling

Comparing the results from the top 1 mm slices pooled from all locations within each joint surface, the water content of talar (TA) cartilage was lower than that of F and TP, while F was lower than TP (Figure 2.2A). The swelling ratio (SR), defined as the wet weight of the sample measured at 0.15 M (isotonic) normalized to that measured after re-equilibration in the hypotonic solution of 0.01 M, was higher in TP than TA or F (Figure 2.2B). sGAG content normalized to wet weight (sGAG/WW) was significantly higher in TA than F or TP (Figure 2.2C). HYPRO/WW was significantly lower in TP than TA (Figure 2.2D).

2.4.2 Physical Properties

Data from pooled samples of the top 1 mm slices of cartilage surfaces showed that the equilibrium modulus (H_A) of TA cartilage was significantly higher than that from both F and TP, and F was higher than TP (Figure 2.3A). This same trend was observed for the dynamic stiffness over the entire frequency range tested (Figure 2.3B shows data at 0.1 Hz). The computed hydraulic permeability was lowest in TA and, along with that of F, was significantly different from that of the tibial plateau (Figure 2.3C).

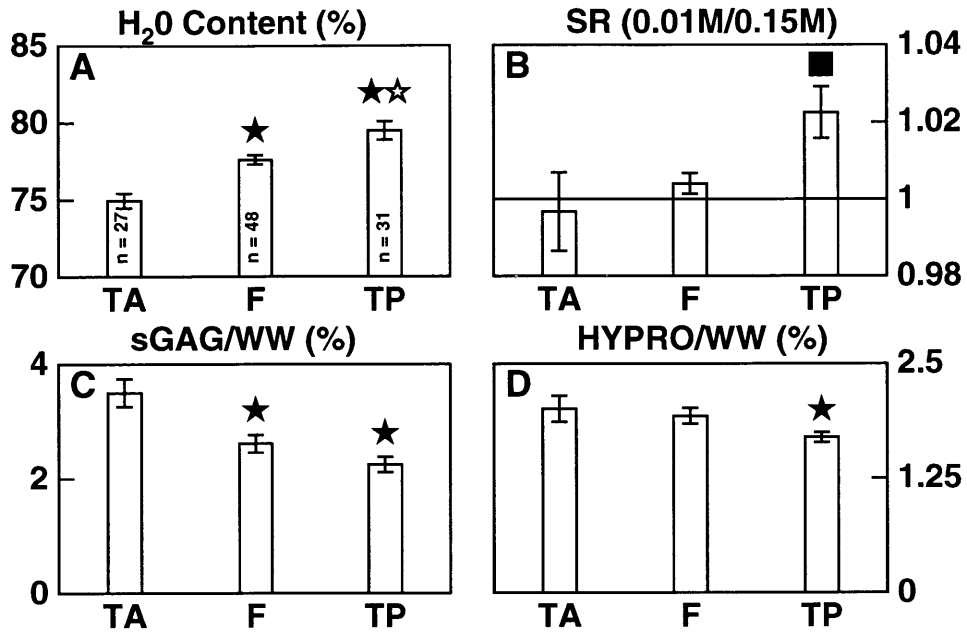

Figure 2.2: The biochemical composition of the pooled cartilage samples of the top 1 mm of talar (TA), distal femur (F), and tibial plateau (TP). (A) The water content of TA was lower than that of the F and the TP, while F was lower than TP. (B) The swelling ratio (SR)(defined in text) was higher in TP than TA or F. (C) The sGAG/WW was higher in the TA than either the F or TP. (D) HYPRO/WW was significantly lower in the TP than the TA. Bars correspond to the mean ± SE, and the differences assessed by ANOVA with Fisher's LSD test: filled star, F or TP significantly different than TA; open star, TP significantly different than F; filled square, TP significantly different than F and TA; all $p < 0.01$.

The streaming potential (shown at 0.1 Hz in Figure 2.3D) was lower in TP than TA in the 0.1-1.0 Hz frequency range. Interestingly, the calculated electrokinetic coupling coefficient (k_e, [68]) did not vary with joint or location in these normal cartilage samples (data not shown). In addition, the electrical conductivity (k_{22}) of the tested samples (computed from the Donnan equilibrium and electroneutrality conditions, and the fixed charge density estimated from the sGAG concentration [30]) was significantly higher in the TA than either the F or TP joint surfaces.

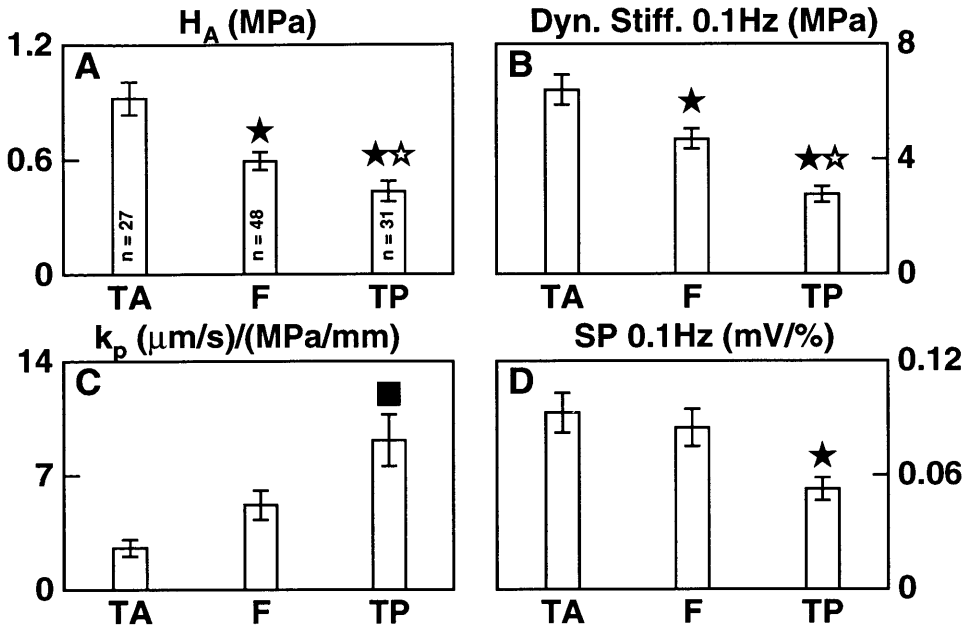

Figure 2.3: The electromechanical properties of the pooled cartilage samples of the top 1 mm of talar (TA), distal femur (F), and tibial plateau (TP). (A) The equilibrium modulus (H_A) was higher for TA than F and TP, and F was higher than TP. (B) The dynamic stiffness (shown at 0.1Hz) exhibited the same trend as H_A over the entire frequency range studied. (C) The hydraulic permeability was lower in TA and F than that of TP. (D) The streaming potential (shown at 0.1Hz) was lower in TP than TA in the 0.1 to 1.0 Hz frequency range. Bars correspond to the mean ± SE, and the differences assessed by ANOVA with Fisher's LSD test: filled star, F or TP significantly different than TA; open star, TP significantly different than F; filled square, TP significantly different than F and TA; all $p < 0.01$.

2.4.3 Site Dependent Inhomogeneities Within a Joint Surface

As examples of the site-to-site variations of the measured variables, sGAG/WW and H_A data are shown in Figure 2.4. The pooled data of Figure 2.2 and 2.3, respectively, are subdivided into the 14 anatomic sites tested (n=6-8 per site) using the nomenclature of Figure 2.1. As mentioned, no significant differences within a joint surface were found (either medial/lateral or between the individual sites within a joint surface). However, differences in sGAG/WW and H_A between cartilages from certain opposing joint surfaces in the knee were noted. For example, the sGAG/WW of the medial aspect of the anterior femoral condyle was significantly higher than the medial

aspect of the anterior tibial plateau ($p<0.05$), while the corresponding H_A differences approached significance ($p=0.062$).

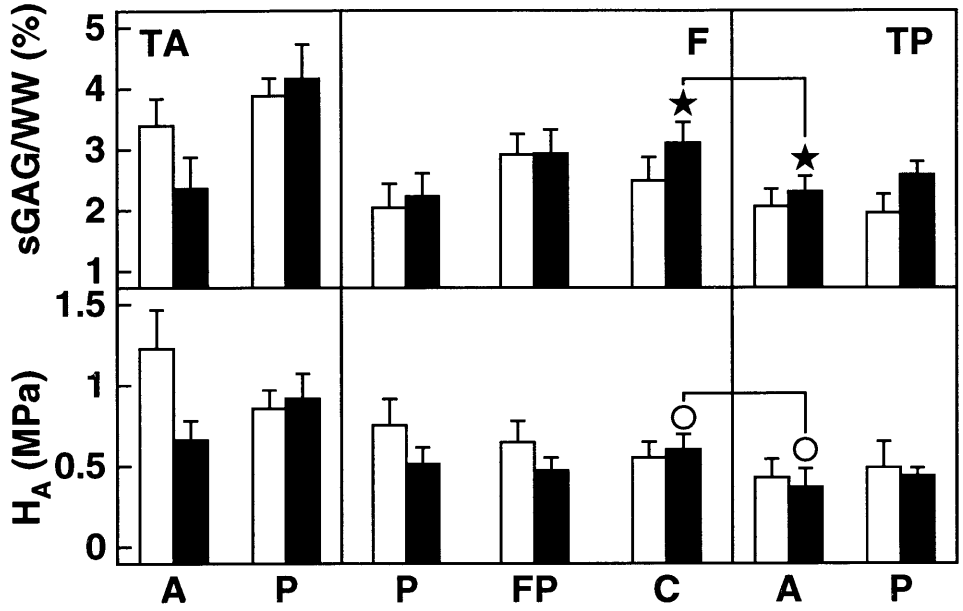

Figure 2.4: sGAG/WW and H_A for the 14 anatomic sites (n=6-8 per site) using the nomenclature of Figure 2.1: talus (TA) separated into anterior (A) and posterior (P); distal femur (F) separated into patellar surface of the femur (FP), and the anterior (C) and posterior (P) aspects of the femoral condyles; and tibial plateau (TP) separated into anterior (A) and posterior (P) aspects. Each location is also separated into medial (black bars) and lateral (white bars). There were no significant differences within a joint surface; However, sGAG/WW of the medial aspect of the anterior femoral condyle was significantly higher than that of the opposing medial aspect of the anterior tibial plateau (filled star, $p<0.05$), and the H_A values of the corresponding opposing surfaces approached significance (open circle, $p = 0.062$). Bars correspond to the mean $\pm$ SE, and the differences assessed by ANOVA and Fisher's LSD test.

2.4.4 Depth Dependent Inhomogeneities in Physical Properties and Biochemical Composition

To investigate inhomogeneities in physical properties and biochemical composition of distal femoral cartilages with depth from the articular surface, the properties of the top 1 mm slices of distal femoral cartilage were compared to those of the remaining cartilage down to the tidemark (Figure 2.5). The top 1 mm slices had significantly

higher water content, lower sGAG/WW, lower equilibrium modulus and lower dynamic stiffness at 0.1 Hz.

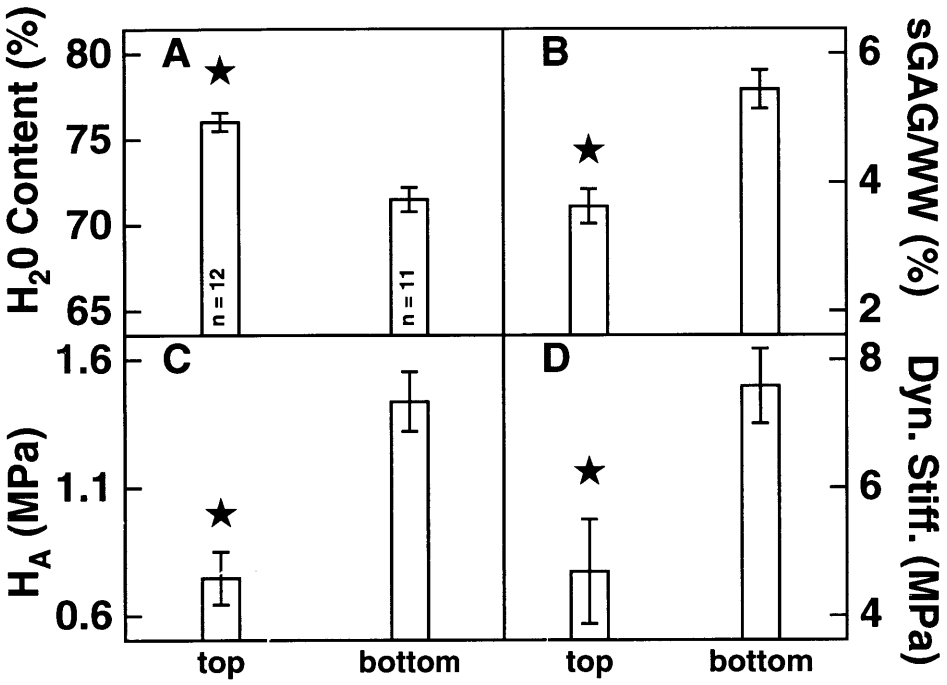

Figure 2.5: Depth dependent properties of pooled cartilage samples from the distal femur. The top 1 mm slice had significantly higher water content (A), lower sGAG/WW (B), lower H_A (C) and lower dynamic stiffness at 0.1 Hz (D) than the second slice containing the remaining cartilage down to the subchondral bone. Bars correspond to the mean ± SE; differences were assessed by ANOVA and Fisher's LSD test: filled star, $p < 0.01$.

2.4.5 Relationships Between Physical and Compositional Properties

Correlative analyses showed, most strikingly, that H_A increased with increasing sGAG/WW for all joint surfaces (Figure 2.6; TA: Pearson's R = 0.617; F: R = 0.594; TP: R = 0.663, all $p<0.01$). With increasing water content, H_A decreased for all joint surfaces (Figure 2.6; TA: R = -0.176; F: R = -0.617, $p<0.01$ and TP: R = -0.376, $p<0.05$). This decrease was significantly steeper in TA than TP ($p<0.05$). These results are consistent with those reported by other investigators [76].

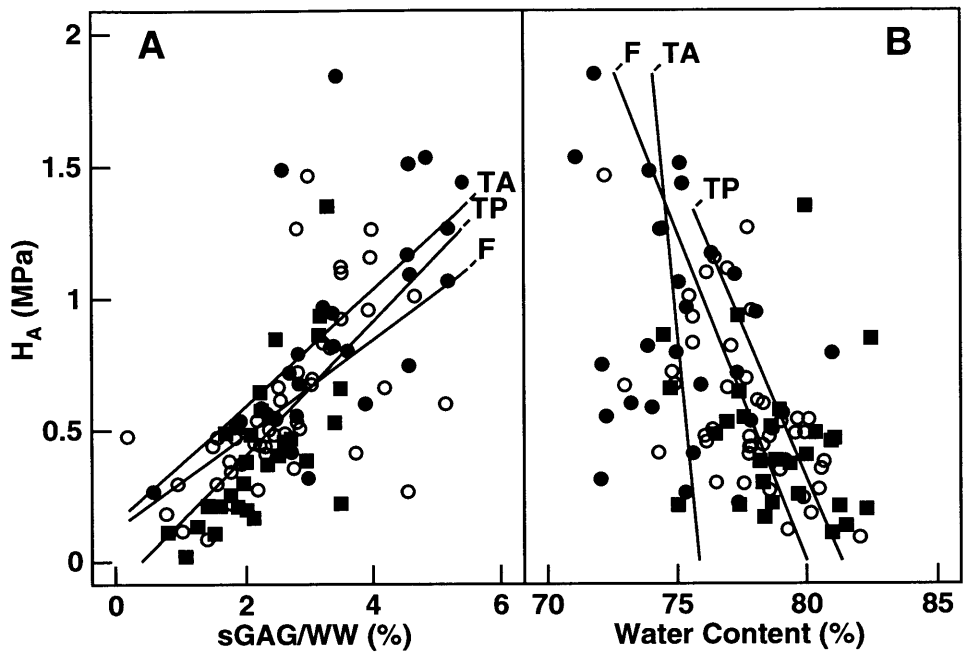

Figure 2.6: Scatter plots showing the variation in equilibrium modulus H_A with sGAG/WW (A) and water content (B). The data are shown for the different joint surfaces: filled circles - talar (TA), open circles - distal femur (F), and filled squares - tibial plateau (TP). H_A increased with increasing sGAG/WW for all joint surfaces (TA: Pearson's R = 0.617, F: R = 0.594 and TP: R = 0.663, all $p < 0.01$). With increasing water content, the H_A decreased for all joint surfaces (TA: R = -0.176, F: R = -0.617, $p < 0.01$ and TP: R = 0.376, $p < 0.05$); this decrease was significantly faster for TA than TP ($p < 0.05$).

2.5 Discussion

A self-consistent picture emerges from the complementary biomechanical and biochemical composition data comparing the top 1 mm slices of human knee and ankle cartilages. The talar cartilage extracellular matrix appears denser with a higher sGAG content and lower water content (Figure 2.2). Together, these properties are consistent with the higher equilibrium modulus and dynamic stiffness found in talar cartilage (Figure 2.3). The lower hydraulic permeability of the TA cartilage (Figure 2.3) would also be expected from the higher dynamic stiffness, decreased water content and higher sGAG content [68]. It is not surprising that the streaming potential coefficient (k_e) of normal knee and ankle cartilages are similar, since the streaming

potential coefficient is proportional to the product of fixed charge (sGAG) density and hydraulic permeability [68], and the higher sGAG of the TA is apparently balanced by its lower permeability. The relationship between water content and the modulus and permeability of cartilage is also consistent with previous studies of human patellar cartilage [6]. What is most striking here, is the finding of such consistent differences between the properties of ankle and knee cartilages. These trends were observed not only in the averaged values for all 8 ankle-knee pairs as shown, but in each individual ankle-knee pair.

Differences in the values of equilibrium modulus of cartilages from the opposing surfaces of a joint (e.g., F and TP in Fig. 2.4) have been reported by previous investigators [7]. Such differences in biomechanical properties of cartilages from opposing joint surfaces are particularly of interest, since the mismatch of mechanical properties will cause different strain profiles, potentially altering congruency and ultimately a redistribution of stress across the joint surface [7]. This may cause natural remodeling of the cartilage to withstand altered stresses during normal physiologic loading, as suggested by Yao and Seedhom [250], or increased wear-and-tear due to the property mismatch as suggested by Meachim [159]. Based on the multifactorial ANOVAs performed, there were no significant differences within the joint surfaces. Qualitatively, however, the variations in H_A and sGAG/WW between the tested sites in TA cartilage were of the same level as that for F and TP (Figure 2.4), in contrast to data from other investigators [7, 222]. More samples will be needed to establish significance.

Tissue biochemical composition and the ultrastructure of the extracellular matrix together determine the resulting biomechanical properties of cartilage. The exact relationships are not well understood and appear to be highly non-linear [144]. An example of such interrelationships is the observed inverse correlation between H_A and water content for distal femur cartilages ($R = -0.617$, $p < 0.01$, Figure 2.6), which is consistent with the previous report of Froimson et al. [76]. In addition, Rivers

et al. [193] reported a positive effect of sGAG/WW on H_A in non OA thumb carpometacarpal joints, although weaker (R = 0.221) than the correlation observed here (R = 0.594, Figure 2.6). In contrast, Froimson et al. [76] found no correlation between H_A and sGAG/WW in cartilage from the proximal and distal trochlea. In the present study, multiple linear regression was also performed to assess whether the intrinsic biochemical composition parameters (water content, sGAG/WW and HYPRO/WW) were predictive of the physical properties of the cartilages. For example, 90% of the total variance in H_A at each joint surface (TA, F and TP) was associated with variations in these biochemical parameters (R^2 = 0.88 for TA, 0.90 for T, and 0.83 for 0.86; all $p<0.001$). On all three joint surfaces sGAG/WW was the most significant factor (all $p<0.001$), with HYPRO/WW only significant for F ($p=0.010$). While most of the variance in H_A can thus be accounted for by multiple linear regression, a physically based non-linear model would ultimately be more illuminating.

Investigators have described the unique cellular, morphological, biochemical, and biomechanical features of the more superficial regions of adult articular cartilage, and the contrasting features of the middle and deep regions [98, 148, 207, 247]. Since cyclic compression of cartilage by several percent during joint loading is confined primarily to the upper regions of the cartilage [68, 208], correlative studies of biomechanical and biochemical properties of these upper regions may be important in understanding the etiology of OA. In this context, the contrasting properties of the upper regions of knee and ankle (TA, F and TP) cartilages described here (Figure 2.2, 2.3) may give additional insight into the intrinsic differences in progression to OA in these joint surfaces.

Thus, the denser extracellular matrix of the talar surface compared to TP and F may retard the movement of molecules through the cartilage (impeding transport), possibly reducing the exposure of ankle chondrocytes to exogenous catabolic stimulation. The biomechanical properties and biochemical composition of talar cartilage may additionally endow it with an increased inherent stability to loading, making

it less sensitive to damage and ultimately, the progression of osteoarthritis. In this regard, additional studies are needed to characterize potential differences between chondrocytes in knee and ankle cartilages in their gene expression and matrix biosynthetic response to normal and abnormal mechanical loads.

The depth-dependent inhomogeneities in biochemical composition and physical properties of human adult articular cartilage have been reported by several investigators [98, 148, 207], along with the depth dependent biosynthetic response to static compression [247]. The 2-fold difference in H_A between the top 1 mm slice and the deeper slice of distal femur cartilage (Figure 2.5) is consistent with the previous studies of Schinagl et al. [207] and Wong et al. [247]. Together, these results demonstrate that superficial adult articular cartilage is significantly softer than that of deeper layers, further suggesting the importance of deformation of superficial cartilage during joint loading, and the corresponding response to compression of superficial chondrocytes.

Chapter III

Effects of MMP-1 and MMP-13 Induced Matrix Degradation on Electrokinetic and Dielectric Properties of Adult Articular Cartilage by Surface Spectroscopy

3.1 Introduction

A variety of physical and biochemical techniques are currently being investigated to enable early detection of cartilage degeneration or the staging of cartilage repair tissue following surgery. A probe that measures the *mechanical* properties of cartilage *in situ* in which indentation is used to assess cartilage stiffness has been developed by Lyrra et al. (Artscan 1000, Artscan Medical Innovations, Helsinki, Finland) [136]. Our approach exploits the *electrical* and *electromechanical* transduction properties of cartilage as a sensitive indicator of cartilage degeneration or repair.

Electromechanical transduction properties of cartilage have been shown to be a sensitive indicator of early matrix degradation [16, 67]. We have developed an electrokinetic surface probe and shown, previously, that electric current-generated mechanical stress measurements could reveal focal, depth-dependent degradation associated with proteoglycan (PG) loss from the tissue [14]. In this approach small sinusoidal electrical currents are imposed by an interdigitated electrode array that rests on the cartilage articular surface [16]. The current causes an electrophoretic motion of the negatively charged cartilage extracellular matrix (ECM) towards the positive electrode and an electroosmotic motion of intratissue fluid towards the negative electrode [67, 199]. These combined effects produce measurable normal mechanical stresses at the tissue surface that can be detected by an overlying piezoelectric stress sensor [16]. The stress produced is at the same fundamental frequency as

the driving current, but out of phase due to the poroelastic nature of the cartilage response. The penetration depth into the tissue is proportional to the spatial wavelength of the interdigitated electrode structure, defined as twice the electrode spacing (Figure 3.1). The applied current not only induces intratissue mechanical stress, but produces an electric field within the ECM and an associated voltage drop across the electrodes. This measured voltage drop, normalized to the driving current, is related to the electrical impedance that represents the mostly resistive nature of the cartilage to the flow of current through the tissue.

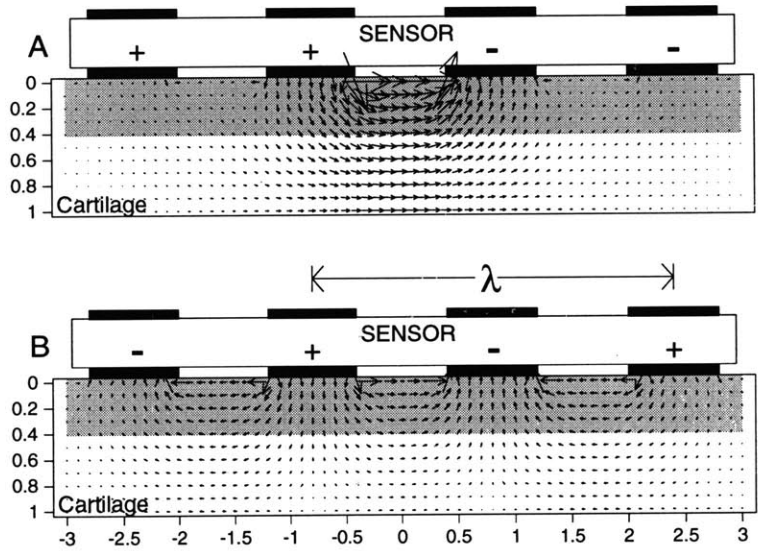

Figure 3.1: When the current is applied in a short wavelength configuration (B) the current is more confined to the upper surface of the tissue. By comparison, with a long wavelength excitation (A), the current can penetrate the full depth, including regions that may not be effected by the enzyme. The crosshatched area represents degraded cartilage where the poroelastic properties may have been altered. By comparing the current-generated stress in both configurations, a short over long stress ratio (SR) can be calculated. The SR will decrease if the surface region is more degraded, allowing spatial localization of degradation. The overlying surface spectroscopy probe has independently addressable piezoelectric and current application (those in contact with the cartilage) electrodes 0.8 mm in width, with a 0.8 mm gap. The spatial wavelength of the interdigitated electrode structure (λ) is defined as twice the electrode spacing. The piezo electrodes are used measure the voltage created by the normal mechanical stresses which is proportional to the current-generated stress, whereas the the voltage drop across the excitation electrodes can be recorded simultaneously for electrical impedance.

Since degradation of cartilage involves alterations in the collagen network as well as PG, it is also important to understand the extent to which surface probe measurements may reflect the status of collagen network, which can be modified *in vitro* using collagenase. The collagenases MMP-1 and MMP-13 are members of the family of matrix metalloproteinases that play an important role in the degradation and turnover of the ECM molecules such as type II collagen and aggrecan during normal remodeling (e.g. embryogenesis) and disease processing [205, 245]. MMP-1 and MMP-13 have been implicated in the progression of osteoarthritis and rheumatoid arthritis since they are found in the associated tissues at higher levels than in normal human tissue [17,212,213,235]. The active enzyme has also been found at the lesions sites on the tibial plateaus of Hartley guinea pig during the progression of spontaneous osteoarthritis [107]. MMP-1 cleaves the three chains of the type II collagen molecule at specific sites, producing helical trimeric fragments of 3/4 (from the N-terminus) and 1/4 in length which can be detected using neoepitope antibodies. MMP-13 initially cleaves type II collagen at this same site, but can additionally cause a second cleavage, residues carboxy terminal to the primary cleavage site [17, 167], and then a third cleavage site another three residues carboxy-terminal to the second cleavage site [233]. The time course of damage induced by MMP-13 was more rapid and transient than that due to MMP-1 [235]; MMP-13 was also found to turn over type II collagen 10 times faster than MMP-1 in humans [167].

Vankemmelbeke et al. [233] recently demonstrated through immunostaining of neoepitopes in cartilage from patients with osteoarthritis that type II collagen degradation was initiated by MMP-1 and MMP-13 at the articular surface and then extended into the middle and deep zones. In addition to this depth dependence, a direct correlation between the Mankin score of OA cartilage degradation and the intensity of the immunostaining of MMPs was recently found [241].

These spatial and temporal changes in the molecular integrity of the collagen network should lead to important changes in the functional mechanical and electrical

properties of the tissue. We therefore hypothesized that simultaneous measurement of current-generated stress (CGS) and tissue electrical impedance via the surface probe's interdigitated electrode array would reflect molecular level changes in the collagen-proteoglycan matrix. Thus, our objectives were to quantify simultaneous changes in the current-generated stress response and the cartilage electrical impedance following treatment with MMP-1 and 13, using the diagnostic surface probe. A non-destructive means of assessing the effects of degradation of collagen and proteoglycans on the physical properties of cartilage *in situ* would help to elucidate the mechanisms of early OA, and could potentially provide a means for *in vivo* physical diagnostics following treatments to initiate cartilage repair.

3.2 Methods

Distal femurs from 1.5-2 year old steers were obtained and never frozen. The femoropatellar groove was isolated (Fig. 3.2A), and 9.5 mm diameter cartilage/bone cores were removed from the medial and lateral facets with the articular surface always intact and as flat as possible using a specially designed coring bit. Freshly harvested cartilage/bone cores were mounted in a cylindrical confining chamber containing buffer (0.1 M NaCl and 0.05 M Trizma, pH 7.4), or buffer + 10 μg/ml rhMMP-1 or rhMMP-13 [167], such that the enzyme could only penetrate into the cartilage from the intact articular surface and enzymatic digestion products would be released only to the bath [14](Fig. 3.2B). The sealed chamber was placed in an incubator at 37^{o}C and gently shaken to minimize formation of stagnant films at the cartilage-buffer interface which could impede transport. The enzymes rhMMP-1,13 had been previously activated.

After digestion times up to 24 hours, the buffer was collected and examined to assess the extent of matrix degradation after treatment by MMP-1 or MMP-13, and the cartilage/bone cores were briefly placed in 10 mM o-phenanthroline to stop the activity of the MMP-1 or 13. Damage to the extracellular matrix constituents

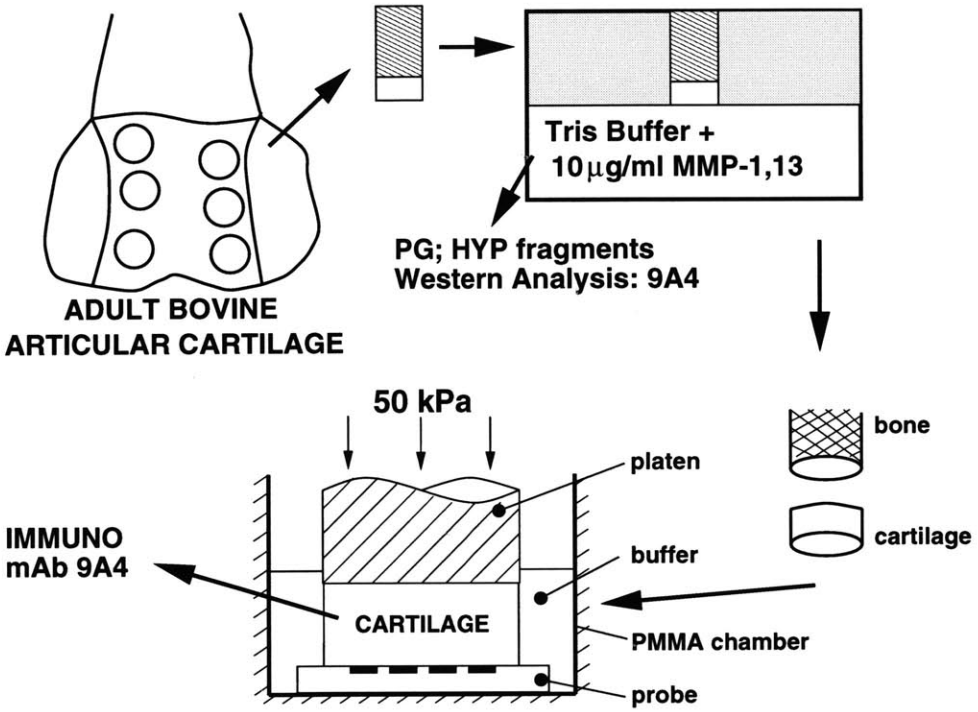

Figure 3.2: Cartilage/bone cores were removed from the femoropatellar groove of adult bovines (A) and mounted in a confining chamber containing buffer (0.1 M NaCl and 0.05 M Trizma, pH 7.4), or buffer + 10 μg/ml rhMMP-1 or rhMMP-13 such that the enzyme could only penetrate into the cartilage from the intact articular surface. After digestion, the buffer was collected and examined to assess the extent of matrix degradation after treatment (B). An 800 μm thick disk was then removed from the cartilage/bone cores (C) without disrupting the articular surface and then placed in contact with a four electrode variable wavelength surface probe for CGS and impedance measurements (D). After testing, the cartilage disks are subject to immunohistochemical analysis, with sections stained by monoclonal antibody 9A4 to localize damage to the collagen matrix (E).

lost to the bathing medium was assessed by quantitative high performance liquid chromatography (HPLC) analysis of hydroxyproline (HYP) using the Gilson (Middlebury, WI) ASTED methods [47,182]. For loss of PG, samples were passed through a 30 X 0.78-cm TSK-GEL 5000PWXL column and the column effluent monitored at 540 nm for proteoglycan fragments with chondroitin sulfate (Seikagaku America, Rockville, MD) as a standard [182, 197]. Hydroxylysyl pyridinoline crosslink release to the buffer after MMP-1 treatment was also measured. In addition, western analysis

of the media fractions were performed using monoclonal antibody 9A4, which recognizes the C-terminal neoepitope -Gly-Pro-Pro-Gly-Pro-Gln-Gly-COOH generated by collagenase treatment of type II collagen.

An 800 μm thick disk was then removed from the cartilage/bone core by a sledge microtome (Fig. 3.2C), without disrupting the articular surface and placed in contact with a four electrode variable wavelength surface probe constructed as described previously [16](Fig. 3.2D). The cartilage disk was held in unconfined compression within a cylindrical poly[methyl methacrylate] testing chamber at a small static tare stress of 50 kPa by a platen held in the jaw of a Dynastat mechanical spectrometer (Hingham, MA) at 25^{o}C in the same (enzyme-free) digestion buffer as used previously.

A sinusoidal current density of 1 mA/cm^2 was applied to the tissue over the frequency range 0.025-1.0 Hz using a bipolar operational amplifier (Kepco, Flushing, NY), such that the total current amplitude was constant at all frequencies, and driven by a programmable frequency generator controlled through a computer. The output of the piezoelectric sensor electrodes are passed through a high impedance electrometer, low pass filtered to remove 60 Hz noise and differentially amplified. The signals are recorded on a computer, and combined with a mechanical sensor calibration done before each test to obtain the current-generated stress (details in [16]). The constant applied current also leads to a distribution of current density and electric field within the tissue, and an associated voltage drop across the electrodes. This voltage drop across the electrodes is simultaneously measured and recorded with a computer. The amplitude of the measured voltage drop between electrodes divided by the applied current amplitude is defined as the electrical impedance. The electrical impedance of the tissue at these frequencies is dominated by the resistance of the hydrated ECM; the latter resistance is inversely proportional to the density of mobile ions within the intratissue fluid. Thus, the electrical impedance of the tissue will increase with decreasing PG fixed charge content on increased swelling at constant PG content,

since both these conditions lead to a lower concentration of mobile ions in the ECM by Donnan equilibrium [148]. In addition, electrode/electrolyte interfacial conditions may affect the total impedance measured at the electrodes [80].

The current-generated stress and electrical impedance are measured for two different electrode configurations (short and long wavelength, Fig. 3.1). Using 0.8 mm wide electrodes spaced 0.8 mm apart and connected in the short wavelength configuration shown in Fig. 3.1B, the applied current density is more concentrated near the upper surface of the tissue. By comparison, with a long wavelength excitation (Fig. 3.1A), the current can penetrate the full depth, including regions that may not be effected by the enzyme. Since each electrode of the interdigitated electrode array is independently addressable, electrode configurations and thus the wavelength of the driving current can be changed externally without disturbing the cartilage sample. By collecting the current generated stress in both configurations, a short over long wavelength current-generated stress ratio (SR) can be calculated. The SR will decrease if the surface region is more degraded, allowing for spatial localization of degradation. In the present study, the long and short wavelengths were 6.5 mm and 3.2 mm respectively. The penetration depth of the current into the tissue is approximately 1/3 the spatial wavelength [16], and the induced current-generated stress was measured at the tissue surface by the piezoelectric stress sensor of the probe. After testing, the residual cartilage disks were saved for immunohistochemical analysis. The sections were stained with monoclonal antibody 9A4 [107] to localize damage to the collagen molecules of the ECM (Fig. 3.2E).

3.2.1 Statistical Analysis

Sample quantities are expressed as mean $\pm$ SE, and the difference between the mean of samples was assessed by a two-tailed t-test.

3.3 Results

3.3.1 Immunohistochemistry

Immunohistochemical staining with mAb 9A4 was absent in control tissue (Fig. 3.3A), and was most intense in the superficial layer of MMP-1 and MMP-13 treated tissue (Fig. 3.3B,C). MMP-1 cleaved to an increasing depth with time; staining was apparent to a depth of 0.8 mm by 24 hours (below the border of Fig. 3.3B). In contrast, staining for MMP-13 appeared confined to the surface, (Fig. 3.3C). Western analyses of media fractions with monoclonal antibodies 9A4 showed concomitant release of 3/4 fragments (data not shown).

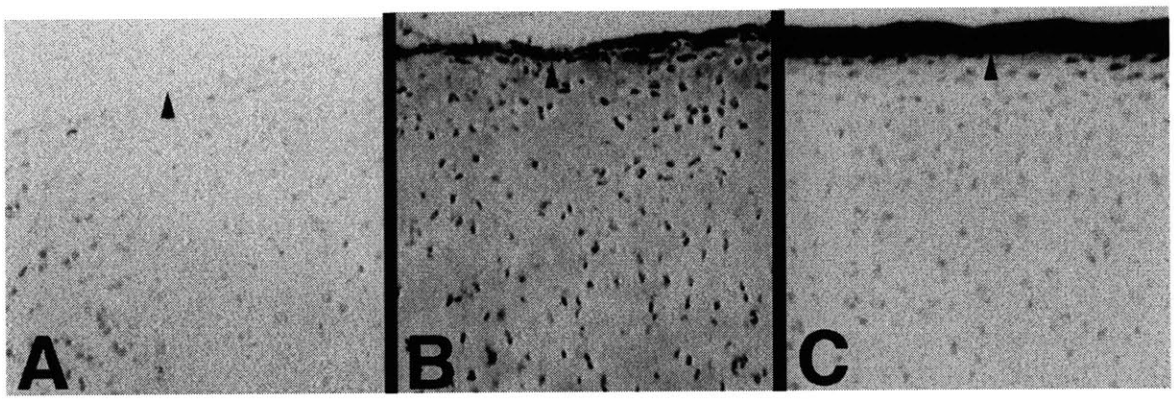

Figure 3.3: Immunohistochemical staining with 9A4 (mAb to collagen C-terminal neoepitope) was absent in control tissue (A), and was most intense in the superficial layer of MMP-1 and MMP-13 treated tissue (B and C). MMP-1 cleaved to an increasing depth with time; staining was apparent to a depth of 0.8 mm by 24 hours (below the border of B). In contrast, staining for MMP-13 appeared confined to the surface, only penetrating 50 μm (C). Arrows indicate the surface of the cartilage.

3.3.2 Quantitative Analysis of Matrix Damage

The release of PG and HYP constituents (as % of total) increased with time of treatment by MMP-1 (Fig. 3.4A), and was greater than that released by MMP-13 treatment by 24 hours (Fig. 3.4B). The PG fragments released by MMP-13 treatment were generally larger than those released by MMP-1, but also contained smaller con-

stituents that could be consistent with decorin or biglycan. In addition, the release of pyridinoline crosslinks were detectable at 24 hours after MMP-1 treatment.

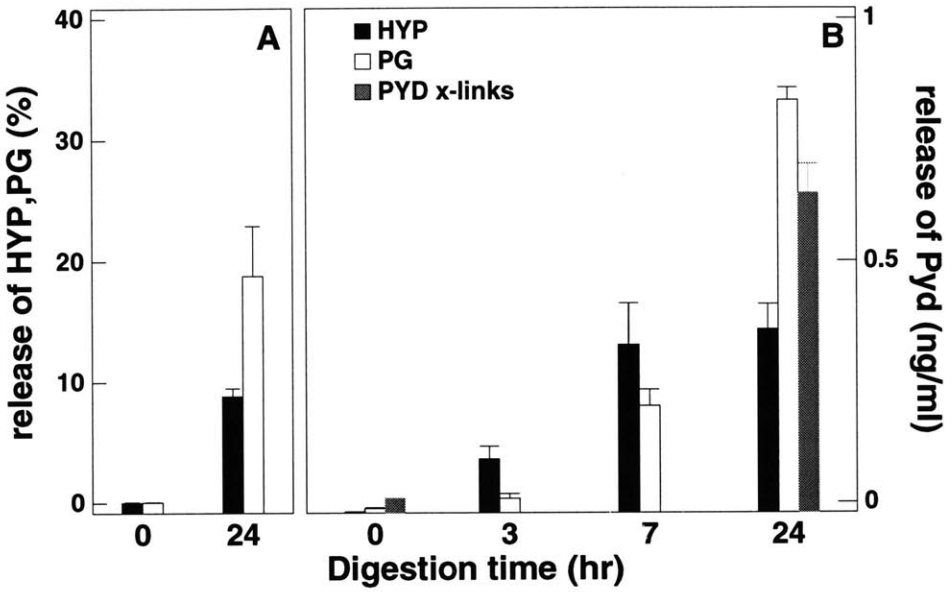

Figure 3.4: The release of PG and HYP constituents (as % of total) increased with time of treatment by MMP-1 (B), and was greater than that released by MMP-13 treatment by 24 hours (A). With MMP-1 treatment, the release of hydroxylysyl pyridinoline cross-links were detected after 24 hours. Bars correspond to the mean ± SE, N=4.

3.3.3 Current-Generated Stress

Figure 3.5 shows the short-wavelength to long-wavelength stress response ratio (SR) for control disks (0 hour) and disks after treatment for 24 hours using MMP-1. The SR ratio decreased significantly by 24 hours at f = 0.025 Hz ($p<0.01$). There were no significant differences between 0 hour controls and disks incubated with buffer alone for 24 hours. Treatment with MMP-13 did not significantly alter the SR ratio compared to controls after 24 hours at all frequencies tested (data not shown).

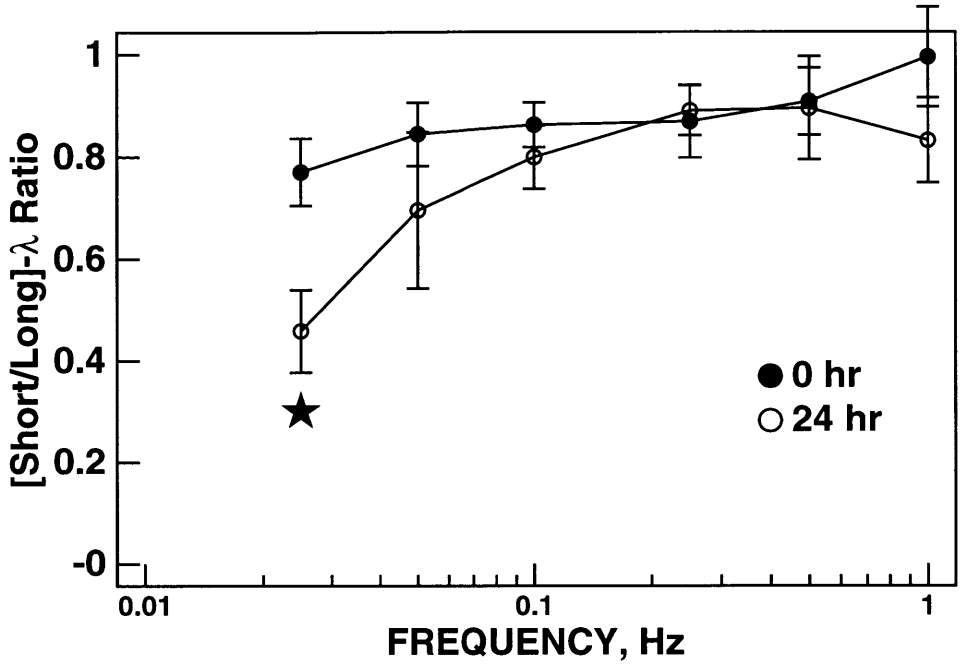

Figure 3.5: The short-wavelength to long-wavelength stress response ratio (SR) for control disks (0 hour) and disks after 24 hours MMP-1 treatment. MMP-1-induced degradation caused a decrease in this ratio by 24 hours, significantly different at 0.025 Hz ($p < 0.01$). In contrast, there were no significant differences between controls and disks treated with MMP-13 by 24 hours (data not shown). Mean ± SE (N=4-7), and the differences against controls assessed by students t-test: filled star, $p < 0.01$.

3.3.4 Impedance

Treatment with MMP-1 and MMP-13 caused a significant increase in the measured total impedance over the broad frequency range used for CGS measurements (Fig. 3.6), using the long wavelength configuration of Figure 3.1. The impedance increased most significantly at frequencies greater than 0.05 Hz ($p<0.05$).

3.4 Discussion

It has been demonstrated previously that current-generated stress measured by surface electromechanical spectroscopy can sensitively detect cartilage degradation using a model in which the PG constituents had been selectively degraded with trypsin. The

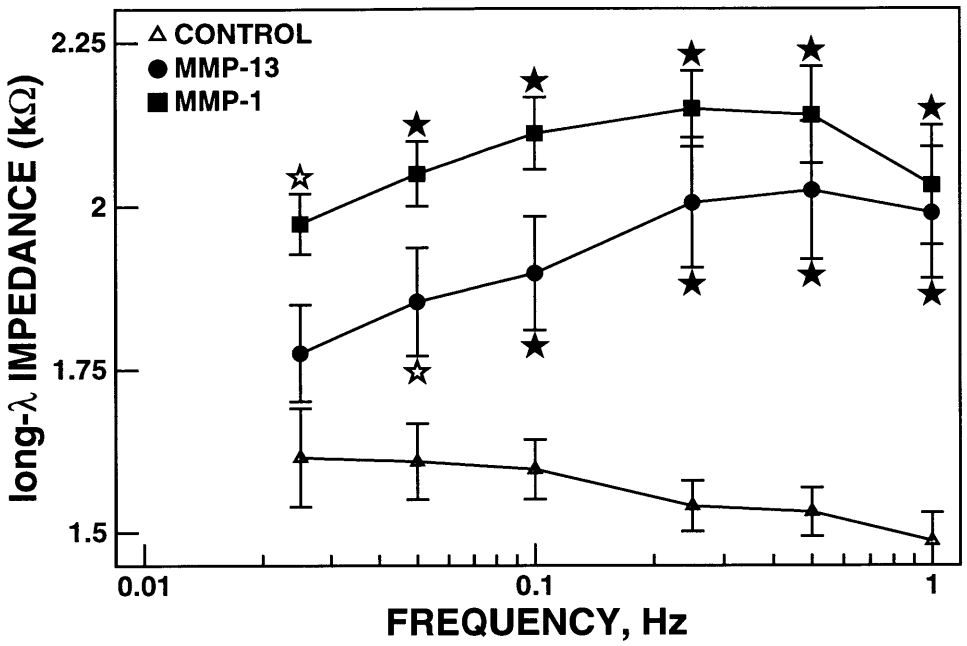

Figure 3.6: The electrical impedance of cartilage treated 24 hours with MMP-13 (filled circles) and MMP-1 (filled square), in the long wavelength configuration compared with controls (triangles). The impedance increased significantly after treatment, particularly at the higher frequencies. Mean ± SE (N=4-11), and the differences against controls assessed by students t-test: filled star, $p<0.01$, and open star, $p<0.05$.

operating principles of the surface probe would dictate that the removal of negatively charged aggrecan by trypsin treatment and the resulting changes to the poroelastic properties of the ECM should decrease the current-generated stress response of the surface probe. Berkenblit et al. [14, 16] showed that this technique was, indeed, sufficiently sensitive to measure such changes using newborn bovine cartilage. However, the influence of collagen matrix damage on the current-generated stress had not been quantified. Selective damage to the collagen network could increase tissue swelling, thereby decreasing the aggrecan concentration and fixed charge density of the ECM, and potentially causing increased loss of aggrecan from the loosened network. In this study, the effects of degradation on current-generated stress and tissue impedance were quantified using surface probe measurements using adult bovine articular cartilage treated with MMP-1 and MMP-13. Significant, repeatable changes

in both physical parameters were observed, consistent with degradation of the collagen/proteoglycan network.

The observed changes in CGS and electrical impedance must be interpreted in the context of the specific matrix alterations caused by MMP-1 and MMP-13. Based on immunohistochemical staining (Fig. 3.3), MMP-13 failed to penetrate $\sim 50\mu$m into the intact articular cartilage surface. Tight binding of the hemopexin domain of MMP-13 to type II collagen may prevent the enzyme from diffusing further into the tissue. Thus, MMP-13 remains localized at the articular surface and caused substantial superficial damage as detected by immunostaining (Fig. 3.3C). In contrast, the 45 kDa MMP-1 molecule is known to undergo autolysis between residues Pro269 and Ile270 resulting in the separation of the hemopexin domain from the catalytic domain. The specificity of the smaller 19 kDa catalytic domain to type II collagen is lower, and increased activity to aggrecan at the N342-343F site is known to occur. This possible activity to aggrecan, along with the increased transport of the smaller catalytic domain, together probably account for the deeper penetration of MMP-1-induced collagen damage (Fig. 3.3B). The loss of PG constituents after MMP-13 treatment suggests that, indeed, a significant portion must be released as a direct result of the collagen damage. The PGs released were of higher molecular weight than those released by MMP-1 and are presumed to be more intact. In addition, lower molecular weight PGs were released by MMP-13 treatment that could be consistent with biglycan or decorin. However, sequencing studies would be needed to confirm this.

Western analysis of the media detected release of 3/4 and 1/4 fragments of type II collagen after treatment with MMP-1 and MMP-13, confirming that collagen network damage occurred. In addition, PG constituents were also found in the medium after treatment with MMP-1 and MMP-13. Their presence could again be attributed to two mechanisms, autolysis of the MMP-1 causing non-specific activity at the IGD site, and/or the loss of PGs caused by damage to their restraining collagen

network. In the TSK-GEL 5000PWXL column, the PGs released formed a precise sharp peak that was consistent with the 342/343 cleavage in the interglobular (G1-G2) domain of the aggrecan molecule, the site also cleaved by stromelysin and other MMPs. The autolysis of the MMP-1 has also been detected in analysis of the ECM fragments found in the joint of patients suffering from osteoarthritis (Therefore, this form of the enzyme may also be more clinically relevant to OA).

As in OA, cleavage and fibrillation of superficial collagen can result in a loss of tissue PG due to local collagen network damage. The observed loss of pyridinoline crosslinks provided further evidence of collagen network loosening. In our cartilage preparation, great care was taken to leave the surface layer of the cartilage undisturbed due to its ultrastructural importance in adult (mature) cartilage as a possible barrier to transport. Since the collagen matrix damage proceeds from the articular surface inward, the disruption could lead to enhanced transport of the PGs from the bulk of the tissue.

Given these patterns of matrix damage, the observed changes in CGS and electrical impedance can now be interpreted. An essential tool in resolving the extent of collagen damage in cartilage is the ability of surface spectroscopy to spatially localize the changes in the CGS with depth from the articular surface. Using four electrodes 0.8 mm wide and spaced 0.8 mm apart (Figure 3.1), the applied current density with short wavelength configuration is more concentrated near the upper surface of the tissue, while in a long wavelength excitation the current can penetrate the full tissue depth, including regions that may not be effected by the enzyme (Fig. 3.1). Thus the short/long SR would decrease if the upper regions of tissue were more degraded as was observed with MMP-1 (Fig. 3.5). In the case of MMP-13 treated tissue we were unable to discriminate between control and 24 hour treated tissue. As the MMP-13 damage extended into the surface by only $\sim 50\mu$m, the four electrode probe design ($\lambda = 3.23$ mm) was insufficient to measure a change in the short/long SR. In contrast, the combined collagenase and PG degradation due to MMP-1 treatment are

consistent with poroelastic changes that are reflected in decreased CGS SR. In future designs, the electrode wavelengths can be made shorter to have the ability to spatially resolve damage closer to the articular surface, thus increasing the diagnostic sensitivity at earlier stages of controlled damage models.

In addition to CGS, the electrical impedance was measured at each frequency tested. Cartilage impedance in this frequency range is essentially resistive in nature, and showed increase with decreasing PG content or increased swelling at constant PG. Thus, damage to collagen and/or PG could both increase the impedance, as was seen with the both short and long wavelength and both MMPs in this study (Fig. 3.6). The detection of an impedance change with MMP-13, implies this measure is sensitive to changes even in the most extreme superficial layer.

As the impedance is a purely electrical measure of the state of the ECM (similar to the stiffness being purely mechanical), it does not have the dynamic range of the current-generated stress, which is dependent on electromechanical coupling. For example, if all the PGs were removed from a cartilage sample the measured stiffness would only decrease by 50% [55] and the impedance by only 28% [13], whereas the CGS will fall to zero. However, the impedance measurement can be made very accurately and simply in smaller geometries than CGS, since there are less constraints on the size of electrodes without the piezoelectric film needed to measure the stress.

Therefore, the two simultaneously measured probe outputs, CGS and impedance, were able to detect controlled degradation *in vitro* that was induced by MMP-1, and both MMP-1 and MMP-13, respectively. We are currently developing a electromechanical spectroscopy probe to make both measurements non-destructively for integration as a diagnostic tool for the arthroscopic surgical suite. With an active area of 4.5 mm, it is an appropriate size for open joint or arthroscopic procedures in humans. An earlier prototype was successfully tested in open joint procedures on the distal trochlear notch of a canine under control of a surgeon [225].

Chapter IV

Effects of Trypsin Induced Matrix Degradation on the Dielectric Properties of Newborn Articular Cartilage by Surface Spectroscopy

4.1 Introduction

In current-generated stress measurements (CGS), small amplitude sinusoidal electrical currents are imposed by an interdigitated electrode array that rests on the cartilage articular surface. The current causes an electrophoretic motion of the negatively charged fixed matrix molecules (proteoglycans) towards the positive electrode and an electroosmotic motion of the mobile ions of the fluid phase towards the negative electrode. These combined effects produce a measurable mechanical stress at the tissue surface that can be detected by an overlying piezoelectric stress sensor. The current that is associated with the CGS described above also simultaneously produces a voltage drop across the electrodes (Figure 4.1), and after it is normalized by the driving current, producing an impedance that represents the mostly resistive nature of the cartilage to the flow of current through the tissue. The electrical impedance is simultaneously measured with the CGS making it practical to apply during an *in vivo* clinical application. Figure 4.1 shows a schematic of the current source that delivers current to the electrokinetic probe at the cartilage surface, where the impedance is defined as:

$$Impedance = Z_{meas} = \frac{V_{out} - V_m}{I_c}$$

After observing the significant increases in impedance with MMP-1 or MMP-

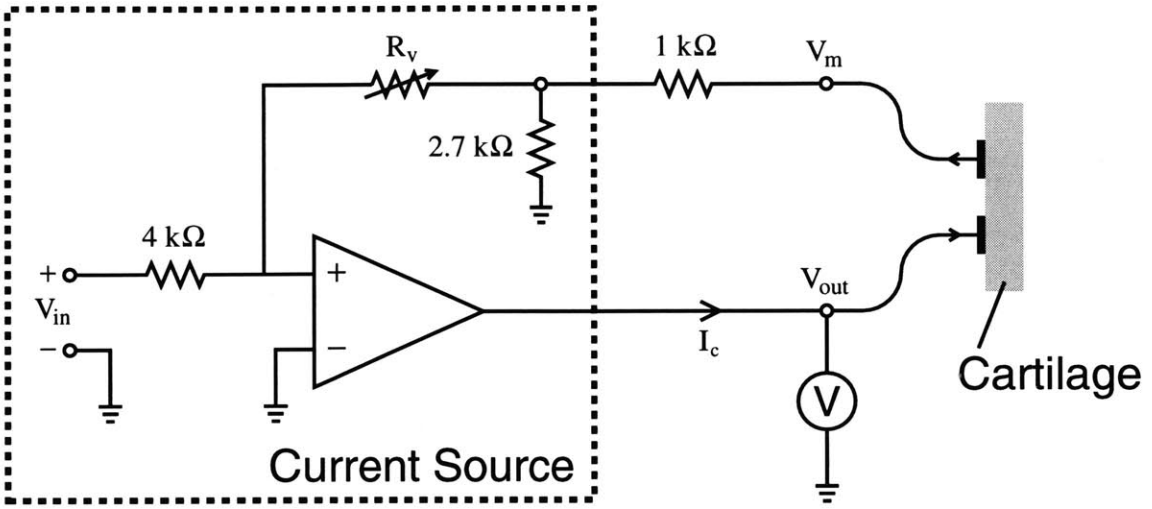

Figure 4.1: Schematic of the current source used for impedance measurements. A sinusoidal input voltage (V_{in}) to the current source resulted in a current I_c to the cartilage. The voltage difference $V_{out} - V_m$, between electrodes on the cartilage, divided by the current I_c is the measured impedance, Z_{meas}. This purely electrical measurement can be made simultaneously with the current generated stress response at the prescribed input frequencies or sequentially at only other frequency (i.e., 1 kHz)[Courtesy S. Berkenblit [13]].

13 treated tissue for 24 hours versus controls in Chapter III, it was of interest to more closely characterize this behavior, and possibly extend the frequency range to 1 kHz as had been previously done by Berkenblit [13]. We hypothesized that the high frequency measurements would provide two benefits: (1) the interfacial impedance between the Ag/AgCl electrodes and the ionic bathing solution would be a lower portion of the total measured impedance, and (2) clinically, this measurement could be taken very rapidly, making it less sensitive to surgeon hand tremor and movement.

The measurement with MMP-13 treated adult bovine articular cartilage (Chapter III) were repeated, while incorporating the high frequency impedance measurements at 1 kHz. The current-generated stress of 24 hour treated tissue was not significantly different from that of control tissue, while the impedance at 0.25 Hz was significantly higher than the control tissue for both the short and long wavelengths (Figure 4.2), corroborating earlier results.

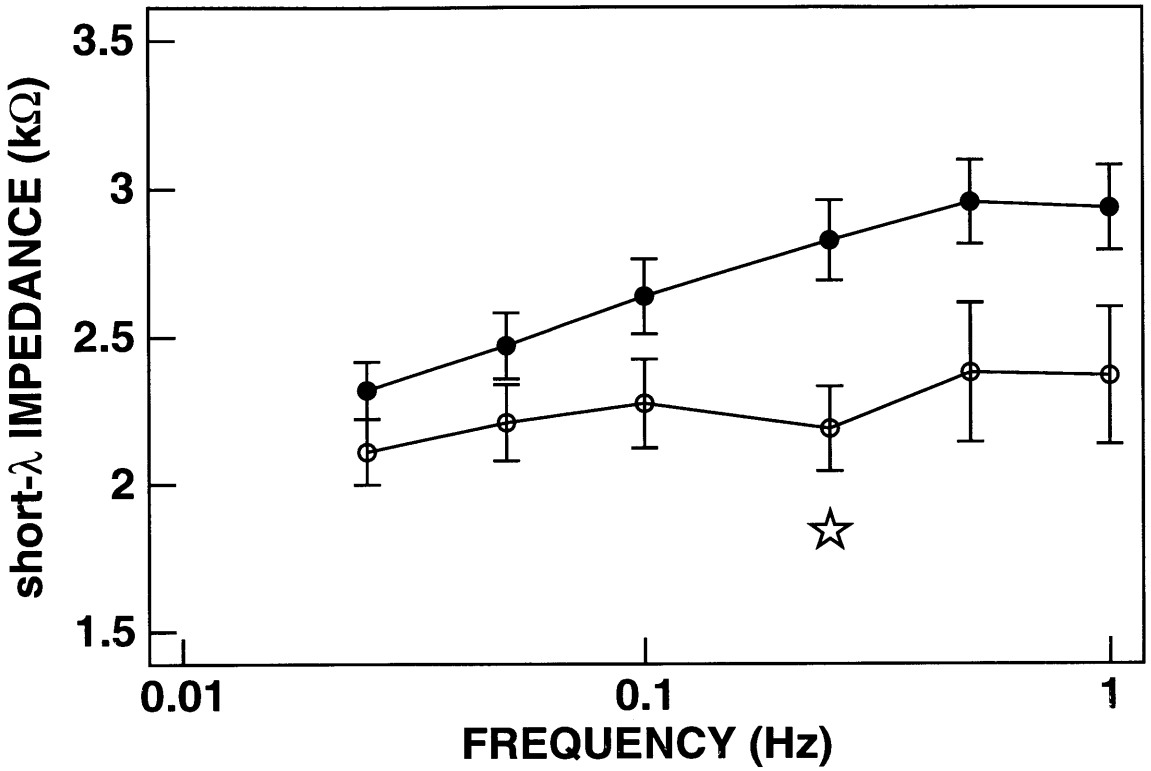

Figure 4.2: The impedance of disks treated 24 hours with MMP-13 (filled circles) versus controls (open circles), in the short-wavelength configuration. The impedance increased significantly after treatment, particularly at the higher frequencies (at 0.25 Hz, open star, $p < 0.05$).

When comparing the impedance at 1 kHz, there was a significant difference between the controls and the 24 hour MMP-13 treated cartilage for the short, long, and extra-long-wavelengths, but the control impedance was larger than the treated tissue (Figure 4.3). The absolute magnitude of the impedance decreased, most likely due to the electrolyte-Ag/AgCl electrode interfacial impedance decreasing with increasing frequency (data not shown). The impedance of the buffer alone at 1 kHz represents the estimated value from simply considering the conductivity of the buffer (by ionic strength) and electrode geometry, indicating that the electrolyte-Ag/AgCl electrode interfacial impedance at 1 kHz is diminishing in magnitude.

There is also a motivation to examine the effect of strain at the cartilage surface on impedance. In the clinical application, if such an impedance measurement is

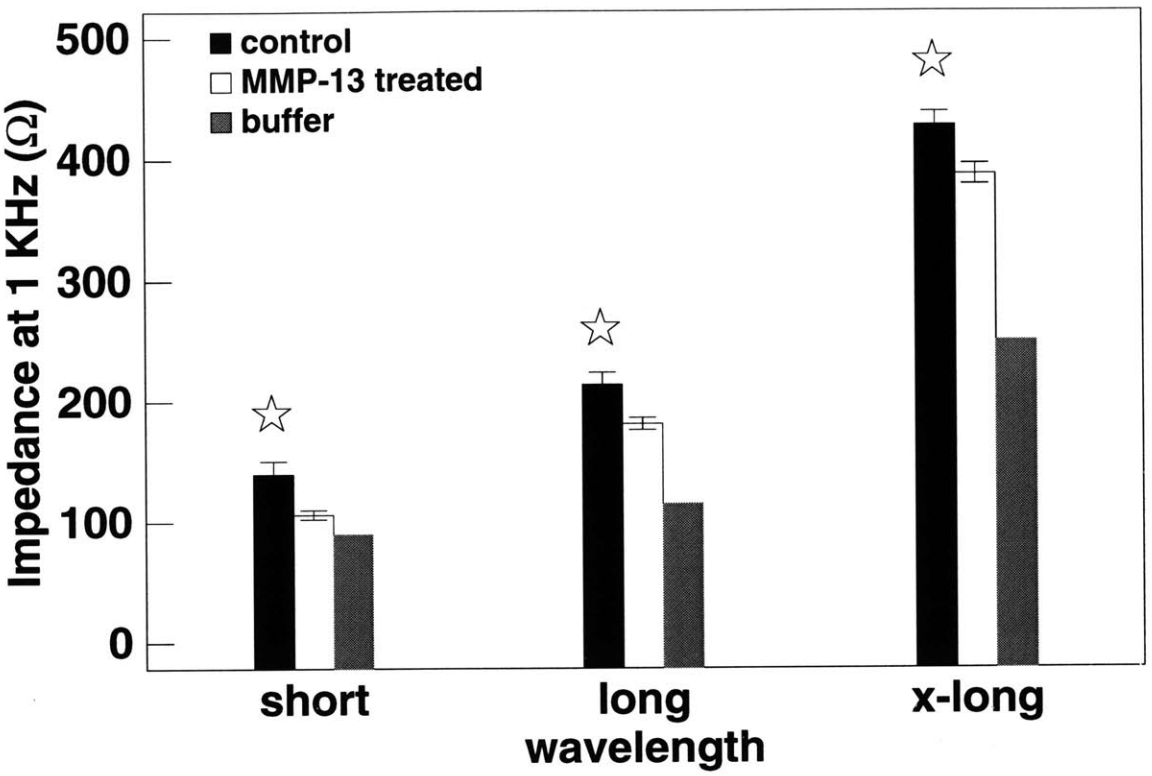

Figure 4.3: The impedance of disks treated 24 hours with MMP-13 at 1 kHz. The impedance decreased significantly after treatment for all wavelengths studied short, long and extra-long (at 0.25 Hz, open star, $p < 0.05$). The associated wavelengths were 2.2, 4.4, and 8.8 mm, respectively. The buffer represent the impedance of the probe electrodes in contact with the buffer only which includes the interfacial impedance of the electrode-electrolyte interface.

to be made successfully, the surgeon would need to create a force between the probe electrodes and the cartilage to ensure proper contact. Therefore, the sensitivity of the impedance to the applied strain becomes important since it will not be known when the measurement is made. Also, as cartilage degrades in from the articular surface (as is seen in OA), a layer of mechanically softer superficial tissue will result at the superficial layer of the tissue. As the tissue deforms under the applied strain the probe will physically move closer to a more PG rich tissue, as this softer layer is compacted. Given this physical situation, it is unclear what the effect on impedance will be since the relative increase of sGAG concentration due to compression will de-

crease impedance while, the compaction of the degraded superficial layer may increase impedance.

Therefore, the objective was to examine the effect of strain (0-50%) on the dielectric properties (impedance) of newborn bovine articular cartilage, over a range of frequencies (0.025 - 1000 Hz) and with duration of controlled trypsin treatment (0-24 hours with 1 mg/ml).

4.2 Theoretical Considerations

In this context, impedance (Z) can be expressed as a function of the strain and sGAG content, which translates into two terms: (1) due to the conductivity of the cartilage and the electrode geometry, and (2) due to the contribution of the electrokinetic response of the cartilage to the applied current density.

$$Z = f\ (\ strain\ ,\ sGAG\ content\ ) = \underbrace{\Xi\ (k_{22})}_{conductivity} + \underbrace{\Phi\ (H_A, k_p, k_e, f, ...)}_{electrokinetics} \tag{4.1}$$

Simulations using a computational implementation of the multi-boundary value problem for finite sized electrodes of prescribed experimental geometry* over a wide range of parameters found the electrokinetics term to be negligible with respect to the conductivity term (see Appendix F). Therefore, the impedance can be estimated from the conductivity of the cartilage alone by the following expression:

$$k_{22} = k_{22}^{o} \underbrace{\left[2\left(\frac{1-v'}{2+v'}\right)\right]}_{Maxwell} \underbrace{\left[\left(\frac{1-v}{1+v}\right)^2\right]}_{Mackie\ and\ Meares} \tag{4.2}$$

where, k_{22}^{o} is due to the fixed charge density and can be modified by two factors due to:

*The work of Sachs et al. [199] was extended for finite sized electrodes by E. H. Frank

(1) cartilage being an heterogeneous media, originally derived by a Maxwell [157] when considering conductive spheres (sGAG molecules) embedded in a medium with null conductivity based on the volume ratio of charged to uncharged species (v'), and (2) the increased tortuosity of flow due to the existence of solids in the media by Mackie and Meares [138] based on volume ratio of solids in the cartilage (v). The electrical conductivity of cartilage (k_{22}^o) is dependent on the intratissue concentrations of sodium and chloride ions, the predominant mobile charged species. The conductivity of a binary electrolyte solution is given by:

$$k_{22}^o = F \left[\left|z^+\right| u^+ c^+ + \left|z^-\right| u^- c^- \right] \tag{4.3}$$

and z, u, and c are the valences, ionic mobilities, and concentrations of the cations and anions within the tissue, and F is Faraday's constant. For this system, $|z^+| = |z^-| = 1$ for NaCl, and the ionic mobilities of sodium and chloride are 1.8 x 10-4 cm^2/Vs and 2.7 x 10-4 cm^2/Vs, respectively.

Applying Donnan equilibrium and electroneutrality to relate the concentrations of the cations and anions ($c_\pm$) to the fixed charge density ($\frac{\rho_m}{F}$) as follows:

$$c_\pm = \mp \frac{\rho_m}{F} + \sqrt{\frac{\rho_m}{F}^2 + c_b^2} \tag{4.4}$$

where c_b is the concentration of the electrolyte bath (0.15 M for our experiments), and the fixed charge density of the tissue is only a function of the concentration of PGs (C_{pg}):

$$\frac{\rho_m}{F} = \beta \, C_{pg} \tag{4.5}$$

where ρ_m is the macrocontinuum fixed charge density, and $\beta = 1$ mole-charge/266g is a constant relating the amount of charge per gram of proteoglycan [30]. Since we

are interested in the effect of strain on the impedance, the C_{pg} becomes:

$$C_{pg} = \frac{Amount\ of\ sGAG}{V_W(1 - \ strain\ )}$$

The tissue water volume (V_W) is calculated using the wet and dry weights of a cartilage sample and corrected for the strain at which the measurements were taken, and the sGAG content can be found by assaying by the DMMB dye binding method.

The effect sGAG content and applied strain can be simulated by using Equations 4.1- 4.6 and a first order estimate of the impedance (resistive) from the electrode geometry,

$$Z = \Xi\ (k_{22}) = \frac{l}{k_{22}\ A} \tag{4.6}$$

where l is the center-to-center distance between two identical electrodes of area A. Using a cartilage disk 9.5 mm in diameter and 1 mm thick that has a sGAG/WW of 4.1% and a hydration 4.4 (or 81.4% water content) as typical values [13]. In addition, the two electrodes have an area of 4.57 mm^2 and a center-to-center distance of 1.62 mm, will produce impedance as a function of strain and sGAG loss shown in Figure 4.4. sGAG loss was modeled as a uniform loss throughout the volume, by directly reducing the amount in Equation 4.6.

The simulation of Figure 4.4 represents the estimates of the same order as the impedance measurements that have been observed. The model also predicts that as sGAG content decreases (i.e. through degradation) the impedance increases. In addition, the behavior of the impedance with strain, depends on the percentage of sGAG lost. At full sGAG content the impedance will increase with strain and begin to decrease at approximately 30%, whereas when sGAG is lost there is a monotonic increase with applied strain to 50%.

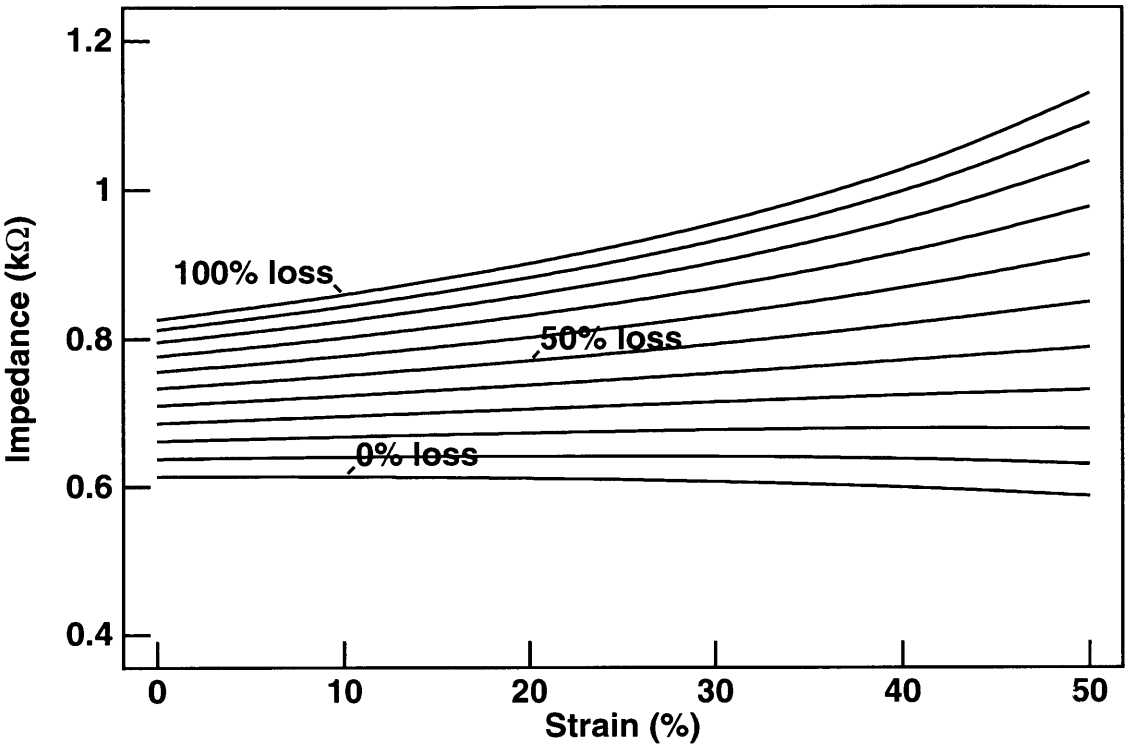

Figure 4.4: The effect sGAG content and applied strain on impedance (resistive) simulated using equations 4.1- 4.6 and a first order estimate of the impedance from the electrode geometry. The simulation assumes typical values for a newborn bovine articular cartilage disk 9.5 mm in diameter and 1 mm thick: a sGAG/WW of 4.1% and a hydration 4.4 (or 81.4% water content). In addition, the two electrodes are modeled having an area of 4.57 mm^2 and a center-to-center distance of 1.62 mm. sGAG loss was modeled as a uniform loss throughout the volume, by directly reducing the amount in Equation 4.6 as indicated.

4.3 Materials and Methods

4.3.1 Specimen Preparation and Experimental Setup

Distal femurs from 1-2 week old (newborn) steers were obtained within hours of slaughter and never frozen. The femoropatellar groove was isolated, and 9.5 mm diameter cartilage/bone cores were removed from the medial and lateral facets using a specially designed coring bit (Figure 4.5A).

Freshly harvested cartilage/bone cores were prepared for exposure to buffer (0.1 M NaCl and 0.05 M Na_2HPO_4, pH 7.2), or buffer + 1 mg/ml trypsin from

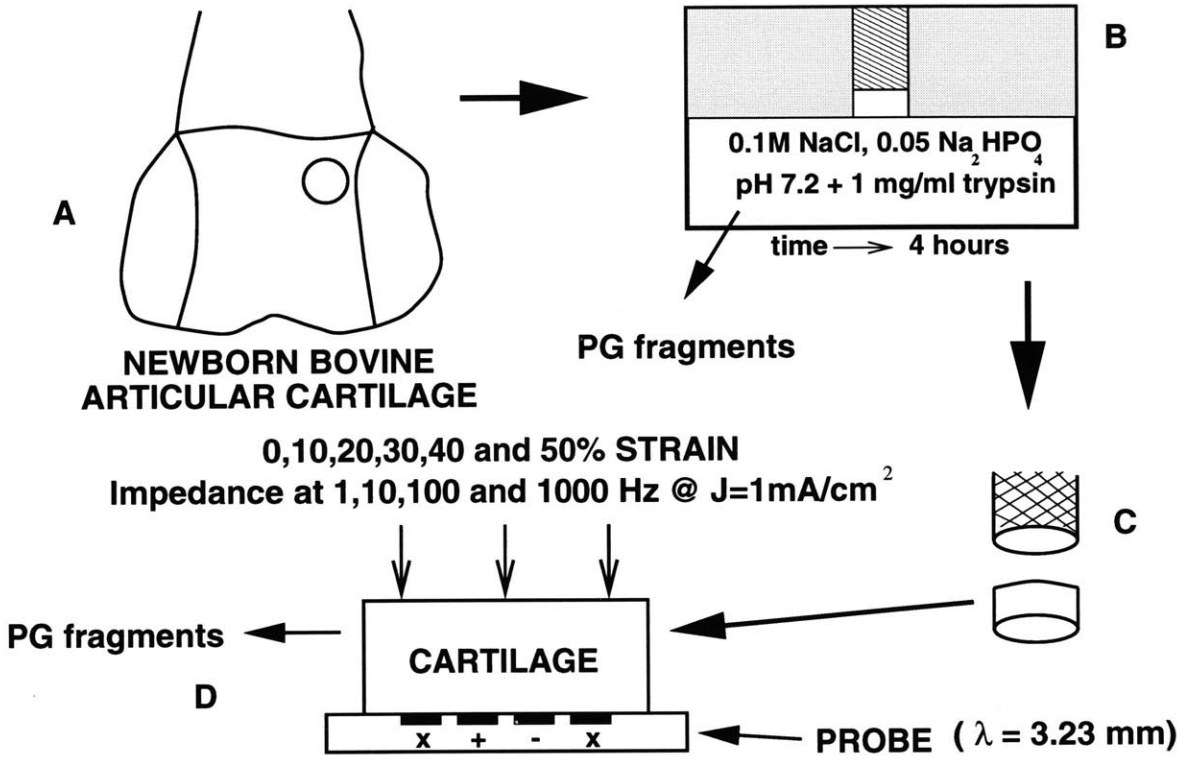

Figure 4.5: The femoropatellar groove from newborn steers were obtained and 9.5 mm diameter cartilage/bone cores were removed (A). The cores randomized to the 4-hour trypsin treatment group were mounted in a confining chamber containing buffer + 1 mg/ml trypsin (B). After 4 hours, the cores were removed from the chamber and a 1 mm thick slice was removed with a sledge microtome, without disrupting the articular surface (C), and placed in contact with a four electrode variable wavelength surface probe (D) in a short-wavelength configuration. The digestion buffer was collected and examined to assess the extent of matrix PGs degradation. The cartilage disk was subjected to increasing strain levels of 0-50% in an unconfined compression arrangement. A sinusoidal current density of 1 mA/cm^2 was applied to the tissue over the frequencies of 1-1000 Hz at each strain level. The cartilage disks were digested and sGAG content found by DMMB dye binding assay.

bovine pancreas. The cartilage/bone cores were first placed in a microtome to create a flat articular surface. For plugs that were to be randomly assigned to the 0 or 24 hours treatment groups, two 1 mm thick slices were further microtomed from the cartilage/bone cores. These cartilage disks were placed in 14 ml polypropylene round bottom tubes (Becton Dickinson, Lincoln Park, NJ) along with either 10 ml buffer or buffer + 1 mg/ml trypsin and placed on a laboratory shaker (Research

Products International Corp, Prospect, IL) to ensure no stagnant diffusion layers are established, thus reducing the efficacy of the enzyme to remove PGs from the cartilage. The buffer only treated plugs were removed at 0, 4 and 24 hours to be assessed as controls (~0% PGs loss). The buffer + trypsin treated plugs were left in this arrangement for 24 hours in an effort to remove all the PGs within (~100% PGs loss), as estimated from previous work with this enzyme on newborn bovine articular cartilage [13].

The final group of cartilage/bone cores randomized to the 4 hour trypsin treatment group were mounted in a confining chamber containing buffer + 1 mg/ml trypsin (Figure 4.5B), such that the enzyme could only penetrate into the cartilage from the flat articular surface and enzymatic digestion products would be released only to the bath [13]. A stir bar was placed in the bath, the chamber was tightly wrapped in parafilm, and placed on a magnetic stirrer for 4 hours at ~25^{o}C, again to prevent stagnant films from forming in the chamber. A 4-hour digestion time was chosen to have an intermediate (~40% PGs loss) release of PGs according to previous data [13]. This method of enzymatic digestion was used for the 4 hour time point to prevent exposure of the entire surface area of the cartilage disk to trypsin for better control of the penetration of the enzyme and in order to more easily interpret the subsequent impedance results. After 4 hours, the cartilage/bone was removed from the chamber and a 1 mm thick slice was removed with a sledge microtome, without disrupting the articular surface (Figure 4.5C).

After the prescribed treatment times in both arrangements, the digestion buffers were collected and examined to assess the extent of matrix PGs degradation and release after treatment with trypsin by DMMB dye binding assay of sulfated proteoglycan constituents [61].

Each 1 mm cartilage disks was then placed in contact with a four electrode variable wavelength surface probe (Figure 4.5D) constructed as described previously [16]. In this case, only the internal two electrodes were used in a short-wavelength con-

figuration (λ = 3.23 mm, penetration depth is ~1 mm) to minimize the shunting of current to the bath solution, which has been previously shown to be as high as 75% in the most extreme cases [13]. The cartilage disk was subsequently subjected to increasing strain levels of 0, 10, 20, 30, 40 and 50% in the Dynastat mechanical spectrometer (Hingam, MA) in an unconfined compression arrangement, at 25^{o}C in the same buffer as above in a cylindrical poly[methyl methacrylate] testing chamber (Figure 4.5D). A sinusoidal current density of 1 mA/cm^2 was applied to the tissue over the frequencies of 1, 10, 100, and 1000 Hz at each strain level. It became evident during the pilot experiments with control plugs that the resultant loads associated with 50% strain levels (between 1-2 kg) became destructive to the probe laminations, thus the control plugs were limited to a upper strain limit of 40%.

After the impedance measurements, the cartilage disks were removed from the Dynastat and allowed to free swell in the experimental buffer for approximately 30 minutes. The disks were then removed from the buffer and the excess water padded away. The disks were cut into 4 quarters (due to their large size) and a weight wet taken of each (AE163 Balance, Mettler Instrument Corp, Hightstown, NJ). After wet weights, the disks were lyophilized, and the dry weights taken. The samples were digested with 2 ml of 200 μg/ml proteinase-K (Sigma, St. Louis, MO) solution at 60^{o}C and aliqouts taken to assay for sGAG content (by dimethylethylene blue dye binding assay) [60].

Sample quantities are expressed as mean $\pm$ SE, and the difference between the mean of samples was assessed by a two-tailed t-test.

4.3.2 Measurement of Cartilage Impedance

The impedance, Z_{meas}, measured across the excitation electrodes of the probe may be represented by an equivalent-circuit model [13] (Figure 4.6A). The impedance of all shunt paths can be lumped into a single equivalent shunt impedance, Z_{sh}, in parallel with the impedance of the cartilage specimen, Z_C. As mentioned, in this series of

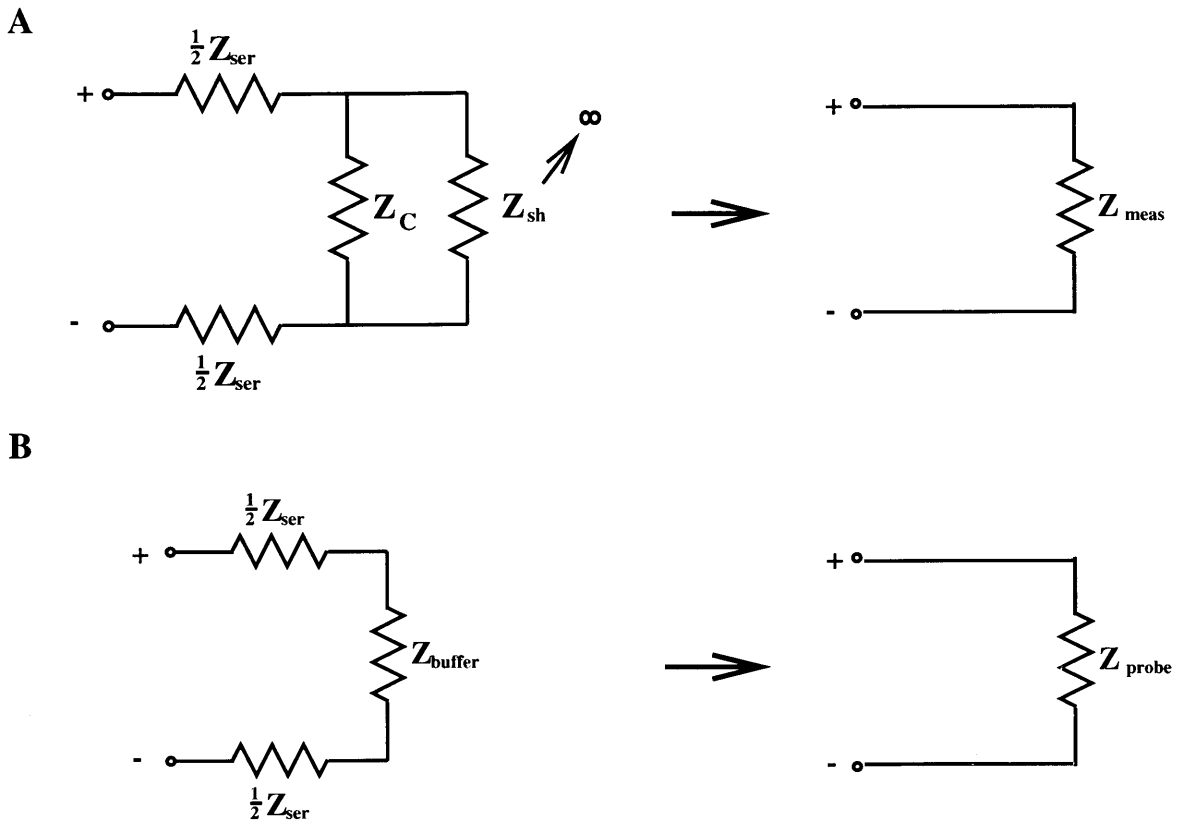

Figure 4.6: A. Equivalent-circuit model for the impedance measured with the surface probe. An equivalent shunt impedance, Z_{sh}, is modeled in parallel with the cartilage impedance impedance, Z_C; in addition, a series component, Z_{ser}, is assumed to be present at the electrode-electrolyte interface, evenly divided between the positive and negative electrodes. B. Similarly, once the cartilage is removed, the probe is in contact with the buffer only.

experiments, only the internal electrodes were used, thus minimizing the shunting of current (therefore, $Z_{sh} = \infty$). A significant series impedance, Z_{ser}, is present at the electrode-electrolyte interface. Although it decreases with increasing frequency [81], it must be accounted for even at 1 kHz. For the purpose of this equivalent circuit, this series component is assumed to be evenly distributed between the positive and negative electrodes (Figure 4.6A). Since a current source is used to drive current to the excitation electrodes, this series impedance would not affect the total amount of current penetrating the tissue; however, it must be taken into consideration when interpreting any measurements of impedance using the probe (and could theoretically

alter the spatial distribution of current density at the electrode surface). Therefore, the cartilage impedance can be expressed:

$$Z_C = Z_{meas} - Z_{ser} \tag{4.7}$$

The measurement of Z_C is then reduced to measuring Z_{ser}. This can be done with two additional equivalent circuits. The first is the removal of the electrodes from the cartilage surface, hence the probe is in contact with the buffer only (Figure 4.6B). Here,

$$Z_{ser} = Z_{probe} - Z_{buffer} \tag{4.8}$$

With the use of a special set of Ag/AgCl electrodes that are assumed to have no interfacial impedance (Annex Research, Costa Mesa, CA), the Z_{buffer} can measured directly. Therefore, combining the measurements together:

$$Z_C = Z_{meas} - \ (Z_{probe} - Z_{buffer}\ ) \tag{4.9}$$

The complex electrical impedances: Z_{meas}, Z_{probe} and Z_{buffer} across the inputs was determined by applying a sinusoidal current at the prescribed frequencies, via a bipolar operational amplifier/power supply (Kepco, Flushing, NY), configured as a current source (Figure 4.1) and driven by a frequency synthesizer via a computer, and measuring the output voltage developed by the current source in order to maintain this current level.

For the two highest frequencies, 100 and 1000 Hz, the measured impedance across the probe inputs, Z_{meas}, Z_{probe} or Z_{buffer}, was computed as the ratio of the voltage drop across the load to the calculated load current:

$$Z_{meas} = \frac{V_{out} - V_m}{I_c} = \frac{\sqrt{2} \cdot V_{RMS}}{I_c} \tag{4.10}$$

where V_{RMS} is the root-mean-square value of the sinusoidal output voltage as mea-

sured by a Fluke digital operating in AC voltmeter mode after one-stage amplification (Gould, Valley View, OH) for increased accuracy. At the frequencies of 1 and 10 Hz, the signals were appropriate to be analyzed by a computer as previously described [23] recording the voltage drop and the driving current. The magnitudes of fundamental Fourier modes at the prescribed frequencies are used to calculate the impedance.

This measurement system was validated by measuring the impedance of several resistors (with nominal resistances in the 10Ω–5kΩ range) placed across the current source outputs; the values determined in this manner agreed within 1% of the resistance values independently measured with a Fluke digital ohmmeter at all frequencies tested.

4.4 Results

Treatment with trypsin significantly reduced the amount of sGAG content in the tissue (Figure 4.7A). Analysis of the control plugs from the 0, 4 and 24 time points, yielded no significant differences, thus the all the control samples are taken as a pooled group for the rest of the comparisons. There was a small (4%) loss of GAGs from the controls, with a significant decrease to 90% from the 4-hour treated tissue and then another significant drop to 99% for those treated for 24-hour. The 0 and 24 hour treatments produced the expected release of sGAG (~0 and ~100, respectively), while the 4-hour time point was more than the 40% that was predicted from prior studies with trypsin on newborn bovine tissue. This loss of sGAG was concomitant with a significant increase in tissue hydration, at the 4 and 24-hour treatment times (Figure 4.7B), which corresponds with previous work [13].

Figure 4.8A-D displays a summary of the results from the impedance measurements, as a function of strain and frequency. As the frequency increases, the magnitude of the impedance decreases for all treatment cases. With increasing strain, there is a monotonic increase of the impedance, for all frequencies. With increasing frequency, the magnitude of the differences between the controls and the treatment

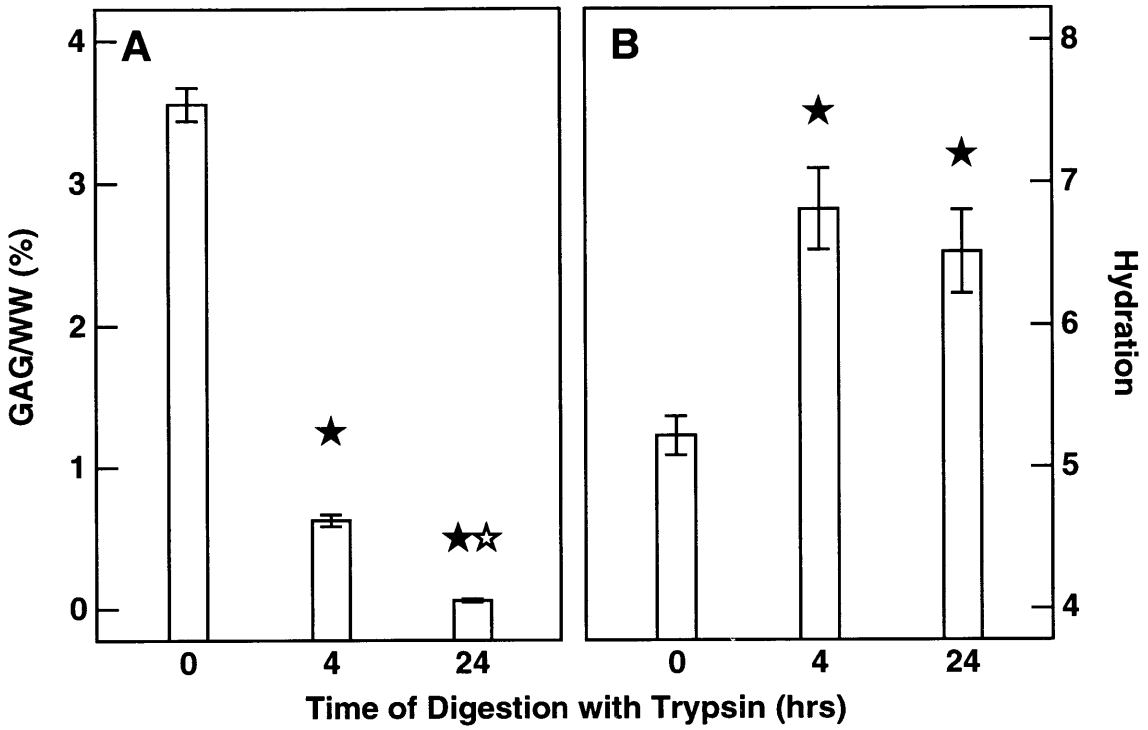

Figure 4.7: Trypsin treatment significantly reduced the amount of sGAG per WW in the tissue (A, open star $p<0.01$ versus 4-hour trypsin treatment, filled star versus control, n=4-6). The 0, 4, and 24 hour controls correspond to a percent loss of sGAG from the tissue of 4, 90, and 99%, respectively. The loss of sGAG content was concomitant with a significant increase in tissue hydration compared to controls(B).

groups decreases, until at 1000 Hz the control (0-hour) falls between the 4 and 24-hour treatment groups for all strain levels. Examining 1 and 1000 Hz at all strain levels, the differences between the two treatment groups (4 and 24-hour) become larger, and significant. At 1 Hz, the enzymatically treated tissue for 4-hours has a higher impedance with respect to controls, while at 1000 Hz, the control tissue has a higher impedance. Qualitatively, this behavior is consistent with previous experiments with MMP-13 treatment of adult bovine articular cartilage.

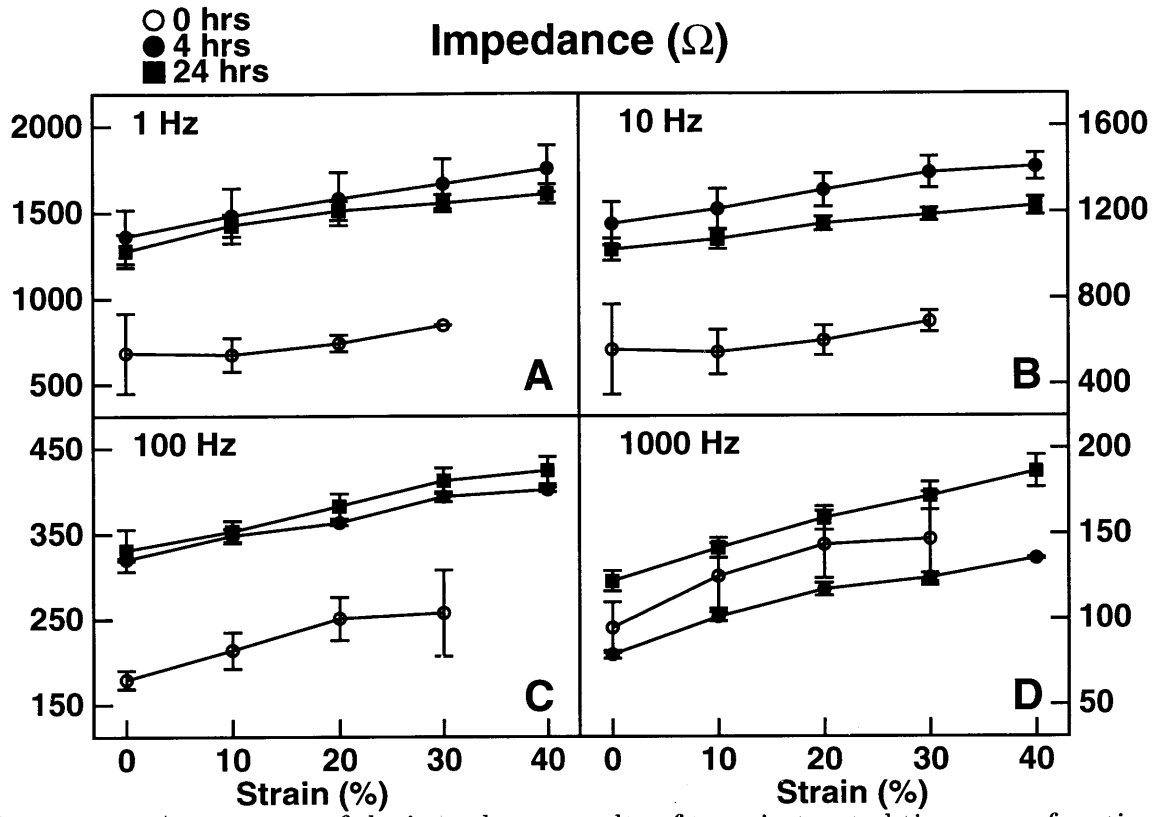

Figure 4.8: A summary of the impedance results of trypsin treated tissue as a function of strain and frequency (A-D). The magnitude of the impedance decreases with increasing frequency for all treatment cases, with increasing strain, there is a monotonic increase of the impedance, for all frequencies. As frequency increases, the difference between the control and the treatment groups decreases, and ultimately at 1000 Hz the control (0-hour) falls between the 4 and 24-hour treatment groups for all strain levels. Also, as the frequency increases the differences between the two treatment groups became more significant at 1 kHz (4 and 24-hour).

4.5 Discussion

Performing impedance measurements using the electrokinetic surface probe is technically simpler and may be more efficient than using the device to measure current-generated stress for several reasons:

1. much higher frequencies (i.e. 1 kHz) can be used, therefore the measurement is performed almost instantaneously without the need for any signal processing,

2. impedance is only dependent on the silver electrode layer of the laminated probe

structure, thus there is no mechanical calibration step required and the system more robust without the difficulties of manufacturing probes with the sensitive behavior of the piezoelectric sensor,

3. the impedance measurements are made simultaneously with the measurement of current-generated stress (in the low frequency range, 0.025-1.0 Hz, where CGS is detectable), simply by monitoring the voltage across the probe inputs, and

4. electrodes can be made arbitrarily small in any arrangement (hence, wavelength) to control the spatial sensitivity of the impedance measurements to possibly diagnose cartilage abnormalities in small animal (i.e. rats) where the cartilage may only be 100 μm thick.

Thus, Figure 4.8 may represent preliminary evidence that an additional method exists to discriminate between normal and degraded cartilage. Indeed, electrical impedance spectroscopy (tomography) has been used as a means of nondestructive materials characterization [137] and biomedical imaging of a variety of tissue types [82, 192]. Measurement of cartilage impedance over a range of frequencies (impedance spectroscopy) could potentially provide additional information about the tissue, such as an estimate of cartilage thickness.

Using a computational implementation of the multi-boundary value problem for finite sized electrodes over a physically realistic range of physical model parameters, it was shown that the contribution of electrokinetics to be negligible with respect to the conductivity of the cartilage. Thus, detecting cartilage degradation with impedance relies on detecting changes in tissue conductivity resulting from loss of charged aggrecan groups. A complete loss of sGAG content from the tissue would decrease the electrical conductivity by only $\sim$25% (calculated from Equations 4.1- 4.6), while the electrokinetic coupling coefficient, and thus the current-generated stress amplitude, would decrease to zero. As with purely mechanical measurements of car-

tilage material properties, purely electrical parameters, such as tissue impedance, would be expected to be a less sensitive indicator of degradative changes due to their smaller dynamic range. However, the impedance measurement may be able to be made more precisely than CGS, thus it may have the ability to discriminate tissue property changes. For example, in Figure 4.8D, the impedance of the cartilage that was treated for 4-hours (~90%) was significantly lower than that treated for 24-hours (~99%). This preliminary data must be confirmed with further studies.

The model developed of impedance as a function of the strain and sGAG content (simulated from Equations 4.1- 4.6) for the experimental geometry, predicted values of the impedance that were of the order of the measurements recorded experimentally at 1 Hz (compare Figure 4.4 and Figure 4.8A, 0 versus 100% loss of sGAG content). In general, with sGAG loss, the model qualitatively predicts that the impedance will increase with increasing strain, as seen experimentally [36]. However, with control cartilage (0% loss), the impedance is initially predicted to increase, but will decrease when the strain reaches 25%, qualitatively agreeing with microcontinuum models developed by Eisenberg et al. and Chammas et al. [36, 56]. The experimentally obtained data reported from adult bovine articular cartilage of k_{22} as a function of strain [36,56], agrees with the early decrease in impedance also predicted by the microcontinuum models [36,56]. The behavior at higher strains in this macrocontinuum model may not agree due to the dominance of the Meares and Mackie tortuosity correction with increasing strain.

The impedance measurement has demonstrated the ability to detect degradation confined to the upper surface (0.05 mm) of adult bovine articular cartilage when induced by MMP-13 treatment (Chapter III). This suggests that the impedance measurement is sensitive to the condition of the contact between the probe electrodes and the cartilage surface. The intact surface layers of undegraded (control) cartilage may prevent interdigitation of the probe electrodes with the cartilage surface, thus providing a impedance measurement with a higher variability. This behavior may reduce

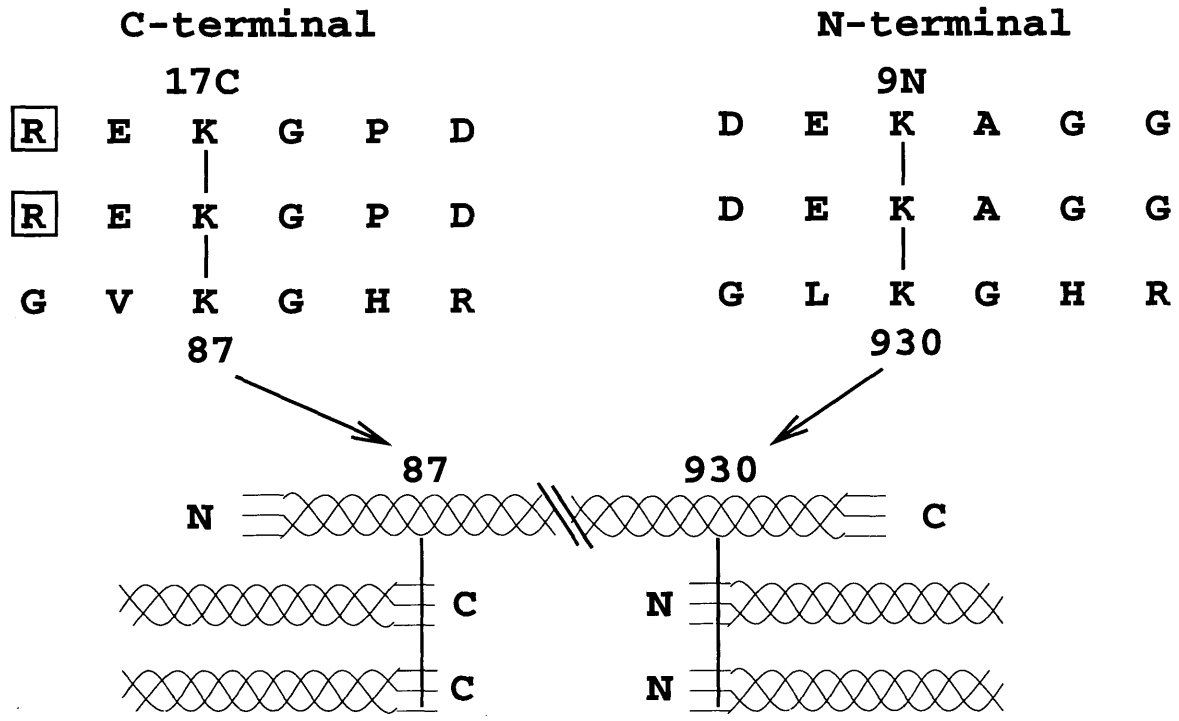

Figure 4.9: The increased hydration while tissue sGAG content is decreasing suggests damage to the collagen although little or no damage can be detected in the trypsin degradation products released to the media. In the C- and N-terminal regions, three lysines (87-17C) form crosslinks between the teliopeptide regions and the helical domain of the type II collagen. Opening of the collagen network structure may occur when trypsin cleaves the arginine site (boxed R) on the C-terminal of teliopeptide region (15C), without releasing crosslinks to the media for detection [Figure adapted from [59]].

the sensitivity of the measurement, in particular as the frequency increases and the difference the magnitude of the impedance between the degraded and control tissue decreases (Figure 4.8D).

The increase in hydration of newborn bovine articular cartilage with trypsin treatment time (Figure 4.7B) could indicate that damage to the collagen network could be occurring. The increased hydration while tissue sGAG content is decreasing (Figure 4.7A) suggests damage to the collagen although little or no damage can be detected in the trypsin degradation products in the media [54, 104, 132]. One possible mechanism involves opening the collagen network structure without changing the

banded pattern of the collagen, with the trypsin cleaving its known arginine site on the C-terminal of teliopeptide region (15C in Figure 4.9). In this region, the three lysines (17C-87) form crosslinks between the teliopeptide regions and the helical domain of the type II collagen. This action would clip the C-terminal crosslinks to the triple helical domain, without releasing the hydroxylysyl pyridinoline crosslink to the media. Another possibility is that the helical crosslink sites are the target (both possess a KGHR secquence), however, this is unlikely, since all the crosslinks would be released, something that has never been reported in the literature. This mechanism also possibly explains the lack of hydroxyproline and hyaluronic acid fragments in the post-enzymatic digestion media following trypsin of articular cartilage. Measurement of the trypsin digestion products in the media of this study revealed that at 24-hours very litle hydroxyproline fragments were detected, and less than 10% of the hydroxylysl pyridinoline crosslinks were released compared to controls (data not shown). This mechanism would suggest that trypsin digestion also is associated with collagen network loosening, altering the physical properties. In addition, suppliers of trypsin preparations document that they may contain other substances with proteolytic activity, but it seems unlikely that these impurities could account for the observed hydration behavior.

In the current construction methodology of the electrokinetic surface probes, the interfacial impedance of the probe Ag/AgCl electrodes with an electrolyte (Z_{ser}) must be carefully controlled. It is quite sensitive to the chloride deposition parameters (current density and time) and frequency of the driving current [80]. Therefore, to ensure the collection of consistent impedance measurements with many probes of similar geometry, a strict chloriding protocol must be adhered to, and the resulting interfacial impedance carefully measured. In contrast to other possible materials for electrode construction, the benefits of Ag/AgCl electrodes far outweighs the slight performance enhancement of that the use platinum black electrodes would provide [209].

The use of the electrokinetic surface probe to perform impedance measurements may be an effective complement to the diagnostic current generated stress measurements *in vivo*. Impedance may be appropriate to detect damage to articular cartilage that is confined to the superficial regions where OA manifests itself in its earliest stages, where CGS may lack sufficient sensitivity.

Chapter V

Development of a Arthroscopic *In Vivo* Electrokinetic Surface Probe

5.1 Introduction: Design Paradigms

After extensive and successful use of the *in vivo* probe developed by Bombard [20] (also known as the HHV4.0 for handheld version 4.0 probe), there were some natural extensions to be made on the design while addressing some of the problems encountered. The HHV4.0 probe had been previously shown to produce reliable results with young and adult bovine tissue and during an open joint procedure in a canine knee [20]. In making the first open joint measurements with a dedicated probe system in a sterile operating room environment, we were exposed to some of the limitations of the HHV4.0 probe. The major enhancements/improvements that needed to be addressed were the following:

1. The 1 cm outer body diameter of the HHV4.0 probe, in addition too being to large to realistically fit into an arthroscopic canula, precluded us from making measurements on joint surfaces that were highly curved. In the adult canine the 6 mm diameter working area needed was too large to get an adequate mapping of the femoropatellar groove or condyles. We were restricted to an area in the region of the trochlear notch of the distal femur, a location that spontaneous OA rarely occurs in the knee joint. A mapping of the joint surface is critical in some applications since in adult (mature) cartilage the mechanical properties and biochemical composition are dependent of the location along a joint surface (see Chapter 2) and are critical to comparison among joints. In future *in vivo* clinical applications, minimizing the surface area required will allow for a more sensitive discrimination between areas considered "damaged"

and adjacent "control" cartilage.

2. The two electrode nature (number of excitation and stress sensor electrodes) of the HHV4.0, does not allow for the spatial localization of lesions, i.e. surface degradation seen in OA-like cartilage damage, that is accessible when interdigitated electrodes are used [15]. The effective wavelength, λ (based on the centroid to centroid distance between its two hemispherical electrodes), of the HHV4.0 is 5.34 mm, meaning the penetration depth of the measurement ($\lambda/3$) is 1.78 mm, which is greater than the thickness of mature canine or bovine cartilage. This indicates that this probe version may be less sensitive in detecting cartilage damage at the earliest possible stage since it is constrained to a bulk property measurement through the thickness. The probe has been shown to be most sensitive when comparing a short wavelength ("surface" measurement) and long wavelength ("bulk" measurement) through the short/long stress ratio (SR) [227]. In addition, the present modeling of the current-generated stress phenomena seems to be unreliable when the thickness of the cartilage (from articular surface to the tidemark in mature cartilage) becomes small relative to the wavelength of the excitation current (E. H. Frank, personal communication).

3. During manufacturing of the HHV4.0, the method of assembly of the electrode transducer structure (ETS) was inconsistent and troublesome. The ETS begins as a flat laminated structure that must be "formed" to fit on a shape that can be represented by the end of a cylinder. At times, the flat end of the ETS would be convex, making the results unreliable and highly dependent on the offset stress applied to the probe body when measuring the stress response. Ideally, the ETS should lay flat against the probe head that contacts the cartilage surface to remove inconsistencies, and their associated measurement errors.

4. In the aforementioned "forming" process, the adhesives holding the laminates together are subject to high shear stresses and stress concentrations. Especially

vulnerable is the conducting silver epoxy layer between the metallized side of the mylar sheet and the Kynar sheet (piezoelectric film). The forming step is thought to reduce the integrity of this bond, thus compromising the shielding between excitation and sensor electrodes, decreasing signal-to-noise ratio of the measurement. In addition, this particular sputtered metallization of the PVDF film is susceptible to microcracking when severely flexed, in some cases rendering the probe unusable.

These problems were addressed in the redesign of the HHV4.0 probe, with the goal to take this version of the probe to the technological limits of the materials and the manufacturing techniques employed. With respect to the itemized problems, the significant enhancements/changes for the HHV5.0 are the following:

- (1) A prior lower limit on the probe body size was associated with the need to run relatively thick connection cables to the Kynar output in the body of the probe. For the new version, a comparable low-noise cable with four carrying wires was investigated (Microtek, USA). The wires were insulated from each other within an insulting sheath of 2 mm diameter, subsequently allowing the diameters of many parts to be reduced. The resulting design called for an outer body diameter of 6 mm, with an active area of 4.5 mm, a 64% and 41% reduction, respectively.

- (2) The four wire bundle now allows monitoring of 4 separate electrodes, making a multiple wavelength approach possible. The smaller active area constrains the electrodes to be smaller and thus, the wavelengths are reduced accordingly. The wavelengths with the HHV5.0 vary from a minimum or "short" wavelength of 2.1 mm (penetration depth of 0.7 mm) to a maximum or "long" of 6.3 mm (penetration depth of 2.1 mm).

- (3) and (4), Reducing the size of the Kynar and method of its assembly to the ETS solved the flatness and the shearing stress issues during the forming

process. The Kynar film is cut to fit the flat active area of the inner core of the probe, therefore the Kynar does not need to be formed around the end of the core reducing shear stresses and stress concentrations. Fortunately, the Kynar film is the stiffest component of the laminate structure; its removal leaves the silver and mylar sheet to be formed which are pliable and easily conform around the chamfered end of the probe body. To address the flatness of the ETS, a cruciform torlon backing plate is attached to the ETS on the Kynar side. It fits into a matching machined recess in the inner core. The backing plate also ensures positioning of the stress sensing electrodes. An additional benefit of making the stress sensor connections on the active area, is the reduction of unstressed Kynar metallization which increased the voltage output from the piezo film per unit stress.

Although the reduction of the area of the Kynar electrodes will concomitantly decrease the voltage output, the design called for signal calibration to be on the order of 2-4 mV/kPa based on previous work in the *in vitro* system. These signal levels have been shown to work well with the prior *in vitro* models. However, the lower signal levels have reduced the inherent signal-to-noise characteristics of signal acquisition, calling for peripheral circuitry to be developed accordingly.

5.2 Design and Construction of the HHV5.0 Probe

The design is a modular structure (Figure 5.1) consisting of a laminated electrode/transducer structure (ETS) mounted in a cylindrical body. The body consists of a four part design incorporating an inner core which makes electrical connections to the electrode/transducer structure, covered with a plastic (torlon) sheath and inserted into a threaded stainless steel outer tube and screw. The sheath and threaded tube, when assembled, allow the silver electrodes on the ETS to be in contact with a cartilage surface while protecting, shielding, and sealing the various connections from

the aqueous working environment necessary to acquire current-generated stress data.

5.2.1 Electrode/Transducer Structure Design

The electrode/transducer structure (ETS) is the working component of the "probe" system, applying current to the cartilage surface and measuring the resultant stress from a piezoelectric film. It is a flexible, 180 μm thick, 3 layer laminated structure. The layers consist of:

- Silver excitation electrodes are etched from a sheet of silver foil and deposited with a layer of silver chloride in an appropriate electrochemical cell. The silver-silver chloride (Ag/AgCl) electrodes are used for applying a sinusoidally varying current to the cartilage surface. These Ag/AgCl electrodes also decrease the low frequency impedance between the electrode and cartilage while stabilizing the electrode potential [80].

- The stress sensor is fabricated from a single sheet of 52 μm thick polyvinylidene fluoride (PVDF) with a thin (100 $\mathring{A}$) sputtered nickel-copper alloy metallization on both sides, known as Kynar (AMP Inc., Norristown, PA). This piezoelectric material transduces the mechanical stress sensed to a measurable voltage signal. The metallization on one surface of the Kynar is etched to form electrodes that register with the silver electrodes on the opposite side of the ETS. The other side of the PVDF is connected to the ground/isolation plane represented by the metallized mylar sheet.

  Kynar was chosen as the stress sensor in this application for several reasons:

  - it has a high sensitivity to mechanical stress especially in this low frequency (0.025 - 1.0 Hz) application, allowing the film to behave as a compact strain gauge with no external power source,
  - the generated dynamic signals are greater than those from typical strain gauges after amplification [183], and

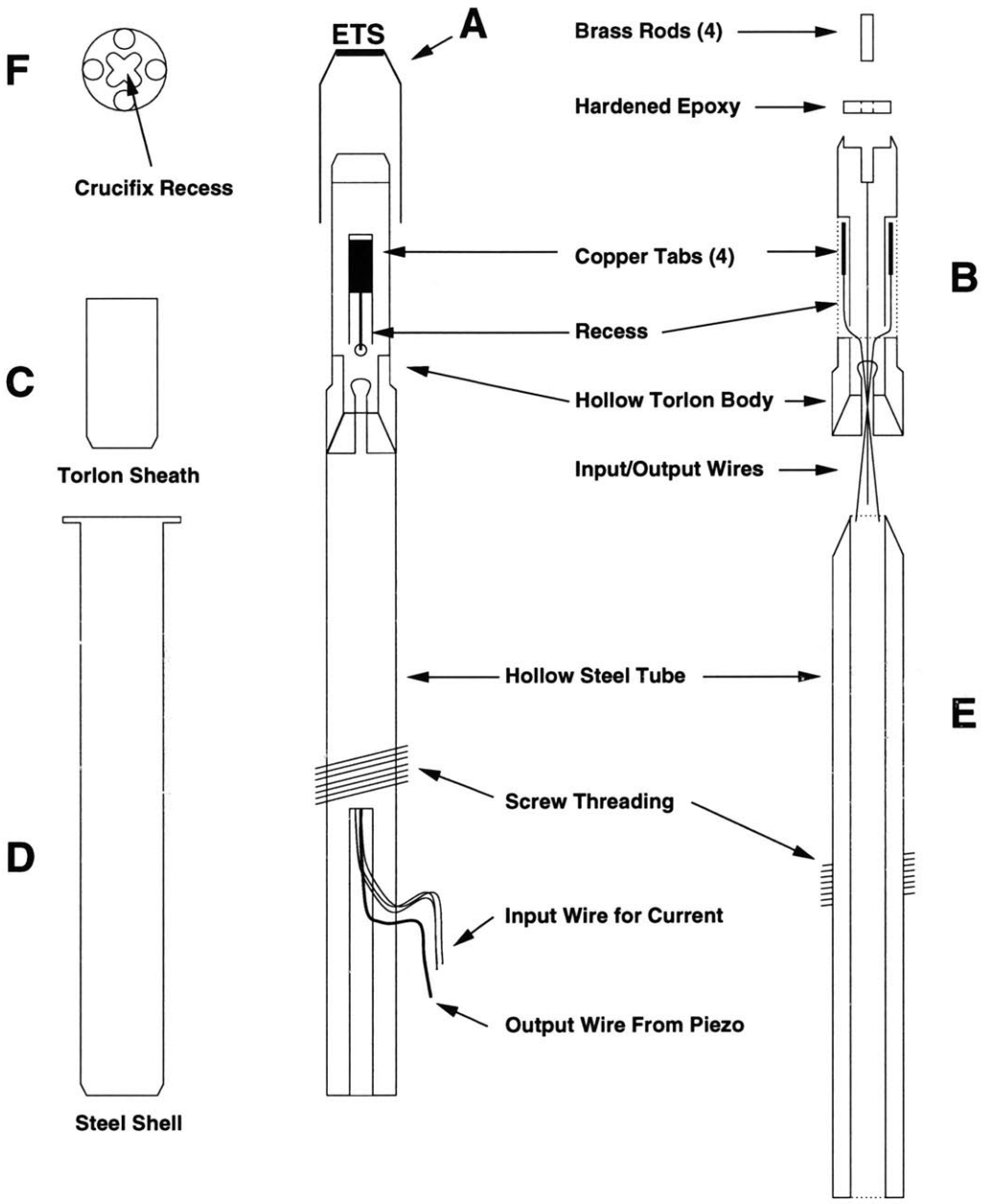

Figure 5.1: An expanded schematic of the handheld version 5.0 electrokinetic surface probe (HHV5.0). The ETS (A) is held in place within a body by an inner core (B) pressing it against a plastic (torlon) sheath (C), then a stainless steel tube (D) with a screwed pusher/plunger (E). A backing plate bonded to the ETS is seated into the inner core (F). A torlon sheath is placed over the core and ETS, while making electrical connections from the silver side to the driving electrode wires. These parts are assembled with a screw from stainless steel tube (D) to a thread on the plunger (E) to create a sealed environment [Courtesy E. Quan [187]].

– the flexible sheets are relatively inexpensive and can be cut into arbitrary patterns.

To characterize the sensor as a stress gauge, a force applied normal (forces in the plane of the electrode are neglected) to the surface of the film develops an electric surface charge on the metallization proportional to the mechanical stress. The charge Q [coulombs] developed by a stress σ [N/m^2] over an area A [m^2] can be described by $Q = d_t \sigma A$, where d_t is an empirically determined piezoelectric strain constant. The open circuit voltage between the metallization on either side of the sheet is this charge divided by the capacitance, $\epsilon A'/\delta$, where ϵ is the dielectric constant of the film and δ is the film thickness. If part of the total metallized area is not being loaded, it adds to the capacitance without generating any charge, thus decreasing the measured voltage. Representing the total area by A' and the active area being loaded by A, the equation for the open circuit voltage signal becomes:

$$V = \frac{Q}{C_{total}} = \frac{d_t \sigma A}{\epsilon A'/\delta} = \frac{d_t \sigma \delta}{\epsilon} \frac{A}{A'} \tag{5.1}$$

For maximum sensitivity, it is desirable to maximize the measured voltage signal, V, for a given stress, σ, thus $A/A' \approx 1$. The voltage output also depends on film thickness. As electrodes are more tightly packed onto the ETS, a thinner film might be needed to gain sufficient spatial resolution with respect to electrode spacing. The AMP company reference [183] contains detailed information on the properties of this piezoelectric film.

- A metallized (with aluminum) mylar layer separates the silver electrodes and stress sensors while also serving as a ground/isolation plane. The metallization is a ground plane that helps shield the sensitive stress sensors from electromagnetic interference (principally electric fields emanating from the excitation electrodes) when the ETS is placed in the probe body.

5.2.2 Probe Body Design

The ETS is held in place within a body by an inner core pressing it against a plastic (torlon) sheath, then a stainless steel tube with a screwed pusher/plunger(Figure 5.1). A backing plate bonded to the ETS is seated into the inner core to provide a smooth, flat mount for the active area of the ETS and to orient the electrical connections to the stress sensor electrodes. A torlon sheath is placed over the core and ETS, while making electrical connections from the silver side to the driving electrode wires. This subassembly is clamped into the stainless steel tube with the screw, providing a sealed environment as the ETS contacts the cartilage surface to make the current-generated stress measurement. Electrical connection to the ETS on the Kynar side are made through pressure to brass contacts on the core. Each of the four brass contacts is connected in turn to one of a bundle of 4 insulated wires that is directly connected to peripheral circuitry. Connections to the silver excitation electrodes are also made through a pressure connection, by pressing the silver on the ETS onto copper contacts to the excitation source when the torlon sleeve is placed over the inner core. The ETS is sealed around its circumference between the torlon sheath by a bead of silicon adhesive to prevent the bathing electrolyte from shorting the electrode connections. Electromagnetic shielding of the piezoelectric sensor is accomplished by completely isolating them from the driving electrodes starting with the metallization on the mylar contacting a stainless steel (SS) rim on the inner core. The SS rim is then continuous with a the braided grounding sheath on the wire (through a silver sheet press fit) to the circuitry.

5.2.3 ETS Fabrication

The ETS may be considered a "disposable" item to be replaced after each diagnostic procedure. The failure mechanism of the ETS may be that the excitation electrodes might delaminate or the shielding can develop gaps as the ETS is repeatedly calibrated and used experimentally. The assembly procedure of the fabricating this laminated

structure is now well characterized in the following phases:

Phase I - ETS Construction

Sheets of the material for the various layers are cut to the appropriate size and then laminated together with appropriate adhesives (Figure 5.2).

- the silver for the excitation electrodes are made from a 25.4 μm thick silver foil (Johnson Matthey, Ward Hill, MA) cut to a size of 18 $\times$ 18 mm with a sharp straight edge.
- the shielding layer is made from 25.4 μm thick Mylar polyester film (MADICO, Woburn MA) metallized (on one surface) with a thin layer of aluminum cut to 15 $\times$ 15 mm.
- the stress sensor is 52 μm thick PVDF piezo film, with a $\approx$ 100$\mathring{A}$ thick nickel-copper alloy metallization on both sides, punched to a disk of 4.5 mm in diameter (the size of the "active" area of the probe).

The sheets are rinsed with a mild detergent and then deionized water, while handling is done with disposable latex gloves to keep all materials clean to prevent contamination with oils and dirt. To aid in the photofabrication, both sides of the silver foil are gently abraded with a fine abrasive and then dipped in a 15% v/v nitric acid solution. To form a laminated structure, the silver foil is bonded to the non-metallized side of the Mylar using a two-part urethane epoxy in a 50:1 ratio (Tycel 7000/7200, Lord Corp., Erie, PA) thinned with methyl ethyl ketone. The silver sheet is larger to allow press fit connections with copper tabs in the periphery of the inner core when the torlon sheath is in place. The piezo film is bonded to the metallized side of the Mylar with a manually applied thin film of silver conducting epoxy (TRA-DUCT 2902, TRA-CON Inc., Medford MA), centered using a custom made jig. The ETS is pressed together for a few minutes to assure good bonding and is allowed to cure overnight.

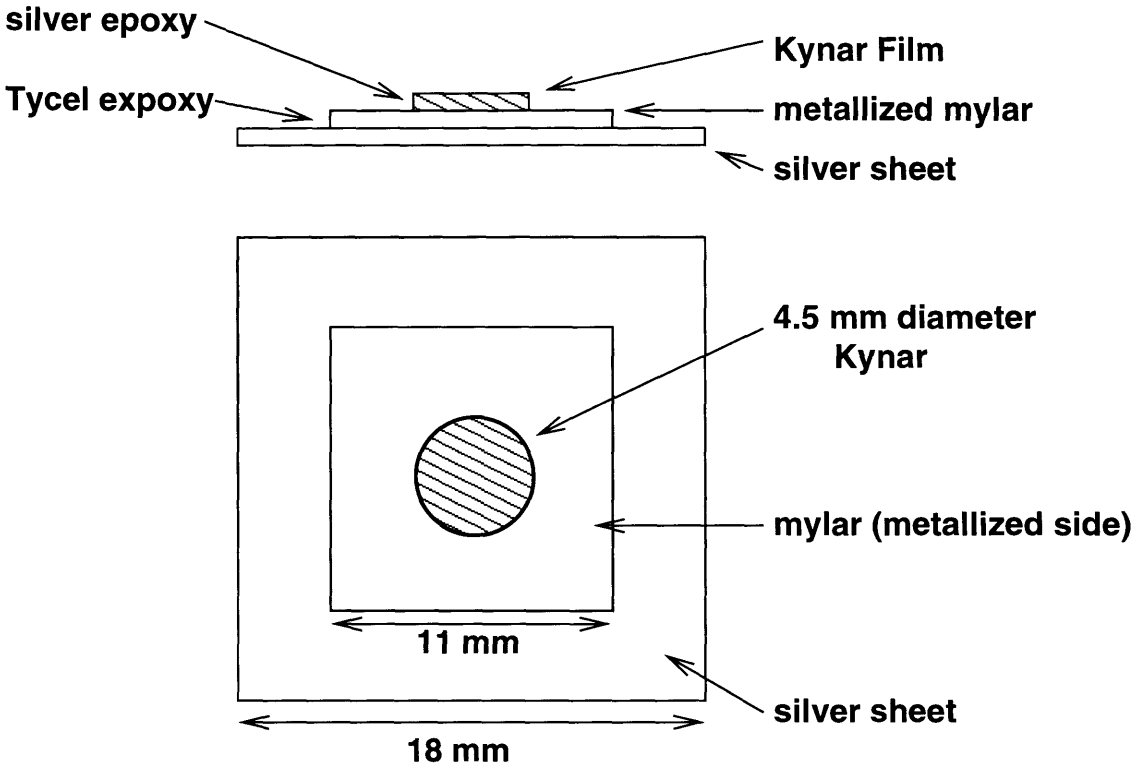

Figure 5.2: Dimensions of each layer of ETS material. Sheets of the material for the various layers are cut to the appropriate size and then laminated together with appropriate adhesives. The 25.4 μm silver sheet for the excitation electrodes is 18×18 mm, the 25.4 μm thick Mylar metallized (on one surface) is 15×15 mm, while the 52 μm thick Kynar film is punched to a disk of 4.5 mm in diameter. The silver sheet is bonded to the non-metallized side of the Mylar using a two-part Tycel epoxy, while the Kynar is bonded to the metallized side of the Mylar with a manually applied thin film of silver conducting epoxy[Courtesy E. Quan [187]].

Phase II - Photofabrication

To form the the silver excitation and the piezoelectric stress sensor electrodes, standard photofabrication techniques are used. The surfaces are coated with a light-sensitive organic polymer, photoresist, that becomes inert to the etching chemicals when cross-linked by ultraviolet light. A negative of the electrode pattern desired is used to selectively cross-link the photoresist, then etching chemicals are used to isolate the electrodes.

The ETS is dehydration-baked at 80°C for 10 minutes in a convection oven

to remove residual moisture, and both sides are coated with a photoresist compound (KPR Photoresist, KTI Chemicals, Sunnyvale, CA), hung to dry for 30 minutes in a darkroom, and then baked between paper and glass plates (to keep them flat) at 80°C for another 10 minutes. Electrode patterns created by the Postscript language (Adobe Systems, CA) were converted to negative images (masks) on two photographic transparencies (Fotobeam, Waltham, MA). A dry, photoresist coated ETS is placed between the two masks, aligned so the electrodes are registered on opposite sides of the ETS, then exposed to ultraviolet light for 15 minutes. The ETS is then bathed in a xylene-based developer solution (KPR Developer, KTI Chemicals, Sunnyvale CA) for 30 seconds, transferred to another bath of developer for 30 seconds, and then rinsed under warm tap water and blotted dry. The developer removes the uncrosslinked photoresist, leaving the resist behind in the desired electrode pattern (Figure 5.3).

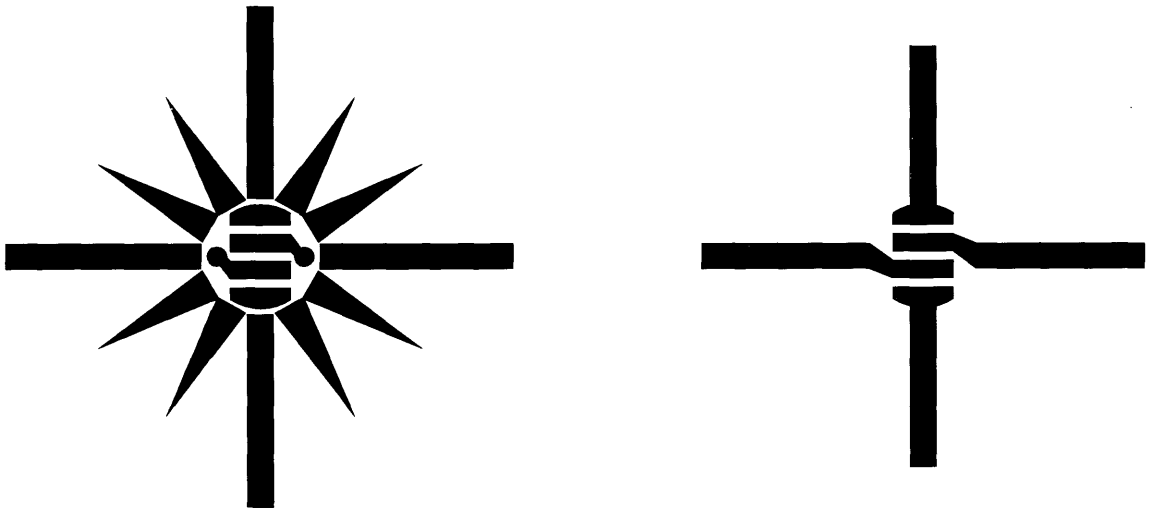

Figure 5.3: Patterns created for the excitation electrodes on the silver sheet (right), and sensor electrodes on the Kynar sheet (left) with the Postscript language. The patterns were converted to negative images (masks) on two photographic transparencies for photofabrication. The rosette pattern around the Kynar electrodes are a template for cutting during the probe assembly stage.

Phase III - Etching

Etching of the silver metallization occurs while the ETS is mounted in a custom made two-part poly(methyl methacrylate) (PMMA) holder with a rubber O-ring gasket to contain the etchant. An appropriate etchant is a 55% w/v solution of ferric nitrate heated to 45^{o}C, with the silver side of the ETS exposed to a fresh etchant bath every two minutes. The thin metallization on the piezo film is etched, by carefully placing a few drops of etchant on the surface, waiting only 5-10 seconds, and quickly rinsing with deionized water. The photoresist is finally removed from both sides with a cotton swab dipped in xylenes.

5.2.4 HHV5.0 Probe Body Construction

The body consists of three separate parts (Figure 5.1): (1) an inner core for making electrical contacts, (2) sealing/non-conducting sheath, (3) an outer threaded stainless steel tube, and a screw. Machining of the designed parts was done by David Breslau (MIT, Center for Space Research), Laboratory of Nuclear Science (MIT), and by the author.

Inner core

The first part of two is a stainless steel head, to accept the Kynar contacts and must be conducting to provide part of the required shielding. The Kynar contacts were formed by 0.03 in diameter brass rods at 90^o intervals, potted into a recess in the stainless head with a non-conducting two-part epoxy. A cruciform pattern was machined in the hardened epoxy to accept a "backing plate" constructed to the ETS. The backing plate allowed for easier orientation of the electrodes and provided a flat surface for the ETS when contacting the cartilage. The contacts were electrically isolated from each other and the ground plane (SS part). Prior to potting, each of the 4 brass rods were carefully soldered to a wire of the Microtek cable, that would eventually lead to the peripheral circuitry. The cable accommodates four coaxial

cables that are especially tailored for low noise applications. The second part is a torlon body, that provides a means of making the electrical connections to the sliver sheet, through 4 slots on the periphery that each hold a copper tab connected to a thin wire to carry the driving current. The pressure connections are made by the sealing/non-conducting sheath when placed on the inner core. The ground plane, is completed by the braided ground shield of the cable by a thin film of silver foil press fit between the torlon and SS head.

Sealing sheath

The insulating (non-conducting) sheath is a thin cylindrical shell made of torlon. The sheath is fitted over the ETS that is placed over the end of the inner core. The end of the sheath is open, exposing the surface of the ETS to the cartilage during the measurement. The sheath is long enough to cover the copper tabs on the side of the torlon body to prevent its contact with the stainless steel outer body, thus isolating the driving current from ground. In addition, the edge of the sheath is angled to press fit the ETS over the rim of the SS head of the inner core. The contacts between the silver electrode arms of the ETS and the copper tabs of the inner core are also stabilized by the sheath. The bead of silicon adhesive to seal the probe against the aqueous environment is placed around the periphery of the angled edge before final assembly.

Stainless steel tube and screw

The outer body stainless steel tube is a cylindrical stainless steel tube that acts as a stiff cover to protect the inner components of the probe. One end of the outer body is open to expose the surface of the ETS but angled to catch the edge on the end of the probe. The other end of the outer body is flared outward. The outer body is slid over the sheath/inner core. A nut is then slipped over the outer body, making contact with the threads on the inner core while pulling down upon the flared end of the

outer body. As the nut is screwed, the outer body is tightened over the sheath/inner core. The parts work in tandem to presses the ETS flat and make a rigid structure to measure current-generated stress.

5.2.5 Probe Assembly

The next step in ETS fabrication involves cutting the ETS into a pattern that enables it to be fit onto the head of the probe. During the photofabrication step, the outlines of the border were also marked onto the ETS. Cutting is performed along the borders with a sharp scalpel. After cutting, a 0.33 mm thick crucifix shaped plastic backing plate is attached to the piezo side of the ETS by a two-part epoxy and dried overnight (Figure 5.4). The backing plate helps with the alignment of the ETS onto the probe and ensures it to be flat. The head of the probe has a machined recess in the shape of the crucifix so that the ETS can fit with the proper orientation to line up the electrical contacts. The brass contacts at the head of the probe receive signals from the piezo electrodes while the copper tabs on the side of the torlon body connect with the arms of the silver electrodes. The current is driven through wires leading up to the copper tabs and onto the silver electrodes while the current generated stress is transferred to the piezo electrodes and transmitted through the brass contacts to the output wires. Once contacts have been made, the torlon sheath is fitted over the head of the probe, making sure the ETS is lying flat on the surface of the head. Before the torlon sheath is completely fitted over the head, the silver leads are slipped under the copper tabs, and the electrical connections are tested to the silver electrodes. Once all contacts are established, a thin layer of waterproof RTV108 silicon rubber adhesive (GE, Waterford NY) is placed on the inside edge of the torlon sheath. Finally the outer stainless steel cylindrical body is slipped over the probe. Adhesive is also placed on the inside edge of the outer body before the probe finally assembled. Excess adhesive is wiped off the edges. The sealed probe is allowed to dry for at least 24 hours. The active surface of the ETS extends slightly beyond the tube end and makes

unobstructed contact with the cartilage surface.

The present design consisting of the backing plate and the smaller Kynar disk means that the ETS does not have to formed into its final three dimensional shape with a die as with the HHV4.0, eliminating the stresses to the adhesives holding the laminate together. The final active area of the ETS is flat, wrinkle-free surface against the top surface of the core, with no small fold or wrinkle introducing large local stress concentrations that are sensed by the piezo film, significantly distorting the measured signal.

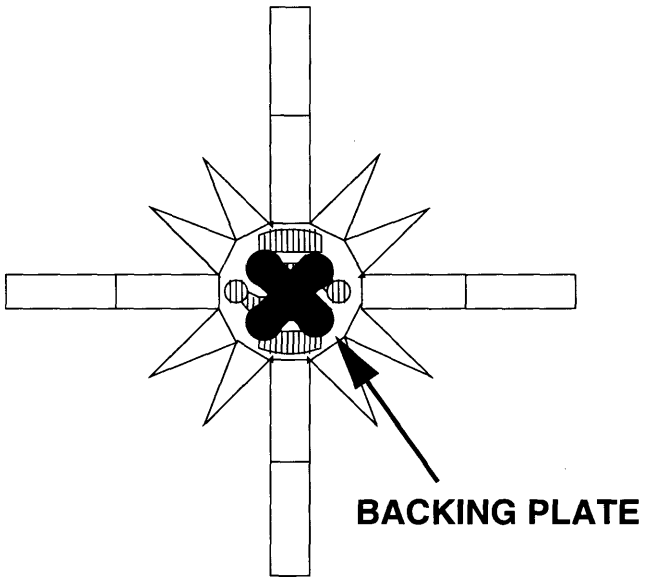

Figure 5.4: During the probe assembly stage, a 0.33 mm thick crucifix shaped plastic backing plate is attached to the piezo side of the ETS. The backing plate aligns the ETS onto the probe within a machined recess on the end of the inner core and, thus ensures it to be flat, while creating the proper orientation to line up the electrical contacts[Courtesy E. Quan [187]].

5.2.6 Electrode Chloridation

As a final step, a layer of silver chloride is layered onto the silver excitation electrodes. The fully assembled probe is suspended in a bath of unbuffered 0.1M NaCl, titrated to pH 4.0 with 1 N HCl, and the positive terminal of a variable DC power supply

(Hewlett Packard) connected to one of the silver electrode wires, in series with an ammeter and a 47 kΩ resistor. The negative terminal is connected to a platinum strip and suspended in the electrolyte. A current of 120 μA is run for 10 minutes, corresponding to a total chloride deposition of 1000 (mA-seconds)/cm^2, for each electrode of 1.59 mm^2 which is acceptable for bioelectric applications [80]. This protocol is then repeated for the other electrodes. A picture of the fully developed probe is shown in Figure 5.5.

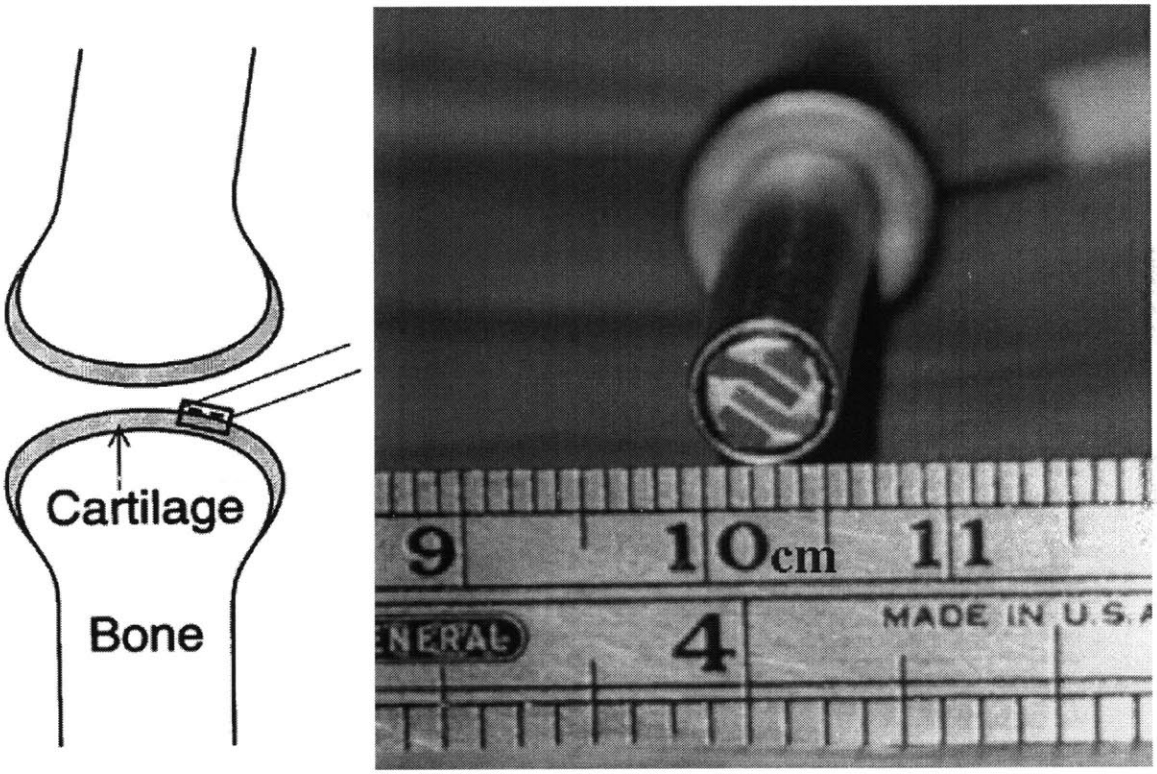

Figure 5.5: Schematic of proposed embodiment within a joint cavity left), and a photograph of an assembled HHV5.0 probe (right).

5.3 Calibration

As mentioned, calibration of the piezo sensor is performed in order to correlate the signal output of the piezo electrode to a known mechanical stress. Subsequently, the output during current-generated stress experiments can be converted to a mechanical

stress. In the assembly phase, calibration also gave reassurance that the connections between the piezo electrodes and the brass contacts in the inner core, while being properly sealed. An insufficiently sealed probe head would enable seepage of the buffer fluid into the probe and risk short-circuiting the system, thus producing no measurable output voltage.

5.3.1 Hardware setup

Outputs from the probe through two coaxial cables were attached to a two channel electrometer that allowed for the control of the signal drift associated with the piezo electrodes*. Output from the electrometer was low-pass filtered (Model 1022F, Rockland Systems, West Nyack NY), and displayed on a chart recorder (Brush 2200, Gould Electronics, Cleveland OH) and processed with an analog to digital converter (ADC) box to a computer for data acquisition/recording. The computer also controlled a mechanical-servo material testing device (DynaStat, IMASS, Hingham MA), through a digital to analog converter (DAC) producing applied loads needed for sensor calibration.

5.3.2 Procedure

With the probe mounted in the DynaStat, a static offset stress of 50 kPa was imposed. After the addition of a buffer (phosphate buffered saline), the system was thermally equilibrated for 15 min. A computer controlled the DynaStat to apply dynamic stress amplitudes of 2.5 and 10 kPa in a frequency range of 1.0 to 0.025 Hz. In this arrangement, two electrodes were calibrated at a time, therefore all four channels were individually calibrated. The Microtek cable from the probe went to a split box which separated each channel to an individual coaxial cable output, and an external gain of 20 dB was applied.

*A detailed description of the experimental hardware and protocol appear in Berkenblit [13]

5.4 Current-Generated Stress

5.4.1 Hardware Setup

Outputs from the probe were attached to an electrometer, passed through the Rockland filter, and differentially amplified (Model 11-4113-01, Gould Electronics, Cleveland OH). The differential signal was displayed on the chart recorder, and recorded on a computer. The computer also controlled the current input to the probe through a DAC box, to a current source (Kepco, Flushing NY).

5.4.2 Procedure

Calf knee joints were delivered within 24 hours of slaughter (Research 87, Boston MA). The distal femur knee joint was dissected and a 9.5 mm core was removed from the femoropatellar groove. A 1.0 mm slice of cartilage was microtomed, placed in a chamber, mounted in the DynaStat, and the probe was lowered onto the tissue. Buffer (PBS) was added to the chamber and an offset stress of 50 kPa was placed on the tissue. The current passes through a switch box that can vary the polarity pattern of the silver electrodes. The polarity of the four silver chloride electrodes could be externally connected into short, or extra-long spatial wavelengths. In the short wavelength configuration (Figure 5.6A), for a current density of J = 0.5 mA/cm^2, the amplitude of the driving current amplitude was 15.9 μA (A = 1.59 mm^2). The electrometer could only measure two electrodes at a time, therefore the test was repeated twice: The first run acquired the differential output between channels 1 and 2, and the second run between channels 3 and 4. For the extra-long wavelength (Figure 5.6B), for a J = 0.5 mA/cm^2, the driving current amplitude was 8 μA (A = 0.80 mm^2).

5.4.3 Correcting for Parasitic Capacitance

Testing of parasitic capacitance was performed to measure any artefactual response that may have been induced by application of the current but not related to the me-

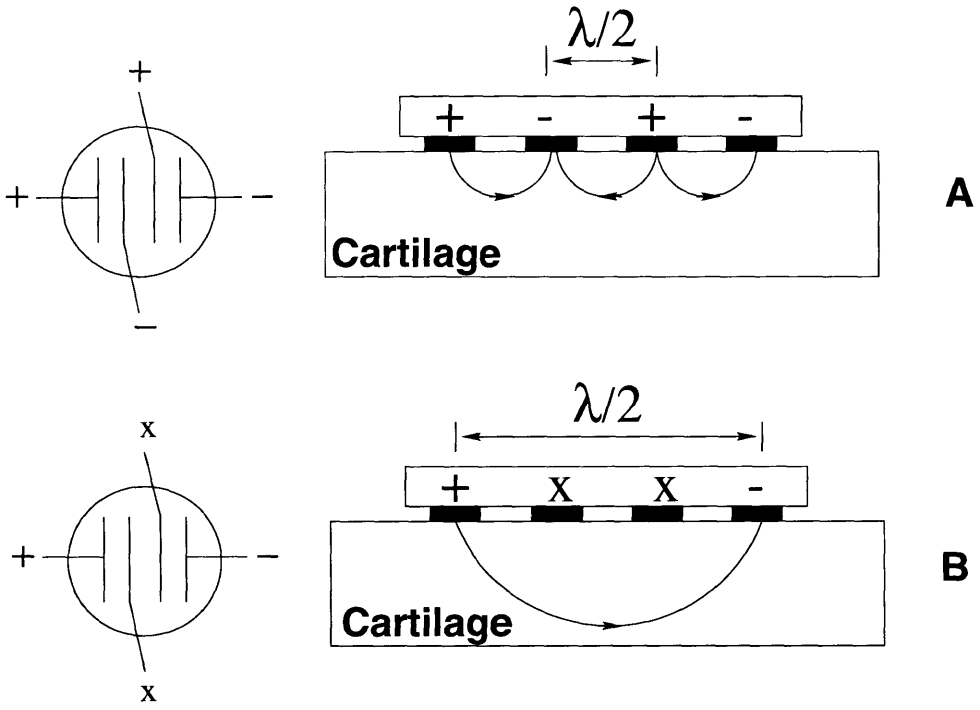

Figure 5.6: Electrode polarity configurations short (A) and extra-long (B) wavelengths. The polarity of the four silver chloride electrodes could be externally connected. When the current is applied in a short wavelength configuration (A) the current is more confined to the upper surface of the tissue. By comparison, with a extra-long wavelength excitation (B), the current can penetrate the full depth, including regions that may not be effected by a tissue degradation. By comparing the current-generated stress in both configurations a short over long stress ratio (SR) can be calculated. The SR will decrease if the surface region is more degraded, allowing spatial localization of degradation [Adapted from Courtesy E. Quan [187]].

chanical stresses within the cartilage. Testing for the parasitic response was done by suspending the probe in buffer, not in contact with the cartilage. However, parasitic signals either created by incomplete shielding or perhaps by some other unknown coupling phenomenon have been previously observed. Measuring the parasitic response was important to correct for CGS for this artifact. Parasitic runs were performed using the short wavelength configuration at J = 0.5 and 1.0 mA/cm^2.

5.5 Results

The calibration of the HHV5.0 probe produced output signals below 1 mV/kPa per piezo channel expected, however it followed the trends that were previously characterized for the piezo response. The piezo channels whose signals had variations amongst each other (Figure 5.7). The voltage output from channel 2 was higher than those from channels 1, 3, and 4.

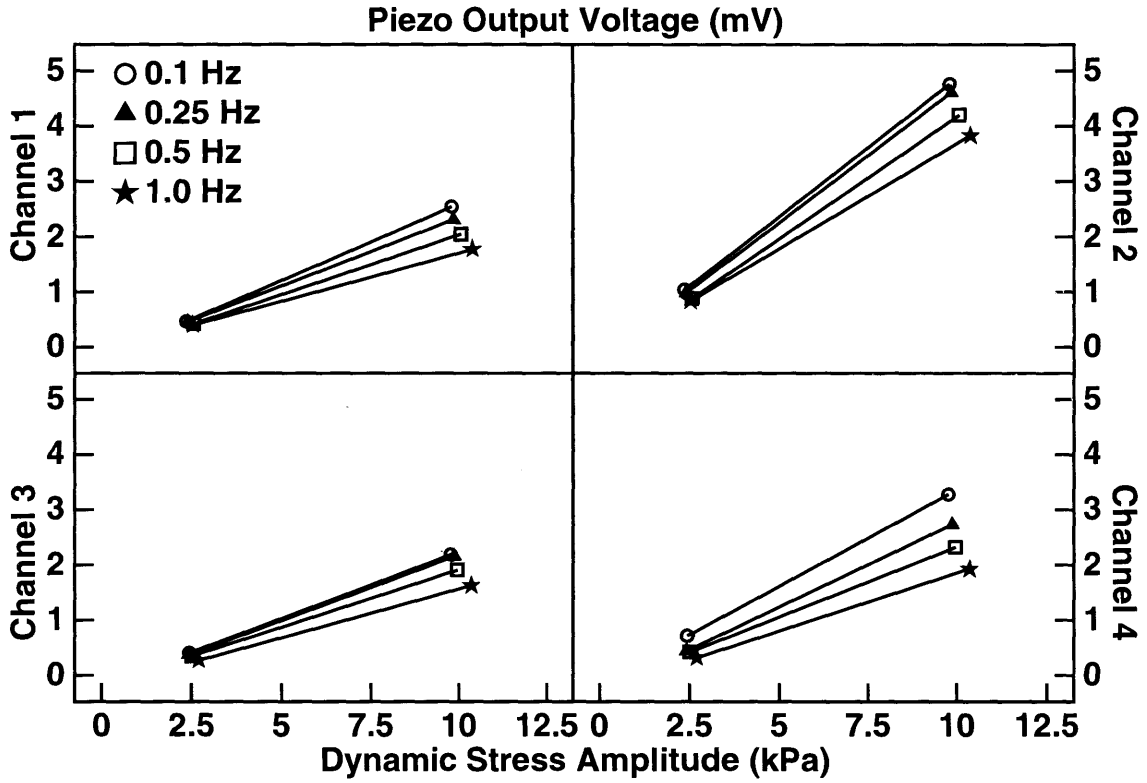

Figure 5.7: Piezo response for each channel at various dynamic amplitudes and frequencies. As with previous probe designs, the calibration signals increased linearly with increasing dynamic amplitude and decreased with increased frequency.

When testing the excised bovine disks for current-generated stress in a short wavelength configuration ((Figure 5.6A), the differential response from piezo channels 1-2 and 3-4 were recorded (Figure 5.8A,B). The differential output increased with increasing current density (J) and decreased with increasing frequencies as previously characterized by earlier probe version and theoretical predictions. The results from

the combinations of channels showed that the differential response from channels 1-2 were different then the output from channels 3-4.

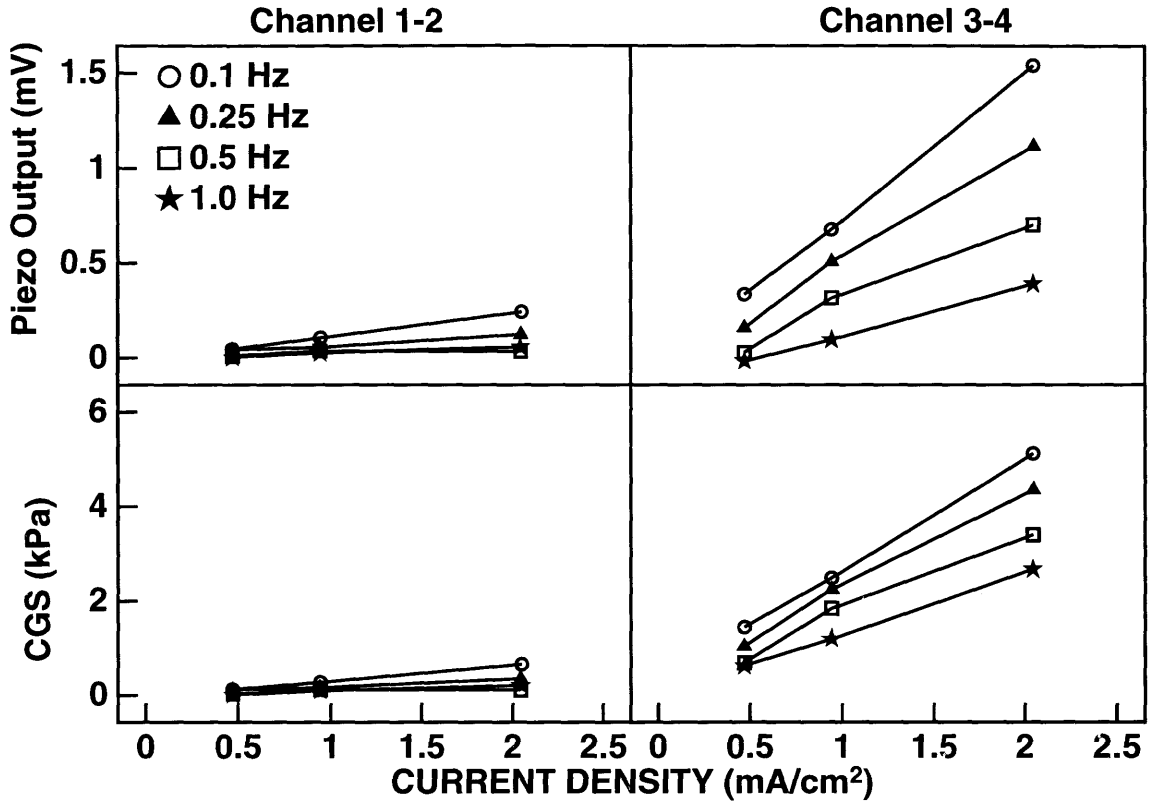

Figure 5.8: Differential amplitude from channels 1-2 and channels 3-4 at various applied current densities and frequencies (A,B). Driving current is in a short wavelength configuration. The differential output increased with increasing current density and decreased with increasing frequencies as previously characterized. The calculated CGS, using calibration results, showed similar trends to the differential piezo output (C,D). These results suggest the importance of observing the individual responses of each electrode separately, rather than pooling electrode responses.

The calculated CGS, using calibration results, showed similar trends to the differential piezo output (Figure 5.8C,D). These results show the importance of observing the individual responses of each electrode as opposed to averaging the signals, which was the method used in past experiments involving multiple interdigitated electrodes [14]. In addition, the results presented were extreme in the channel differences, and not the norm for all the other experiments made by the HHV5.0 probe.

Measurements were also performed while driving a current with an extra long wavelength configuration(Figure 5.9). The differential output from channels 1-4 and the calculated CGS along with the phase were consistent with previous results with the v4.0 probe (Figure 5.9). The extra-long wavelength results, as expected, are larger in magnitude than the short wavelength. Calculating the normalized stress amplitude (CGS divided by the current density, J) and then plotting the results versus frequency, the expected trend of a decreased amplitude with increasing frequency emerges. The magnitude of the the CGS was of the order of the previous results with the *in vitro* probe.

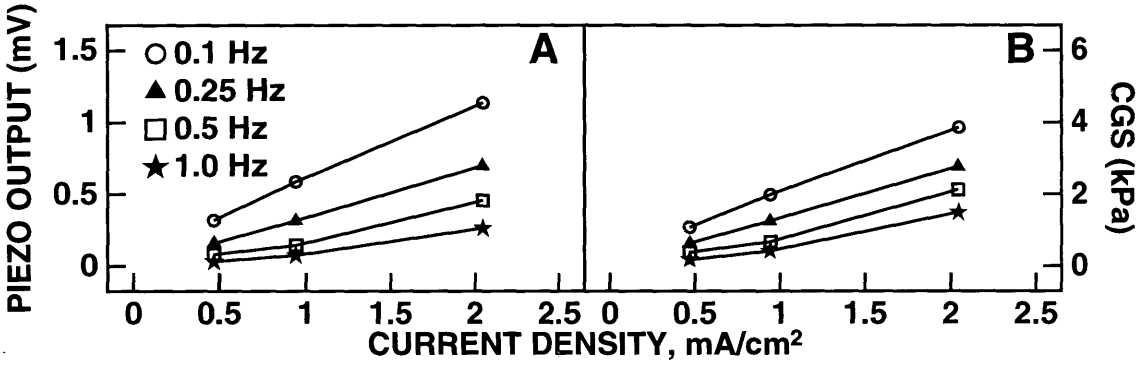

Figure 5.9: Differential amplitude and CGS response from an extra-long wavelength configuration (electrodes 1-4) at various applied current densities and frequencies The results were consistent with previous results with the HHV4.0 probe. The extra-long wavelength CGS results, as expected, are larger in magnitude than the short wavelength and decreased with increasing frequency.

The amount of parasitic signal was measured to be less than 10% of the output from each experimental run, where in contrast, the HHV4.0 probe had parasitic signals upwards of 50% (data not shown).

5.6 Discussion

In pushing the the present technology to its maximal capabilities to miniaturize the probe for arthroscopic use, a significant portion of the shortcomings with previous versions have been eliminated. To optimize probe performance and reliability, several

issues still need to be addressed in the current electrokinetic probe system (HHV5.0). HHV5.0 is generated less voltage per unit applied dynamic stress than was predicted from HHV4.0 measurements and the performance of the piezoelectric film (Equation 5.1). The linear relationship between active electrode area and voltage output may not hold when such small areas are reached. Additional hardware to amplify and filter the signal will be required for appropriate signal analysis. The calibration difference between electrode pads (channels) suggests the use of an separate calibration for each Kynar electrode when calculating the CGS to increase the sensitivity, especially at low signal levels. The level of artefactual parasitic capacitance contributing to the CGS measurement have been drastically reduced with the HHV5.0 probe. Mainly due to better shielding through design adjustments. The parasitic capacitance, along with sealing of the probe in this aqueous environment, are two issues that contribute to failure of the ETS, and thus must be closely monitored for reliability.

Chapter VI

Summary

Establishing the link between macroscopic electromechanical properties, biochemical composition and ultrastructural organization in cartilage will elucidate the role of mechanical forces in regulating the biosynthetic activity of chondrocytes to maintain a functional extracellular matrix (ECM). To this end, non-destructive cartilage diagnostic procedures are needed by clinicians for applications including: detecting the early stages of cartilage degeneration in diseases like osteoarthritis (OA) and evaluating the functional properties of cartilage repair tissue.

In this thesis, a protocol was developed to assess the biomechanical properties and biochemical composition of human knee and ankle cartilage. It was found that the ECM of the talar (ankle) cartilage is denser with higher charged glycosaminoglycan content and lower water content, consistent with a higher equilibrium modulus and dynamic stiffness, and lower hydraulic permeability. This denser ECM may be chondroprotective. Its biomechanical properties may endow it with an increased stability to loading, protecting the chondrocyte and making the cartilage less susceptible to OA. These findings demonstrate the utility of diagnostic tools which assess the physical properties of cartilage.

The hypothesis that surface electromechanical spectroscopy measurements could sensitively detect degradative changes in cartilage matrix caused by collagenases MMP-1 and MMP-13 was tested. We found that MMP-1 induced damage to the collagen-aggrecan network was detected by changes in the current-generated stress response. In addition, the measurement of total tissue impedance using interdigitated electrodes placed on the cartilage surface was capable of detecting superficial (MMP-13) and deeper (MMP-1) lesions caused by collagenase *in vitro*. The ability of surface electromechanical spectroscopy to detect changes in both electrokinetic and impedance properties enhances its potential diagnostic capabilities *in vivo*.

For diagnostic applications *in vivo*, an electrokinetic surface probe was designed with a 4.5 mm diameter active area that is capable of measuring current-generated stress and impedance non-destructively during arthroscopic or open joint procedures. Its size now makes it possible to use it within an arthroscopic canula. Its multiple wavelength capability permits the spatial localization of surface cartilage lesions typical of early progressive OA. This a step toward providing physicians with a diagnostic tool for determining cartilage degeneration in the clinic.

Appendix A

Past, Present and Future of Cartilage Repair & Electromechanical Property Assessment in Cartilage Repair Model Systems

A.1 Introduction

The repair of cartilage focal defects is one topic that has seen a huge amount of increased attention in recent years since the publication of a paper by Brittberg et al. [24] in the New England Journal of Medicine in 1994. The enormous amount of research into cartilage repair is demonstrated by the extensive body of literature over the past two centuries. This interest is well warranted since repairing such defects may reduce the future need for surgical procedures like total knee arthroplasty (total knee replacements) and arthroscopies. For the patient, this means significantly augmenting their quality of life by increasing mobility and reducing day to day pain. Ultimately, in today's world of cost conscience managed care through health maintenance organizations (HMO), healing cartilage damage could lower the $55 billion that the United States spends per year on arthritis.

Brittberg et al.'s work centered on the transplantation of cartilage cells (chondrocytes) to a site of focal damage after these cells were expanded in culture. Their report of positive results has re-energized the public interest into the repair of focal lesions in cartilage and possibly preventing osteoarthritis, topics that have been studied for centuries.

A.2 Scope

The scope of this appendix will cover the past, present and future of techniques used to repair focal defects in cartilage. It will attempt to project what the standard of care will be into the next century, and what challengers face researchers to provide an optimal cartilage repair tissue. In addition, recent examples through collaboratory work of electromechanical property assessment in cartilage repair model systems will be provided. This represents an attempt towards making functional electromechanical measurements of cartilage repair tissue to assess its potential success *in vivo*.

A.3 Past

As far back as 1743, Hunter [108] boldly stated "from Hippocrates to the present age it is universally allowed that ulcerated cartilage ... once destroyed, it is not repaired". This is especially a troublesome thought for a young person with a painful focal cartilage lesion resulting from a traumatic injury. This patient may have to endure the pain of this focal lesion progressing to osteoarthritis for the better part of their lives. Luckily, Hunter's observation was not accepted as dogma. The debate as to whether cartilage can be repaired still rages to this day, with increasingly better prospects for a solution as technology continues to evolve*.

Trimbell Fisher [65] lecturing to the Physiological Society of the Middlesex Hospital in England in 1923, urged those in attendance not to be awed by the work of the "bone-setter" in the healing of joint pain. A bone-setter at this point in medical history was one who would immobilize a painful joint to provide the patient pain relief at the expense of mobility. He urged that research was needed into the pathological principles of joint degeneration to increase the quality of life for the public suffering

*The repair of damaged articular cartilage is a unique problem within the human body with regard to its response to injury in its soft tissues. This behavior stems from articular cartilage lacking a blood supply, thus being unable to undergo the classical cascade of events that lead to repair, as will be discussed.

from joint pain. His experiments confirmed an observation made in earlier published works, that incisions into articular cartilage heal sluggishly without a cartilaginous repair tissue. These observations were made through the use of histological and microscopic methods. In fact, even presently, histology persists as the only method used by some investigators today in an effort to compare repair tissue to native articular cartilage.

In a separate experiment, Fisher removed the cartilage down to the subchondral bone, creating a granulation tissue response that covered the denuded zone (bone no longer covered by cartilage) due to the blood supply now provided to the defect. He also observed that during osteoarthritis (cartilage erosion due to wear and tear), the cartilage attempts to cover defects by extending its surface from unaffected areas to cover those that have been compromised. At the time he noted these capabilities as "one of the most striking adaptations of the human body". This contradicted Hunter's earlier observation and showed the potential of articular cartilage to attempt to repair damaged or degraded areas.

Bennett [11] summarized the conflicting reports in the literature of whether cartilage could be repaired in 1932. The goal of his subsequent research was to help resolve the issue with some novel experiments. In adult dogs he did three separate and illustrative studies: 1) he removed a thin strip of articular cartilage from the weight bearing surface of the medial condyle and the middle of patellar groove, 2) removed cartilage from patellar region, cut it in half, with one half then replaced as a "joint mouse" [†], and 3) cartilage and bone was taken from the concavity of the patellar groove, with half again used as joint mouse. These lesions were examined at 4, 12, 20 and 28 weeks with histological methods. Of 9 defects, 7 had repair tissue, with the 2 unrepaired from the patellar groove region. The defects in the subchondral bone were covered by pannus (inflammatory tissue), and replaced in stages by a fibrous

[†]In general, a "joint mouse" is any loose body in the knee joint. In this case, the loose body is replaced into a void to act a filling material. This is analogous to replacing a divot on the golf course.

tissue, then an imperfect hyaline cartilage at 28 weeks. The "joint mouse" did not have intra-articular changes and the bone underlying the defect was resorbed.

In a further study published 3 years later [12], Bennett reflected back on his first study, concluding that the repair was better at the perichondrial margins and on weight bearing surfaces, but in general, he felt it was incomplete. He hypothesized the mechanism of repair to be by one of the following three methods:

1. independent proliferation of the original cartilage cells,

2. proliferation of the vascular tissue from the perichondrial margins, or

3. ingrowth of vasculature from the subchondral bone.

A second study was done with newborn dogs to see if the quality of repair was superior to that of the adult believing younger chondrocytes have a better regenerative capacity. He hypothesized that younger chondrocytes have a greater capacity to regenerate damaged or removed cartilage. Incidentally, he choose to use tissue from the center of the femoropatellar groove, which is subject to lower loads in normal activity than cartilage from the femoral condyle[‡]. Bennett found that the repair was not better than he observed in the adult dogs, but did note that the proliferative activity of the cells was increased in the deep cartilage layers, where the concentration of cells is higher in comparison to the superficial zone.

Thus, early work established that articular cartilage had some repair capacity, but continued research was needed for further improvements and understanding.

[‡]Recent studies have indicated that this may be true for bipeds, but in quadripeds the femoropatellar regions can be highly loaded (A.J. Grodzinsky, personal communication).

A.4 Present

A.4.1 Cartilage Basics

Since cartilage repair deals directly with its constituent materials, some characteristics of cartilage should be addressed due to their impact on the repair mechanisms[§].

Scanning electron microscopy has shown that cartilage is not smooth, but undulates in relation the cellular distribution close to the articular surface. This and many other studies combine to highlight the importance of the highly organized extracellular matrix around the chondrocytes to allow the cartilage to be fully mechanically functional. The proteoglycan content gives it the ability to withstand compressive load, and its high collagen content allows it to resist shear loads.

Cartilage is aneural, thus relying on capsular, synovial, subchondral bone, and muscular nerve endings to feel pain and for proprioception. Thus, cartilage can not directly report abnormal stress states resulting from blunt trauma, or mechanical overloading. Its avascularity renders it unable to proceed with a classic inflammatory response that is mediated through the vascular system for most other tissues.

Central to the issue of healing is the ability of the cartilage cells (chondrocytes) to replicate. Looking at immature tissue with light microscopy, cells can be found in various stages of mitosis in two distinct zones: those that are close to the articular surface that provide cartilage mass and a deeper zone, where the cells resemble those of the epiphyseal growth plate. As the animal matures, the mitotic index decreases, and only a zone of cells just above where the vasculature invades the very deep layers of cartilage remains active.

It seems as maturity is reached, chondrocytes seems to cease to divide. One relevant questions is raised; Do chondrocytes "turn off" or "break" the switch for DNA replication and thus cell division? It has been conclusively shown that the former is true, that mature chondrocytes can display further replication under the

[§]Some of the material in this section was inspired by a review article by Trippel et al. [228].

appropriate conditions.

A.4.2 Response to Injury

In vascular mammalian tissues, the normal cascade in response to injury for most organs and structures consists three phases: necrosis, inflammation and repair. Articular cartilage undergoes necrosis, as cells die locally and the extracellular matrix is disrupted. No local inflammation occurs due to the absence of the vascular system to mediate the process. Superficial lesions are left to repaired by the cartilage itself due to the absence of the fibrin clot that would be present in other mammalian tissues. When deep defects are accompanied by damage to the bone, the normal healing mechanism is triggered, resulting in fibrocartilage.

Blunt Impact

Whether there is a single or repetitive impact loads applied to the cartilage surface, it has been shown that damage occurs (chondrocyte death and matrix fissuring) when a threshold of 20% strain is exceeded. This lesion can progress to osteoarthritis, but it has been showed by Radin et al. [189] that sometimes the damage can be reversed especially if the damage is mild.

Superficial Injury

Following a superficial lacerative injury (does not penetrate below the tidemark to evoke a vascular response), most investigators have been unable to show that cartilage is making sufficient tissue to connect the edges of the damaged cartilage. The injury evokes a short-lived metabolic and enzymatic response that is unable to repair the most trivial lesion, like that made by a scalpel blade. This brief response consists of: increased mitotic activity in tissue adjacent to the defect, an increase incorporation of [^{35}S]sulfate (an indicator of glycosaminoglycan synthesis), [^{3}H]glycine (indicates protein synthesis), and cell replication measured by [^{3}H]thymidine incorporation oc-

curs [50, 141]. Within a week all indicators revert to "sham" or control numbers. Fuller et al. [77] made tangential partial-thickness cuts in young rabbit articular cartilage with no repair reaction. Ultrastructural studies showed cell death at the cut edges, with surviving chondrocytes displaying a higher metabolism to maintain matrix integrity.

Several studies following such injuries for 6 months show the healing process has ceased, but such injuries don't proceed to osteoarthritis even after 1 year later which is a positive for young patients with such injuries ¶.

Full Thickness-Penetrating Injury

When the injury penetrates the subchondral bone, the repair can proceed from the multiple cell types and blood constituents from the plasma. The defect fills with blood, then organizes into a fibrin clot trapping red blood cells, white cells and platelets with progenitor cells multiplying and laying down a vascular fibroblastic tissue that undergoes progressive hyalinization to a fibrocartilaginous mass. Bone eventually refills its original region.

As with the lacerative injury, at the margin of defects there is a burst of synthetic activity but only enough to replace some of cells and matrix damaged by the original wound.

The fate of the fibrocartilaginous mass becomes the focus for the repair research community. In a rabbit model the mass has been shown to display mitotic activity with the formation of aggrecan and type II collagen. After 12 months, the appearance becomes less hyaline and the mechanical quality of the tissue is suspect [40, 166].

¶The fact that such scalpel cut injuries don't progress to osteoarthritis is great news to the young patient undergoing arthroscopy for a torn meniscus. To repair the damaged meniscus, it must be excised with a long scalpel-like instrument. Since the scalpel can be hard to control for the orthopedic surgeon in tight joints, slips accompanied by slicing into the adjacent cartilage can occur (S. Treppo, personal observation). This is regarded as a frequent complication of arthroscopy. As mentioned, this type of superficial lacerative injury does not heal, but it does not progress to osteoarthritis either. Therefore, surgeons are not overly concerned when an accidental slice occurs.

Adult dogs were used to test the biomechanical properties of full thickness osteochondral defects by Nelson [176]. This model is very similar to the aforementioned rabbit model, and the repair tissue showed poor biomechanical quality that contributed very little function in joint loading. Interestingly, the observation was made that the cartilage adjacent to the defect did not degenerate due to the higher loads it now experiences, even after 11 months.

Large defects were created in the distal femur of horses and followed for almost a year in a study by Convery [45]. The repair was more or less as described, but had a dependency of the original lesion size. Defects less than 3 mm in diameter completely healed, and signs of repair were hard to find after 9 months. Defects greater than 9 mm had complete repair but with a variety of types of tissue. Fibrous tissue, fibrocartilage and hypercelluar hyaline-like cartilage were all present in the defect.

This combines into two significant problems that are relevant to clinical joint disease:

- the failure of cartilage injuries to heal; nonprogressive slices are of little concern, but the focal lesion with progressive destruction leading to osteoarthritis is a clinical concern. For better healing, the replicative and synthetic abilities of chondrocytes must be addressed, and

- deep injury to cartilage; there is a rapid repair response, but it is the nature of the fibrocartilage that fills the defect that is of concern. The tissue never becomes true articular cartilage and proper repair must insure that the proper cell types are present to induce the proper matrix.

A.4.3 Present Clinical Approaches to Healing of Articular Cartilage

Debridement

Prior to total knee arthroplasty becoming a reliable procedure, removal of irritating/painful material like abnormal synovium, osteophytes, and softened fibrillated

cartilage was an acceptable procedure. The use of debridement again increased with the perfection of the arthroscope as a frequently used clinical tool to access the surface of articular cartilage. Some clinicians believe the "shaving" of the offending material promotes healing, whereas more skeptical surgeons believe other aspects of the procedure provide relief from pain for the patient. Debridement is different from abrasion arthroplasty, where drilling into the bone is performed. As discussed, with shaving repair is not expected, while drilling will create a repair tissue, although a suboptimal tissue.

Stimulating Repair: Continuous Passive Motion and Electrical Fields

Salter et al. [203] drilled subchondral bone defects in distal femur of rabbits and found that continuous passive motion enhances the healing of the cartilage compared to immobilized controls based on histological staining.

An attempt was also made to heal deep defects in cartilage using an electrode placed under the bone and creating a local electrical field [8]. Histology showed hyaline cartilage filling the defect although the mechanisms are still unclear. More recent techniques are reviewed by Aaron et al. [1].

Grafting of Defects

The inability of the endogenous chondrocytes to repair defects has created interest in rib perichondrium as an exogenous sources of cells for repair. Such grafts have been successful in rabbit defect models, but have had mixed results treating hand arthritis in humans [210]. Periosteum, was also used by Rubak [196] to fill defects successfully for up to 1 year, and has shown that the repair cells migrate into the defect from the periosteum, not the cartilage. These grafts when combined with continuous passive motion has significantly less degenerative changes at 1 year than controls [180] and were biomechanically stronger [248] (although these mechanical differences disappeared with time).

Cell grafts

A landmark study in the repair of focal defects in cartilage, was that of Brittberg et al. [24] in 1994. A method to repair focal lesions could lower the 150,000 procedures now done to alleviate patients pain. The procedure in humans is an extension of their earlier work in rabbits, that showed its efficacy over the past 10 years [84]. The technique involves transplanting autologous cells harvested from the anterior aspect of the distal femur during arthroscopy (300-500 mg of tissue)[‖]. The cells were cultured for 14 - 21 days and re-implanted into the 23 patients' (ages 14-28) for full thickness cartilage defects (size from 1.6 to 6.5 cm^2) confined to the articular cartilage. The cultured chondrocytes were injected into defects on the femoral condyle (16 patients) and the patella (7 patients), after the defects were covered with a harvested periosteal flap sutured around the affected area. Patients were followed for 16-66 months. The initial pain and swelling was reduced for all patients assessed by physical exam. At three months arthroscopy was done, showing the sites filled with a "spongy" tissue (assessed subjectively by a blunt arthroscopic probe) with delineated borders. A second arthroscopy was performed 12-46 months later, and revealed a "firmer" tissue. At this time the focal repair sites were biopsied to perform histology and staining for type II collagen.

At two years, 14 of 16 patients had good to excellent results for the femoral condyle repairs. The 2 poor cases showed central wear of the joints. The patellar transplants were not as successful, with good results found only in 2 of 7 defects. Histology showed a hyaline-like material filling the original defects, that positively stained for type II collagen (a hallmark for articular cartilage) with the periosteal tissue still present, and incorporated into the repair tissue at the articular surface. The authors admit that this is a procedure that may be most effective to repair a

[‖]The anterior part of the distal femur were the chondrocytes are harvested, is known to be exposed to a relatively low level of mechanical loading due to the anatomy of the knee joint. Loading occurs in this location when the knee is in full flexion, like in a deep knee bend. Some orthopedists are hesitant to harvest such cartilage because of the concern of the defect progressing to osteoarthritis in future years.

focal defect, like those found accompanying traumatic injury in younger people rather than the larger defects that are associated with wear and tear in older adults.

Although the results brought a lot of positive publicity to cartilage repair efforts and returned an old concept back into the mainstream, skepticism in the orthopedic community remains. Dr. Henry Mankin, in a comment to New England Journal [146], cautions that the progression to osteoarthritis is so slow that we must not delude ourselves into thinking this is the solution to the cartilage repair question, but to keep trying to perfect the associated techniques.

The authors also conjectured 3 explanations for the repair tissue they observed:

1. cells repopulate the defect as the periosteal flap holds them in,
2. periosteum stimulates the transplanted chondrocytes, or
3. the transplanted chondrocytes and periosteum attract cells from the border to grow in and repair the defect.

These conclusions, if compared to those supplied by Bennett [12] some 65 years earlier, represent little advancement in the knowledge regarding the mechanisms driving cartilage repair. Therefore, more research needs to be done, and with the present interest high, there are great prospects for the future.

In recent published results, repair tissue from different types of failed cell based procedures to repair focal defects were analyzed [175]. Repair tissue from filled defects was analyzed from 22 revision surgeries of 20 patients with a mean age of 40 years. The repair tissue was sampled from center of the failed graft for histology and to assess "cartilage development" using collagen type II stains. The repair when sutured perichondrium was used to hold the cells in place was the best with respect to proteoglycan content and collagen type II staining, but the subchondral bone grew toward the articular surface, making the "cartilage" thin. When cells were put under the periosteal flap (the procedure originally used by Brittberg et al.), little type II was found within a thick layer of fibrous tissue. Tissue from areas that were subjected

to abrasion arthroplasty, had degenerating cartilaginous tissue that was not suitable for biomechanical loading.

Although this study looked at failed grafts, this does not confirm that the patients with successful grafts (painless knees that do not need revision) do not have a similar suboptimal repair tissue. Unfortunately, it is presently difficult to obtain repair tissue samples from patients with successful grafts to assess its quality.

Questions Raised by the Brittberg Procedure

- What are the phenotype of implanted cells? The authors believe that the cells maintain a chondrocytic phenotype, but the resulting repair tissue does not always correlate. When the cells are expanded in culture, they revert back to the a more primitive fibroblastic phenotype for replication. Perhaps not all cells re-differentiate into chondrocytes when re-implanted.

- What is the effect of mechanical stimulation? The patients that were allowed to ambulate within days of the procedure had a lower success rate, especially with patellar defects. This may be due to higher forces experienced. Earlier studies in animals had shown no difference in the repair tissue between loaded and unloaded areas.

- What will be the results at long time points? The animal studies generally show some degradation at 6 months, thus it will be interesting to see the fate of the transplant repair tissue at 5-10 years.

- What is the source of repair cells? Is it the implanted chondrocytes or those made available to the defect from the periosteal flap that holds in the cultured chondrocytes? Defects have successfully been treated pre-clinically with periosteum and/or cells [229]. To prove the source of the repair cells, the Brittberg study needed a periosteal only control in humans, although they have previously

reported in their rabbit model that implanted cells with the periosteal flap had better repair than the periosteal only control [84].

A.5 Future

A.5.1 Cell Based Cartilage Resurfacing

Researchers** have come to the consensus that the common methodology needed for any successful system of cell based cartilage resurfacing includes:

- a source of cells,
- a means of fixing the cells in place, and
- an adequate biomechanical and biochemical signals to ensure cell survival and matrix synthesis.

These techniques optimized with an arthroscopic method of implantation would be the embodiment that has been visualized as the most appropriate for future patient care in an orthopedic clinical setting.

Source of Cells

Chondrocytes There are two distinct candidate sources to use for implantation: autogenous or allogenous cells. The use autogenous cells (the patients own cells) will avoid the problem of an adverse immunological reaction to foreign cell-surface antigens for the recipient. However, recent studies [101] have shown that allograft cells used in a three-dimensional matrix to resurface cartilage do not have a detectable immune response. This behavior may be a consequence of a newly formed pericellular

**Parts of this section were motivated by a workshop at the 43rd Orthopedic Research Society meeting in San Francisco, California in February 1997 entitled "Cell-based Articular Cartilage Repair: Research Considerations" led by Dr. Ernst Hunziker.

matrix surrounding the cells, thus blocking the immune response of the host to the delivery vehicle (i.e. fibrin, polymer, etc.) by immediately isolating the cells.

Autogenous cartilage must be harvested from the knee joint, and the search for a non debilitating site on the distal femur is a clinical concern[††], with the possible use of sternal cartilage chondrocytes suggested. The integration of the transplants with the surrounding tissue is an issue which can be assessed experimentally through histology or histochemical analysis. Repair tissue integrates with rough subchondral bone, therefore the removal of the layer of calcified cartilage is important in cell based grafting.

Researchers also have the choice of using immature or mature donor allograft cells. Chondrocytes from immature animals are more prolific in culture, more metabolically active, have a longer survival in liquid N_2, and better activity when thawed than mature animals. Fetal chondrocytes are most active but, their survival in grafts is, as yet, unknown.

Mesenchymal Stem Cells There has been much recent interest in using stem cells since they are autogenous and synthetically active cells [33] with the following advantages:

- readily accessible in pools of bone marrow,
- general anesthesia is not necessary for harvesting, and
- pluripotent cells can be manipulated with growth factors to a chondrogenic pathway in culture before implantation and the local condition of vascular access and oxygen tension will drive chondrogenesis and osteogenesis in a full thickness defect.

And the disadvantages:

[††]The concern of site selection for cell harvesting on the distal femur is two fold; 1) not to create damage that will progress to osteoarthritis later in life, and 2) obtaining enough cells to populate the defect when re-implanted after expanded in culture.

- pleomorphic cell population that subsequently have been shown to exist in monolayer, suspension cultures or fibrin vehicles, and
- the difficulty to deal with stem cells in culture.

Vehicles

A key issue is the use of biologic or a synthetic material. Both materials provide a three-dimensional support, fix the cells in place, and provide some biomechanical integrity.

Biologic These include fibrin, collagens, alginates and hyaluronates. Fibrin can be used during arthroscopy due to its injectable delivery for chondrocytes using fibrinogen and thrombin components. Additional anchorage for fibrin can be provided by poly-L-lactone tacks. Collagen meshes have been shown to support chondrocyte growth *in vitro* [177], but most are type I collagen, so *in vivo* results have been unsatisfactory [204]. Hyaluronates support chondrocytes, but are not yet viable long enough *in vivo* to support chondrocyte attachment.

Synthetics In general, three structures are considered: polymer meshes, pads, and porous lattices, which include polyglycolic acid, polylactic acid, poly-L-lactone, and polybutalone. These can be seeded with chondrocytes then implanted to fill cartilage defects. The vehicles can also be laden with growth factors during polymerization for enhance cell growth.

Growth Factors

Many growth factors have been evaluated in cartilage culture environments. Factors that positively influence cartilage behavior are TGF-β, EGF, bFGF, and IGF-1. TGF-β has been used successfully in tissue culture as a stimulus to chondrocytes. Intra-articular injections result in arthrofibrosis, while higher concentrations

have been shown to be cytotoxic. IGF-1 has been shown to be well tolerated intra-articularly and can be mixed with a fibrin vehicle to be slowly released. This will maintain an optimal concentration to provide a mitogenic stimulus and an increased biosynthetic rate for the chondrocytes that need to fill the defects with the extra-cellular matrix they produce.

Age of Patient

Clinically, repair of focal defects in young children have shown a great outcome. This motivates a cartilage repair model in young animal to elucidate the molecules and mechanisms involved. Interestingly, in this model, integration of the defect tissue is a success, while the cells that repopulate the defect are not from the marrow below as usually seen with the natural repair of the adult tissue. Thus, this is a great model for integration, but not for the repair sequence that is more apparent in more mature cartilage.

Repair Tissue Integration

An other problem that must addressed is the integration of tissue to the native tissue. Integration seems to be impeded by the inability of chondrocytes to adhere to the lesion surface. Possible approaches include the use of a proteoglycan depletion and the use of a biological glue like transglutaminase.

A.5.2 Assessing the Success of Focal Repair for the Long Term

In most of the animal repair models studied, the assessment of the repair quality has been based on gross and microscopic morphological features. Detailed studies have established that the repair tissue is generally good in the short term, but degenerates with time. At present the behavior is difficult to explain as the literature shows only a minimal attempt at the molecular characterization of the types of molecules and their distribution as the cartilage repair process unfolds. The more that is known of

the repair process, presumably the higher chances to produce the optimal outcome; a repair tissue integrated in the native cartilage and biomechanically intact to prevent degeneration.

To assess the quality of the repair tissue, researchers must attempt to compare as many properties as completely as possible to native tissue:

- biochemical - proteoglycan content, molecular size, and sulfation; collagen content and typing,
- morphologic - histologic, histochemical, immunohistochemical, and *in situ* hybridization, and
- biomechanical.

In particular, the comparison of the repair tissue's electromechanical properties to native tissue have not been stressed. This is probably due to a lack of tissue, and of a non-destructive means of assessing cartilage electromechanical properties. An electrokinetic surface probe is in development (see Chapter V) that will allow a non-destructive measurements of cartilage electromechanical properties during clinical arthroscopy. This method may be used not only to compare repair tissue properties to those native cartilage, but how the properties change over time.

A.5.3 Case Study: Growth-Factor Induced Repair of Partial Thickness Articular Cartilage Defects

As mentioned, a defect confined to the surface articular cartilage, regardless of how it came to be, will not heal spontaneously. A series of experiments performed in Dr. Ernst Hunziker's Lab in Bern, Switzerland provide an illustration of the limitations that undermine cartilage repair, and possible targets for future improvements [110–112].

Hunziker et al.'s study followed from the initial working hypothesis that the natural anti-adhesive properties of the proteoglycan-rich extracellular matrix was pre-

venting the chondrocytes from being able to attach to the damaged matrix to initiate repair. The proteoglycans were removed with an enzymatic degradation (chondroitinase ABC or trypsin) to expose the underlying collagen network and matrix proteins that allow for mesenchymal-type repair cells to adhere. This produced a transient response of repair cell coverage that was unable to fill the entire tissue volume. Even with the addition of mitogenic growth factors (IGF-I, bTGF, TGF-β or EGF) complete filling was still not achieved, although the cells were able to lay down a substantial layer of connective tissue. This points to the inability of the mesenchymal-type repair cells to be spatially aware and the need of a material (vehicle) to delineate the defect boundaries. When fibrin was added, the defect was populated at only a low density. This was then remedied by the addition of growth factors. The fibrin matrix was eventually remodeled to an avascular, scar-like loose connective tissue that persisted for up to a year with no differentiation to cartilage. This implied that the repair cell population lacks the ability to spontaneously differentiate to the chondrocytic phenotype, and the need for the release the transforming factor TGF-β at high concentrations when the matrix begins to remodel to promote such differentiation. The addition of TGF-β caused a cartilage-like repair tissue [111, 112] to evolve.

The repair cartilage exhibited the characteristics of early postnatal development without any of the changes towards the anisotropic structure of adult cartilage. It has recently been shown that this transformation of cartilage is a result of tissue resorption and neoformation and *not* internal reorganization [110]. This means that the optimal repair tissue may never be achieved from a cell based system as has been proposed.

A.5.4 Summary of Factors Affecting Future Development

Five key areas to be optimized for researchers to produce an optimal synthetic repair tissue are:

1. recruitment of cells to the defect,

2. three dimensional matrix to give cells spatial awareness,

3. integration of repair with native tissue,

4. differentiation of pleiomorphic cells to chondrocytes to produce the proper extracellular matrix with a suitable biomechanical integrity, and

5. create the anisotropy to be congruent with the structure of adult cartilage.

Although a perfect cartilage repair tissue may not be possible [110], the clinical realization from the patient point of view is the relief of pain and restoration of lost of motion. Researchers may not need to duplicate cartilage, but provide a functional, pain free repair tissue that will be durable for many years. This seems like an attainable goal in the near future.

A.6 Examples Electromechanical Property Assessment in Cartilage Repair Model Systems

As mentioned, the assessment of the electromechanical properties of cartilage repair tissue would complement the histological data, and provide a functional measure of its performance. In addition to being able to diagnose cartilage degradation, electromechanical properties can also be a hallmark of the formation (growth) of a functional extracellular matrix [29]. In this section, two such examples are given: (1) the effect of cultivation techniques on the composition and electromechanical properties of tissue engineered cartilage (TEC), and (2) the integration of this TEC into native cartilage as a preliminary step to *in vivo* repair applications.

A.6.1 Bioreactor Cultivation Conditions Modulate the Composition and Mechanical Properties of Tissue Engineered Cartilage

Introduction

The relationships between composition and electromechanical mechanical properties of TEC constructs were studied by culturing bovine calf articular chondrocytes on fibrous polyglycolic acid (PGA) scaffolds in three different environments: static flasks, mixed flasks, and rotating vessels. After 6 weeks of cultivation construct composition, and the mechanical function in radially confined static and dynamic compression were dependent on the conditions of *in vitro* cultivation[‡‡].

Articular cartilage derives its form and electromechanical function from its matrix, which consists of tissue fluid and a framework of structural macromolecules. Adult articular cartilage has a limited capacity to repair damage resulting from injury or disease, and there have been many different approaches to restore tissue composition, structure and function, including the development of engineered cartilage for potential implantation. Fibrous PGA scaffolds permitted chondrocytes to maintain their differentiated phenotype and provided a three-dimensional framework for tissue regeneration [74], while bioreactors provided control over the conditions of cell seeding and tissue cultivation and affected construct structures and compositions [238]. Experiments were performed to investigate if conditions of flow and mixing in tissue culture bioreactors could be utilized to modulate the mechanical function of engineered cartilage. Functional assessment would permit evaluation whether *in vitro* grown constructs might withstand physiological loading, and enable further optimization of the cultivation of cartilage-like tissue substitutes.

[‡‡]A more detailed version of this study appears in Vunjak-Novakovic et al. [239]

Methods

Full thickness articular cartilage was harvested from the femoropatellar grooves of 2-3 week old bovine calves and cells were isolated. Control samples of cartilage (3 mm diameter x 2 mm thick discs) were also harvested for later comparison. PGA scaffolds were produced as previously described [74] at Albany International (Mansfield, MA) by extruding PGA into 13 μm diameter fibers and processing these into fibrous disks measuring 5 mm in diameter x 2 mm thick (void volume 97%, bulk density 62 mg/cm^3). Scaffolds were seeded with freshly isolated chondrocytes in well mixed spinner flasks. After 3 days, cell-polymer constructs were cultured for 6 weeks at 37^{o}C, 10% CO_2 in 3 groups: static flasks, well mixed flasks, or rotating vessels. Samples for biochemical analyses (six constructs per group) were frozen, lyophilized, and digested for 15 hours at 56^{o}C with 1 mg/cm^3 proteinase-K solution. The number of chondrocytes per construct was assessed from the DNA content measured using Hoechst 33258 dye, sGAG content was determined spectrophotometrically (DMMB dye binding assay), and total collagen content was determined from the measured hydroxyproline content using a ratio of hydroxyproline to collagen of 0.1 [105].

For electromechanical evaluation, 3 mm diameter by 2 mm thick disks were harvested from central regions of explanted cartilage plugs or engineered constructs (N = 3-4 samples per group) and subjected to static and dynamic confined compression. Disks were compressed at sequential increments of 10% strain up to a maximum of 40% strain, i.e. in the range where equilibrium stress varied linearly with applied strain for both the engineered constructs and cartilage explants. After stress relaxation, the equilibrium stress was measured and plotted against applied strain; the equilibrium modulus was determined from the slope of the best linear regression fit. At a static offset strain of 30%, sinusoidal strains of 0.5% amplitude were superimposed at frequencies in the range 0.025 to 1 Hz. The amplitude of the oscillatory streaming potential was simultaneously measured and normalized by the amplitude of the applied strain. Equilibrium modulus and dynamic stiffness were used in con-

junction with the method of Frank et al. [68] to calculate the effective hydraulic permeability of the sample.

Results

The conditions of flow and mixing during cultivation in static flasks, mixed flasks and rotating vessels are summarized as follows: In static flasks, constructs were fixed in place and cultured with diffusionally limited mass transfer of nutrients and gases and without hydrodynamic shear at tissue surfaces. In mixed flasks, constructs were fixed in place and exposed to turbulent flow of medium [238], which enhanced mass transfer of nutrients and gases but also caused shear at construct surfaces. In rotating vessels, constructs were dynamically suspended in a laminar, rotational flow field, with their flat circular areas aligned perpendicular to the direction of motion [73].

After 6 weeks of cultivation, constructs from rotating vessels had significantly higher wet weights (WW) than constructs from either static or mixed flasks or the initial 3-day constructs, and all constructs contained significantly more water than cartilage explants. sGAG fractions in 6-week constructs from rotating vessels were lower, but not significantly, than those in cartilage explants, and two-fold higher than those in constructs from either static or mixed flasks (Figure A.1). The fraction of total collagen in 6-week constructs from rotating vessels was comparable to that in mixed flasks, significantly higher than that in static flasks and significantly lower than that in cartilage (Figure A.1). The amount of PGA decreased by approximately 60% [71], from 2.4 mg at 3 days (4% WW) to 1 mg at 6 weeks (i.e. < 0.6 % WW).

Electromechanical characteristics of constructs improved with increasing cultivation time and depended on the hydrodynamic conditions of cultivation. Initial 3-day constructs were too fragile to allow the measurement of mechanical properties (data not shown). After 6 weeks of cultivation, the equilibrium modulus, H_A, was comparable for constructs grown in static and mixed flasks and about 4-fold higher for constructs grown in rotating vessels (Figure A.2). In all groups, 6-week constructs

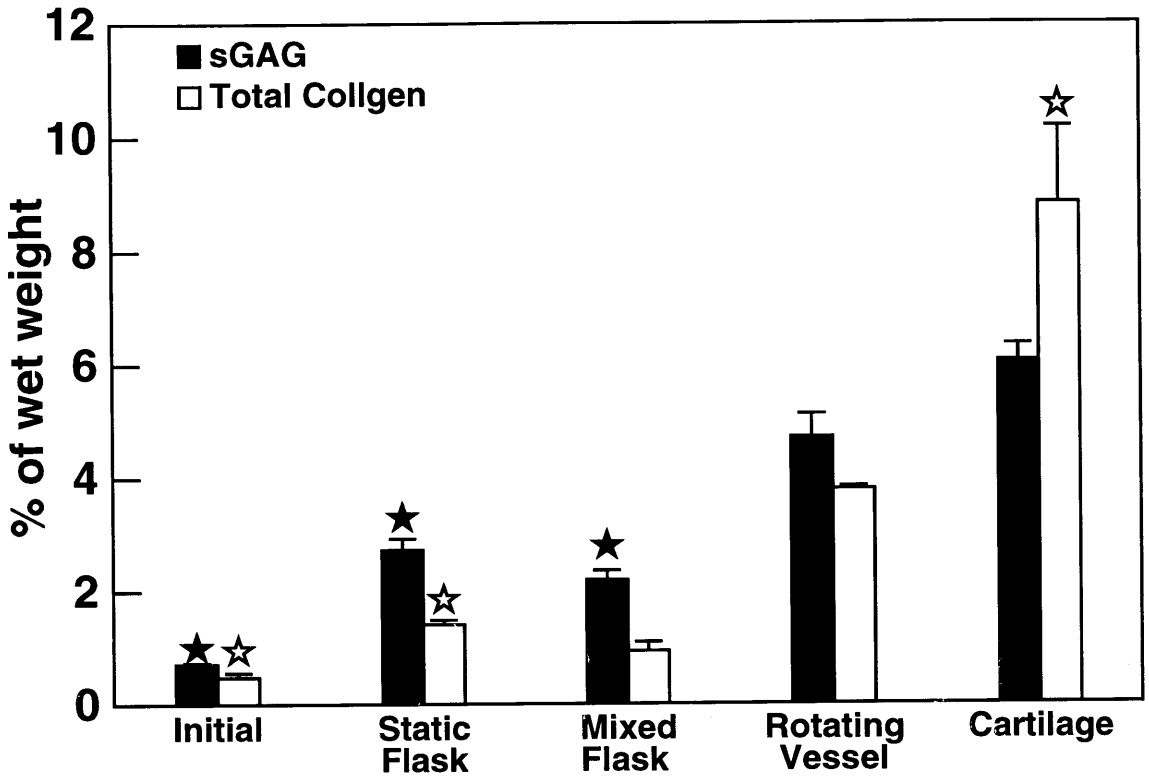

Figure A.1: Tissue growth and composition: sulfated glycosaminoglycan (sGAG) and total collagen as % of wet weight. Data represent mean±SD (N = 6) for the initial 3-day cell-polymer constructs, 6-week tissue constructs from static flasks, mixed flasks and rotating vessels, and freshly explanted bovine calf articular cartilage. Pairwise comparison between the rotating vessels and other experimental groups for sGAG (filled stars, $p < 0.01$) and total collagen (open stars, $p < 0.05$).

remained mechanically inferior to cartilage explants. Hydraulic permeability, k_p, was lower in constructs that had higher H_A (Figure A.2). The permeability of statically grown constructs was significantly higher than that for constructs from rotating vessels or for cartilage, and higher but not significantly than that for constructs from mixed flasks. The permeabilities of constructs grown in mixed flasks and rotating vessels were not significantly different from each other or from natural cartilage.

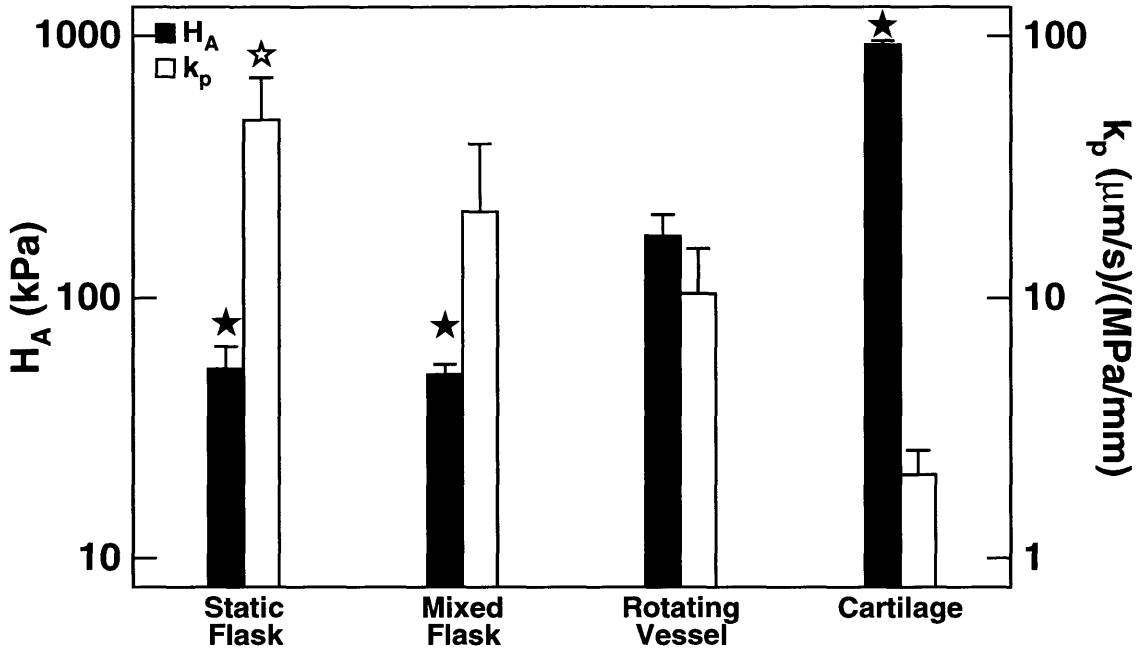

Figure A.2: Tissue biomechanics in static and dynamic confined compression: equilibrium confined-compression modulus, H_A, and hydraulic permeability, k_p, at 30% strain, calculated using the equilibrium modulus and dynamic stiffness. Data represent mean±SD (N = 3-4) 6-week constructs from static flasks, mixed flasks and rotating vessels and bovine articular cartilage. Pairwise comparison probabilities between the rotating vessels and other experimental groups for sGAG (filled stars, $p < 0.001$) and total collagen (open stars, $p < 0.05$).

Discussion

Tissue engineering may offer the possibility of creating functional, cartilaginous equivalents for joint repair. Other approaches have included transplanting collagen gels containing chondrocytes or undifferentiated mesenchymal cells [240]. In this study, the effects of cultivation conditions and time on H_A, and k_p were correlated with changes in construct compositions. While 3-day constructs contained mostly cells and were too fragile to be mechanically tested, 6-week constructs could support load, presumably due to the accumulation of proteoglycans and collagen and their assembly into functional cartilaginous matrix. Constructs grown in rotating vessels, which had the highest wet weight fractions of measured tissue components, also had the highest

H_A, and the lowest k_p (Figure A.2). As compared to chondrocytes cultured statically for 5 weeks in agarose gels (6), chondrocyte-PGA constructs cultured for 6 weeks in rotating vessels had about 3-fold higher sGAG fractions and about 2-fold higher H_A. As compared to cartilage explants, 6-week constructs from all groups were structurally and functionally inferior. However, these same 6-week constructs contained about 78% as much sGAG and 43% as much collagen as compared to fresh cartilage explants on a wet weight basis, implying that either the accumulation of GAG and collagen preceded their assembly into a functional ECM, or that ECM assembly in constructs was different from that in natural cartilage.

Construct mechanical properties reflect the amounts and quality of matrix macromolecules, their ability to assemble into a functional ECM, and collagen-proteoglycan and fluid-matrix interactions. With additional cultivation, constructs more closely approximated cartilage with respect to composition and function, i.e. constructs cultured for 7 months in rotating vessels contained markedly more GAG and had better mechanical properties than constructs cultured for 3 months [72] or 6 weeks (Figure A.2). The cell-polymer-bioreactor system for tissue engineering can thus provide a basis for studying structural and functional properties of the cartilaginous matrix during its development, because tissue concentrations of sGAG and collagen can be modulated by the time and conditions of tissue cultivation.

A.6.2 Integration of Engineered Cartilage into Natural Cartilage: *In Vitro* Studies

Introduction

The controlled bioreactor model system described in Section A.6.1 was used to investigate the effects of construct cultivation time on its potential to integrate with adjacent natural cartilage, and to study the progression of the integration process at the construct-explant interface [178]. Cultivation in rotating bioreactors has resulted in active synthesis of ECM components and a formation of mechanically functional

tissue. A fundamental question with regard to the *in vivo* application is the potential of the TEC constructs to integrate with adjacent host tissue following implantation. Reindal et al. [191] also used an *in vitro* culture system to study the adhesion strength of the repair tissue that forms between pairs of cartilage explants maintain in opposition. Mechanical assessment was performed after 3 weeks in a tensile single lap configuration, and increased linearly with time (per week of incubation). As the percentage of fetal bovine serum in the media increased up to 20%, so did the adhesive strength, with cell division detected histologically at the free surfaces of the explants.

Materials and Methods

Chondrocytes were isolated from full thickness bovine calf articular cartilage and seeded onto PGA scaffolds (5 million cells per each 5 mm diameter x 2 mm thick disc, 97% void volume) in well mixed spinner flasks. Two independent studies were carried out with two groups of constructs: (1) constructs cultured for 3-6 days in spinner flasks (containing mostly cells and small amounts of ECM), and (2) constructs cultured for an additional 4-5 weeks in rotating bioreactors, which became continuously cartilaginous over their entire cross-sections. Constructs were sutured into ring-shaped cartilage explants, and these construct-explant composites were cultured for an additional 4-8 weeks in rotating bioreactors, with explant-explant composites used as a control (Figure A.3). Tissue samples were evaluated biochemically (amounts of DNA, sGAG, and collagen).

Biomechanical integrity was assessed by adhesive strength of the construct-explant interface measured as the stress required to fracture the integration site by a plunger applied to the construct surface. The annular nature of the native cartilage rings and the TEC constructs cores, suggested a push-through test by the apparatus in Figure A.4. The sample is placed in the apparatus between an annular support ring and the main body covered with a fine sandpaper to ensure no-slip (Figure A.4). The top housing was screwed on the main body to secure the annulus surrounding

the interface. The plunger was connected to a load cell and advanced toward to the interface under displacement control. A typical load-displacement curve as the plunger was forced through the construct-explant interface is shown in Figure A.5. As a measure of adhesion strength, the force at ultimate failure, F_{ult}, was normalized to the cross-sectional area of the interface.

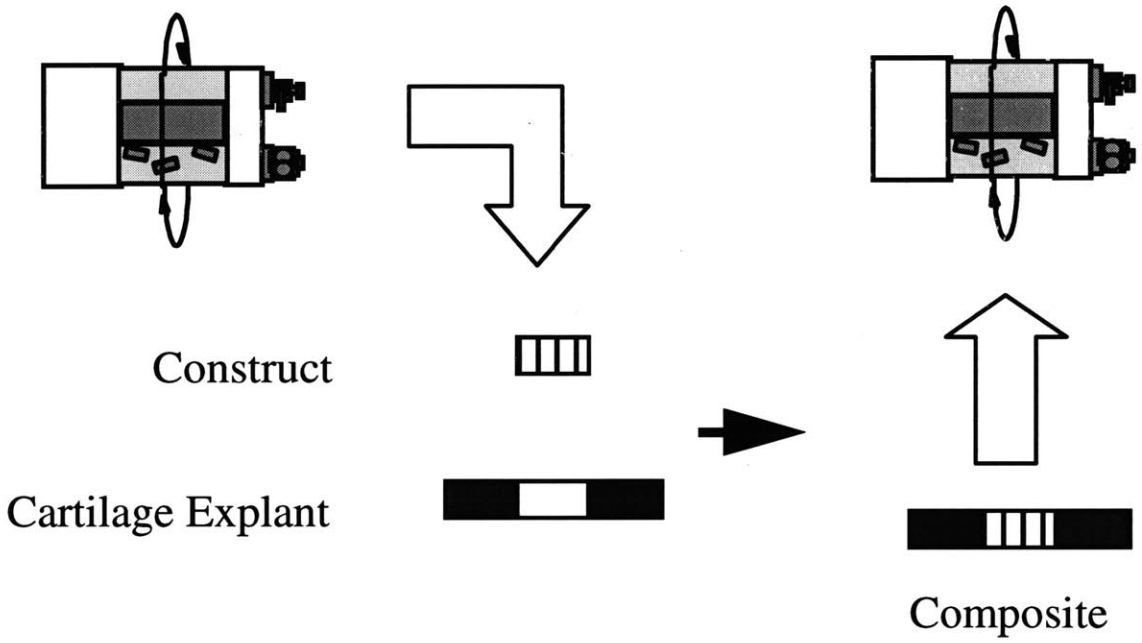

Figure A.3: Model system. Cell-polymer constructs cultured for 3-6 days in spinner flasks (group 1) or for 4-5 weeks in rotating bioreactors (group 2) were sutured into cartilage rings and cultured for 4-8 weeks in rotating bioreactors.

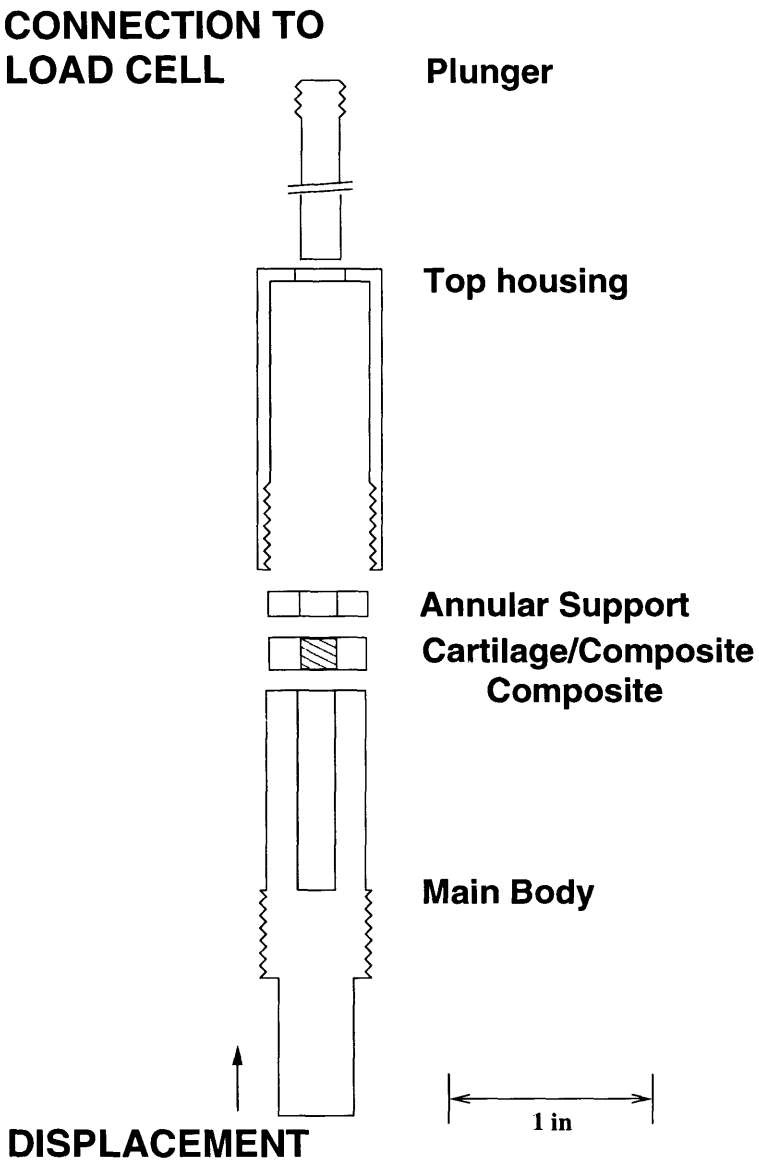

Figure A.4: Biomechanical integrity was assessed by adhesive strength of the construct-explant interface measured as the stress required to fracture the integration site by a plunger applied to the construct surface during a push-through test. The sample is placed in the apparatus between an annular support ring and the main body covered with a fine sandpaper to ensure mechanical no-slip. The top housing is screwed on the main body to secure the annulus surrounding the interface. The plunger is connected to a load cell and the main body is advanced toward to the engage the interface against the plunger under displacement control.

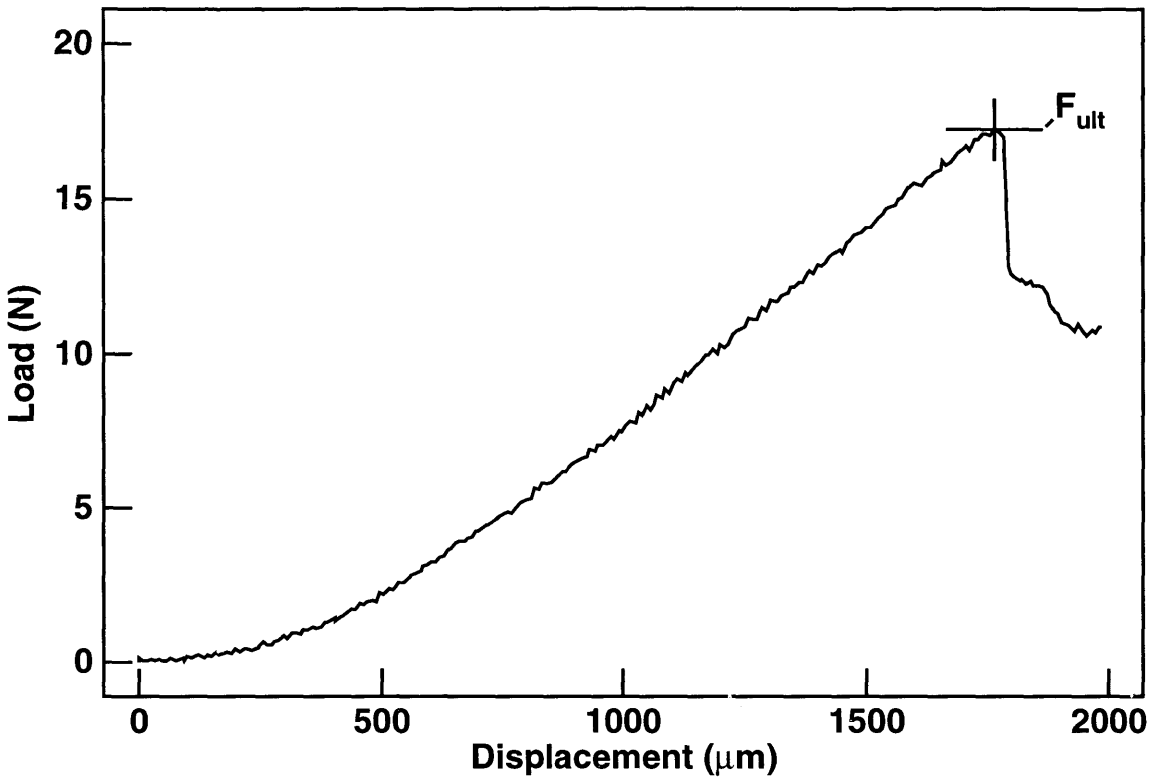

Figure A.5: A typical measured load-displacement curve as the plunger is forced through the construct-explant interface in the push-through test. As a measure of adhesion strength, the force at ultimate failure, F_{ult}, is normalized to the cross-sectional area of the interface.

Results

At early stages of cultivation (1-2 weeks), fibrous-like tissue filled the gap at the construct-explant interface. This bond was 10-15 cell layers thick in group 1, and only 1-2 cell layers in group 2. Over 8 weeks of cultivation, the interfacial fibrous tissue progressively developed into cartilaginous tissue (data not shown), such that the biochemical composition and histological appearance of the TEC constructs and explants approached. The adhesive strength at construct-explant interface was approximately 65% higher for composites made with 6 day rather than 5 week constructs (Figure A.6). These data indicate that the time of construct cultivation needs to be optimized to achieve a certain minimum compressive stiffness, which is important for

construct survival while maintaining sufficient potential for its integration with the adjacent tissue.

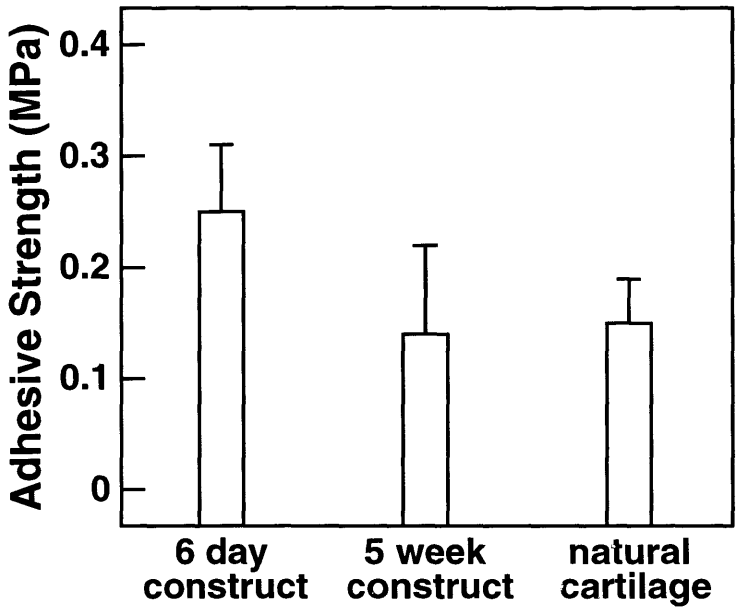

Figure A.6: The adhesive strength at construct-explant interface was approximately 65% higher for composites made with 6 day rather than 5 week constructs or native cartilage controls. These data indicate that the time of construct cultivation needs to be optimized to achieve a certain minimum compressive stiffness, which is important for construct survival while maintaining sufficient potential for its integration with the adjacent tissue.

Appendix B
Measurement of the DNA Content in Human Adult Articular Cartilage Using Hoechst Dye 33258

B.1 Introduction

Calculation of cell density is frequently required to normalize incorporation results from tissue biosynthetic studies and biochemical composition measurements (i.e. sGAG, HYPRO), giving an amount that is on a "per cell" basis. Many methods over the past decades have been proposed and successfully used to measure the amount of DNA in tissue like articular cartilage, whose abundant ECM makes it difficult to count cells. Early methods used histological sections to count the cellular density, but the need to process many samples quickly obviated the need for more rapid assessments. Fluorimetric measurements with 3,5 DABA and ethidium bromide require extra sample processing techniques since the ECM interferes with 3,5 DABA [181] and RNA effects measurement with ethidium bromide [195], adding to sample cycle times. Teixeira et al. [223] recently treated chondrocytes in monolayer with triton X-100 and the nucleic acids of the extract were measured by DNA fluorescence with Hoechst dye 33258. However, first the DNA had to be precipitated with alcohol and resolubilized with EDTA, since the triton X-100 was interfering with the fluorescence (autofluorescing) of the DNA-Hoechst Dye 33258 complex. Other methods are plagued by a lack of sensitivity, requiring many samples to be pool-processed to lower variation, which can be troublesome if a limited amount of material is available (i.e. clinically obtained human articular cartilage).

A method developed by Kim et al. [123], was developed and characterized for the rapid assessment of DNA content of papain digested samples of newborn

bovine (1-2 weeks old) cartilage. In processing the adult articular cartilage samples from Chapter II, it has become evident that the Kim et al. method can severely overestimate the cell density. The cell density of human adult articular cartilage has been measured histologically as approximately 15 x 10^6 cells/ml [218]. In applying the methodology of Kim et al. to the cartilage of Chapter II, the cell densities were measured to be on the order of 30 - 40 x 10^6 cells/ml. This was believed to be caused by components of the ECM, other than the DNA-Hoechst Dye 33258 complex, fluorescing during assay conditions [232]. This appendix will characterize this behavior for the adult human AC from Chapter II and present a solution based on making measurements of the background autofluorescence. In addition, other possible more efficient solutions will be proposed, since the present solution requires extra assay time and is not the optimal one-step procedure analogous to that of Kim et al. [123].

B.2 Materials and Methods

The methods and solutions used are those described previously by Kim et al. [123]. Samples were prepared as described in Chapter II, and fluorescence was measured using a spectrofluorometer (SPF 500C, SLM Instruments, Urbana, IL). Measurements were taken with buffer + Hoechst Dye 33258 (with dye) and with buffer alone (without dye). In addition to the excitation wavelength of 365 nm and emission wavelength of 458 nm normally used ("regular"), measurements were also taken at an excitation wavelength of 350 nm and an emission wavelength of 530 nm ("adjusted"). The band pass for the excitation was 5 nm and 10 nm for the emission, in either case. The adjusted excitation and emission wavelengths were established by examining spectra (and will hence be discussed) that were produced by scanning the excitation wavelengths of 300 - 500 nm and emission wavelengths of 300 - 600 nm with 10 nm band passes with a step size of 10 nm. All measurements were taken in ratio mode, with 100 μL of sample and 2 ml of buffer alone or buffer + Hoechst Dye 33258 after

gentle shaking and before the signal degraded (within 30 minutes [123]). Cells were calculated based on 7.7 pg/chondrocyte.

B.3 Results

The difference between the apparent cell density (using the Kim et al. method directly) and the corrected cell density appear in Figure B.1 for selected cartilage samples from Chapter II (n = 56). The corrected cell density was calculated from separate measurements of the sample by adding buffer + Hoechst Dye 33258 (apparent cell density) or buffer alone to another sample aliquot. The ratio measurement from the fluorimeter without dye is taken to represent the autofluorescence, and thus subtracted from the with dye measurement. This corrected ratio measurement is then used in conjunction with the standard curve to solve for the amount of DNA present in the sample. The lines on Figure B.1 that indicate the expected cell density clearly show that the apparent cell density is an overestimate at $33.1 \pm 9.9 \times 10^6$ cells/ml. However, the corrected method lowers the values into a more appropriate range with a of $18.3 \pm 4.5 \times 10^6$ cells/ml.

The sample dye/no dye corrected method presented yields promising results, but there are drawbacks. Namely, it takes double the assay time and sample amounts to complete. Besides, the extra time, the fact that up to total 500 μl (with duplicates) of a 1 ml papain digested sample is needed can be problematic if other assays need to be completed. Therefore, it would be preferable to have a correction method analogous to the Kim et al. method, where only one measurement per sample was necessary. A proposed solution was to investigate other combinations of emission and excitation wavelengths with the Hoechst Dye 33258 that still produce dye enhancement in the presence of DNA, but where the autofluorescence was negligible. Figure B.2 shows a 3-D plot assembled from performing spectra of the no dye ratio measurement subtracted from the dye measurement (dye enhancement) at the emission wavelengths of 300-600 nm and the excitation wavelengths of 300-500 nm.

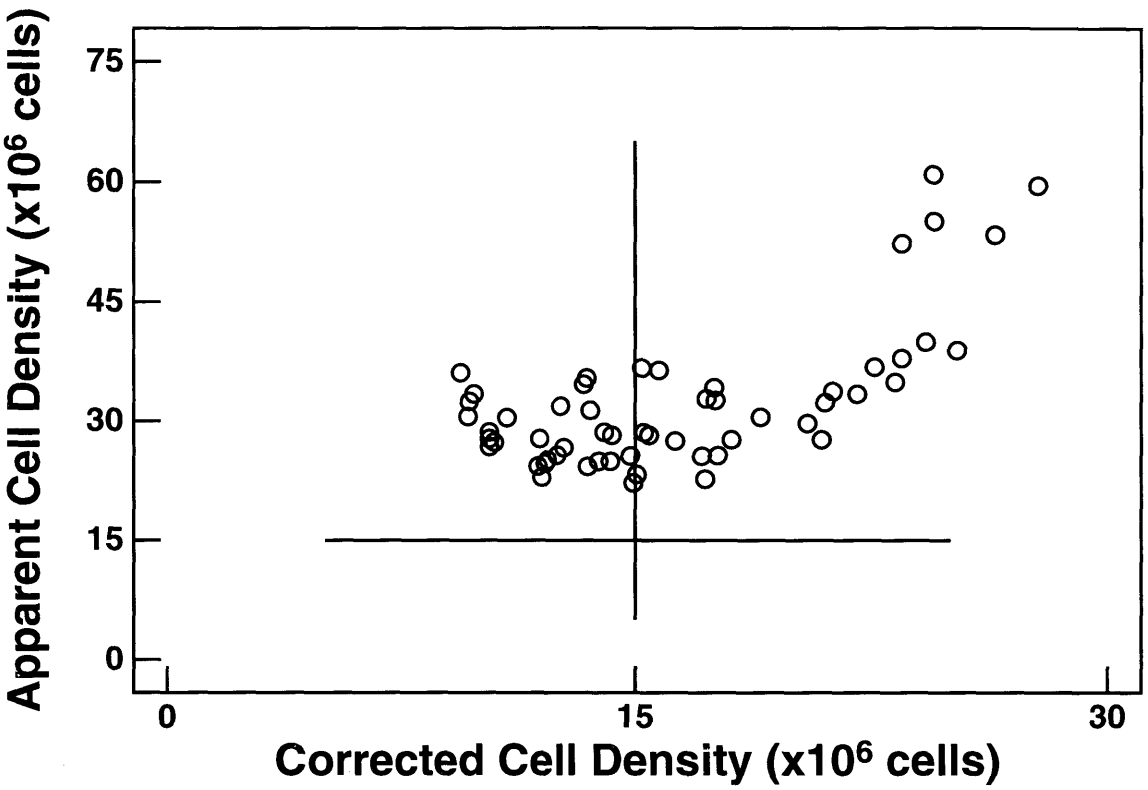

Figure B.1: A scatter plot comparing the apparent cell density (using the Kim et al. method directly) and the corrected cell density for selected cartilage samples from Chapter II. The corrected cell density was calculated from the difference of separate measurements by adding buffer + Hoechst Dye 33258 or buffer alone to the samples. The lines indicate the expected cell density (15.0 x 10^6 cells/ml). Thus, the apparent cell density is an overestimate at 33.1±9.9 x 10^6 cells/ml (n = 56), while the correction method lowers the values into a more appropriate range at 18.3±4.5 x 10^6 cells/ml.

The maximal dye enhancement was approximately at an excitation of 350 nm and emission of 530 nm. To check whether the autofluorescence was close to zero, the data was re-plotted to show the spectra at an excitation of 350 nm and emission of 530 nm (Figure B.3 left and right).

The adjusted excitation and emission wavelength combination (350 nm and 530 nm, respectively) show that in the case of the sample of Figure B.3 the autofluorescence is close to zero. This contrasts to the regular wavelength combination (excitation 358 and emission 458, respectively), where a significant autofluorescence exists.

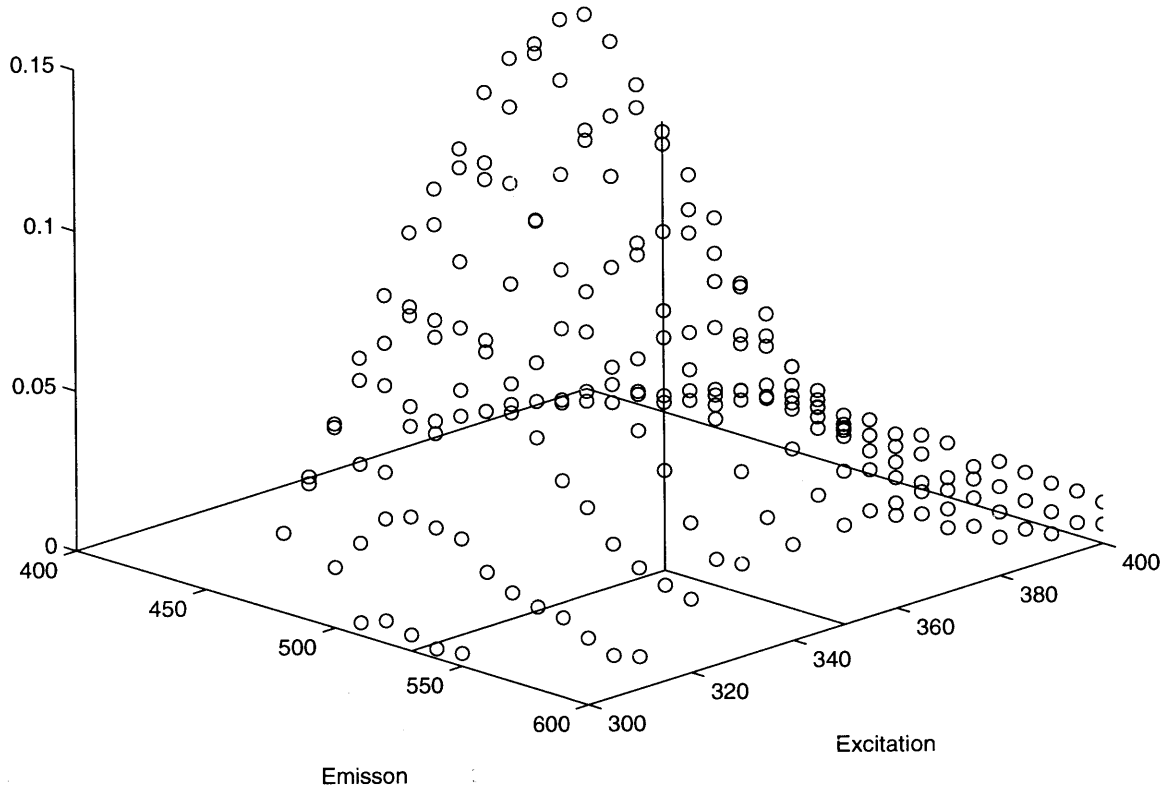

Figure B.2: The Hoechst Dye 33258 enhancement (no dye ratio measurement subtracted from the dye measurement) of an adult human articular sample. The three dimensional plot was created by acquiring spectra at emission wavelengths from 300-600 nm and the excitation wavelengths from 300-500 nm. The maximal dye enhancement was approximately at an excitation of 350 nm and emission of 530 nm as indicated.

To investigate the feasibility of the adjusted wavelength, a second series of selected cartilage samples (n = 40) from those of Chapter II were selected. The samples spanned an age range of 14 - 45 years of age and were obtained from a variety of sites within human knee and ankle joints. Unfortunately, for all samples, the autofluorescence was not reduced to zero, thus the apparent overestimated the corrected cell density at the adjusted wavelength ($55.4 \pm 12.0 \times 10^6$ vs $21.5 \pm 12.3 \times 10^6$ cells/ml). At the regular wavelength, a similar situation was evident with the apparent

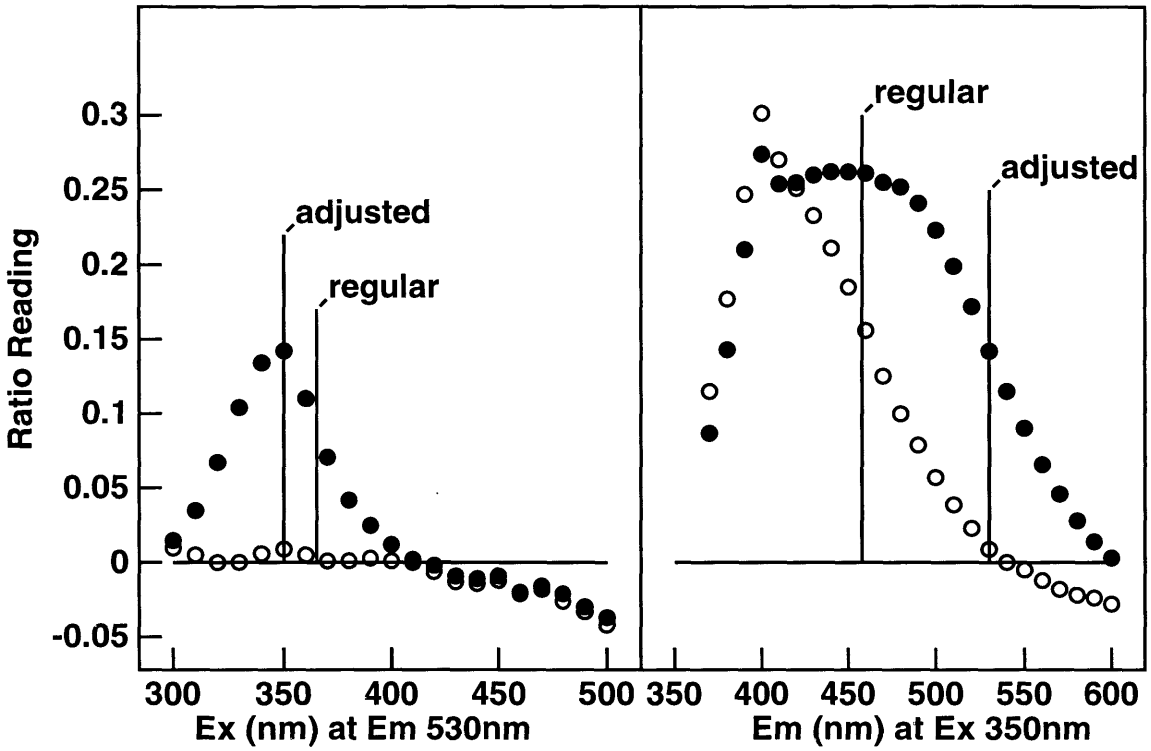

Figure B.3: The data of Figure B.2 is re-plotted to separate the buffer + Hoechst dye (filled circles) and the buffer only (open circles) to more closely examine the spectra at an excitation of 350 nm (left) and emission of 530 nm (right). The adjusted excitation and emission wavelength combination (350 nm and 530 nm, respectively) show that in this case the autofluorescence is close to zero. This contrasts to the regular wavelength combination (excitation 358 nm and emission 458 nm, respectively), where a significant autofluorescence exists.

cell density (34.0±10.6 x 10^6 cells/ml) larger than the corrected cell density (7.0±3.4 x 10^6 cells/ml). The cell densities at the adjusted wavelength were significantly higher than those at the regular wavelength combination. Although, the values are much closer to those expected, the cause of this discrepancy must be resolved.

B.4 Discussion

Adult human articular cartilage is associated with fluorescence that emanates not only from the DNA-Hoechst dye 33258 complex, but also from ECM components that are

not destroyed by the papain digestion process. The presented solution involves is to performing a buffer + Hoechst dye 33258 and a buffer alone measurement, to correct for the autofluorescence that is represented by the buffer alone measurement. When this method was used (Figure B.1), the cell density of adult human articular cartilage sample were corrected to be in the range previously measured histologically [218].

This technique seems to be a time and procedural improvement over the method proposed by Urban et al. [232], where a DNAse digestion of the sample is used to estimate the autofluorescence in place of the buffer alone measurement. With respect to the corrected cell densities, limited data at this point shows the addition of DNAse is equivalent to performing the buffer alone measurement (data not shown), but needs to be confirmed. However, in some extreme circumstances (intervertebral disk) when the cell density is low or the autofluorescence is high, even using the correction method can be unreliable [232].

Although the solution presented seems to be successful to date, it does not optimize assay time and the amount of sample consumed, therefore a one-step procedure would be preferable. Several ideas were considered, including using another nucleic acid stain or the addition of a chemical to neutralize the autofluorescence. Elucidating these solutions would be time consuming and possibly difficult to implement since the nature of the autofluorescence has not been characterized. A possible solution that was investigated involved using an adjusted excitation and emission wavelength where enhancement of the ratio measurement existed (due to the DNA-Hoechst dye 33258 complex), while the autofluorescence was not present. If possible, this would be analogous to the Kim et al. method for newborn bovine articular cartilage.

Potential wavelengths candidates where found by examining the spectra of the buffer + Hoechst Dye 33258 and buffer alone, and a range of appropriate excitation and emission wavelengths were identified (Figure B.2). When the excitation and emission wavelengths were inspected for the existence of autofluorescence, the buffer alone ratio measurements was negligible at 350 nm and 530 nm, respectively (Figure B.3),

lending evidence that potential candidates have been identified. Unfortunately, when a large sample set was examined at the adjusted excitation and emission wavelength combination, the absence of autofluorescence did not hold. This may be attributed to basing the adjusted wavelengths on too few sample measurements. A possible correction could involve setting the excitation wavelength at a median value (say 362 nm), and obtaining the spectra of emission wavelengths. With this procedure, an emission wavelength may emerge that indeed has no autofluorescence consistently, establishing it for future assays.

Using the adjusted wavelength, the correction method was successful in lowering the measured cell density, but was inconsistent with the results of the regular wavelength combination (excitation 365 nm and emission 458 nm, respectively). The discrepancies in these results need to further investigated, but could attributed to the length of time the samples have been stored (up to 1.5 years when the second study was performed) and the number of freeze-thaw cycles the samples were exposed to, increasing the risks of DNAse contamination.

Appendix C

Determination of Hydroxyproline Content of Articular Cartilage Samples

C.1 Introduction

In comparing the biomechanical and biochemical properties of cartilage from human knee and ankle in Chapter II, it was clear that the additional measurement of collagen content (by hydroxyproline) was required in addition to sGAG and DNA content assays already routinely performed. Several methods to determine the hydroxyproline content of tissue samples have been successfully used [216, 217]. The method present here is adapted from Woessner [244]. Unlike other methods that require a vacuum oven to capture HCl vapors when the sample is hydrolyzed, this method neutralizes the acid by titration, making this approach much less corrosive and hazardous. In addition, improvements to assay sensitivity are provided in the protocol, along with additional experiments validating its results against other methods, determining the lower bound of sensitivity of the assay, and determining the conversion factor to collagen content*.

C.2 Materials and Methods

C.2.1 Chemicals/Supplies

Obtained from Fisher Scientific Chemicals: p-dimethylaminobenzaldehyde (pDAB, Ehrlich's reagent) Cat# D71-100 and Methyl Red Solution (0.02%) Cat#SI16-500. From Mallinckrodt: perchloric acid (60%) analytic reagent Cat#2765-500, Chloramine-T Cat# 7708-500, sodium hydroxide AR pellets Cat# 7708-500, and

*The starting protocol for this assay was originally obtained from I. Martin at MIT and modified.

sodium acetate tri-hydrate Cat# 7364-500, citric acid monohydrate AR Cat# 0627-500. L-4 hydroxyproline Cat# 56250 was obtained from FLUKA Chemicals. From MIT lab supplies: isopropyl alcohol, toluene, hydrochloric acid, glacial acetic acid, pyrex Tubes #9826 16x125mm Cat#60827-533, disposable culture tubes Cat# 60825-618 Kimax 51 borosilicate glass 16 x 100 mm, and marbles.From Sigma: type II collagen.

C.2.2 Protocol

1. The following solutions can be made up and stored for three months at room temperature:

   (a) "pH 6 buffer" for use in making Chloramine-T solution: Place 250 ml dH_20 and stir bar in 500 ml beaker. While stirring add: 17 g NaOH, 25 g citric acid monohydrate, 36.17 g sodium acetate anhydrate (or 60 g sodium acetate trihydrate), and 6 ml glacial acetic acid. When dissolved, transfer solution to a 500 ml volumetric flask and bring to 500 ml. Transfer solution to an appropriate glass storage container, which will hold at least 750 ml total volume. Then add: 150 ml isopropanol and 100 ml dH_20 and mix well. Bring to pH 6 with concentrated HCl while stirring. Add 5 drops toluene. Wrap with parafilm to avoid evaporation.

   (b) Hydroxyproline standard stock solution: Place 10 mg of hydroxyproline in a 100 ml volumetric flask and add dH_20 to 100 ml. This gives you a stock solution of 100 μg/ml.

2. The day before the assay the following must be prepared [†].

   (a) Chloramine-T solution (enough for approximately 90 samples[‡]): In a 100

[†]Each sample to be assayed requires 0.5 ml of both of the following solutions so ensure enough is made in advance, including for standards and multiple dilutions, if necessary

[‡]You can go through as many as 45 samples in one assay batch. If you have more samples split them into two batches and do the assay on two consecutive days

ml glass bottle add: 0.705 g Chloramine-T, 40ml of above "pH 6 buffer" and 5 ml Isopropanol. Shake Well to mix, wrap with parafilm and let sit at room temp for 24 hours.

(b) pDAB solution (enough for approximately 90 samples): In a 100 ml brown bottle (or regular bottle wrapped with aluminum foil) add 7.5 g p-dimethylaminobenzaldehyde, 30 ml isopropanol and stir bar. Place bottle in a glass bowl containing ice and place on a stirrer in the fume hood. While stirring, slowly add 13 ml of 60% perchloric acid. Allow to stir for 10 min in hood and then cap, wrap with parafilm and leave at room temp for 24 hours[§].

(c) Weigh appropriately labelled empty capped pyrex tubes to be used for the assay, and record their weights. Then, 100 μl aliquots of the papain digested cartilage into the pyrex tube and hydrolyze in 900 ml μl of of 6 N HCl at 115^{o}C (110-120^{o}C) for 18 hours in a temperature controlled oven[¶].

3. On the day of the assay: Turn on microplate reader in advance and set it to 560 nm. Bring water bath up to 60^{o}C for final incubation step. Make sure you have at least 100 ml of the following solutions: 2.5 M NaOH, 0.5M NaOH and 0.5M HCl.

4. Make the final working solution of the hydroxyproline (HYPRO) standard: dilute 10 ml of 100 μg/ml stock solution into 100 ml volume with deionized water. This gives you a working solution of 10 μg/ml. Set up seven standard curve tubes into a disposable Kimax tube appropriately labelled as follows:

5. Remove tubes containing hydrolyzed samples from the oven and allow to cool

[§]Perchloric acid is highly reactive with any organic substance and you should take great care when using and handling it. Also, place a layer of bench paper on all surfaces in which you will be using to minimize staining.

[¶]Make sure caps are tight so sample does not evaporate and HCl does not escape and corrode oven

Tube #	μl working solution	μl H_20	μg/ml HYPRO
1	0	1000	0
2	50	950	0.5
3	100	900	1.0
4	200	800	2.0
5	300	700	3.0
6	400	600	4.0
7	500	500	5.0

to room temperature. Vortex samples and tip tubes to collect all the condensed liquid from sides of tube. Bring samples to fume hood for titration. Add 1-2 drops of methyl red indicator to each sample. Then add approximately 2 ml of 2.5 M NaOH to each tube while vortexing until red color just disappears. Next add 0.5 M HCl dropwise while vortexing until pink color just reappears. Finally add 1-2 drops of 0.5 M NaOH to bring sample back to a faint straw color to signify pH balance.

6. Add enough dH_20 to bring the volume in each tube up to the same amount ($\sim$ 15 ml) by eye to dilute salts. Replace and tighten the caps on each tube and weigh again[‖]. If necessary, the assay can be interrupted and the diluted samples placed in the fridge for up to 2 days for later continuation without introducing error.

7. Transfer 1 ml of each diluted sample into a disposable Kimax tube appropriately numbered. Then, bring standard curve tubes and samples to a fume hood. Add 0.5 ml Chloramine-T solution to each tube and vortex. Place a marble on each tube to prevent evaporation as they sit for 20 minutes.

8. Add 0.5 ml of pDAB to each solution while vortexing. Vortex until no milky white "schlieren" is visible. Replace marble caps on tubes and incubate in 60^{o}C

[‖]The difference in tube weights allows the estimation of the fluid in the tube for increased measurement accuracy during analysis

water bath. After 30 minutes remove rack from the bath and place in tub of cool water for approximately 5 minutes to cool to room temperature.

9. Prepare microplate reader and take a zero reading of the blank microplate that will used. Aliquot 200 μl duplicates of each standard and sample into the microplate. Read microplate. The color of the solutions is stable for about 1 hour after removal from bath.

C.3 Theoretical Considerations

In this section, relationships are derived to represent the underlying mathematics that correlate assay conditions to the amount of HYPRO in the original sample. The development is done generally, to provide flexibility in the amount of each solution used during the assay. A similar treatment can be simply applied for other routinely performed assays like sGAG or DNA content.

The general approach involves solving for the final concentrations in the samples and standards at the stage when the absorbances of the solution are recorded and compared. Along the steps of the assay the concentration of the sample must be followed closely. When the absorbance values of the samples are properly converted to concentrations using the standard curve, the amount of HYPRO in the original sample can be back-calculated.

The original amount of sample in the cryovial (Figure C.1), is processed through several steps until absorbance is measured. Table C.1 represents the concentration of HYPRO as the sample is processed: from the cryovial, to pyrex tube, to Kimax tube, and finally to the well of the microplate for the absorbance measurement (Note: The mass of HYPRO at each stage can be directly found using $m = CV$).

Therefore, the relationship for each sample linking the concentration of the original sample with that when the absorbance is derived from as Figure C.1 and

Table C.1 as follows:

$$C_4 = C_1 \left[\frac{V_S^2}{V_S^3 + V_{CT}^3 + V_{pDAB}^3}\right] \left[\frac{V_S^3}{V_T^2}\right] \tag{C.1}$$

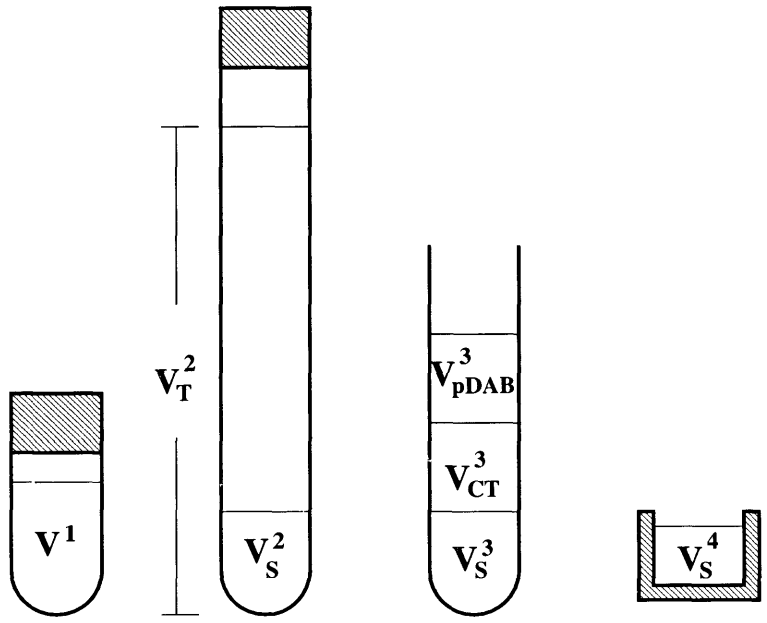

Figure C.1: The original amount of sample in the cryovial (1) is processed through the pyrex tube (2), the Kimax tube (3), and finally the absorbance is measured in the microplate (4). The volume are defined as that of the: V^1 original papain digest, V_S^2 amount transferred for hydrolyzation, V_T^2 post-titration, V_S^3 amount transferred to Kimax tube, V_{CT}^3 amount of Chloramine-T added, V_{pDAB}^3 amount of pDAB added, V_S^4 amount aliqouted to the well of the microplate.

The analogous relationship for the standards, that are not hydrolyzed, is derived from as Figure C.1 and Table C.2 as follows:

$$^{std}C_4 = {}^{std}C_1 \left[\frac{^{std}V_S^3}{^{std}V_S^3 + {}^{std}V_{CT}^3 + {}^{std}V_{pDAB}^3}\right] \tag{C.2}$$

The final step in the analysis is to solve for the concentration of the samples,

Sample	Volume (ml)	Concentration ($\frac{\mu g}{ml}$)
sample tube	V^1	$C_1 = m_1/V^1$
pyrex tube	V_T^2	$C_2 = \frac{m_1}{V_T^2}\frac{V_S^2}{V^1}$
kimax tube	$V_S^3 + V_{CT}^3 + V_{pDAB}^3$	$C_3 = m_1 \frac{\frac{V_S^2}{V^1}\frac{V_S^3}{V_T^2}}{V_S^3+V_{CT}^3+V_{pDAB}^3}$
microplate	V_S^4	$C_4 = C_3$

Table C.1: Table that represents the concentration of HYPRO as the sample is processed: from the cryovial, to pyrex tube, to Kimax tube, and finally to the well of the microplate for the absorbance measurement.

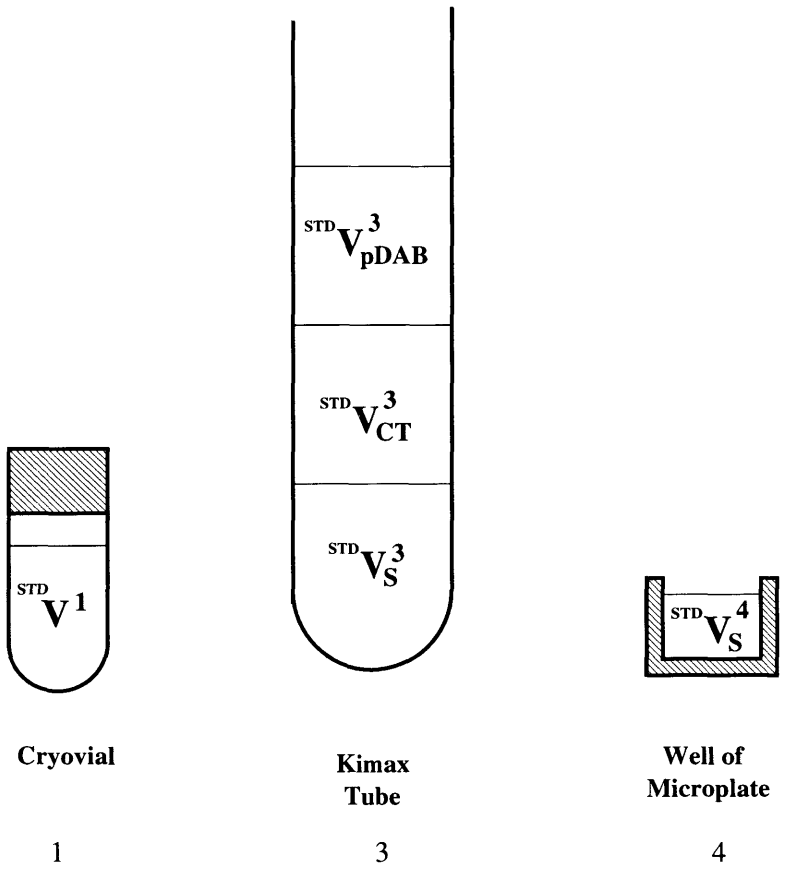

Figure C.2: The original amount of standard in the cryovial (1) is processed through the Kimax tube (3), and the absorbance is measured in the microplate (4). The volume are defined as that of the: ${}^{std}V^1$ original papain digest, ${}^{std}V_S^3$ amount transferred to Kimax tube, ${}^{std}V_{CT}^3$ amount of Chloramine-T added, ${}^{std}V_{pDAB}^3$ amount of pDAB added, ${}^{std}V_S^4$ amount aliqouted to the well of the microplate.

Sample	Volume (ml)	Concentration(μg/ml)
sample tube	${}^{std}V^1$	${}^{std}C_1 = {}^{std}\, m_1 / {}^{std}V^1$
kimax tube	${}^{std}V_S^3 + {}^{std}\, V_{CT}^3 + {}^{std}\, V_{pDAB}^3$	${}^{std}C_3 = {}^{std}\, m_1 \, \frac{\frac{{}^{std}V_S^3}{{}^{std}V^1}}{{}^{std}V_S^3 + {}^{std}V_{CT}^3 + {}^{std}V_{pDAB}^3}$
microplate	${}^{std}V_S^4$	${}^{std}C_4 = {}^{std}\, C_3$

Table C.2: Table that represents the concentration of HYPRO as the standards are processed: from the cryovial, to Kimax tube, and finally to the well of the microplate for the absorbance measurement.

using the standard curve created by plotting the absorbance values against the known concentrations. An example of such a standard curve is shown in Figure C.3.

The sample absorbance values are, in turn, used to solve for the concentration of the sample (C_1), by rearranging Equation C.1

$$C_1 = C_4 \left[\frac{V_S^3 + V_{CT}^3 + V_{pDAB}^3}{V_S^2}\right] \left[\frac{V_T^2}{V_S^3}\right] \sim 300\, C_4 \qquad \text{(C.3)}$$

since $V_S^3 = 1\ ml$, $V_{CT}^3 = 0.5\ ml$, $V_{pDAB}^3 = 0.5\ ml$, $V_S^2 = 100\ \mu l$, and $V_T^2 \sim 15\ ml$ (the exact volume is determined from the volume of liquid in the tubes post-titration).

C.4 Validation

Using the outlined methodology, the assay was validated against an ultra-sensitive quantitative HPLC analysis of hydroxyproline (kindly performed HYPRO by I. G. Otterness, Pfizer Central Research, Groton, CT) [182]. A variety of samples from various sites within the human knee and ankle joints (N=60) from Chapter II were chosen for processing by HPLC and the calorimetric methods discussed. The results of Figure C.4 show a high correlation (R^2=0.84) between the two methods. In general, the calorimetric method underestimates with respect to the HPLC method in the range of 50 - 125 μg HYPRO per 1 ml of the original papain digest.

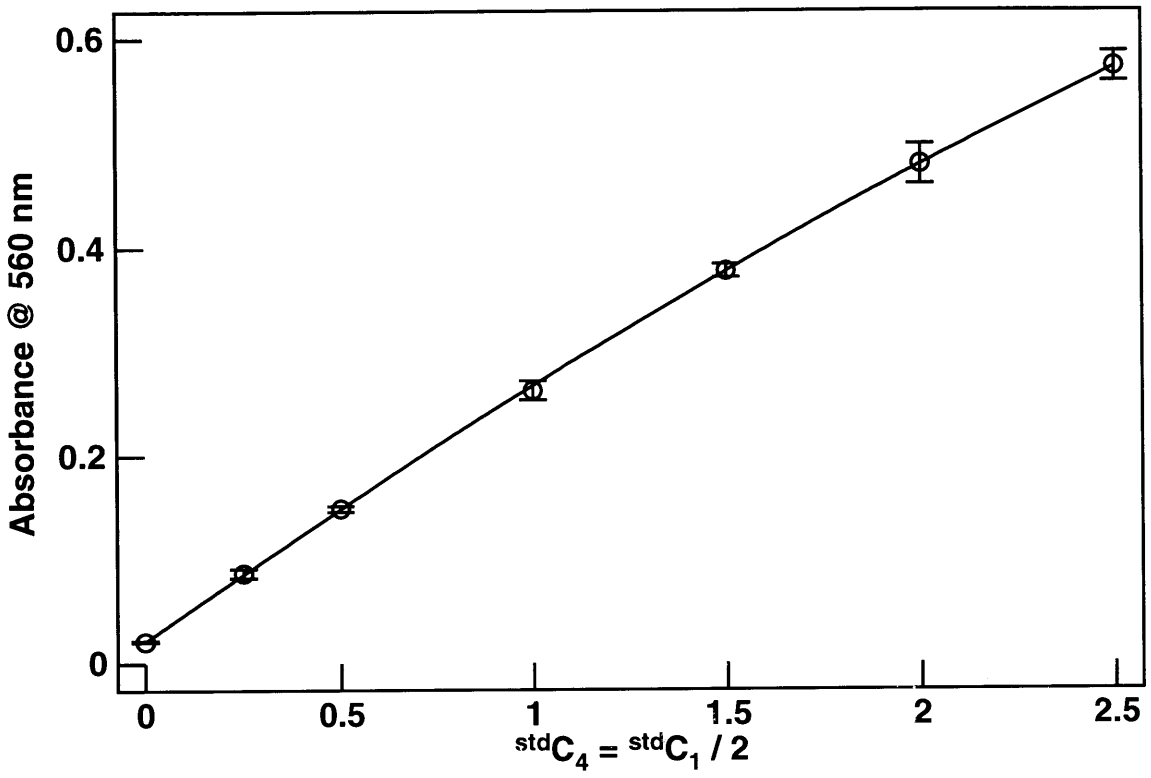

Figure C.3: The standard curve is created by plotting the absorbance values at 560 nm against the known concentrations, where ${}^{std}C_4 = \frac{{}^{std}C_1}{2}$ for the volumes used: ${}^{std}V_S^3 = 1$ ml, ${}^{std}V_{CT}^3 = 0.5$ ml, and ${}^{std}V_{pDAB}^3 = 0.5$ ml. In this case, the best fit relationship is: Absorbance = -0.01695 $[{}^{std}C_4]^2 + 0.2626\ {}^{std}C_4 + 0.02153$ (R=0.9970).

C.5 Sensitivity and Conversion to Collagen Content

In a second set of experiments, the sensitivity of the measurement and the conversion factor to collagen content was established by processing samples of pure type II collagen through the given protocol. Type II collagen from Sigma (St. Louis, MO) was dissolved in 0.5% acetic acid and prepared into solutions of 1-1000 μg/ml. These samples were processed and the amount of corresponding hydroxyproline was determined. Figure C.5 shows a summary of the results of the correlating the HYPRO measured to the collagen in the original solutions. The lower bound of the sensitivity of the method was determined to be $\sim$100μg/ml of type II collagen or $\sim$10μg/ml of HYPRO. This value of the lower bound on HYPRO was also separately established on

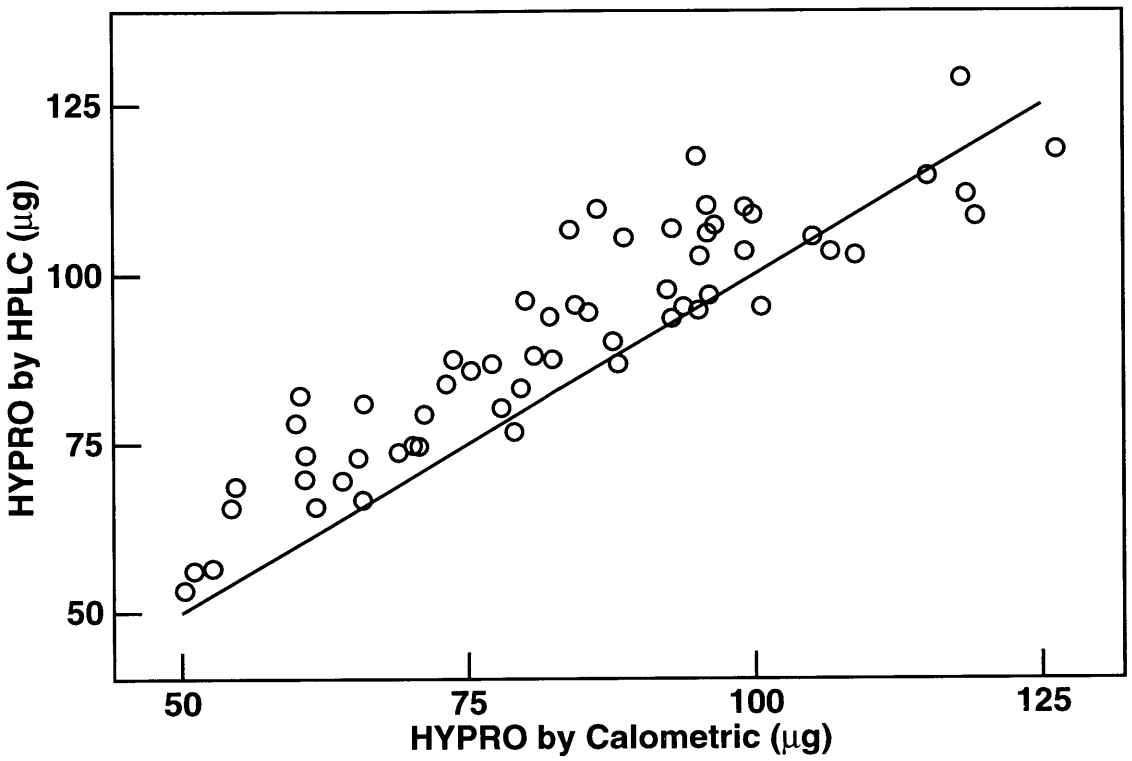

Figure C.4: A scatterplot of the the hydroxyproline measured by calorimetric method correlated with the corresponding value measured by HPLC (N=60). Samples are from various sites within the human knee and ankle joints from Chapter II. The two methods are highly correlated (R^2=0.84), and the calorimetric method underestimates with respect to the HPLC method in the range of 50 - 125 μg HYPRO.

HYPRO standards similarly processed (data not shown). The samples in the range of 100-1000 μg/ml collagen content were used to establish that the ratio of collagen to HYPRO at $\sim$7.4 for this assay. This value compares favorably with the values generally used in practice, generally between 7-10 [105].

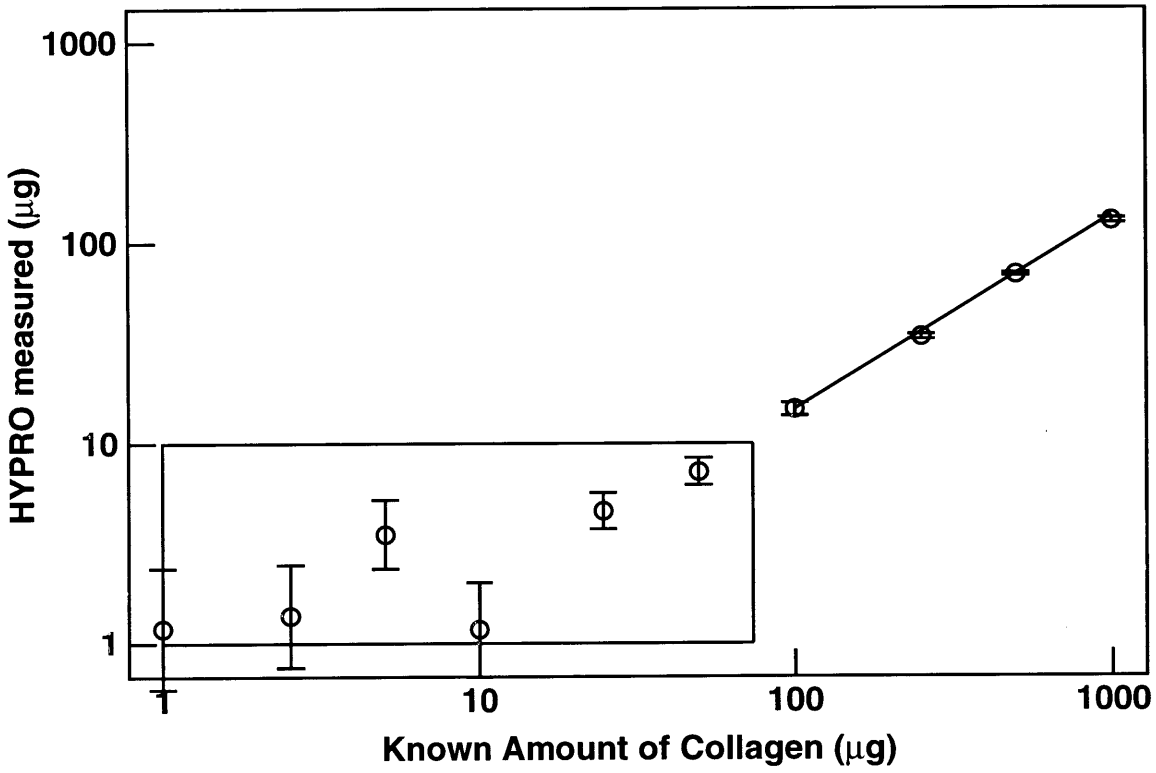

Figure C.5: Scatterplot of the HYPRO measured versus its known collagen content. The lower bound of the sensitivity of the method was determined to be $\sim 100 \mu g/ml$ of type II collagen or $\sim 10 \mu g/ml$ of HYPRO. The samples included in the boxed area were insufficiently resolved using this method. The samples in the range of 100-1000 $\mu g/ml$ collagen content were used to establish that the ratio of collagen to HYPRO at ~ 7.4 for this assay (straight line).

Appendix D

Development of a Arthroscopic *In Vivo* Electrokinetic Surface Probe - Details

D.1 Hand Held Version 5.0 Probe

Figure D.1 present a detailed dimensional drawing of the probe parts discussed and shown in Figure 5.1.

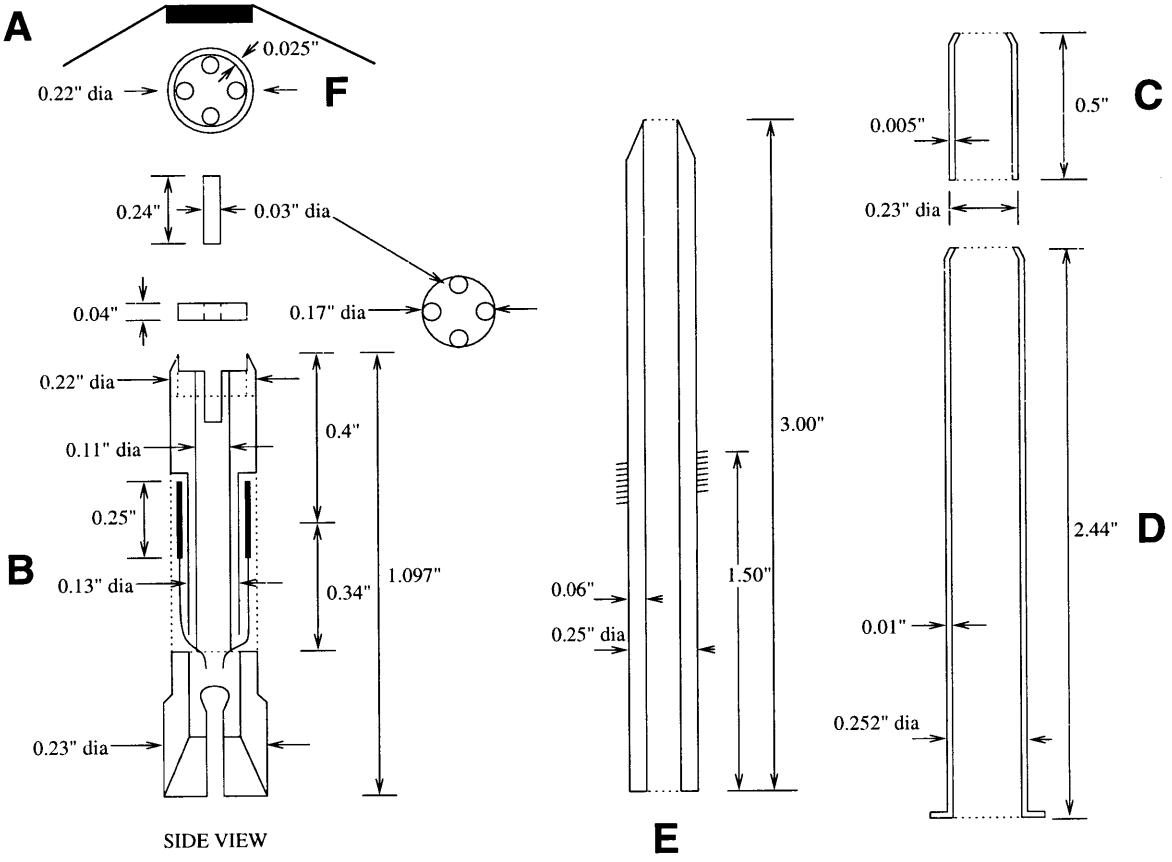

Figure D.1: Dimensioned drawing of the components of the HHV5.0 probe: (A) the ETS, (B) inner core, (C) torlon sheath, (D) stainless steel tube, (E) screwed pusher/plunger, and (F) recess for backing plate in the inner core [Courtesy E. Quan [187]].

D.2 Design Iterations of ETS Electrode Patterns

The first design of the HHV5.0 ETS electrodes had piezo electrodes which made contact with the brass rods through four 0.03 inch diameter circular extensions Figure D.2, and the total active area of each piezo electrode was 0.63 mm^2.

The second design of the HHV5.0 ETS electrodes took advantage of the empty areas not utilized by the smaller electrodes in the first design (Fig. 5.3). One significant change was the expansion of the top and bottom piezo electrodes to cover over the brass rods. This enabled both an increase in electrode area and the transfer of response signal to the brass contact. The overall area for each piezo and silver electrode was increased to 1.59 mm^2. The increased piezo area corresponded to increased signal output. The width of the connection between the silver electrode and silver arm was increased to prevent fracture and disconnection during the mounting phase when the arms are folded over the head of the probe. Also patterns to assist in the cutting of the ETS were placed on the masks (Fig. 5.3).

Figure D.2: First iteration of HHV5.0 ETS electrode patterns. Left - Piezo electrodes; Right - Silver electrodes. The piezo electrodes made contact with the brass rods through four 0.03 inch diameter circular extensions Figure D.2, and the total active area of each piezo electrode was 0.63 mm^2. The subsequent design took advantage of the empty areas not utilized by making the contact a subportion of the electrode, increasing the area per electrode. Compare to Figure 5.3.

D.3 Wavelength Calculation For Circular Electrodes

For earlier *in vitro* probe designs with rectangular electrodes, the wavelength is twice the center-to-center spacing. For the hemispherical shape of the electrodes of the HHV4.0 and HHV5.0, the centroids of the areas are used to estimate the spatial wavelength. The following expression is applicable for calculating the centroids of area A_1 in Figure D.3).

$$\bar{x} = \frac{\int_{A_1} x dA}{\int_{A_1} dA} = \frac{2 \int_0^{Rsin\theta} \int_{Rsin\theta}^{\sqrt{R^2-y^2}} x dx dy}{2 \int_0^{Rsin\theta} \int_{Rsin\theta}^{\sqrt{R^2-y^2}} dx dy} = \frac{2}{3} \frac{R\ sin^3\theta}{[\theta\ -\ sin\theta\ cos\theta]} \tag{D.1}$$

where for the limit where $\theta \rightarrow \frac{\pi}{2}$ then $\bar{x} \rightarrow \frac{4R}{3\pi}$, which is consistent with the centroid for a half circle and for $\theta \rightarrow 0$ then $\bar{x} \rightarrow R$ for an infinitely small electrode at radius R. For compound areas, i.e. A_1 and A_2 in Figure D.3, the following well known expression can be used to combine centroids:

$$\bar{x} = \frac{A_1\ \bar{x}_1\ +\ A_2\ \bar{x}_2}{A_1\ +\ A_2} \tag{D.2}$$

parameter	unit	HHV4.0	HHV5.0	
			Version 1	Version 2
w_1	mm	-	0.00	0.46
l	mm	4.90	1.96	2.29
w	mm	-	0.32	0.70
g	mm	-	0.32	0.35
A_{total}	mm^2	14.66	2.53	6.38
A_{sing}	mm^2	7.33	0.63	1.59
λ_{12}	mm	5.34	1.35	2.10
λ_{23}	mm	-	1.28	2.09
λ_{14}	mm	-	3.98	6.30

Table D.1: A comparison of the design parameters for the various probe designs, along with the resultant wavelengths. HHV4.o was not a multiple wavelength probe. The design of HHV5.0 was always constrained that each of the four electrodes had the same area.

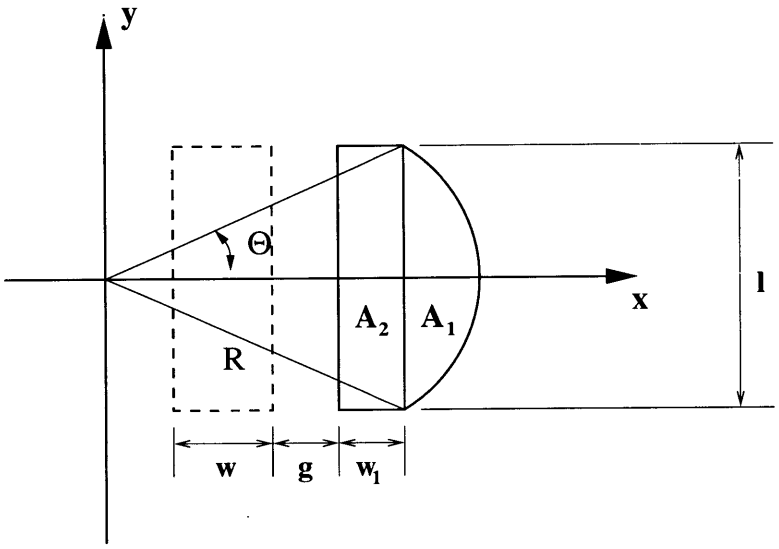

Figure D.3: A schematic layout of the HHV5.0 and HHV4.0 for design purposes, used in Table D.1. The areas (A_1 and A_2), and lengths (w,g,w_1,l) are adjustable parameters in electrode design.

Appendix E

Intrinsic Parameter Estimation Based on Electromechanical Surface Spectroscopy Measurements

E.1 Introduction

With the electrokinetic probe measurements to date, current-generated stress (CGS) magnitude was used as an indication for changes in the ECM such as the loss of PGs or damage to type II collagen molecules [16, 227]. Ultimately, the CGS response is controlled by the intrinsic properties of the material that can be described by a model of cartilage as an electromechanically coupled poroelastic medium [200]. Using a parameter estimation scheme (or solving the "inverse" problem) to get the intrinsic physical properties of the tissue from the spectroscopic CGS measurements may yield are more specific and sensitive diagnostic method of interpreting the state of tissue. The system outlined in this appendix allows one to investigate the feasibility of this approach.

The objectives was to use CGS from the electrokinetic surface probe measurements to infer the intrinsic material properties of articular cartilage and to validate the results by comparing to properties measured on excised tissue via confined compression (CC). A idealized chamber system has been developed in which both measurements can be performed simultaneously on newborn bovine articular cartilage samples. The duality of the physical system, due to coupling of the mechanical and electrical domains, allows the experiments to be compared in two ways: (1) the parameters obtained from confined compression tests can be used to estimate the expected CGS, which is then compared to the measured CGS; or (2) the parameter estimation algorithm can be used with the spectroscopic CGS data to solve for the

intrinsic parameters, which are then compared to values obtained from the confined compression study (Figure E.1).

The state of cartilage can be changed by treating it with enzymes that degrade ECM constituents, or by using cartilage from an aged donor (Figure 1.10). The confined compression test result in physical property measurements of static and dynamic stiffnesses, and streaming potentials.The surface probe measurements give current generated stress data. These data along with an appropriate continuum model of cartilage electromechanics in each system, can be used to estimate the material properties of the tissue. Thus study will investigate the applicability of the current available models, by validating the physical property measurements from both experiments *.

E.2 Material and Methods

E.2.1 Electrokinetic Probe Fabrication

The electrokinetic surface probe construction is described in detail elsewhere [13]. In this case, only the size of the laminates, adhesives, and the electrodes patterns are different. The silver foil (25.4 μm thick) is cut into pieces 68 x 28 mm, metallized Mylar (25.4 μm thick) into 70 x 32 mm, and the stress sensor Kynar film into 70 x 18 mm, with a sharp blade, and straight edge. The laminated structure is formed by first bonding the metallized surface of the mylar to the PVDF film using a thin film adhesive (PM212, Norwood Industries Inc., Frazer, PA). The Kynar film overlaps one end of the Mylar by 4 mm to allow connection to a ground plane when mounted in the test chamber. Next the silver is bonded to the non-metallized side of the Mylar using Tycel epoxy. The ETS is pressed together firmly and then allowed to cure overnight to ensure proper bonding (Figure E.2).

The photofabrication process is similar to that previously described, except

*A more detailed description of these experiments appear in Batra [10]

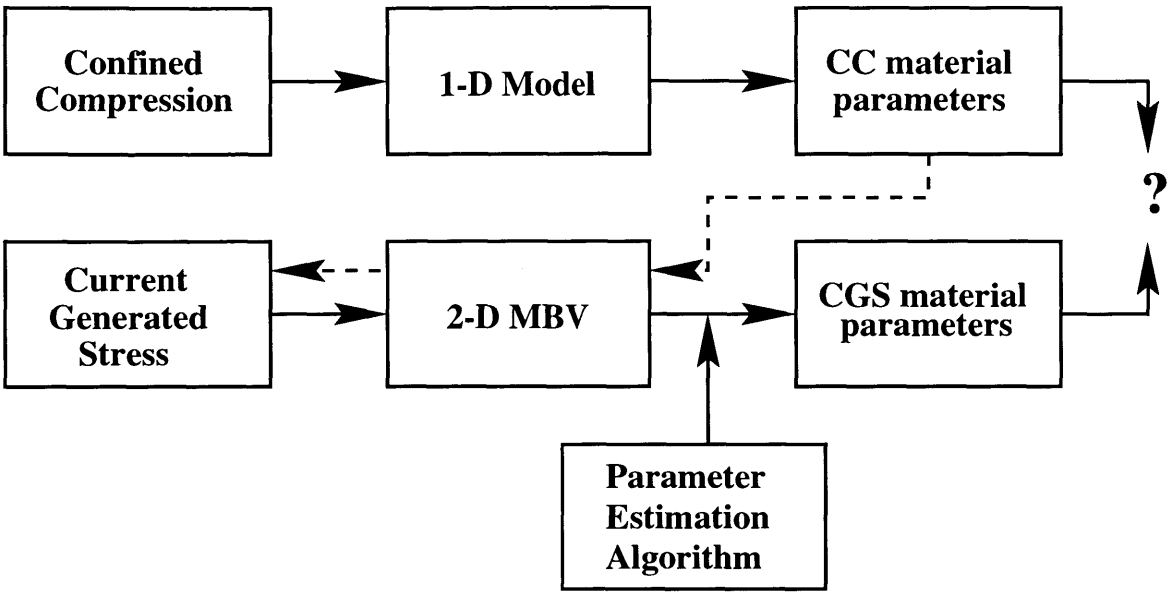

Figure E.1: Schematic of modeling and fitting performed to yield material parameters using both CC and CGS data. The CC data are inputs into a 1-D model which utilizes the uniaxial configuration used during testing. The probe measurements give data in the form of current-generated stress. The aspect ratio of the probe electrodes with respect to the cartilage approximates a two-dimensional geometry where a 2-D multi-boundary value problem is appropriate. Both techniques are used to estimate the material properties of cartilage and can be compared. In addition, the parameters estimated by the CC model can be used as inputs into the 2-D MBV and the expected CGS can be computed and compared to the measured CGS.

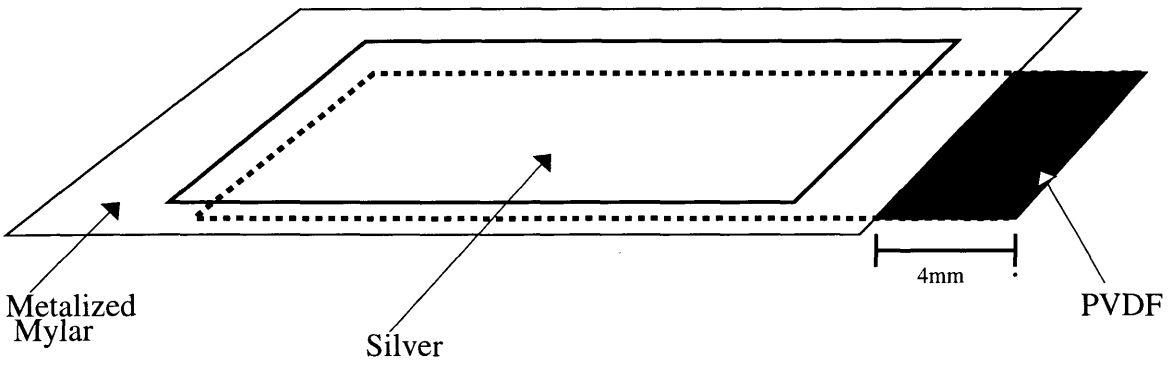

Figure E.2: Schematic of the different layers of the ETS structure. The 4mm overlap of the Kynar film is used for grounding in the test chamber.

the electrode patterns are significantly different. On the silver side, the electrode structure consists of two inner rectangular electrodes, measuring 1 x 10 mm each, used for applying current, and two hemispherical shaped electrodes are used as the ground electrodes for measuring streaming potentials during the confined compression tests. Only the inner electrode pattern need be identically registered on the Kynar side (Figure E.3).

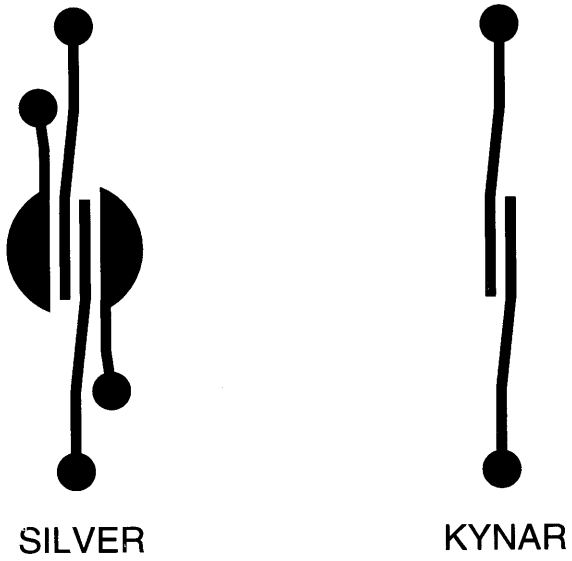

Figure E.3: Electrode patterns on the silver (right) and Kynar (left) sides of the ETS. The inner electrodes on both the silver and Kynar sides are used for applying current and measuring sensor voltage output, respectively. The hemispherical outer electrodes on the silver side are used for measuring streaming potentials during CC testing.

E.2.2 Experimental Chamber

It is patterning of the ground electrodes for CC on the probe, that has allowed for both experiments to be performed on a cartilage sample, in the custom designed chamber of Figure E.4. The silver electrode pads are connected to the current source via spring loaded copper pads which are in contact with copper leads that screw into the side of the chamber. The kynar electrode pads lie on top of copper pads which

are accessed from the bottom of the lower part of the chamber. The upper and lower parts of the chamber are secured, with the ETS pressed in between. The chamber allows 13.5 mm diameter cartilage discs to be placed on top of the Ag/AgCl electrodes in a confined arrangement.

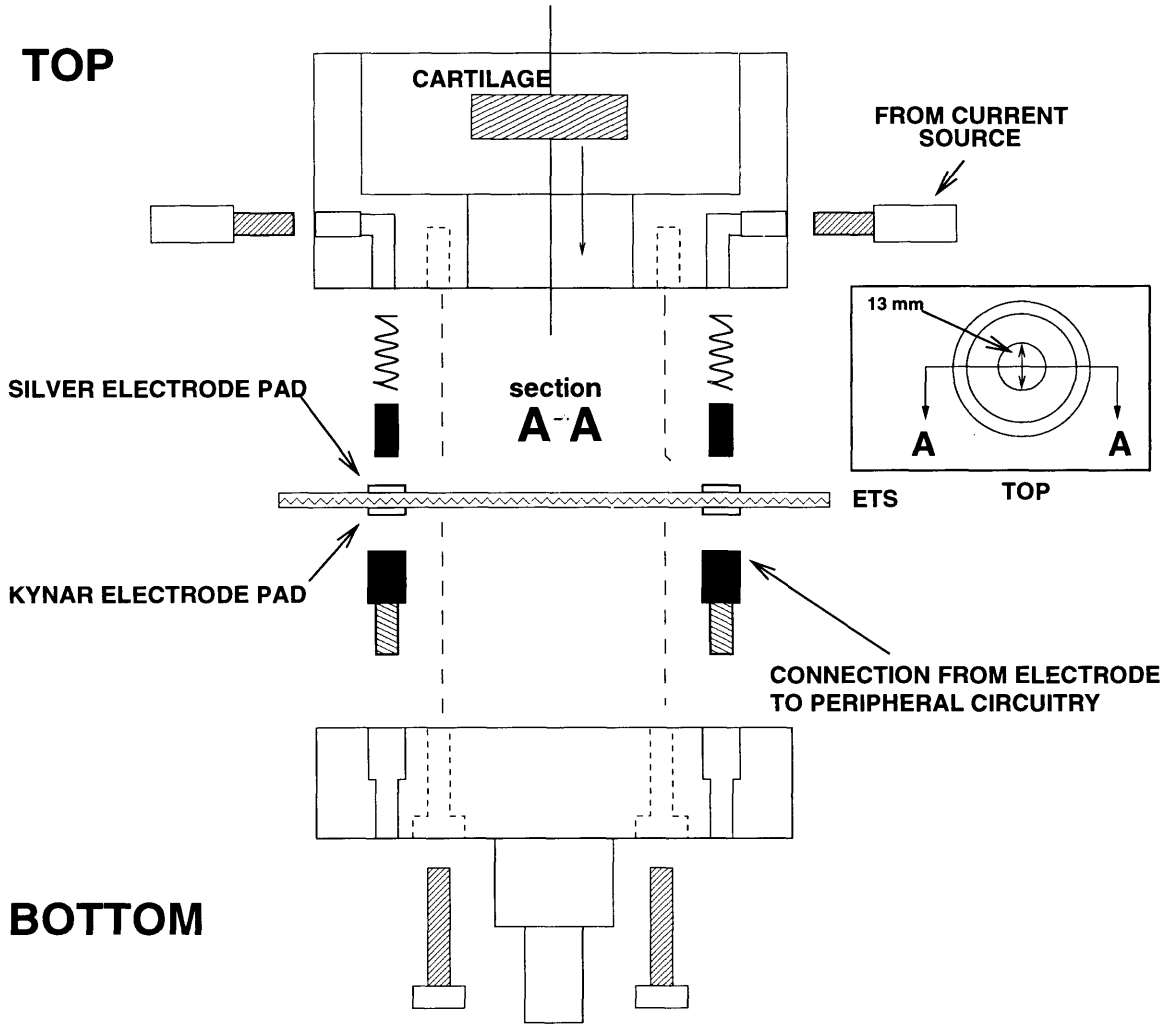

Figure E.4: Cross sectional view showing all relevant connections of the upper and lower parts of the PMMA confining chamber with the ETS mounted in between. Inset - Top view of the upper part of the PMMA confining chamber.

E.2.3 Cartilage Explants

Cartilage discs were taken from the femoropatellar groove of calfs (Figure E.5A) (1-2 weeks old) on the day of slaughter (Research 87, Hopkington, MA). The femoropatellar groove was exposed (Figure E.5B), and then sections were removed along with the underlying bone from the distal femur using a fine toothed saw. The groove was then cut in half between the superior and inferior ends (Figure E.5C). Each half was then mounted in sledge microtome holder with the sample clamped in place by the subchondral bone. A portion of the surface cartilage was sliced away by the microtome in order to achieve a flat planar profile. Once this was achieved, a 0.5-2 mm thick slice was removed. This process was repeated for the other half of the groove, to yield as many as four 1 mm thick slices (two from each half of the groove). Discs of 13.5 mm in diameter were punched out of the slices using a stainless steel punch. At all stages of the cutting, sterilized tools were used in addition to bathing the cartilage with sterile phosphate buffered saline at pH 7.0, with a penicillin, streptomycin and anti-fungal additive to prevent bacterial infection that may effect material properties.

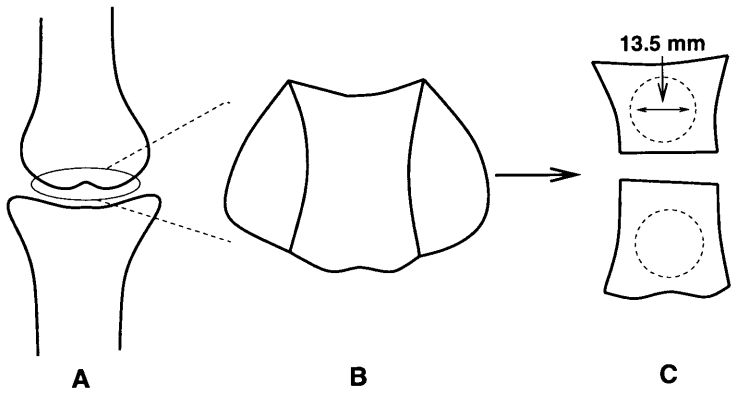

Figure E.5: Cartilage explant process; (A) Femoropatellar groove is exposed. (B) The groove and underlying bone are removed. (B) The groove is halved and sliced to yield 2 slices of cartilage from which 13.5 mm discs are punched using a stainless steel punch.

Calf cartilage was used because of the thickness of the cartilage in the femoropatellar groove (up to 4mm), which facilitates the excision of the larger 13.5

mm discs, and because of its more homogeneous material properties with respect to skeletally mature tissue [13]. The geometry and experimental set up have been designed to maximize the number of known parameters in this homogeneous system to facilitate testing the effectiveness of existing electrokinetic models which describe the observed CC and CGS responses.

E.2.4 Confined Compression Testing

An excised 13.5 mm cartilage disc (with the thickness determined with a current sensing micrometer) was placed in the custom designed PMMA chamber (Figure E.4). The chamber was mounted in the collet of a servo controlled materials testing machine, or Dynastat mechanical spectrometer (IMASS, Hingham, MA). A porous platen (ultra high molecular weight polyethylene with 20 μm pore size, Porex Technologies, Fairburn, GA) was placed above the sample and NaCl buffer (0.1 M NaCl, 0.05 M Trizma, pH 7.4) was added to the chamber (Figure E.6). Incremental strains (1-3% at a time) up to 9-15% were imposed on the sample, and the resultant stress relaxation data was recorded by a data acquisition system. The percent strain imposed depended on the disc used, but in general a 200-500 g static offset was desired for performing dynamic displacements and probe measurements. The offset load was noted for later calibration of the piezo film. Dynamic displacements (typical amplitude of 0.4-0.5% strain) were performed around this static offset at frequencies ranging from 0.01 - 1 Hz.

E.2.5 Current-Generated Stress

After the dynamic strains are imposed, the connections were switched to those appropriate for CGS measurements. For a detailed description of the peripheral electronics see [13]. A 1 mA/cm^2 current density or 100 μA current was applied to the sample at frequencies of 0.025, 0.05, 0.1, 0.25, 0.5, and 1 Hz, while the sample was compressed at the same static offset strain as the dynamic displacements. Afterwards,

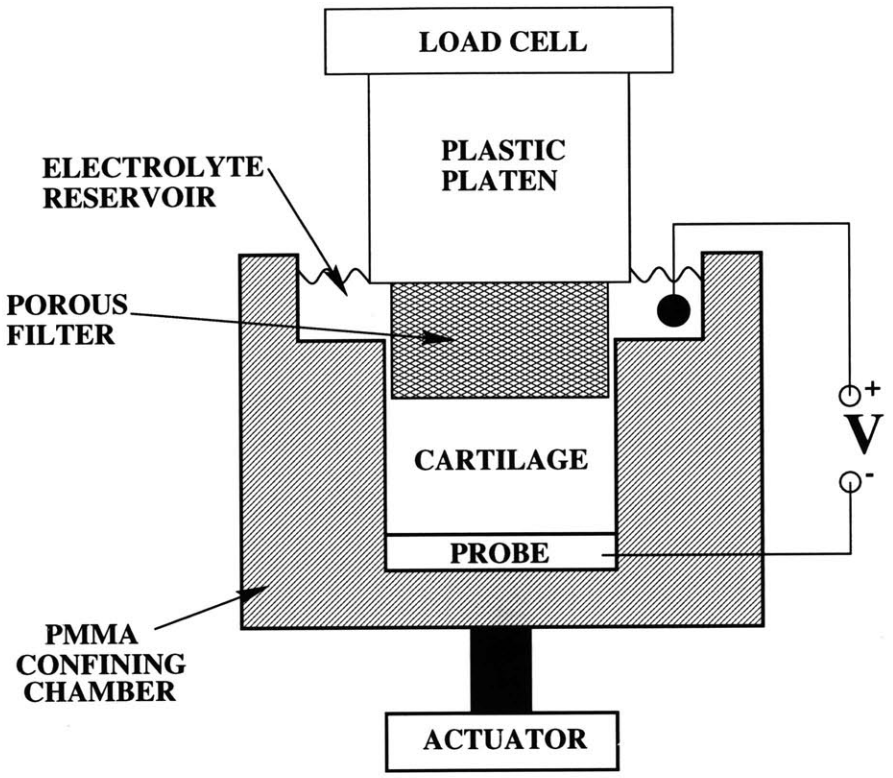

Figure E.6: Figure showing the set up for CC and CGS measurements. The cartilage is placed above the probe in the PMMA confining chamber. A porous platen is placed on top of the sample and the chamber is filled with 0.15M Trizma/NaCl buffer. The chamber is mounted in the Dynastat, which imposes strains with a servo controlled actuator and measures stresses via a load cell placed in contact with the porous platen. Streaming potentials are measured from a platinum electrode submerged in the electrolyte bath and grounded to the large Ag/AgCl electrodes fabricated onto the probe.

the connections were switched back to the confined compression set-up, and incremental strains up to 25-30% or 1 kg load were applied to obtain a more complete equilibrium stress-strain profile of the tested sample.

E.2.6 Piezo Calibration

Since each ETS structure has a different stress voltage relationship and a single ETS may change over time, it is necessary to determine this relationship between applied stress and measured voltage for the Kynar film after each experiment. This relation-

ship is linear, with the applied sinusoidal stress and measured voltage of the same frequency, but out of phase. The transfer function that defines this relationship is determined by applying stresses of known amplitude and frequency, and measuring the piezo sensor output. The previous experimental static offset stress is applied to the film, and then dynamic stresses of 10 and 2.5 kPa are applied around the static offset at frequencies of 0.025, 0.05, 0.01, 0.25, 0.5, and 1.0 Hz. The magnitude and phase of the voltage response are used to determine the transfer function (Figure E.7).

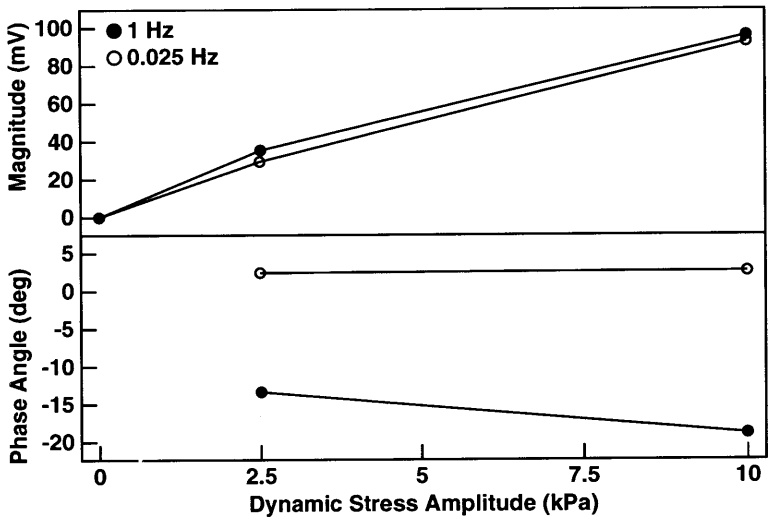

Figure E.7: Typical piezo calibration plot, showing magnitude and phase for either electrode (left or right) for lowest and highest frequency (others in between). Here the calibration is approximately 10 mV/kPa for each Kynar electrode both pads at all frequencies.

E.2.7 Biochemical Compositional Analysis

After the CC and CGS measurements were complete, a wet weight of the sample was taken by first cutting the cartilage disc into 1/8ths due to its large size, and weighing each section on a digital balance after removing surface water. The eight sample sections were then placed in individual cryovials and freeze dried in a lyophilizer. Dry weights of the freeze dried sections were taken after which they were digested with 1-2 ml of papain (0.125 mg/ml). The papain digests were assayed for sulfated gly-

cosaminoglycan (sGAG) content by the DMMB dye binding assay [61], and collagen by a calorimetric assay for hydroxyproline [244] on each of the eight disc sections. An average of all eight sections was performed to obtain a value for the cartilage sample tested.

E.3 Theoretical Considerations - Modeling and Parameter Estimation

E.3.1 Relevant Parameters

The idealized chamber system allows estimation or measurement of almost all the parameters relevant to the model independently [200]. The parameters involved in using the existing linear model of CGS fall into the following categories:

- geometrical
  - the thickness (δ) of the sample is measured directly using a current sensing measurement device and thus a fixed parameter in the analysis.
- mechanical
  - the aggregate modulus (H_A) is estimated using the stress strain behavior during confined compression (fixed in analysis).
  - the hydraulic permeability (k_p) can be estimated by analyzing the stiffness vs. frequency behavior in dynamic confined.
  - Poisson's ratio (ν) is not directly measurable in our system since it is a confined compression setup, but has been measured by other investigators [118], using various methods, to be approximately 0.1 for immature bovine (calf) tissue (fixed in analysis).
- electrical

– the electrical conductivity (k_{22}) can be estimated from the sGAG content by the following procedure:

The sGAG assay gives information about the concentration of proteoglycans and thus can be related to the fixed charge density of the tissue by:

$$\frac{\rho_m}{F} = \beta\, C_{pg} \tag{E.1}$$

where ρ_m is the macrocontinuum fixed charge density, is F Faraday's constant, β is a constant relating the amount of charge per gram of proteoglycan, and C_{pg} is the concentration of proteoglycan [30]. We can calculate $\frac{\rho_m}{F}$ since we know that $\beta = 1$ mole-charge/266g, and $C_{pg} = \frac{amount\ GAG\ (mg)}{water\ vol\ (ml)}$. The tissue water volume is calculated using the wet and dry weights and corrected for the strain at which CGS measurements were taken. The electrical conductivity of cartilage, k_{22}, is dependent on the intratissue concentrations of sodium and chloride ions, the predominant mobile charged species. The conductivity of a binary electrolyte solution is given by:

$$k_{22} = F\left[\left|z^+\right| u^+ c^+ + \left|z^-\right| u^- c^-\right] \tag{E.2}$$

where z, u, and c are the valences, ionic mobilities, and concentrations of the cations and anions within the tissue. We know that $|z^+| = |z^-| = 1$ for NaCl, and the ionic mobilities of sodium and chloride are 1.8 x 10-4 cm^2/Vs and 2.7 x 10-4 cm^2/Vs, respectively. From Donnan equilibrium we can also relate the concentrations of the cations and anions to the fixed charge density as follows:

$$c_\pm = \mp\frac{\rho_m}{F} + \sqrt{\frac{\rho_m}{F}^2 + c_b^2} \tag{E.3}$$

where c_b is the concentration of the electrolyte bath (0.15 M for our experiments). From the amount of GAG we can determine the fixed charge

density; from the fixed charge density we can calculate the concentrations of sodium and chloride ions in the tissue; from these concentrations we can then solve for the electrical conductivity, k_{22} (fixed in analysis).

- electromechanical
  - the electrokinetic coupling coefficient (k_e) can not be measured directly. This is the key parameter in the system since it is the coupling of the mechanical and electrical domains of the system. k_e is similar to k_p in that it is a fit parameter in the model.
- biochemical
  - the porosity (ϕ) is determined by knowing the water content of the tissue from the wet and dry weights, and adjusting for the strained conditions when the measurements were taken (fixed in analysis).

E.3.2 Response of the CGS Model to Parameter Changes

The appropriate existing model for this physical situation is a two dimensional model of a linear electromechanically coupled poroelastic medium, for which a numerical solution exists. In solving the inverse problem, a parameter estimation technique [139, 163] in conjunction with the model is used to estimate model parameters.

To get a sense of the sensitivity of CGS to variations in the model parameters in a physically relevant range, simulations were performed [†].

Since Poisson's ratio is not directly measurable in this system, an approximation for the calf cartilage often used is 0.1 [118]. Figure E.8 shows that the CGS is fairly constant over a wide range in Poisson's ratio, justifying constraining its value in the analysis of experiments.

[†]A more detailed discussion can be found in Appendix F

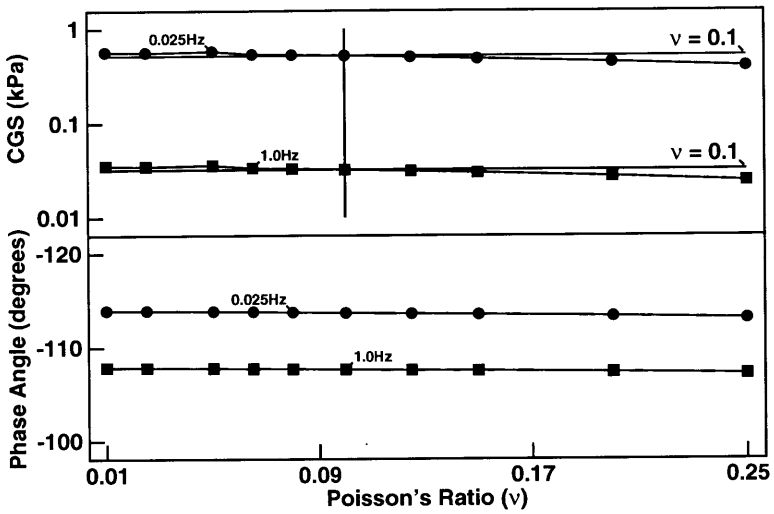

Figure E.8: Dependency of model CGS prediction on varying Poisson's ratio from 0.01 to 0.25. The boundary conditions are identical to those from the actual experiment (reflecting boundary at y = 4.87 mm, 1 electrode pair, spacing and width=1 mm), the cartilage thickness was set at 2 mm, applied current density of 1 mA/cm^2; the porosity, k_{22}, k_e, and the aggregate modulus H_A were also set at 0.71, 0.94 S/m, 9.0 mV/kPa, 3.0 μm/s)/(MPa/mm), and 0.6 MPa respectively. Varying Poisson's ratio does not significantly change the predicted CGS with respect to 0.1.

The effect on CGS of varying the aggregate modulus H_A, permeability k_p, or electromechanical coupling coefficient k_e is shown in Figure E.9 while keeping all other parameters fixed. The magnitude of the CGS increases directly with increasing H_A, decreases with increasing k_p, and increases with increasing k_e. The large changes in the phase only with H_A.

E.4 Preliminary Experimental Results

E.4.1 Results From a Typical Experiment

A typical experiment consists of performing static and dynamic confined compression tests, switching to the CGS set up and performing probe measurements, and then completing the static confined compression data acquisition. The typical time course of an experiment is best shown in Figure E.10.

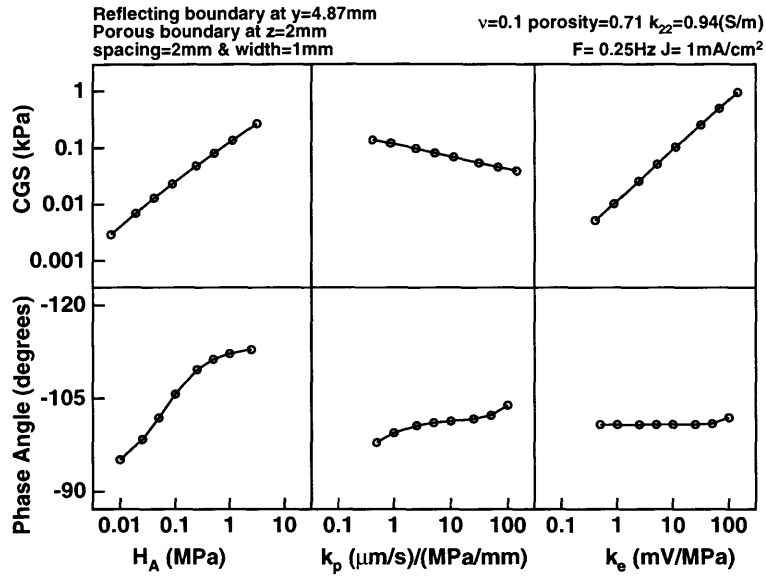

Figure E.9: The effect on CGS of varying the aggregate modulus H_A, permeability k_p, or electromechanical coupling coefficient k_e at an applied current density frequency of 0.25 Hz (the behavior is similar for other frequencies). Note that increasing H_A and k_e results in an increase in CGS magnitude, while increasing k_p has the inverse effect. The phase becomes more negative for increasing H_A and k_p, but does not change significantly for variations in k_e.

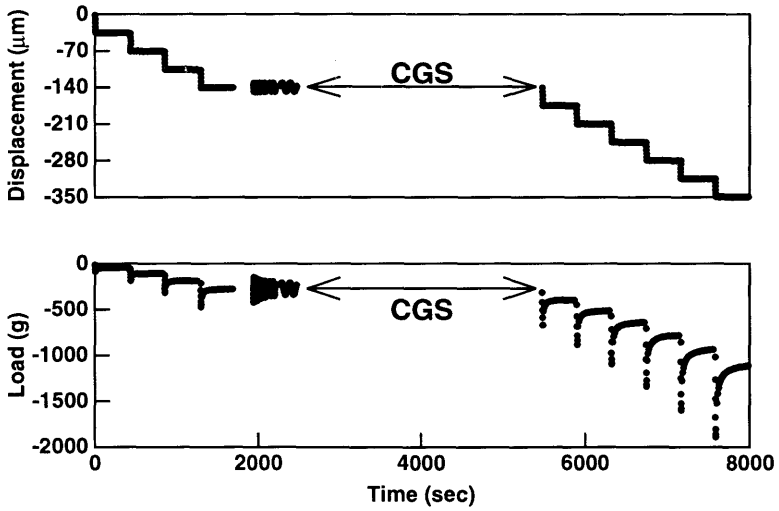

Figure E.10: Plot of displacement and load during a typical experiment. The time course is as follows: step displacements up to experimental offset stress with stress relaxation, dynamic displacements, CGS measurements, and step displacements to complete static CC data acquisition. Values are negative since positive displacement is defined as tension.

E.4.2 Confined Compression Results

From the static confined compression data we are able to estimate the aggregate modulus from the stress vs. strain curve (Figure E.11). H_A is the slope of the curve around the static offset strain used for dynamic displacements and probe measurements. The results of the dynamic CC testing are presented in Figures E.12. The stiffness vs. frequency data and the streaming potential vs. frequency data are shown along with the fitting results from the 1-D Model using previously established methods [67,68]. From the fitting we are able to estimate k_p and k_e. The phase data for the streaming potential is not used in the fitting, which explains the discrepancy between the data points and the fit line in the phase plots.

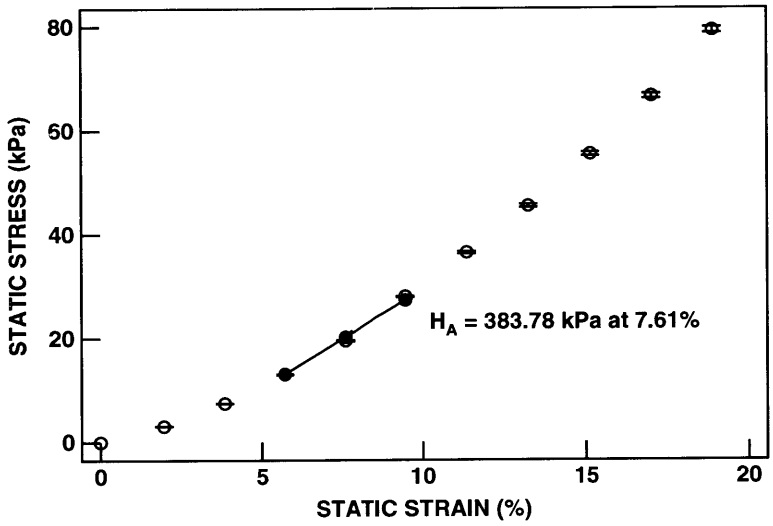

Figure E.11: Stress strain behavior of cartilage. In this experiment, the experimental offset strain was 7.61%. H_A is calculated by the slope of the curve around this offset.

E.4.3 CGS and Parameter Estimation Results

The current-generated stress data and fitting results are shown in Figures E.13 and E.14. The experimental CGS magnitude data and the magnitude predicted by applying the parameter estimation algorithm coincide very well with each other (Figure E.14). For the experiment shown, the MBV fitting gives a k_p of 1.64

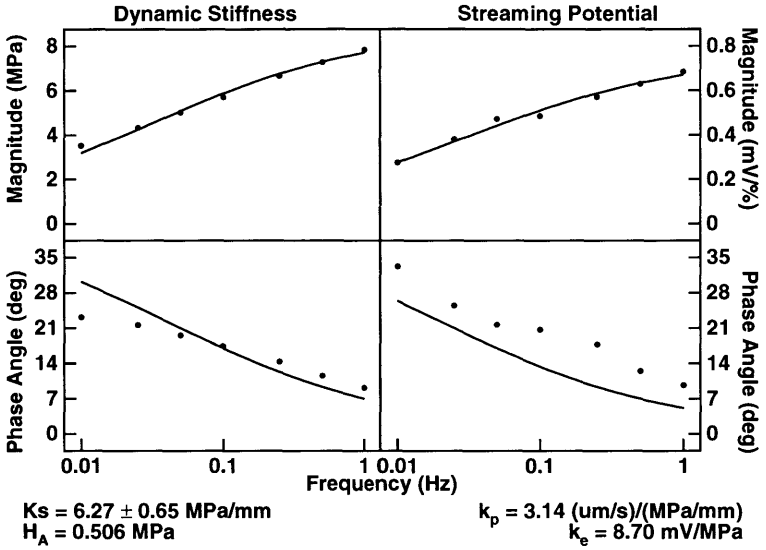

Figure E.12: Plot showing the dynamic stiffness and streaming potential versus frequency results for a typical experiment. The free parameters in the model used to fit the data (dots) are k_p, k_e, and H_A. Ks is a stiffness assigned to the porous platen which contributes to the overall stiffness sensed by the load cell. The modulus, H_A, shown above is a free parameter in the fitting, and is different from the value obtained from the stress strain behavior, because it is fitted allowing for the contribution of electrokinetic effects rather than the classical equilibrium modulus. The phase angle data for the streaming potential is not used in the model fitting, as a result there is a slight discrepancy between the fit curve and data.

(μm/s)/(MPa/mm), which is very close to the value of 3.150 obtained from the fitting of the dynamic CC data. However, the value of k_e = 22.65 mV/kPa obtained from the MBV fitting is more than two times the value of k_e = 8.700 obtained from the CC fitting. Figure E.14 also shows the CGS predicted by the MBV model when the parameters estimated by the CC fitting are used as inputs (see Figure E.1). The plot shows that, for this experiment, the predicted CGS, using the CC parameters as inputs into the MBV, underestimates the observed CGS data, due to the lower predicted k_e.

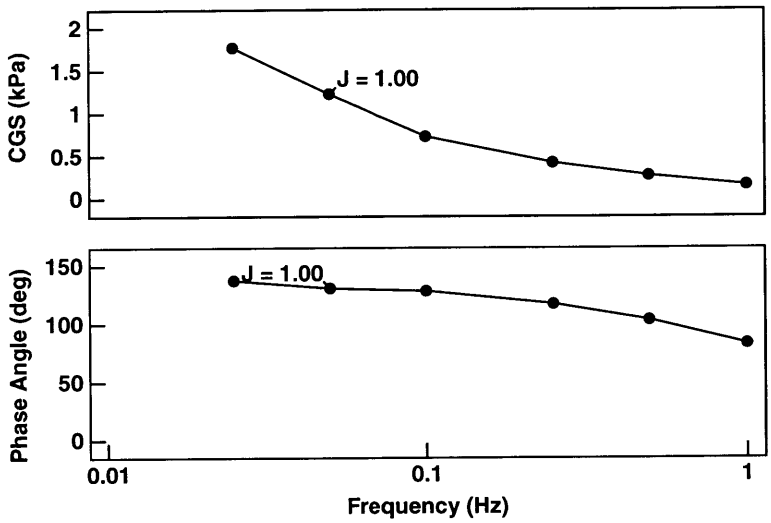

Figure E.13: Plot of current-generated stress vs. frequency for the same experiment shown in Figure E.12. A current density of 1.00 (mA/cm^2) was applied at frequencies of 0.025, 0.05, 0.1, 0.25, 0.5, and 1 Hz. This data is a result of applying the calibration as discussed.

E.4.4 Summary of Results

A summary of the results of the six experiments performed thus far is in Table E.1. The thicknesses in these experiments ranged from 1 mm to 3 mm, while the experimental strain varied from 4% to 17% compression. Values of the porosity and k_{22} were obtained from biochemical analysis. The values of H_A shown in the table were determined from the stress strain behavior of the AC disc. While the values predicted by the two approaches are within an order of magnitude, there is not a good quantitative agreement between the values. The k_e from the CGS fitting is consistently higher than that predicted by the CC results. This could be an explanation for the fact that the predicted CGS, using the CC parameters as inputs, always underestimates the observed and MBV fitted CGS, since smaller values of k_e lead to a smaller CGS magnitude (Figure E.9). Since the k_e determined from the CC tests are always smaller than those obtained from the CGS fitting, when these values are used as inputs in the MBV which predicts the expected CGS, it always underestimates the observed data. The results in Table E.1 show a consistent trend of the differences in k_p and k_e

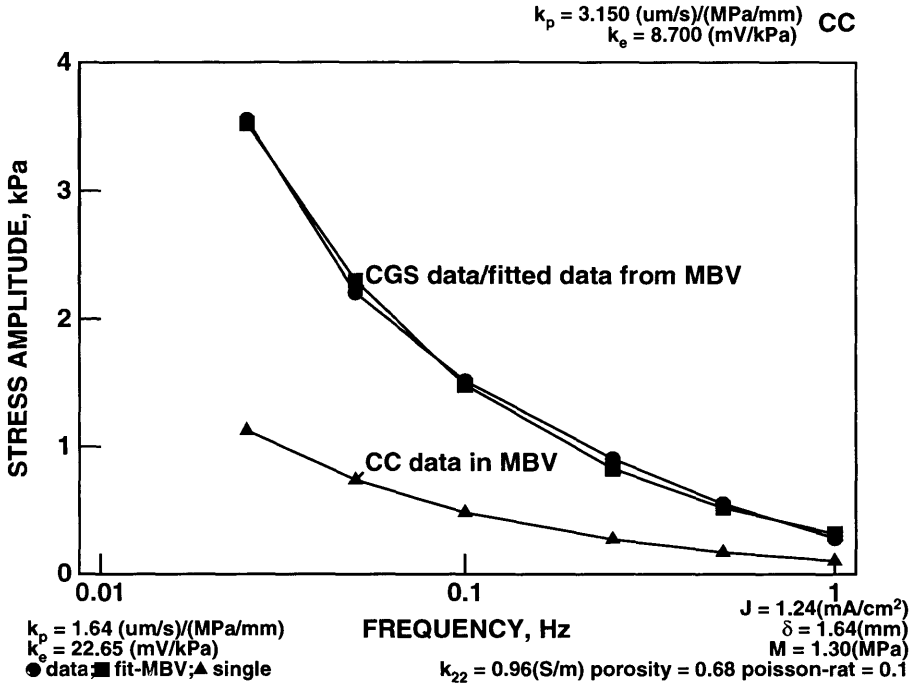

Figure E.14: Typical parameter estimation results and predicted CGS compared to observed CGS. The predicted CGS (filled squares) agrees well with the observed CGS (filled circles). In this particular experiment the k_p value obtained from the fit matches the k_p obtained from the CC results well. However, the MBV k_e is higher than the CC k_e. In addition, if the k_p and k_e obtained from CC are used in the computational model, the expected current-generated stress (filled triangles) is less than the observed CGS, due to the predicted k_e.

obtained from the two different diagnostic approaches.

E.5 Discussion

The preliminary results indicate that the parameters obtained from the CC tests are consistently different than those obtained from CGS measurements. First, since the CC and CGS measurements produce very different profiles of strain, pressure, fluid velocity, etc., it is not clear that the assumptions of infinitesimal strain and linearity the existing model require are satisfied equivalently in both experiments as performed. The effect of consolidation, finite deformation, and a non-linear strain profile must

exp	thickness	strain	porosity	k_{22}	H_A	CC		CGS-PE	
	mm	(%)		(S/m)	MPa	k_p	k_e	k_p	k_e
1	1.64	-14.0	0.676	0.962	1.30	3.15	8.66	1.64	22.65
2	1.07	-16.9	0.686	0.871	0.40	7.96	12.40	47.81	67.65
3	2.70	-9.0	0.737	0.922	0.83	3.63	13.73	45.18	177.66
4	2.50	-11.6	0.702	0.938	0.49	20.67	9.95	49.36	47.92
5	2.31	-3.9	0.754	0.993	1.05	13.99	8.73	2.91	9.30
6	1.85	-7.6	0.721	0.966	0.38	8.21	8.68	2.86	18.56

Table E.1: The results of six experiments performed. The thicknesses in these experiments ranged from 1 mm to 3 mm, while the experimental strain varied from 4% to 17% compression. Values of the porosity and k_{22}, the electrical conductivity, which were obtained from biochemical analysis of the sample following the experiment are also shown. The values of H_A shown in the table were determined from the stress strain behavior of the AC disc. A current density of 1.00 mA/cm^2 was applied the cartilage in all but the first experiment in which 1.24 mA/cm^2 was applied. k_p (μm/s)/(MPa/mm); k_e (mV/kPa).

be considered when extending the existing models for a more realistic interpretation of these results. For example, at higher frequencies, the majority of the strain is occurring near the cartilage surface, thus the calculated k_p is a localized permeability, and does not reflect the "bulk" permeability of the entire tissue. Whereas, the application of current may not induce such a non-linear strain profile, and as a result the calculated k_p may better represent the aggregate or "bulk" permeability. This suggests that it is not clear that one should expect identical parameter values from the both, CC and CGS measurements.

Experimentally, the discrepancies could suggest a problem with the voltage signal coming from the piezo film. This could be due to parasitic capacitance from incomplete shielding by the metallized Mylar layer or stresses induced on the Kynar film by the thin silver electrodes deforming as current is driven to the cartilage (E. H. Frank, personal communication). Other factors contributing to the discrepancies may arise from modeling issues. In our modeling, we assume only normal stresses are sensed by the ETS at the cartilage-probe interface. However, there may be other stresses (shear) that are developed when current is applied which could contribute to

the piezo signal. Another possibility is that the linear model we use for CC and CGS analysis is inappropriate and more detailed nonlinear model may be required.

More experiments need to be done to fully characterize the parameter discrepancies resulting from the two diagnostic techniques. In addition, impedance measurements can also be incorporated (to determine k_{22}) and include the phase angle data in the modeling.

The ultimate goal is to estimate cartilage physical properties from probe measurements (CGS and impedance) to be a more sensitive diagnostic tool. In the *in vivo* system all the relevant parameters will not be accessible (i.e. thickness or sGAG content), thus the ability of the model to estimate parameters accurately can be assessed in this idealized system. Extensions to a non-homogeneous or mature cartilage system are possible to mimic a more relevant clinical application of such probe measurements since adult bovine and human cartilage has been shown to be non-homogeneous with depth and along a joint surface [226]. A more complex mathematical model (finite element model) would be needed to properly capture this behavior.

Appendix F

Development of an Analytical Approximation to CGS Using a Dimensional Analysis Technique

F.1 Introduction

Dimensional Analysis (DA) is a technique that can be used to plan experiments, present data compactly, and even in theoretical studies [243]. In essence, it reduces the number and complexity of variables which are chosen to affect a particular physical phenomena under study. At minimum, the number of variables (n) will be reduced by the number of fundamental dimensions involved (k). In the case of electromechanical problems, the fundamental units are mass M, length L, time T, and amperes A (or voltage V). DA has the potential to save time and money, by reducing the amount of experimental conditions needed to be tested when characterizing an empirical system, or by allowing one to create a approximate function between variables in a complex simulation (this is how it will be used in this application). It is powerful tool to investigate how independent variables affect dependent ones; in the trends and their strength. Whether the function dependence is linear, quadratic, etc, and it may clearly eliminate variables to which the analysis is not sensitive. For example, in aerodynamic applications, it also provides scaling laws where data from models can be inferred to a full scale prototype. DA began with writings by Euler in 1765, and culminated in the Buckingham pi theorem published in 1914. Controversy rages until today (with tens of books published on the topic) due to the subtlety and art of DA, while mathematicians search for more rigorous approaches [215].

The technique is based on the principle of dimensional homogeneity, where all additive terms in a relationship will have the same dimensions if an equation is truly proper. Each of these equations can be written in an equivalent non-dimensional manner which will be more compact. It can't be overstated that, in general, the vari-

ables chosen to describe a complex physical situation require considerable judgment and experience.

In this application, DA will be used to find a functional dependence between current-generated stress (CGS) and impedance, and the intrinsic variables of the articular cartilage. A model to describe the phenomena of current-generated stress was developed by Sachs et al. [199], and extended to the practical case of finite sized electrodes by E. H. Frank [13]. The case of finite sized electrodes requires the computational solution of a complex mathematical multi-boundary value problem. The goal here was to use the computational solution along with DA to elucidate the functional dependence of CGS and impedance on the variables in the Sachs et al. model. This will result in a better physical understanding of the sensitivity of electrokinetic probe output to model parameters, and to find an approximate analytical solution to aid in understanding typical output expected based on known tissue parameters.

F.2 Current-Generated Stress

The current-generated stress can be written as the following functional dependence based on the variables from the model of Sachs et al.*:

$$\sigma = f\left(H_A, k_p, k_e, k_{22}, f, \nu, \phi, J, h\right) \tag{F.1}$$

where H_A is the equilibrium modulus, k_p the hydraulic permeability, k_e the electromechanical coupling coefficient, k_{22} the electrical conductivity, f the frequency, ν the Poisson's ratio, ϕ the porosity, J the applied current density, and h the thickness. Similar dependencies could be written for fluid velocity U, displacement u and pressure P. Using the MKS units system (plus amperes, A) the variables of interest have the following units ([] denotes dimensions of):

*For completeness, time, spatial variables, and wavelength (λ) could be added.

$$
\begin{aligned}
[H_A] = [\sigma] &= \left[\frac{kg}{m\ s^2}\right] \\
[k_p] &= \left[\frac{s\ m^3}{kg}\right] \\
[k_e] &= \left[\frac{m^3}{A\ s}\right] \\
[k_{22}] &= \left[\frac{A^2\ s^3}{m^2\ kg\ m}\right] \\
[f] &= \left[\frac{1}{s}\right] \\
[\phi] = [\nu] &= [1] \\
[J] &= \left[\frac{A}{m^2}\right] \\
[h] &= [m]
\end{aligned}
$$

There are 10 variables and 4 distinct units, therefore 6 dimensionless groups should result at the end of the analysis. Picking k_{22}, J, h and H_A as the variables, the following can be written by equating exponents for the case of k_e, and solving for the exponents to form the dimensionless group k_e^*:

$$
[k_e] = \left[\frac{m^3}{A\ s}\right] = \left[\frac{A^2\ s^3}{m^2\ kg\ m}\right]^a \left[\frac{kg}{m\ s^2}\right]^b \left[\frac{A}{m^2}\right]^c [m]^d \tag{F.2}
$$

$$
\begin{matrix} m: \\ s: \\ kg: \\ A: \end{matrix}
\begin{bmatrix} -3 & -1 & -2 & 1 \\ 3 & -2 & 0 & 0 \\ -1 & 1 & 0 & 0 \\ 2 & 0 & 1 & 0 \end{bmatrix}
\begin{bmatrix} a \\ b \\ c \\ d \end{bmatrix}
=
\begin{bmatrix} 3 \\ -1 \\ 0 \\ -1 \end{bmatrix}
\qquad
\begin{bmatrix} a \\ b \\ c \\ d \end{bmatrix}
=
\begin{bmatrix} -1 \\ -1 \\ 1 \\ 1 \end{bmatrix}
\tag{F.3}
$$

$$
k_e^* = \frac{k_{22}\ H_A\ k_e}{J\ h} \tag{F.4}
$$

Therefore, the functional dependence can be written as:

$$\sigma^* = f\left(k_p^*, k_e^*, f^*, \nu, \phi\right) \tag{F.5}$$

or, after analyzing the full set of dimensional groups:

$$\frac{\sigma}{H_A} = f\left(\frac{k_{22}\, H_A^2\, k_p}{J^2\, h^2},\ \frac{k_{22}\, H_A\, k_e}{J\, h},\ \frac{k_{22}\, H_A\, f}{J^2},\ \nu,\ \phi\right) \tag{F.6}$$

Next, the computational solution of the mathematical multi-boundary value problem can be used for a range of model physical parameters that cover realistic physical values for articular cartilage during typical experimental protocols:

$$\begin{aligned}
[H_A] &= 0.025 - 1.25\ MPa \\
[k_{22}] &= 0.8 - 1.2\ S/m \\
[h] &= 0.5 - 2.5\ mm \\
[J] &= 5 - 25\ A/m^2 \\
[k_p] &= 1.0 - 100\ (\mu m/s)/(MPa/mm) \\
[k_e] &= 1.0 - 100\ mV/MPa \\
[\phi] &= 0.7 \\
[\nu] &= 0.1
\end{aligned}$$

The geometry of the electrodes and boundary conditions are set according to that used in Appendix E. The computation model can be used to solve for the current-generated stress for the range of parameters and given geometry.

To utilize the DA to produce an analytical relation between dimensionless groups, functional dependencies of the independent variables to the dependent dimensionless groups must be chosen but physical intuition, experimental data or otherwise.

The earlier parametric results in Figure E.9 from Appendix E, suggest approximate power law relationships between the dimensionless groups. Therefore, using a simple power law relationship the following functional dependence can be found:

$$\frac{\sigma}{H_A} = 10^{-0.6843} \left[\frac{k_{22}\ H_A\ k_e}{J\ h}\right]^{1.0058} \left[\frac{k_{22}\ H_A^2\ k_p}{J^2\ h^2}\right]^{-0.2667} \left[\frac{k_{22}\ H_A\ f}{J^2}\right]^{-0.7332} \tag{F.7}$$

The power law fit with an R^2=0.99 (n=6561, corresponding to all combinations of parameters used to cover the range of parameter interest, Figure F.1).

In turn, the dimensionless expression can be re-arranged to form the following first order expression:

$$\sigma\,[kPa] \approx \frac{k_e\,[mV/kPa]\ J\,[A/m^2]}{10^{2.884}\ h\,[mm]^{0.472}\ k_p\left[\frac{\mu m/s}{MPa/mm}\right]^{0.267}} \left[\frac{H_A\,[MPa]}{f\,[Hz]}\right]^{0.733} \tag{F.8}$$

Equation F.8 is referred to as a "peculiar" equation since it is defined only for a specific set of units shown and a choice of functional dependence. Therefore, it should be used carefully ensuring that the parameters used have the proper units shown. It is appropriate over the range of parameters given, the geometry and the boundary conditions prescribed for the simulation.

Nevertheless, the first order Equation F.8 gives some physical insight into the model sensitivity to parameter variations when computing the current-generated stress. To the first order, the CGS is not dependent on electrical conductivity, k_{22}, and is linearly dependent on electromechanical coupling coefficient, k_e and current density, J. In addition, CGS is directly proportional to the equilibrium modulus, H_A, while inversely proportional to the thickness, h, permeability, k_p, and frequency, f.

Of the parameters that can be independently controlled, J, h, and f, experimental data has shown qualitative agreement with the predicted trends. The CGS has been found to be directly proportional to the current density, and in fact, CGS is

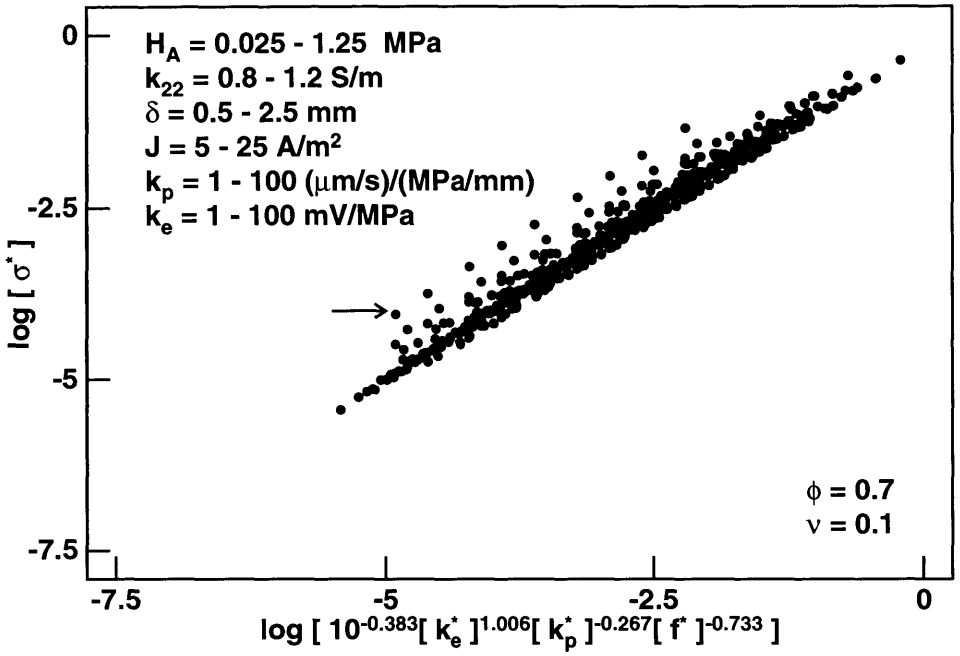

Figure F.1: A scatter plot of the computational solution of the current-generated stress multi-boundary value problem plotted against the dimensionless groups combined by a power law. The log-log representation of the data suggests the power law fit to the output of the computational model approximates the CGS quite well over a 5 decade range with a R^2 of 0.99. The simulation was over the range of parameter values given in the upper left and the subsequent permutations (n=6561). The values of ν and ϕ were not varying due to the lack of sensitivity of the model to these parameters. The deviatory points from the upper part of the scatter plot (indicated by the arrow) represent points simulated with $k_p = 100$ (μm/s)/(MPa/mm) and $k_e =$ 100 mV/MPa, that are the upper limit of the physical values expected from articular cartilage measurements.

normalized to J to formed a normalized stress amplitude in the prior work of Berkenblit. The decrease of CGS with increasing frequency is a prediction of the poroelastic theory on which the computational model is based and the expected trend found experimentally. In addition, Berkenblit has shown experimentally that as the thickness increases the CGS decreases, qualitatively validating Equation F.8. The other parameters, H_A, k_p, and k_e, are difficult to vary independently in articular cartilage, and k_e can not be directly measured. Even in an enzymatic digestion model (i.e. trypsin) it is difficult to perturb any one of the three independently. However, it may

be possible to construct electrolyte gels to control these properties to investigate their functional dependence on CGS.

Therefore, Equation F.8 seems to be able to represent the CGS predicted by the computational implementation of the multi-boundary value problem over a wide range of parameters that are relevant to experimentation with articular cartilage relatively accurately. The analytic first order relationship based on power law dependence between the dependent and independent dimensionless groups also seems to make sense qualitatively with prior experimental results. It can provide some physical insight into the dependence of CGS on the model variables and provide a quick estimate of the experimentally expected CGS given parameter values.

F.3 Impedance

Similarly, the following functional dependence based on dimensionless groups can be written for the impedance (Z):

$$Z^* = Z\ k_{22}\ h = f\left(\frac{k_{22}\ H_A^2\ k_p}{J^2\ h^2},\ \frac{k_{22}\ H_A\ k_e}{J\ h},\ \frac{k_{22}\ H_A\ f}{J^2},\ \nu,\ \phi\right) \qquad \text{(F.9)}$$

where the dimensions of impedance is: $[\mathrm{Z}] = \left[\frac{V}{A}\right] = \left[\frac{kg\ m^2}{A^2\ s^3}\right]$.

As with CGS, simulations were performed to examine the effect of model parameters on impedance over a physically relevant range (similar to CGS, except the frequency range was extended to 1 kHz and 10 mV/kPa was used as the upper limit of k_e). It was found that the electrokinetic effects (due to $H_A, k_p, k_e, f, ...$) were negligible, and the impedance was solely a function of the electrical conductivity, k_{22}, in the following form: [Z] = 271 - 136 k_{22}. The variations in impedance due to model parameters would be below the level of measurement sensitivity, making the cartilage conductivity the first order effect for this homogeneous, linear poroelastic model.

Bibliography

[1] Aaron RK, Ciombor DM: Therapeutic effects of electromagnetic fields in the stimulation of connective tissue repair. *J Cell Biochem*, 52:42–6, 1993

[2] Akizuki S, Mow VC, Muller F, Pita JC, Howell DS, Manicourt DH: Tensile properties of human knee joint cartilage: I. Influence of ionic conditions, weight bearing, and fibrillation on the tensile modulus. *J Orthop Res*, 4:379–392, 1986

[3] Ali SY: Mineral-containing matrix vesicles in human osteoarthritic cartilage. In G Nuki, editor, *The aetiopathogenesis of osteoarthritis*, pp 105–116. Pitman Medical Publishing Co, 1980

[4] Altman RD, Gray R: Diagnostic and therapeutic uses of the arthroscope in rheumatoid arthritis and osteoarthritis. *Am J Med*, 75:50–55, 1983

[5] Altman RD, Pita JC, Howell DS: Degradation of proteoglycans in human osteoarthritic cartilage. *Arthritis Rheum*, 16:179–185, 1973

[6] Armstrong CG, Mow VC: Variation in the intrinsic mechanical properties of human articular cartilage with age, degeneration, and water content. *J Bone Joint Surg*, 64A:88–94, 1982

[7] Athanasiou KA, Niederauer GG, Schenck RC: Biomechanical topography of human anakle cartilage. *Ann Biomed Eng*, 23:697–704, 1995

[8] Baker B, Becker RO, Spadaro J: A study of electrochemical enhancement of articular cartilage repair. *Clin Orthop*, 102:251–267, 1974

[9] Bassett CAL, Pawluk RJ: Electrical behavior of cartilage during loading. *Science*, 178:982–983, 1972

[10] Batra N. Validation of electrokinetic surface probe output. MIT, S.B. Thesis, 1998

[11] Bennett GA, Bauer W: A study of the repair of articular cartilage and the reaction of normal joints of adult dogs to surgically created defects of articular cartilage, "joint mice" and patellar displacement. *Am J Pathol*, 8:499–524, 1932

[12] Bennett GA, Bauer W: Further studies concerning the repair of articular cartilage in dogs joints. *J Bone Joint Surg*, 17:141–150, 1935

[13] Berkenblit SI: *Spatial Localization of Cartilage Degradation Using Electromechanical Surface Spectroscopy With Variable Wavelength and Frequency*. PhD thesis, Massachusetts Institute of Technology, 1996

[14] Berkenblit SI, Frank EH, Grodzinsky AJ: Spatial localization of cartilage degradation using variable-wavelength surface spectroscopy. *Trans Orthop Res Soc*, 20:98, 1995

[15] Berkenblit SI, Frank EH, Grodzinsky AJ: Spatial localization of cartilage degradation using electromechanical surface spectroscopy with variable wavelength and frequency. *J Orthop Res*, submitted

[16] Berkenblit SI, Frank EH, Salant EP, Grodzinsky AJ: Nondestructive detection of cartilage degeneration using electromechanical surface spectroscopy. *J Biomech Eng*, 116:384–392, 1994

[17] Billinghurst RC, Dahlberg L, Ionescu M, Reiner A, Bourne R, Rorabeck C, Mitchell P, Hambor J, Diekmann O, Tschesche H, Chen J, Van Wart H, Poole AR: Enhanced cleavage of type II collagen by collagenases in osteoarthritic artilcular cartilage. *J Clin Invest*, 99:1534–1545, 1997

[18] Biot MA: Theory of elasticity and consolidation for a porous anisotropic solid. *J Appl Physics*, 26:182–185, 1955

[19] Biot MA: General solutions of the equations of elasticity and consolidation for a porous material. *J Appl Mech*, 23:91–96, 1956

[20] Bombard DL: A surface probe for *in situ* detection of cartilage degradation via electromechanical spectroscopy. Master's thesis, Massachusetts Institute of Technology, Cambridge, MA, 1995

[21] Bonassar LJ, Frank EH, Murray JC, Paguio CG, Moore VL, Lark MW, Sandy JD, Wu JJ, Eyre DR, Grodzinsky AJ: Changes in cartilage composition and physical properties due to stromelysin degradation. *Arthritis Rheum*, 38:173–183, 1995

[22] Bonassar LJ, Sandy JD, Lark MW, Plaas AHK, Frank EH, Grodzinsky AJ: Inhibition of cartilage degradation and changes in physical properties induced by IL-1β and retinoic acid using matrix metalloproteinase inhibitors. *Arch Biochem Biophys*, 344:404–412, 1997

[23] Bonassar LJ, Stinn JL, Paguio CG, Frank EH, Moore VL, Lark MW, Grodzinsky AJ: Activation and inhibition of endogenous matrix metalloproteinases in articular cartilage: Effects on composition and biophysical properties. *Arch Biochem Biophys*, 333:359–367, 1996

[24] Brittberg M, Lindahl A, Nilsson A, Ohlsson C, Isaksson O, Peterson L: Treatment of deep cartilage defects in the knee with autologous chondrocyte transplantation. *N Engl J Med*, 331:889–95, Oct 1994

[25] Buckland-Wright JC, Macfarlane DF: Radioanatomic assessment of therapeutic outcome of osteoarthrits. In KE Kuettner, VM Goldberg, editors, *Osteoarthritic Disorders*, pp 51–65. American Academy of Orthopaedic Surgeons, 1995

[26] Buckwalter J, Hunziker E, Rosenberg L, Coutts R, Adams M, Eyre D: Articular cartilage: composition and structure. In SLY Woo, JA Buckwalter, editors, *Injury and repair of the musculoskeletal soft tissues*, pp 405–425. American Academy of Orthopaedic Surgeons, Park Ridge, IL, 1988

[27] Bullough PG: The geometry of diarthrodial joints, its physiologic maintenance and the possible significance of age-related changes in geometry-to-load distribution and the development of osteoarthritis. *Clin Orthop*, 156:61–66, 1981

[28] Burgeson RE, Nimni ME: Collagen types: Molecular structure and tissue distribution. *Clin Orthop*, 282:250–272, 1992

[29] Buschmann MD: *Chondrocytes in Agarose Culture: Development of a Mechanically Functional Matrix, Biosynthetic Response to Compression, and Molecular Model of the Modulus*. PhD thesis, Massachusetts Institute of Technology, Cambridge, MA, 1992

[30] Buschmann MD, Grodzinsky AJ: A molecular model of proteoglycan-associated electrostatic forces in cartilage mechanics. *J Biomech Eng*, 117:179–192, 1995

[31] Byers PD, Contemponi CA, Farkas TA: A post mortem study of the hip joint. *Ann Rheum Dis*, 29:15–31, 1970

[32] Byers PD, Maroudas A, Oztop F, Stockwell RA, Venn MF: Histological and biochemical studies on cartilage from osteoarthritic femoral heads with special reference to surface characteristics. *Calcif Tissue Res*, 5:41–49, 1977

[33] Caplan AI: Mesenchymal stem cells. *J Orthop Res*, 9:641–650, 1991

[34] Caron JP, Tardif G, Martel-Pelletier J, DiBattista JA, Geng C, Pelletier JP: Modulation of matrix metalloproteinase 13 (collagenase 3) gene expression in equine chondrocytes by interleukin 1 and cortosteroids. *Am J Vet Res*, 57:1631–1634, 1996

[35] Cawston T: Blocking cartilage destruction with metalloproteinase inhibitors: a valid therapeutic target? *Ann Rheum Dis*, 52:769–770, 1993

[36] Chammas P, Federspiel WJ, Eisenberg SR: A microcontinuum model of electrokinetic coupling in the extracellular matrix: Perturbation formulation and solution. *J Colloid and Interface Science*, 168:526–538, 1994

[37] Champion BR, Poole AR: Immunity to homologous type III collagen after partial meniscectomy and shear surgery in rabbits. *Arthritis Rheum*, 25:274–285, 1972

[38] Chang RW, Falconer J, Stulberg SD, Arnold WJ, Manheim LM, Dyer AR: A randomized, controlled trial of arthroscopic surgery versus closed-needle joint lavage for patients with osteoarthritis of the knee. *Arthritis Rheum*, 36:289–296, 1993

[39] Chen AC, Schinagl RM, Sah RL: Inhomogeneous and strain-dependent electromechanical properties of full-thickness articular cartilage. *Trans Orthop Res Soc*, 23:225, 1998

[40] Cheung HS, Lynch KL, Johnson RP, Brewer JP: *In vitro* synthesis of tissue specific type II collagen by healing cartilage. I. Short-term repair of cartilage by mature rabbits. *Arthritis Rheum*, 2:211–219, 1980

[41] Chubinskaya S, Huch K, Mikecz K, Cs-Szabo G, Hasty KA, Kuettner KE, Cole AA: Chondrocyte matrix metalloproteinase-8: Up-regulation of neutrophil collagenase by interleukin-1β in human cartilage from knee and ankle joints. *Lab Invest*, 74:232–240, 1996

[42] Chubinskaya S, Koepp H, Kuettner KE, Cole AA: Expression of matrix metalloproteinases in adult normal, damaged and osteoarthritic human articular cartilage. *Trans Orthop Res Soc*, 23:152, 1998

[43] Clark IM, Cawston TE: Fragments of human fibroblast collagenase. Purification and characterization. *Biochem*, 263:201–206, 1989

[44] Collins DH: *The Pathology of Articular and Spinal Diseases*, pp 74–115. Edward Arnold, London, 1949

[45] Convery FR, Akeson WK, Keown G: The repair of large osteochondral defects. An experimental study in horses. *Clin Orthop*, 82:253–262, 1972

[46] Cooper C, McAlindon T, Coggon D, Egger P, Dieppe P: Occupational activity and osteoarthritis of the knee. *Ann Rheum Dis*, 53:90–93, 1994

[47] Cooper J, Turnell D, Green B, Demmarais D, Pesquin P: The analysis of primary and secondary free amino acids in biological fluids; a completely automated process using online membrane sample preparation, precolumn derivatization with orthophthaldehype, 9-fluorenyl methyl chloroformate and HPLC separation. Gilson-ASTED method #9.2.2, Gilson Instrument Manual, Middlebury, WI, 1991. p. A.G.9.1

[48] Dashefsky JH: Arthroscopic measurement of chondromalacia of patella cartilage using a microminiature pressure transducer. *Arthroscopy*, 3:80–85, 1987

[49] Dean DD, Martel-Pelletier J, Pelletier JP, Howell DS, Woessner JF Jr: Evidence for metalloproteinase and metalloproteinase inhibitor imbalance in human osteoarthritic cartilage. *J Clin Investig*, 84:678–685, 1989

[50] DePalma AF, McKeever C, Subin DK: Process of repair of articular cartilage demonstrated by histology and autoradiography and tritiated thymadine. *Clin Orthop*, 48:45, 1966

[51] Dieppe P: The classifacation and diagnosis of osteoarthritis. In KE Kuettner, VM Goldberg, editors, *Osteoarthritic Disorders*, pp 5–12. American Academy of Orthopaedic Surgeons, 1995

[52] Dieppe P: Osteoarthritis and molecular markers. A rheumatologist's perspective. *Acta Orthop Scand*, 66:1–5, 1995

[53] Dieppe P, Cushnaghan J, Jasani M, McCrae F, Watt I: A two year, placebo-controlled trial of non-steroidal anit-inflammatory therapy in osteoarthritis of the knee joint. *Br J Rheumatol*, 32:595–600, 1993

[54] Drake MP, Davison PF, Schmitt FO: Action of proteolytic enzymes on tropocollagen and insoluble collagen. *Biochemistry*, 5:301–312, 1966

[55] Eisenberg SR, Grodzinsky AJ: Swelling of articular cartilage and other connective tissues: Electromechanochemical forces. *J Orthop Res*, 3:148–159, 1985

[56] Eisenberg SR, Grodzinsky AJ: Electrokinetic micromodel of extracellular matrix and other polyelectrolyte networks. *Physicochem Hydrodyn*, 10:517–539, 1988

[57] Evered D, Whelan J: Functions of the proteoglycans. *Ciba Foundation Symposium*, 124, 1986

[58] Eyre D, Wu JJ, Woods P: Cartilage-specific collagens: Structural studies. In KE Kuettner, R Schleyerbach, JG Peyron, VC Hascall, editors, *Articular Cartilage and Osteoarthritis*, pp 119–132. Raven Press, New York, 1992

[59] Eyre DR, Dickson IR, van Ness K: The collagens of articular cartilage. *Sem Arthritis Rheum*, 21:2–11, 1991

[60] Farndale RW, Buttle DJ, Barrett AJ: Improved quantitation and discrimination of sulphated glycosaminoglycans by use of dimethylmethylene blue. *Biochim Biophys Acta*, 883:173–177, 1986

[61] Farndale RW, Sayers CA, Barrett AJ: A direct spectrophotometric microassay for sulfated glycosaminoglycans in cartilage cultures. *Connect Tissue Res*, 9:247–248, 1982

[62] Felson DT, Naimark A, Anderson J, Kazis L, Castelli W, Meenan RF: The prevalence of knee osteoarthritis in the elderly. The Framingham Osteoarthritis Study. *Arthritis Rheum*, 30:914–918, 1987

[63] Fife RS: A short history of osteoarthritis. In RW Moskowitz, DS Howell, VM Goldberg, HJ Mankin, editors, *Osteoarthritis. Diagnosis and Medical/Surgical Management*, pp 11–14. W. B. Saunders, Philadelphia, 1992

[64] Fife RS, Brandt KD, Braunstein EM, Katz BP, Shelbourne KD, Kalasinski LA, Ryan S: Relationship between arthroscopic evidence of cartilage damage and radiographic evidence of joint space narrowing in early osteoarthritis of the knee. *Arthritis Rheum*, 34:377–382, 1991

[65] Fisher T: Injuries and diseases of the articulations. *The Lancet*, pp 541–548, Sep 1923

[66] Fosang AJ, Last K, Knauper V, Murphy G, Neame PJ: Degradation of cartilage aggrecan by collagenase-3 (mmp-13). *FEBS Lett*, 380:17–20, 1996

[67] Frank EH, Grodzinsky AJ: Cartilage electromechanics-I. Electrokinetic transduction and the effects of electrolyte pH and ionic strength. *J Biomech*, 20:615–627, 1987

[68] Frank EH, Grodzinsky AJ: Cartilage electromechanics-II. A continuum model of cartilage electrokinetics and correlation with experiments. *J Biomech*, 20:629–639, 1987

[69] Frank EH, Grodzinsky AJ, Koob TJ, Eyre DR: Streaming potentials: A sensitive index of enzymatic degradation in articular cartilage. *J Orthop Res*, 5:497–508, 1987

[70] Frank EH, Grodzinsky AJ, Phillips SL, Grimshaw PE: Physicochemical and bioelectrical determinants of cartilage material properties. In VC Mow, A Ratcliffe, SLY Woo, editors, *Biomechanics of Diarthrodial Joints*, pp 261–282. Springer-Verlag, New York, NY, 1990

[71] Freed LE, Grande DA, Lingbin Z, Emmanual J, Marquis JC, Langer R: Joint resurfacing using allograft chondrocytes and synthetic biodegradable polymer scaffolds. *J Bone Min Res*, 28:891–899, 1994

[72] Freed LE, Langer R, Martin I, Pellis NR, Vunjak-Novakovic G: Tissue engineering of cartilage in space. *Proc Nat Acad Sci*, 94:13885–13890, 1997

[73] Freed LE, Vunjak-Novakovic G: Cultivation of cell-polymer constructs in simulated microgravity. *Biotech Bioeng*, 46:306–313, 1995

[74] Freed LE, Vunjak-Novakovic G, Biron RJ, Eagles D, Lesnoy D, Barlow SK, Langer R: Biodegradable polymer scaffolds for tissue engineering. *Bio Technology*, 20:689–693, 1994

[75] Frisch SM, Werb Z: Collagen: Molecular biology. In BR Olsen, ME Numni, editors, *Molecular biology of collagen degradation*, volume IV, pp 85–108. CRC Press, Boca Raton, Florida, 1989

[76] Froimson MI, Ratcliffe A, Gardner TR, Mow VC: Differences in patellofemoral joint cartilage material properties and their significance to the etiology of cartilage surface fibrillation. *Osteoarthritis Cartilage*, 5:377–386, 1997

[77] Fuller JA, Ghadially FN: Ultrastructural observations on surgically produced partial -thickness defects in articular cartilage. *Clin Orthop*, 86:193, 1972

[78] Gallagher JT: The extended family of proteoglycans: Social residents of the pericellular zone. *Curr Opin Cell Biol*, 1:1201–1218, 1989

[79] Garcia AM: *Mechanisms of Macromolecular Transport Through Articular Cartilage: Relevance to Loading*. PhD thesis, Massachusetts Institute of Technology, Cambridge, MA, 1996

[80] Geddes LA: *Electrodes and the Measurement of Bioelectric Events*. Wiley-Interscience, New York, 1972

[81] Geddes LA, Baker LE, Moore AG: Optimum electrolytic chloriding of silver electrodes. *Med Biol Eng*, 7:49–56, 1969

[82] Gersing E, Osypka M: EIT using magnitude and phase in an extended frequency range. *Physiol Meas*, 15:A21–A28, 1994

[83] Gore DM, Higginson GR, Minns RJ: Compliance of articular cartilage and its variation through the thickness. *Phys Med Biol*, 28:233–247, 1983

[84] Grande DA, Pitman MI, Peterson L, Menche D, Klein M: The repair of experimentally produced defects in rabbit articular cartilage by autologous chondrocyte implantation. *J Ortho Res*, 7:208–18, 1989

[85] Grant GA, Eisen AZ, Marmer BL, Roswit WT, Goldberg GI: The activation of human skin fibroblast collagenase. sequence identification of the major conversion products. *J Biol Chem*, 262:5886–5889, 1987

[86] Greenwald RA, Golub LM, Ramamurthy NS, Chowdury M, Moak SA, Sorsa T: *In vitro* senstitivity of the three mammalian collagenases to tetracycline inhibition: relationship to bone and cartilage degeneration. *Bone*, 22:33–38, 1998

[87] Grimshaw PE, Eisenberg SR, Grodzinsky AJ, Koob TJ, Eyre DR: The kinetics of *in vitro* neutralization and enzymatic extraction of cartilage charge groups: Characterization by isometric compressive stress. *Trans Orthop Res Soc*, 8:122, 1983

[88] Grodzinsky AJ: Electromechanical and physicochemical properties of connective tissue. *CRC Crit Rev Bioeng*, 9:133–199, 1983

[89] Grodzinsky AJ, Berger E, Hung HK, Frank EH, Hunziker EB: Compression of cartilage alters morphology of intracellular organelles: A potential link between mechanical stimuli and aggrecan structure. *Trans Orthop Res Soc*, 1999 (accepted)

[90] Grodzinsky AJ, Lipshitz H, Glimcher MJ: Electromechanical properties of articular cartilage during compression and stress relaxation. *Nature*, 275:448–450, 1978

[91] Gross J, Lapière CM: Collagenolytic activity in amplibian tissues: a tissue culture assay. *Proc Matl Acad Sci USA*, 54:1197–1204, 1962

[92] Hall LD, Tyler JA: Can quantitative magnetic resonance imaging detect and monitor the progression of early osteoarthritis? In KE Kuettner, VM Goldberg, editors, *Osteoarthritic Disorders*, pp 67–84. American Academy of Orthopaedic Surgeons, 1995

[93] Hall LD, Watson PJ, Tyler JA: Osteoarthritis: Public health implications for an aging population. In D Hamerman, editor, *Magnetic Resonance Imaging and the Progression of Osteoarthritis, Osteoporosis and Aging*, pp 215–229. The Johns Hopkins University Press, 1997

[94] Hardingham T, Bayliss M: Proteoglycans of articular cartilage: changes in aging and in joint disease. *Sem Arthritis Rheum*, 20:12–33, 1990

[95] Hardingham TE, Fosang AJ: Proteglycans: many forms and many functions. *FASEB*, 6:861–870, 1992

[96] Hardingham TE, Fosang AJ, Dudhia J: Aggrecan, the chondroitin sulfate/keratan sulfate proteoglycan from cartilage. In KE Kuettner, R Schleyerbach, JG Peyron, VC Hascall, editors, *Articular Cartilage and Osteoarthritis*, pp 5–20. Raven Press, New York, 1992

[97] Häuselmann HJ, Fernandes RJ, Block JA, Schmid TM, Thonar EJMA: Adult articular chondrocytes retain their phenotype after 8 months of culture in alginate. *Trans Orthop Res Soc*, 18:624, 1993

[98] Häuselmann HJ, Flechtenmacher J, Mollenhauer J, Kuettner KE, Aydelotte MB: Differences in responsiveness and in receptor numbers for interleukin-1 between adult human chondrocytes from superficial and deep zones of articular cartilage. *Trans Orthop Res Soc*, 19:363, 1994

[99] Heinegard D, Oldberg A: Structure and biology of cartilage and bone matrix noncollagenous macromolecules. *FASEB J*, 3:2042–2051, 1989

[100] Heinegard D, Paulsson M: Structure and metabolism of proteoglycans. In KA Piez, AH Reddi, editors, *Extracellular Matrix Biochemistry*, pp 277–328. Elsevier, New York, 1984

[101] Hendrickson DA, Nixon AJ, Grande D, Todhunter RJ, Minor RM, Erb H, Lust G: Chondrocyte-fibrin matrix transplants for resurfacing extensive articular cartilage defects. *J Orthop Res*, 12:485–497, 1994

[102] Hirsch C: The pathogenesis of chondromalacia of the patella: A physical, histologic, and chemical study. *Acta Chir Scand*, 90:1–106, 1944

[103] Hoch DH, Grodzinsky AJ, Koob TJ, Albert ML, Eyre DR: Early changes in material properties of rabbit articular cartilage after meniscectomy. *J Orthop Res*, 1:4–12, 1983

[104] Hodge AJ, Highberger JH, Deffner GGJ, Schmitt FO: The effects of proteases on the tropocollagen macromolecule and on its aggregation properties. *Biochemistry*, 46:197–206, 1960

[105] Hollander AP, Heathfield TF, Webber C, Iwata Y, Bourne R, Rorabeck C, Poole AR: Increased damage to type II collagen in osteoarthritic articular cartilage detected by a new immunoassay. *J Clin Invest*, 4:1722–1732, 1994

[106] Huch K, Kuettner KE, Dieppe P: Osteoarthritis in ankle and knee joints. *Sem Arthritis Rheum*, 26:1–8, 1997

[107] Huebner JL, Otterness IG, Freund EM, Caterson B, Kraus VB: Collagenase 1 and collagenase 3 expression in a guinea pig model of osteoarthritis. *Arthritis Rheum*, 41:877–890, 1998

[108] Hunter W: On the structure and diseases of articulating cartilage. *Philos Trans R Soc Lond*, 42b:514–521, 1743

[109] Hunziker EB: Articular cartilage structure in humans and experimental animals. In KE Kuettner, R Schleyerbach, JG Peyron, VC Hascall, editors, *Articular Cartilage and Osteoarthritis*, pp 183–199. Raven Press, New York, 1992

[110] Hunziker EB, Geiss J, Kapfinger E: Postnatal changes in cartilage in articular cartilage structure: Internal reorganization of tissue or resorption and neoformation? *submitted*, 1997

[111] Hunziker EB, Rosenberg LC: Repair of partial-thickness articular cartilage defect. cell recruitment from the synovium. *Am J Bone Joint Surg Am*, 78A:721–733, 1996

[112] Hunziker EB, Rosenberg LC: Repair of partial-thickness articular cartilage lesions by the timed release of transforming growth factor-β. *submitted*, 1997

[113] Hutton CW: Generalized osteoarthritis: An evolutionary problem? *Lancet*, 1:1463–1465, 1987

[114] Ike RW, O'Rourke KS: Detection of intraarticular abnormalities in osteoarthritis of the knee: A pilot study comparing needle arthroscopy with standard arthroscopy. *Arthritis Rheum*, 36:1352–1363, 1993

[115] Inerot S, Heinegard D, Olsson SE, Telhag H, Audell L: Proteoglycan alterations during developing experimental osteoarthritis in a novel hip joint model. *J Orthop Res*, 9:658–673, 1991

[116] Ishizue KK, Ehrlich MG, Mankin HJ: Drug-induced inhibition of proteoglycanase activity in the Hulth-Telhag model. *J Orthop Res*, 7:806–811, 1989

[117] Jackson RW: The role of arthroscopy in the management of the arthritic knee. *Clin Orthop*, 101:28–35, 1974

[118] Jurvelin JS, Buschmann MD, Hunsiker EB: Optical and mechanical determination of Poisson's ratio of adult bovine humeral articular cartilage. *J Biomech*, 30:235–41, 1997

[119] Kang Y, Koepp H, Cole AA, Kuettner KK, Homandberg GA: Cultured human ankle and knee cartilage differ in susceptibility to damage mediated by fibronectin fragments. *J Orthop Res*, 16:551–556, 1998

[120] Kellgren JH, Lawrence JS: *Atlas of Standard Radiography. The epidemiology of chronic rheumatism*, volume 2. Blackwell Scientific Publication, 1963

[121] Kempson GE: Mechanical properties of articular cartilage. In MAR Freeman, editor, *Adult Articular Cartilage, 2nd ed.*, pp 333–414. Pitman, Tunbridge Wells, England, 1979

[122] Kempson GE: Age-related changes in the tensile properties of human articular cartilage: a comparative study between the femoral head of the hip joint and the talus of the ankle joint. *Biochim Biophys Acta*, 1075:223–230, 1991

[123] Kim YJ, Sah RLY, Doong JYH, Grodzinsky AJ: Fluorometric assay of DNA in cartilage explants using Hoechst 33258. *Anal Biochem*, 174:168–176, 1988

[124] Kiviranta I, Jurvelin J, Tammi M, Saamanen AM, Helminen HJ: Weight bearing controls glycosaminoglycan concentration and articular cartilage thickness in the knee joints of young beagle dogs. *Arthritis Rheum*, 30:801–809, 1987

[125] Kiviranta I, Lyyra T, Väätäinen U, Seuri R, Jaroma H, Jurvelin J: Knee joint articular cartilage shows general softening in patients with chondromalacia of the patella. *Trans Orthop Res Soc*, 20:197, 1995

[126] Knudson CB: Hyaluronan receptor-directed assembly of chondrocyte pericellular matrix. *J Cell Biol*, 120:825–834, 1993

[127] Koepp H, Eger W, Muehlemen C, Valdellon A, Buckwalter JA, Kuettner KE, Cole AA: Articular cartilage degeneration in the ankle and knee joints of human organ donors. *J Orthop Sci*, 1998 (submitted)

[128] Krane SM: Inhibition of matrix metalloproteinases therapeutic potential. In RA Greenwald, LM Golub, editors, *Clinical Importance of Metalloproteinases and Their Inhibitors*, volume 732, pp 1–10. The New York Academy of Sciences, New York, New York, 1994

[129] Kuettner KE, Goldberg VM: *Osteoarthritic Disorders*, pp 86–87. American Academy of Orthopaedic Surgeons, 1995

[130] Kuettner KE, Goldberg VM: *Osteoarthritic Disorders*, p xix. American Academy of Orthopaedic Surgeons, 1995

[131] Kuettner KE, Goldberg VM: *Osteoarthritic Disorders*, p xxi. American Academy of Orthopaedic Surgeons, 1995

[132] Kühn K, Fietzek P, Kühn J: The action of proteolytic enzymes on collagen. *Biochem Z*, 344:418–434, 1966

[133] Lee RC, Frank EH, Grodzinsky AJ, Roylance DK: Oscillatory compressional behavior of articular cartilage and its associated electromechanical properties. *J Biomech Eng*, 103:280–292, 1981

[134] Levenston ME, Frank EH, Grodzinsky AJ: Nonuniform spatial profiles of compression-induced electromechanical fields: relevance to chondrocyte biosynthesis. *Trans Orthop Res Soc*, 22:410, 1997

[135] Little CB, Ghosh P: Variation in proteoglycan metabolism by articular chondrocytes in different joint regions is determined by post-natal mechanical loading. *Osteoarthritis Cartilage*, 5:49–62, 1997

[136] Lyyra T, Jurvelin J, Pitkänen P, Väätäinen U, Kiviranta I: Indentation instrument for the measurement of cartilage stiffness under arthroscopic control. *Med Eng Phys*, 17:395–399, 1995

[137] Macdonald JR: Impedance spectroscopy. *Ann Biomed Eng*, 20:289–305, 1992

[138] Mackie JS, Meares P: The diffusion of electrolytes in a cation-exchange resin. I. Theoretical. *Proc R Soc London*, 232:498–509, 1955

[139] Madded TR: Transmition system and network analogies to geophysical forward and inverse problems. Technical report, MIT, 1972

[140] Mak AF, Lai WM, Mow VC: Biphasic indentation of articular cartilage-I. Theoretical analysis. *J Biomech*, 20:703–714, 1987

[141] Mankin HJ: Localization of tritiated thymadine in articular cartilage of rabbits. II. Repair of immature cartilage. *J Bone J Surg Am*, 44:688, 1962

[142] Mankin HJ, Brandt KD: Biochemistry and metabolism of cartilage in osteoarthritis. In RW Moskowitz, DS Howell, VM Goldberg, HJ Mankin, editors, *Osteoarthritis: Diagnosis and Management*, pp 43–79. W.B. Saunders, Philadelphia, 1984

[143] Mankin HJ, Dorman H, Lippiello L, Zarins A: Biochemical and metabolic abnormalities in articular cartilage from osteoarthritic human hips. II. Correlation of morphology with biochemical and metabolic data. *J Bone J Surg Am*, 52:523–537, 1971

[144] Mankin HJ, Mow VC, Buckwalter JA, Ianotti JP, Ratciffe A: Structure and function of articular cartilage. In SR Simon, editor, *Orthopaedic Basic Science*, pp 1–44. Amer Acad Orthop Surg Pub, Rosemont, IL, 1994

[145] Mankin HJ, Thrasher AZ: Water content and binding in normal and osteoarthritic human cartilage. *J Bone Joint Surg [Am]*, 57-A:76–80, 1975

[146] Mankin H: Chondrocyte transplantation - one answer to an old question. *N Engl J Med*, 331:940–941, 1994

[147] Maroudas A: Balance between swelling pressure and collagen tension in normal and degenerate cartilage. *Nature*, 260:808–809, 1976

[148] Maroudas A: Physicochemical properties of articular cartilage. In MAR Freeman, editor, *Adult Articular Cartilage, 2nd ed.*, pp 215–290. Pitman, Tunbridge Wells, England, 1979

[149] Maroudas A, Evans H: A study of ionic equilibria in cartilage. *Connect Tissue Res*, 1:69–77, 1972

[150] Maroudas A, Mizrahi J, Ben Haim E, Ziv I: Swelling pressure in cartilage. In NC Staub, editor, *Advances in Microcirculation, Interstitial-Lymphatic Liquid and Solute Movement*, volume 13, pp 203–212. Karger, New York, NY, 1987

[151] Maroudas A, Muir H, Wingham J: The correlation of fixed negative charge with glycosaminoglycan content of human articular cartilage. *Biorheology*, 12:233, 1969

[152] Maroudas A, Schneiderman R, Popper O: The role of water, proteoglycan, and collagen in solute transport in cartilage. In KE Kuettner, R Schleyerbach, JG Peyron, VC Hascall, editors, *Articular Cartilage and Osteoarthritis*, pp 355–371. Raven Press, New York, 1992

[153] Maroudas A, Venn MF: Chemical composition and swelling of normal and osteoarthritic tissues II: Swelling. *Ann Rheum Dis*, 36:399–406, 1977

[154] Maroudas A, Wachtel E, Grushko G, Katz EP, Weinberg P: The effect of osmotic and mechanical pressures on water partitioning in articular cartilage. *Biochim Biophys Acta*, 1073:285–294, 1991

[155] Matsui Y, Maeda M, Nakagami W, Iwata H: The involvement of matrix metalloproteinases and inflammation of the lumber disc herniation. *Spine*, 23:863–868, 1998

[156] Maxian TA, Brown TD, Weinstein SL: Chronic stress tolerance levels for human articular cartilage: Two nonuniform contact models applied to long-term follow-up of CDH. *J Biomech*, 28:159–166, 1995

[157] Maxwell JC: *A Treatise on Electricity and Magnetism*, pp 81–108. Dover Publications, New York, 1954

[158] McCarty D: *Arthritis and Allied Conditions*. Henry Kimpton Co, 9th edition, 1979

[159] Meachim G: Articular cartilage lesions in osteo-arthritis to the femoral head. *J Pathol*, 107:199–210, 1972

[160] Meachim G, Brook G: The pathology of osteoarthritis. In RW Moskowitz, DS Howell, VM Goldberg, HJ Mankin, editors, *Osteoarthritis*, pp 29–42. W.B. Saunders, Philadelphia, 1984

[161] Meachim G, Ghadially FN, Collins DH: Regressive changes in the superficial layer of human articular cartilage. *Ann Rheum Dis*, 24:23–30, 1965

[162] Melcher JR, Zaretsky MC. Apparatus and methods for measuring permittivity in materials. United States Patent number 4,814,690, Mar 1989

[163] Mijailovich SM: *Elasticity and Energy Dissipation in Lung Connective Tissue.* PhD thesis, MIT, 1991

[164] Minas T, Nehrer S: Current concepts in the treatment of articular cartilage defects. *Orthopedics*, 20:525–538, 1997

[165] Mink JH, Reicher MA, Crues JV III: *Magnetic Resonance Imaging of the Knee.* Raven Press, New York, 1992

[166] Mitchell N, Shepard N: The resurfacing of adult rabbit articular cartilage by multiple perforations through the subchondral bone. *J Bone Joint Surg Am*, 23:211, 1976

[167] Mitchell PG, Magna HA, Reeves LM, Lopresti-Morrow LL, Yocum SA, Rosner PJ, Geoghegan KF, Hambor JE: Cloning, expression, and type II collagenolytic activity of matrix metalloproteinase-13 from human osteoarthritic cartilage. *J Clin Investig*, 97:761–768, 1996

[168] Morales TI, Hascall VC: Factors involved in the regulation of proteoglycan metabolism in articular cartilage. *Arthritis Rheum*, 32:1197–1201, 1989

[169] Moskowitz RW, Howell DS, Goldberg VM, Mankin HJ, editors: *Osteoarthritis: Diagnosis and Medical/Surgical Management.* W.B. Saunders, Philadelphia, 2nd edition, 1992

[170] Mow VC, Holmes MH, Lai WM: Fluid transport and mechanical properties of articular cartilage: a review. *J Biomech*, 17:377–394, 1984

[171] Mow VC, Kuei SC, Lai WM, Armstrong CG: Biphasic creep and stress relaxation of articular cartilage in compression: Theory and experiments. *J Biomech Eng*, 102:73–84, 1980

[172] Mow VC, Setton LA, Guilak F, Ratcliffe A: Mechanical factors in articular cartilage and their role in osteoarthritis. In KE Kuettner, VM Goldberg, editors, *Osteoarthritic Disorders*, pp 147–171. American Academy of Orthopaedic Surgeons, 1995

[173] Muehlemann C, Bareither DJ, Huch K, Cole AA, Kuettner KK: Prevelance of degenerative morphological changes in the joints of the lower extremity. *Osteoarthritis Cartilage*, 5:23–37, 1997

[174] Nagase H, Woessner JF Jr: Role of endogenous proteinases in the degradation of cartilage matrix. In JF Woessner Jr, DS Howell, editors, *Joint Cartilage Degradation*, chapter 7, pp 159–186. Dekker, New York, 1993

[175] Nehrer S, Young G, Spector M, Minas T: Mechanisms of failure of cartilage repair procedures in humans - histological analysis of retreived tissue. *Trans Orthop Res Soc*, 23:247, 1997

[176] Nelson B, Anderson DD, Brand RA, Brown TD: Effect of osteochondral defects on articular cartilage. Contact pressure studied in dog knees. *Acta Orthop Scand*, 59:574, 1988

[177] Nixon AJ, Sams AE, Lust G, Grande D, Mohammed HO: Temporal matrix synthesis and histologic features of a chondrocyte-laden porous collagen analogue. *Am J Vet Res*, 54:349–356, 1993

[178] Obradovic B, Martin I, Padera RF, Treppo S, Freed LE, G VN: Integration of engineered cartilage into natural cartilage: *In Vitro* studies. *AIChE Annual Meeting*, 1998 (submitted)

[179] O'Connor P, Orford CR, Gardner DL: Differential response to compressive loads of zones of canine hyaline articular cartilage: Micromechanical light and electron microscopic studies. *Ann Rheum Dis*, 47:414–420, 1988

[180] O'Driscoll SW, Salter RB: The induction of neochondrogenesis in free intra-articular periosteal autografts under the influence of continuous passive motion. An experimental investigation in the rabbit. *J Bone Joint Surg Am*, 66:1248–1257, 1984

[181] Oegema TR, Carpenter BJ, Thompson RC: Fluorometric determination of DNA in cartilage of various species. *J Orthop Res*, 1:345–351, 1984

[182] Otterness IG, Eskra JD, Bliven ML, Shay AK, Pelletier JP, Milici AJ: Exercise protects against articular cartilage degeneration in the hamster. *Arthritis Rheum*, 41:2068–2076, 1998

[183] Pennwalt Corp. : *Kynar Piezo Film*. Pennwalt Corp., Valley Forge, PA, 1987. Technical Manual

[184] Peyron JG: The epidemiology of osteoarthritis. In RW Moskowitz, DS Howell, VM Goldberg, HJ Mankin, editors, *Osteoarthritis. Diagnosis and Treatment*, pp 9–27. W. B. Saunders, Philadelphia, 1984

[185] Plaas AHK, Sandy JD: Proteoglycan anabolism and catabolism in articular cartilage. In KE Kuettner, VM Goldberg, editors, *Osteoarthritic Disorders*, pp 103–116. American Academy of Orthopaedic Surgeons, 1995

[186] Press WH, Flannery BP, Teukolsky SA, Vetterling WT: *Numerical Recipes in C*. Cambridge University Press, New York, 1988

[187] Quan E: Design of an *in vivo* probe to detect cartilage degeneration. Master's thesis, MIT, 1998

[188] Quinn TM: *Articular Cartilage: Matrix Assembly, Mediation of Chondrocyte Metabolism, and Response to Compression*. PhD thesis, Massachusetts Institute of Technology, Cambridge, MA, 1996

[189] Radin EL: Effects of repetitive impulsive loading on the knee joint of rabbits. *Clin Orthop*, 131:288–293, 1978

[190] Ragan PM, Badger AM, Dodds RA, Cook M, Connor JR, Grodzinsky AJ, Lark MW: Mechanical compression affects chondrocyte matrix gene expression in cartilage explants. *Trans Orthop Res Soc*, 23:918, 1998

[191] Reindel ES, Ayroso AM, Chen AC, Chun DM, Schinagl RM, Sah RL: Integrative repair of articular cartilage *in vitro*: Adhesive strength of the interface region. *J Bone Joint Surg*, 13:751–760, 1995

[192] Rigaud B, Hamzaoui L, Chauveau N, Granié M, Di Rinaldi JS, Morucci J: Tissue characterization by impedance: A multifrequency approach. *Physiol Meas*, 15:A13–A20, 1994

[193] Rivers PA, Wang H, Strauch RJ, Athesian GA, Pawluk RJ, Rosenwasser MP, Ratcliffe A, Mow VC: Osteoarthritic changes in the biochemical composition of carpometacarpal joint cartilage and correlation with compressive modulus. *Trans Orthop Res Soc*, 23:754, 1998

[194] Rogers J, Watt I, Dieppe P: Comparison of visual and radiographic detection of bony changes at the knee joint. *Br Med J*, 300:367–368, 1990

[195] Royce PM, Lowther DA: Fluorimetric determination of DNA in papain digests of cartilage, using ethidium bromide. *Connect Tissue Res*, 6:215–221, 1979

[196] Rubak JM: Reconstruction of articular cartilage defects with free periosteal grafts. An experimental study. *Acta Orthop Scand*, 53:187–191, 1982

[197] Saari H, Tulamo RM, Konttinen YT, Sorsa T: Methylprednisolone acetate induced release of cartilage proteoglycans: Determination by high performance liquid chromatography. *Ann Rheum Dis*, 51:214–9, 1992

[198] Sabiston CP, Adams ME, Li DKB: Magnetic resonance imaging of osteoarthritis: Correlation with gross pathology using an experimental model. *J Orthop Res*, 5:164–172, 1987

[199] Sachs JR, Grodzinsky AJ: An electromechanically coupled poroelastic medium driven by an applied electric current: surface detection of bulk material properties. *Physicochem Hydrodyn*, 11:585–614, 1989

[200] Sachs JR: *A Mathematical Model of an Electromechanically Coupled Poroelastic Medium*. PhD thesis, Massachusetts Institute of Technology, Cambridge, MA, 1987

[201] Sah RL, Kim YJ, Doong JH, Grodzinsky AJ, Plaas AHK, Sandy JD: Biosynthetic response of cartilage explants to dynamic compression. *J Orthop Res*, 7:619–636, 1989

[202] Salant EP: *Surface Probe for Electrokinetic Detection of Cartilage Degeneration*. MD thesis, Harvard-MIT Division of Health Sciences and Technology, Cambridge, MA, 1991

[203] Salter RB: The effect of continuous passive motion on the healings of articular cartilage defects. *J Bone Joint Surg Am*, 57:570, 1975

[204] Sams AE, Minor RR, Wootton JA, Mohammed HO, Nixon AJ: Local and remote matrix response to chondrocyte-laden collagen scaffold implantation in extensive cartilage defects. *Osteoarthritis Cartilage*, 3:61–70, 1995

[205] Sang QA, Douglas DA: Computational sequence analysis of matrix metalloproteinases. *J Pro Chem*, 15:137–160, 1996

[206] Schiller AL: Pathology of osteoarthrits. In KE Kuettner, VM Goldberg, editors, *Osteoarthritic Disorders*, pp 95–101. American Academy of Orthopaedic Surgeons, 1995

[207] Schinagl RM, Gurskis D, Chen AC, Sah RL: Depth-dependent confined compression modulus of full-thickness bovine articular cartilage. *J Orthop Res*, 15:499–506, 1997

[208] Schinagl RM, Ting MK, Price JH, Sah RL: Video microscopy to quantitate the inhomogeneous equilibrium strain within articular cartilage during confined compression. *Ann Biomed Eng*, 24:500–512, 1996

[209] Schwann HP: Alternating current electrode polarization. *Biophysik*, 3:181–201, 1966

[210] Seradge H: Perichondrial resurfacing of the hand. *J Hand Surg [Am]*, 9:880–886, 1984

[211] Setton LA, Mow VC, Müller FJ, Pita JC, Howell DS: Mechanical properties of canine articular cartilage are significantly altered following transection of the anterior cruciate ligament. *J Orthop Res*, 12:451–463, 1994

[212] Shapiro SD, Fliszar CJ, Broekelmann TJ, Mecham RP, Senior RM, Welgus HG: Activation of the 92-kd gelatinase by stromelysin and 4-aminophenyl mercuric acetate. Differential processing and stabilization of the carboxyl-terminal domain by tissue inhibitor of metalloproteinases (TIMP). *J Biol Chem*, 270:6351–6356, 1995

[213] Shlopov BV, Lie WR, Mainardi CL, Cole AA, Chubinskaya S, Hasty KA: Osteoarthritic lesions: Involvement of three different collagenases. *Arthritis Rheum*, 40:2065–2074, 1997

[214] Simon WH, Friedenberg S, Richardson S: Joint congruence: a correlation of joint congruence and thickness of articular cartilage in dogs. *J Bone Joint Surg*, 55A:1614–1620, 1973

[215] Sonin AA: Physical basis of dimensional analysis. Technical report, Massachusetts of Technology, 1992

[216] Stegemann H: Mikrobestimmung von hydroxyprolin mit chloramin-t und p-dimethylaminobenzaldehyd. *Hoppe-Seylers Z Physiol Chem*, 311:41–45, 1958

[217] Stegemann H, Stalder K: Determination of hydroxyproline. *Clin Chim Acta*, 18:267–273, 1967

[218] Stockwell RA: The cell density of human articular and costal cartilage. *J Anat*, 101:753–763, 1967

[219] Stockwell RA, Meachim G: The chondrocytes. In MAR Freeman, editor, *Adult Articular Cartilage, 2nd ed.*, pp 69–144. Pitman, Tunbridge Wells, England, 1979

[220] Strobel M, Stedtfeld H: *Diagnostic Evaluation of the Knee*, pp 276–316. Springer-Verlag, New York, 1990

[221] Sumner DR, Koepp H, Berzins A, Eger W, Muehleman C, Cole AA, Kuettner KE: Bone density of the human talus does not vary as a function of the cartilage damage score. *Trans Orthop Res Soc*, 23:722, 1998

[222] Swann AC, Seedhom BB: The stiffness of normal articular cartilage and the predominant acting stress levels: Implications for aetiology of osetoarthrosis. *Br J Rheum*, 32:16–25, 1993

[223] Teixeira CC, Hatori M, Leboy PS, Pacifici M, Shapiro IM: A rapid and ultrasensitive method for the measurement of DNA, calcium and protein content, and alkaline phosphatase activity of chodrocyte cultures. *Calcif Tissue Int*, 56:252–256, 1995

[224] Tkaczuk H: Human cartilage stiffness. *in vivo* studies. *Clin Orthop*, 206:301–312, 1986

[225] Treppo S, Berkenblit SI, Bombard DL, Frank EH, Grodzinsky AJ: Physical diagnostics of cartilage degeneration. In *Advances in Osteoarthritis*, pp 59–73. Springer-Verlag, Tokyo, 1999

[226] Treppo S, Koepp H, Quan EC, Cole AA, Kuettner KE, Grodzinsky AJ: Comparison of biomechanical and biochemical properties of cartilage from human knee and ankle pairs. *Trans Orthop Res Soc*, 23:202, 1998

[227] Treppo S, Otterness IG, Milici AJ, Berkenbilt SI, Grodzinsky AJ: Effects of MMP-1 and MMP-13 induced matrix degradation on electrokinetic and dielectric properties of adult articular cartilage by surface spctroscopy. *Trans Orthop Res Soc*, 23:153, 1998

[228] Trippel SB, Mankin HJ: Traumatic disorders of the knee. In JM Salinski, editor, *Articular cartilage injury and Repair*. Springer-Verlag, 1994

[229] Trippel S: Autologous chondrocyte transplantation. *N Engl J Med*, 332:539–540, 1995

[230] Unsworth A: Tribology of human and artificial joints. *Proc Inst Mech Eng*, 205:163–172, 1991

[231] Urban JPG, Maroudas A, Bayliss MT, Dillon J: Swelling pressures of proteoglycans at the concentrations found in cartilaginous tissues. *Biorheology*, 16:447–464, 1979

[232] Urban MR, Fermor B, Lee RB, Urban JPG: Measurement of DNA in intervertebral disk and other autofluorescent cartilages using dye hoechst 33258. *Anal Biochem*, 262:85–88, 1998

[233] Vankemmelbeke M, Dekeyser PM, Hollander AP, Buttle DJ, Demeester J: Characterization of helical cleavages in type II collagen generated by matrixins. *J Biochem*, 330:633–640, 1998

[234] Vignon E, Arlot M: Macroscopically normal cartilage from the human osteoarthritic femoral head. I. Histological evaluation. *J Rheumatol*, 8:440–446, 1981

[235] Vincenti MP, Coon CI, A MJ, Yocum S, Mitchell P, Brinckerhoff CE: Cloning of the gene for interstital collagenase-3 (matrix metalloproteinase-13) from rabbit synovial fibroblasts: Differential expression with collagenase-1 (matrix metalloproteinase-1). *J Biochem*, 131:341–346, Apr 1998

[236] Voet D, Voet JG: *Biochemistry*. J. Wiley & Sons, Toronto, second edition, 1995

[237] von Guggenberg PA, Melcher JR: A three-wavelength flexible sensor for monitoring the moisture content of transformer pressboard. In *3rd International Conference on Properties and Applications of Dielectric Materials*, pp 1262–1265. IEEE, 1991

[238] Vunjak-Novakovic G, Freed LE, Biron RJ, Langer R: Effects of mixing on the composition and morphology of tissue engineered cartilage. *AIChE J*, 42:850–860, 1996

[239] Vunjak-Novakovic G, Martin I, Obradovic B, Treppo S, Grodzinsky AJ, Langer R, Freed LE: Bioreactor cultivation conditions modulate the composition and mechanical properties of tissue engineered cartilage. *J Orthop Res*, 1999 (in press)

[240] Wakitani S, Kimura T, Hirooka A, Ochi T, Yoneda M, Yasui N, Owaki H, Ono K: Repair of rabbit articular cartilage surfaces with allograft chondrocytes embedded in a collagen gel. *J Bone Joint Surg [Br]*, 71:74–80, 1989

[241] Walter H, Kawashima A, Nebelung W, Neumann W, Roessner A: Immunohistochemical analysis of several proteolytic enzymes as parameters of cartilage degradation. *Pathol Res Pract*, 194:73–81, 1998

[242] Walter JH, Spector A: Traumatic osteoarthrosis of the ankle joint secondary to ankle fractures. *J Am Podiatric Med*, 81:399–405, 1991

[243] White FM: *Fluid Mechanics*. McGraw-Hill, Toronto, second edition, 1986

[244] Woessner JF: The determination of hydroxyproline in tissue and protein samples containing small proportions of this imino acid. *Arch Biochem Biophys*, 93:440–447, 1961

[245] Woessner JF Jr: Matrix metalloproteinases and their inhibitors in connective tissue remodeling. *FASEB J*, 5:2145–2154, 1991

[246] Woessner JF Jr: Inhibition of matrix metalloproteinasesl therapeutic potential. In RA Greenwald, LM Golub, editors, *The Family of Matrix Metalloproteinases*, volume 732, pp 11–21. The New York Academy of Sciences, New York, New York, 1994

[247] Wong M, Wuethrich P, Buschmann MD, Eggli P, Hunziker E: Chondrocyte biosynthesis correlates with local tissue strain in statically compressed adult articular cartilage. *J Orthop Res*, 15:189–96, 1997

[248] Woo SL, Kwan MK, Lee TQ, Field FP, Kleiner JB, Coutts RD: Perichondrial autograft for articular cartilage. Shear modulus of neocartilage studied in rabbits. *Acta Orthop Scand*, 58:510–515, 1987

[249] Xu L, Strauch RJ, Ateshian GA, Pawluk RJ, Mow VC, Rosenwasser MP: Topography of the osteoarthritic thumb carpometacarpal joint and its variation with regard to gender, age, site, and osteoarthritic stage. *J Hand Surg [Am]*, 23A:454–464, 1998

[250] Yao JQ, Seedhom BB: Mechanical conditioning of articular cartilage to prevalent stresses. *Br J Rheum*, 32:956–965, 1993

[251] Zaretsky MC, Mouayad L, Melcher JR: Continuum properties from interdigitated electrode dielectrometry. *IEEE Trans Electr Insul*, 23:897–917, 1988